DEPARTAMENT OF CHEMISTRY

CHALCOGEN-DOPED LUMINESCENT ZEOLITES FOR NEAR-INFRARED APPLICATIONS

CATARINA SOFIA MIRANDA VIOLA

Master in BioOrganic Chemistry

DOCTORATE IN CHEMISTRY

NOVA University Lisbon

July, 2024

DEPARTAMENT OF CHEMISTRY

CHALCOGEN-DOPED LUMINESCENT ZEOLITES FOR NEAR-INFRARED APPLICATIONS

CATARINA SOFIA MIRANDA VIOLA

Master in BioOrganic Chemistry

Adviser: João Carlos dos Santos Silva e Pereira de Lima
Full Professor, NOVA School of Science and Technology

Co-advisers: Andreia Filipa Cardoso Ruivo
Assistant Researcher, NOVA School of Science and Technology

João Miguel Ribeiro Avó
Assistant Researcher, NOVA School of Science and Technology

Examination Committee:

Chair: António Jorge Dias Parola,
Full Professor, NOVA School of Science and Technology

Rapporteurs: Svetlana Mintova,
Director of Research do Laboratoire Catalyse et Spectrochimi, France

Luís António Ferreira Martins Dias Carlos,
Full Professor, Aveiro University

Adviser: João Miguel Ribeiro Avó,
Assistant Researcher, NOVA School of Science and Technology

Members: Fernando Manuel Baião Dias,
Associate Professor, Durham University

António Jorge Dias Parola,
Full Professor, NOVA School of Science and Technology

César António Tonicha Laia,
Assistant Professor, NOVA School of Science and Technology

DOCTORATE IN CHEMISTRY

NOVA University Lisbon
July, 2024

Chalcogen-doped Luminescent Zeolites for Near-Infrared Applications

Copyright © Catarina Sofia Miranda Viola, NOVA School of Science and Technology, NOVA University Lisbon.

The NOVA School of Science and Technology and the NOVA University Lisbon have the right, perpetual and without geographical boundaries, to file and publish this dissertation through printed copies reproduced on paper or on digital form, or by any other means known or that may be invented, and to disseminate through scientific repositories and admit its copying and distribution for non-commercial, educational or research purposes, as long as credit is given to the author and editor.

To everyone who helped me during this journey,
especially to my family, for their
unconditional support.

ACKNOWLEDGMENTS

First of all, I would like to express my gratitude to the Cultural Heritage and Responsive Materials (CHARM) group and the Glass and Ceramic for the Arts (VICARTE) group for supporting my PhD thesis. I would also like to thank my supervisor, Professor João Carlos Lima, for accepting me under his guidance, even though it was unexpected. His vast knowledge about literally everything was incredibly enriching during these years. I would like to thank my co-supervisor, Andreia Ruivo, for all her knowledge, patience, and availability. She was always tireless in her support. I would also like to thank my co-supervisor, João Avó, for his critical analysis and always giving me the other perspective.

To all of the above, thank you for being my mentors, for the challenge, and for trusting in me (sometimes too much) during this time.

I would like to offer my special thanks to Professor Fernando Pina for his encouragement and interest in my work (maybe next time it will involve anthocyanins). He was always incredibly enthusiastic and ready to share his vast knowledge. I would like to express my sincere gratitude to Professor César Laia for always being supportive and introducing me to this zeolite world. I would like to extend my sincere thanks to Dr. Eduardo Coutiño González for the important insights he provided during this thesis, which guided me to a better outcome.

I would like to acknowledge Dr. Svetlana Mintova for the great opportunity she gave me to spend one month in her LCS group in Caen, France. She was always incredibly generous and welcoming. A special thanks to Sajjad Ghojavand for all his patience and time. Without him, this experience would not have been the same. I learned so much about nanomaterials and met many good people during this time.

Next, I would like to thank Dr. Mani Outis, Professor Luís Filipe Ferreira, Dr. Luís Alves, and Professor Miguel Teixeira for their crucial contributions to the work developed in this thesis, which allowed me to work with a wide variety of different characterizations. A special thanks

to Filipe Folgosa, who was always available for a good scientific discussion. He made me believe that EPR spectroscopy was easy.

To all individual members of the CHARM group and VICARTE group, thank you for walking beside me during this journey. The experienced ones: Artur Moro, Nuno Basílio, Cláudia Pereira, Sandra Gago and my colleagues Andreia Forte, Ana Lúcia, Carina Figueiredo, Tiago Moreira, Joana Martins, Miriam Colaço, André Seco, Liliana Gomes, Ambrósio Camuenho, Ana Pinheiro, Mani Outis, Ângela Santos, Carla Machado, Catarina Santos, Fernanda Carvalho, and all the others! I would also like to thank Clara Gomes and Vítor Rosa. Thank you for everything, especially the fun times.

I would like to give a special thanks to Cremilde, who always helped me when I needed it, and to José Luís, who never said 'no' to my crazy ideas and even made them come to life. A huge part of the success of this thesis is due to him.

This thesis would not have been possible without the financial support granted by Fundação para a Ciência e Tecnologia under the scholarship SFRH/BD/145009/2019.

Finalmente, quero agradecer à minha família: Mãe, Pai, Luís, aos meus avós, e a todos os outros. Muito obrigada pelo apoio incondicional!

"No amount of experimentation can ever prove me right;
a single experiment can prove me wrong."
(Albert Einstein).

ABSTRACT

The exploration of new near-infrared (NIR) luminescent materials has gained significant attention due to their potential in optical communications, anticounterfeiting, and bioimaging applications. However, many existing materials face low availability and photo- and chemical stability challenges. Addressing these limitations requires the development of new emitters. In this thesis, NIR emission was achieved using available and sustainable materials by synthesizing chalcogen-doped zeolites with varying chalcogen-to-chloride ratios. A comprehensive photophysical characterization employing various optical and structural techniques and computational calculations was conducted. NIR-emitting zeolites were obtained at high S/Cl and Se/Cl ratios, with the responsible emitters tentatively assigned to novel $[S_3]^{2-}$ and $[Se_3]^{2-}$ species. Tellurium was also explored, with a NIR emission detected at low Te/Cl ratios due to the presence of $[Te_2]^-$ clusters. In this system, the presence of the larger species, $[Te_3]^{2-}$, at high Te/Cl ratios was not conclusive. However, the photoluminescence decay times suggest the presence of a second emitting species besides $[Te_2]^-$. External quantum efficiencies, photoluminescence decay times, electron paramagnetic resonance spectra, and emission and excitation spectra of these several chalcogen-emitting clusters were reported for the first time. Proof-of-concept demonstrations were conducted in security systems and phosphor-converted NIR LEDs (pc-NIR LEDs) for veins imaging. Additionally, the synthesis of highly dispersible selenium NIR-emitting nanozeolites was attempted for application in *in vivo* imaging. The choice of this chalcogen was driven by its availability and photophysical properties of the NIR emitter, characterized by excitation at 400 nm and emission at 820 nm. Dispersibility studies demonstrated that the optimal approach to handling these nano-sized materials is to work exclusively in solution, ensuring high dispersibility and preventing aggregation issues. Alternatively, high-temperature solid-state synthesis using nanozeolites led to the first report of single selenium NIR-emitting

zeolites, contrasting with the previously observed mixture of red-emitting $[Se_2]^-$ and NIR-emitting $[Se_3]^{2-}$ clusters.

Keywords: Chalcogen-doped zeolites, Near-infrared emission, Luminescent materials, Photophysical characterization, Nanozeolites, High-temperature synthesis

---

RESUMO

O desenvolvimento de novos materiais luminescentes no infravermelho próximo (NIR) tem recebido uma atenção significativa devido ao seu potencial em comunicações ópticas, combate à contrafação e aplicações de bioimagem. No entanto, muitos dos materiais existentes enfrentam desafios relacionados com a sua baixa disponibilidade e com a sua fotoestabilidade e estabilidade química. Abordar estas limitações requer o desenvolvimento de novos emissores. Nesta tese, a emissão NIR utilizando materiais disponíveis e sustentáveis foi alcançada através da síntese de zeólitos dopados com calcogénios, usando para tal diferentes rácios calcogénio/cloro. Foi realizada uma caracterização fotofísica abrangente utilizando diversas técnicas ópticas e estruturais assim como cálculos computacionais. Os zeólitos emissores de NIR foram obtidos a elevados rácios S/Cl e Se/Cl, com os emissores responsáveis sendo atribuídos à provável presença das espécies novas $[S_3]^{2-}$ e $[Se_3]^{2-}$. O telúrio também foi investigado, com uma emissão de NIR detetada a baixos rácios Te/Cl devido à presença dos aglomerados $[Te_2]^{-}$. Neste sistema, a presença de espécies maiores, $[Te_3]^{2-}$, a elevados rácios Te/Cl, não foi conclusiva. No entanto, os tempos de decaimento da fotoluminescência sugerem a presença de uma segunda espécie emissora além de $[Te_2]^{-}$. As eficiências quânticas externas, os tempos de decaimento da fotoluminescência, assim como os espetros de ressonância paramagnética eletrónica e os espetros de emissão e excitação destes vários aglomerados de calcogénio emissores foram obtidos pela primeira vez. Demonstrações de prova de conceito em sistemas de segurança e de LEDs NIR convertidos por fósforo (pc-NIR LEDs) para imagem de veias foram bem-sucedidas. Além disso, a síntese de nanozeólitos altamente dispersáveis dopados com selénio e emissoras de NIR foi tentada para aplicação em sistemas de imagens *in vivo*. A escolha deste calcogénio foi motivada pela sua disponibilidade e propriedades fotofísicas do respetivo emissor NIR, caracterizado por uma excitação a 400 nm e uma emissão a 820 nm. Os estudos de dispersão demonstraram que a abordagem óptima para lidar com estes

nanomateriais é trabalhar exclusivamente em solução, garantindo uma alta dispersão e prevenindo problemas de agregação. Alternativamente, a síntese a altas temperaturas em estado sólido utilizando nanozeólitos levou ao primeiro estudo de zeólitos exibindo exclusivamente uma emissão NIR, contrastando com a mistura previamente observada de aglomerados $[Se_2]^-$ emissores no vermelho e de aglomerados $[Se_3]^{2-}$ emissores no NIR.

Palavras chave: Zeólidos dopados com calcogénios, Região do infravermelho próximo, Materiais luminescentes, Caraterização fotofísica, Nanozeólitos, Síntese a altas temperaturas

---

CONTENTS

ACKNOWLEDGMENTS IX

ABSTRACT XIII

RESUMO XV

CONTENTS XVII

LIST OF FIGURES XXIII

LIST OF SCHEMES XLIII

LIST OF TABLES XLV

ABBREVIATION LIST XLIX

1 INTRODUCTION 1

1.1 Motivation and Aim of the Dissertation 1

1.1.1 Motivation 1

1.1.2 Aim 2

1.2 Thesis Layout 3

1.3 Near-infrared (NIR) region 5

1.3.1 NIR emitting applications 7

1.4 Sodalite zeolite 16

1.4.1 Solid-state synthesis of sodalite 18

1.4.2 Optical properties of chalcogen-doped sodalite 22

2 NIR-EMITTING SULFUR-DOPED ZEOLITES 37

2.1 Influence of NaCl and Synthesis Duration on Optical Properties 40

2.1.1 Synthesis and structural characterization 41
2.1.2 Optical properties 45
2.1.3 Conclusions 50
2.2 Impact of Starting from Sodalite Zeolite Instead of Na-LTA Zeolite on Optical Properties 51
2.2.1 Synthesis and structural characterization 51
2.2.2 Optical characterization 53
2.2.3 Samples comparison starting from Na-LTA and from sodalite zeolites 57
2.2.4 Conclusions 59
2.3 Unraveling NIR Emission and Applicability of Sulfur-Doped Zeolites 61
2.3.1 Synthesis and structural characterization 61
2.3.2 Optical and NIR emission characterization 65
2.3.3 Computational studies 83
2.3.4 Suitable applications for these materials 85
2.3.5 Conclusions 86
2.4 General Chapter Conclusions 89
3 SELENIUM-DOPED ZEOLITES: EXPLORING RED AND NIR EMISSIONS AND THEIR APPLICABILITY 91
3.1 Synthesis and structural characterization 92
3.2 Absorption spectra 94
3.3 Emission and excitation spectra 96
3.4 Red emission 99
3.4.1 Temperature studies 104
3.5 NIR emission 109
3.5.1 Temperature studies 113
3.6 NIR-emitting species and their location in the aluminosilicate matrix 117
3.7 Applications of the NIR emitters 124
3.8 Conclusions 126

4 SELENIUM-DOPED EMITTING NANOZEOLITES 129
4.1 Single NIR-Emitting Selenium-Doped Zeolites Starting From Nanozeolites 132
4.1.1 Synthesis and structural characterization 132
4.1.2 Optical and NIR photophysical characterization 142
4.1.3 Conclusions 155
4.2 Exploring Several Synthetic Strategies to Obtain NIR-Emitting Nanozeolites 157
4.2.1 Dispersibility studies of non-doped nanosodalite zeolites 157
4.2.2 Solid-state reduction 159
4.2.3 Selenium reduction in solution 173
4.2.4 Conclusions 177
5 NIR-EMITTING TELLURIUM-DOPED ZEOLITES 179
5.1 Synthesis and structural characterization 179
5.2 Optical characterization 181
5.3 Conclusions 196
6 GENERAL CONCLUSIONS AND FUTURE PERSPECTIVES 199
7 MATERIALS AND METHODS 205
7.1 Synthesis 205
7.1.1 High-temperature synthesis starting from commercial Na-LTA zeolite 205
7.1.2 Sol-gel synthesis of nanosodalite zeolite 207
7.1.3 High-temperature synthesis starting from nanosodalite zeolite 208
7.1.4 Selenium precursor solid-state reduction 208
7.1.5 Reduction of selenium-doped nanosodalites in solution 209
7.1.6 Selenium precursor reduction in solution 209
7.2 Experimental Techniques and Sample Characterization 209
7.2.1 Absorption Spectroscopy 209
7.2.2 Diffuse Reflectance Spectroscopy 211
7.2.3 Steady-State Emission 213

7.2.4 Photoluminescence Decay Times 216
7.2.5 Time-Resolved Emission Spectroscopy (TRES) 218
7.2.6 Transient Absorption (TA) spectroscopy 220
7.2.7 Electron Paramagnetic Resonance (EPR) spectroscopy 223
7.2.8 Micro-Raman Microscopy 224
7.2.9 Dynamic Light Scattering (DLS) 225
7.2.10 Particle-Induced X-ray Emission (PIXE) 227
7.2.11 Wavelength Dispersive X-ray Fluorescence (WDXRF) 229
7.2.12 Differential Scanning Calorimetry (DSC) 229
7.2.13 Powder X-Ray Diffraction (PXRD) 230
7.2.14 Scanning Electron Microscopy (SEM) 232
7.2.15 Transmission Electron Microscopy (TEM) 233
7.2.16 Computational Studies 234
7.3 Dispersibility studies of non-doped nanosodalites 236
7.4 External quantum efficiencies calculations of phosphorescent species in a mixture with two emitting species 236
7.5 Humidity/water-sensitive emission studies 240
7.6 Oxygen-sensitive emission studies 241
8 WORK DISSEMINATION 243
8.1 Papers Contributing to the Dissertation 243
8.2 Other Research Papers 243
8.3 Communications in Conferences 243
BIBLIOGRAPHY 245
A APPENDIX: CHAPTER 2 255
B APPENDIX: CHAPTER 3 263
C APPENDIX: CHAPTER 4 273
D APPENDIX: CHAPTER 5 281

I ANNEX: CHAPTER 4 283
Selenium reduction in solution 283

LIST OF FIGURES

Figure 1.3.1 - Electromagnetic spectrum from UV to far-infrared regions, based on IUPAC recommendations[23]. 5

Figure 1.3.2 - Overview of the most commonly used NIR emitters (both organic and inorganic), with a particular emphasis on the chalcogen species that will be studied in this thesis. Additionally, some NIR applications are also referenced. D-A-D stands for donor-acceptor-donor molecules; RENPs stand for rare-earth nanoparticles and CNTs stand for carbon nanotubes. Adapted from reference **33**. 6

Figure 1.3.3 - (**A**) Structure of the GRPR-targeted NIR probe. (**B**) Absorption and emission spectra of the free-NIR probe (without the RM26). This probe is based on a D-A-D scaffold. Adapted from reference **35**. 7

Figure 1.3.4 - NIR images of PC3 tumor-bearing mice (n=3 per group) at different times (2, 4, 8, 12 and 36h) after tail vein injection of GRPR-targeted NIR probe with or without blocking agent RM26 under 808 nm excitation. Note that the white arrows represent the site where the tumor is. Adapted from reference **35**. 8

Figure 1.3.5 - Driven current-dependent electroluminescence spectra of the fabricated pc-NIR-LED with $K_2NaInF_6:Cr^{3+}$. The insets show photographs of the produced NIR LED. Adapted from reference **38**. 10

Figure 1.3.6 - **NIR application of pc-LED with $K_2NaInF_6:Cr^{3+}$ for veins imaging** - (**A**) Illustration of hand veins imaging using a high-power NIR LED device in its as-fabricated state. (**B**) Photographs of **1)** the illuminated NIR device and the transmission photographs of the veins in the **2)** fingers, **3)** palm and **4)** wrist taken with a NIR camera. Adapted from reference **38**.. 10

Figure 1.3.7 - Driven current-dependent electroluminescence spectra of the fabricated pc-NIR-LED with $K_3LuSi_2O_7:Eu^{2+}$. The insets show photographs of the produced NIR LED. Adapted from reference **39**. 11

Figure 1.3.8 - **NIR application of pc-LED with $K_3LuSi_2O_7:Eu^{2+}$ for the non-visible light source -** Photographs under **1)** natural light, **2)** without light and **3)** under NIR pc-LED light, captured by the corresponding visible and NIR camera. Adapted from reference **39**. 12
Figure 1.3.9 - Emission spectra of single-doped Sb^{3+}- $Cs_2NaLuCl_6$ perovskite and Sb^{3+}/Sm^{3+}-codoped $Cs_2NaLuCl_6$ perovskite. Adapted from reference **40**. 13
Figure 1.3.10 - Demonstration of the applicability of the NIR emitting material as an anticounterfeiting tag. Adapted from reference **40**. 14
Figure 1.3.11 - Emission spectra of fiber and bulk-doped glass. Adapted from reference **41**. 15
Figure 1.3.12 - Process of fiber fabrications through rod-in-tube technique. Adapted from reference **41**. 15
Figure 1.4.1 - Examples of applications in which zeolites are used. 17
Figure 1.4.2 - Composition of β-cages (sodalite cages), which link together to form the sodalite zeolite structure. 17
Figure 1.4.3 - Structures of $[Na_4Cl]^{3+}$ tetrahedron and the four $[NaO_3Cl]$ tetrahedrons inside the β-cage. Chloride is represented in green, sodium in pink and oxygen in red. 18
Figure 1.4.4 - Structures of Na-FAU, Na-LTA and sodalite zeolites and their building units. 19
Figure 1.4.5 - Two chloride ions (in two adjacent β-cages) are substituted by one $[S_2]^{2-}$ cluster, creating a chloride vacancy (V_O). 23
Figure 1.4.6 - Proposed photochromism mechanism of sulfur- and selenium-doped sodalites. Adapted from references **80** and **83**. 24
Figure 1.4.7 - Diffuse reflectance spectra of sulfur- and selenium-doped sodalites before and after UV irradiation. Δ symbol represents heat. Adapted from references **80** and **83**. 25
Figure 1.4.8 - General diagram of molecular orbitals of ground and excited states of the luminescent chalcogen diatomic radical species, where n = 3, 4 e 5 for S, Se e Te, respectively. 26
Figure 1.4.9 - Resume of the absorption (dotted) and emission (line) spectra of the diatomic chalcogen radicals. Adapted from references **19**, **78**, **87** and **86**. 28
Figure 1.4.10 - Proposed mechanism of the persistent luminescence phenomenon found in sulfur-doped sodalites. Adapted from references **75**, **81** and **88**. 29
Figure 1.4.11 - Persistent luminescence spectra of sulfur-doped samples after applying a 1-minute delay using two different wavelengths (254 and 365 nm). The insets show photographs of the produced samples. Adapted from reference **75**. 29

Figure 1.4.12 - (**A**) Color intensity of sulfur-doped sodalite after 10 seconds of exposure to different UVC doses. (**B**) Fabric knitted from 3.5% of sodalite in (A.) staple fibers and its color intensity dependency with UVC dose. Adapted from references **22** and **89**. 30
Figure 1.4.13 - Illustration of a smartphone application developed by Laine et al.[90] for this specific system, allowing the user to estimate the UV index. Adapted from references **22** and **89**. 31
Figure 1.4.14 - (**A**) Diffuse reflectance spectra of two irradiated samples considered for wavelength-sensitive photochromism. (**B**) Corresponding induced-color intensities according to the excitation wavelength. Adapted from reference **80**. 31
Figure 1.4.15 - (**A**) Diffuse reflectance maximum for a similar mix to that present in **Figure 1.4.14** concerning the excitation wavelength. (**B**) A film created from a sodalite mix, marked with the inscription 'IMC', after irradiation with different UV radiation. Adapted from reference **80**. 32
Figure 1.4.16 - (**A**) Emission spectra of starting sulfur-doped sodalite and Ag-exchanged sulfur-doped sodalite, with insets of photographs of samples under 350 nm excitation. (**B**) **Left -** Film of the Ag-exchanged sulfur-doped sodalite, excited by a NUV-LED (340 nm); **Right -** NUV-LED (340 nm). Adapted from references **20** and **91**. 33
Figure 1.4.17 - (**A**) Fading of the persistent luminescence over time after 30 minutes of excitation at 254 nm. The inset shows the corresponding emission spectra of this emission and photographs of this material taken at different times. (**B**) Performance of this material as a phosphor with 310 nm LED excitation followed by glow in the dark. Adapted from reference **88**. 34
Figure 1.4.18 - Transmission Electron Microscopy (TEM) images of $LiNa_7[Si_6Al_6O_{24}](S,Cl)_2$:2%Ti sodalite particles in powder form and aqueous suspensions. Adapted from reference **88**..... 35
Figure 1.4.19 - **Graph:** Effect of $LiNa_7[Si_6Al_6O_{24}](S,Cl)_2$:2%Ti sodalite particle concentration on persistent luminescence intensity observed in aqueous suspension. **Top photograph:** Persistent luminescent in an aqueous suspension with a concentration of 5 mg/mL after 1 min irradiation by a solar simulator lamp (1000 W/m^2). **Bottom photograph:** aqueous suspension under excitation of a 310 nm LED. These photographs were captured using a standard cell phone camera (Nokia Lumia 520). Adapted from reference **88**. 35
Figure 2.1 - Lapis lazuli art pieces present in The Metropolitan Museum of Art, New York - (**Left**) Frog Amulet and (**Right**) Amulet, Ptah[97]. 39
Figure 2.1.1 - (**A**) PXRD diffractograms of sample S/Cl=0.21 according to the synthesis time, comparing with the ICDD standard reference card of 01-086-1844 sodalite ($Na_8Si_6Al_6O_{24}Cl_2$),

00-035-0424 nepheline ($NaSiAlO_4$) and 00-011-0220 carnegieite ($NaSiAlO_4$). (**B**) Corresponding calculated relative phases. 42
Figure 2.1.2 - (**A**) PXRD diffractograms of sample S/Cl=4.5 according to the synthesis time, comparing with the ICDD standard reference card of 01-086-1844 sodalite ($Na_8Si_6Al_6O_{24}Cl_2$), 00-035-0424 nepheline ($NaSiAlO_4$) and 00-011-0220 carnegieite ($NaSiAlO_4$). (**B**) Corresponding calculated relative phases. 43
Figure 2.1.3 - PXRD diffractograms of synthesized samples after 1 hour at 900 °C using S/Cl=0.21 and 4.5 (lighter colors) and corresponding samples with a NaCl excess (darker colors) while comparing the ICDD standard reference cards of sodalite, nepheline and carnegieite phases. 44
Figure 2.1.4 - Diffuse reflectance spectra of samples with S/Cl=0.21 (**A**) and S/Cl=4.5 (**B**) using different synthesis times and a NaCl excess. The insets show photos of the samples under ambient light. 46
Figure 2.1.5 - Emission (**A**) and excitation (**B**) spectra of samples based on S/Cl=0.21, monitoring the $[S_2]^-$ species at λ_{exc}=380 nm and λ_{em}=650 nm. The insets show the corresponding spectra normalized. 47
Figure 2.1.6 - Emission (**A**) and excitation (**B**) spectra of samples based on samples with S/Cl=0.21, monitoring the NIR-emitting species at λ_{exc}=355 nm and λ_{em}=720 nm. The insets show the corresponding spectra normalized and photos of the samples under UV light, λ_{exc}=365 nm. 48
Figure 2.1.7 - Emission (**A**) and excitation (**B**) spectra of samples based on samples with S/Cl=4.5, monitoring the $[S_2]^-$ species at λ_{exc}=380 nm and λ_{em}=650 nm. The insets show the corresponding spectra normalized. 48
Figure 2.1.8 - Emission (**A**) and excitation (**B**) spectra of samples based on samples with S/Cl=4.5, monitoring the NIR-emitting species at λ_{exc}=355 nm and λ_{em}=720 nm. The insets show the corresponding spectra normalized and photos of the samples under UV light, λ_{exc}=365 nm. 49
Figure 2.2.1 - (**A**) PXRD diffractograms of the synthesized samples using Na_2SO_3 as the sulfur precursor, along with the respective comparison with ICDD standard reference cards of sodalite, nepheline and carnegieite crystalline phases. (**B**) Corresponding calculated relative phases. 52
Figure 2.2.2 - (**A**) PXRD diffractograms of the synthesized samples using elemental sulfur (S) as the sulfur precursor, along with the respective comparison with ICDD standard reference cards

of sodalite, nepheline and carnegieite crystalline phases. (**B**) Corresponding calculated relative phases. 53
Figure 2.2.3 - Diffuse reflectance spectra of synthesized samples, using Na_2SO_3 and elemental sulfur as sulfur precursors. The insets show photos of the samples under ambient light. 54
Figure 2.2.4 - Emission (**A**) and excitation (**B**) spectra of $S_{0.3}$ Na_2SO_3 sample, monitoring the behavior of $[S_2]^-$ (λ_{exc}=380 nm and λ_{em}=650 nm) and the NIR-emitting species (λ_{exc}=355 nm and λ_{em}=720 nm). The insets show the corresponding normalized spectra and a photo of the samples under UV light, λ_{exc}=365 nm. 55
Figure 2.2.5 - Emission (**A**) and excitation (**B**) spectra of $S_{0.9}$ Na_2SO_3 sample, monitoring the behavior of $[S_2]^-$ (λ_{exc}=380 nm and λ_{em}=650 nm) and the NIR-emitting species (λ_{exc}=355 nm and λ_{em}=720 nm). The insets show the corresponding normalized spectra and a photo of the samples under UV light, λ_{exc}=365 nm. 55
Figure 2.2.6 - Emission and excitation spectra of the samples prepared from elemental sulfur, using $S_{0.3}$ (**A**) and $S_{0.9}$ (**B**) concentrations. The behavior of $[S_2]^-$ was monitored using λ_{exc}=380 nm and λ_{em}=650 nm (light gray) and the NIR-emitting species using λ_{exc}=355 nm and λ_{em}=720 nm (dark gray). The insets show the corresponding normalized spectra photos of the samples under UV light, λ_{exc}=365 nm. 56
Figure 2.2.7 - (**A**) Diffuse reflectance spectra of the four samples, varying the sulfur amount and the starting zeolite. Normalized spectra of the main absorption band of samples $S_{0.3}$ (**B**) and $S_{0.9}$ (**C**). 58
Figure 2.2.8 - Emission spectra of $S_{0.3}$ (**A**) and $S_{0.9}$ (**B**) samples, monitoring the behavior of $[S_2]^-$ species at λ_{exc}=380 nm and λ_{em}=650 nm and NIR-emitting species at λ_{exc}=355 nm and λ_{em}=720 nm. 59
Figure 2.3.1 - **Structural analysis of sulfur-doped zeolites samples –** (**A**) PXRD diffractograms of the synthesized sulfur-doped zeolites samples with different S/Cl ratios and the ICDD standard reference card of 01-086-1844 sodalite ($Na_8Si_6Al_6O_{24}Cl_2$), 00-035-0424 nepheline ($NaSiAlO_4$) and 00-011-0220 carnegieite ($NaSiAlO_4$). (**B**) Sodalite, nepheline and carnegieite fractions calculated in the synthesized zeolite samples. 62
Figure 2.3.2 - SEM images of the samples with S/Cl=0 (**A, B**), 0.21 (**C, D**) and 4.5 (**E, F**). 63
Figure 2.3.3 - TEM images of samples with S/Cl=0 (**A**, **B**), 0.21 (**C**) and 4.5 (**D**). 64
Figure 2.3.4 - Diffuse reflectance spectrum of samples with different S/Cl ratios. The inset on top depicts photos of the samples under ambient light. The inset on the right shows a close-up of the S/Cl=4.5 sample in the 450-750 nm region. 66

Figure 2.3.5 - (**A**) Steady-state emission spectra of samples with different sulfur content (λ_{exc}=355 nm). The inset on top depicts photos of the samples under UV light, with λ_{exc}=365 nm. (**B**) Excitation spectra of synthesized samples 0.06<S/Cl<0.33 **(left)** and 0.5<S/Cl<4.5 **(right)**, using λ_{em}=725 nm. 66
Figure 2.3.6 - Overlap of the diffuse reflectance spectrum (light-brown) with the excitation spectrum (dark-brown) of sample S/Cl=4.5. 67
Figure 2.3.7 - **Characterization of zeolite Na-LTA sample after 1 hour at 900 °C, under reductive atmosphere –** (**A**) Emission spectra (λ_{exc}=355 nm). (**B**) PXRD diffractogram and relative crystalline phases and comparison with the ICDD standard reference card of 00-035-0424 nepheline ($NaSiAlO_4$) and 00-011-0220 carnegieite ($NaSiAlO_4$)....68
Figure 2.3.8 - Raman spectra of samples S/Cl=0, 0.21 and 4.5 and commercial ultramarine blue pigment (UBP), used as a reference for $[S_3]^-$ cluster. 69
Figure 2.3.9 - Electron paramagnetic resonance (EPR) spectra of samples S/Cl=0, 0.21 and 4.5 and commercial ultramarine blue pigment (UBP), used as a reference for $[S_3]^-$ cluster. Note the multiplication factors applied in S/Cl=0 and 4.5 samples. For EPR spectra deconvolution, see **Figure A.1.1**. 70
Figure 2.3.10 - (**Above)** Photoluminescence decay of sample with S/Cl=4.5 (dotted line) and respective bi-exponential fitting (solid line) at 800 nm (λ_{exc} = 402.9 nm) and (**Below**) corresponding residuals. Note the decay components and respective relative amplitudes in brackets. 72
Figure 2.3.11 - Emission spectra after applying a delay time of 0.1 ms to samples with different S/Cl ratios, with λ_{exc}=380 nm....73
Figure 2.3.12 - **(Above)** Photoluminescence decay (dotted line) and respective bi-exponential fitting (solid line) at 800 nm (λ_{exc} = 402.9 nm) of zeolite Na-LTA sample after 1h at 900 °C, under reductive atmosphere. **(Below)** Corresponding residuals. 74
Figure 2.3.13 - (**A** and **B**) Time-resolved emission spectroscopy of sample S/Cl=4.5 at different delay times, DT, (λ_{exc}=337 nm) 75
Figure 2.3.14 - Transient absorption spectra at different delay times (λ_{exc}=266 nm) of sample S/Cl=4.5....76
Figure 2.3.15 - Emission and corresponding excitation spectra of sample S/Cl=0.21 at 77 K (green) and at room temperature (black). 77
Figure 2.3.16 - Normalized steady-state emission and excitation spectra of sample S/Cl=4.5 acquired at liquid nitrogen temperature (77 K) and at room temperature (RT). The red and

brown arrows indicate the two wavelengths at which the photoluminescence decays were recorded, as presented in **Figure 2.3.17** and **Figure 2.3.18**.....78
Figure 2.3.17 - Photoluminescence decay times of sample S/Cl=4.5 at liquid nitrogen temperature (77 K) and at room temperature (RT) monitoring the emission at 800 nm. The insets show the components resulting from the decay fittings (see the resulting residuals in **Figure A.1.2**) and the average decay time. In brackets is the relative amplitude of each component. Note that the average decay times were calculated using the pre-exponential factors. 79
Figure 2.3.18 - Photoluminescence decay times of sample S/Cl=4.5 at liquid nitrogen temperature (77 K) and at room temperature (RT) monitoring the emission at 600 nm. The insets show the components resulting from the decay fittings (see the resulting residuals in **Figure A.1.2**) and the average decay time. In brackets is the relative amplitude of each component. Note that the average decay times were calculated using the pre-exponential factors. 80
Figure 2.3.19 - Time-resolved emission spectra using a 0.2 millisecond delay time of S/Cl=4.5 sample, varying the temperature from 77 K to 348 K. 81
Figure 2.3.20 - Photoluminescence decay time of selected temperatures monitoring the emission at 800 nm of S/Cl=4.5 sample, using a 0.1 millisecond delay, varying the temperature from 77 K to 348 K. 82
Figure 2.3.21 - Relative amplitudes (**A**), decay time components and average decay times (**B**) of the fitted photoluminescence decay time present in **Figure 2.3.20**. 82
Figure 2.3.22 - **Computational studies –** (**A**) Overlap of the Kubelka-Munk spectrum of sample S/Cl=4.5 (green) and the combined calculated spectra of $[S_3]^{2-}$ and $[S_3]^{-}$ species (orange). (**B**) Proposed energy diagram of $[S_3]^{2-}$ clusters. 84
Figure 2.3.23 - **Prototypes using sulfur-doped zeolites as authentication and anticounterfeiting tags (Middle) and as NIR pc-LEDs (Below).** Photos were taken by a smartphone under ambient (**A, E**) and under UV illumination, around λ_{exc}=365 nm (**B-D** and **F-H**). Without any cutoff filter (**B**, **F**) and using a 665 nm (**C, G**) and a 780 nm (**D**, **H**) cutoff filters. **(Top).** Note the overlap between the emission spectra of the NIR-emitting sample and the transmission spectra of the cutoff filters used. The filled area under the curve represents the emission detected by the smartphone.....86
Figure 3.1 - **Structural analysis of selenium-doped zeolite samples –** (**A**) PXRD diffractograms of the synthesized selenium-doped zeolite samples with different Se/Cl ratios and the ICDD standard reference card of 01-086-1844 sodalite ($Na_8Si_6Al_6O_{24}Cl_2$), 00-035-0424 nepheline

($Na_4Si_4Al_4O_{16}$) and 00-011-0220 carnegieite ($Na_4Si_4Al_4O_{16}$). (**B**) Sodalite, nepheline and carnegieite relative phases calculated in the synthesized zeolite samples. 93
Figure 3.2 - Diffuse reflectance spectrum of samples with different Se/Cl ratios. Inset: photos of the samples under ambient light. 95
Figure 3.3 - **Spectral deconvolution of the experimental diffuse reflectance spectra –** (**A**) Combination of 350 and 490 nm absorption bands, assigned to $[Se_2]^-$ clusters. (**B**) Absorption band peaking at 400 nm. The insets show the calculated peak areas. 95
Figure 3.4 - Diffuse reflectance spectral deconvolution of the sample with Se/Cl=0.75. 96
Figure 3.5 - Steady-state emission spectra of samples with different Se/Cl ratios using different excitation wavelengths, λ_{exc}=350 nm (**A**) and λ_{exc}=490 nm (**B**). Inset: photos of the samples under UV light (λ_{exc}=365 nm). 97
Figure 3.6 - Excitation spectra of the synthesized samples monitoring the emission at 740 nm. 97
Figure 3.7 - Emission (**A**) and excitation (**B**) spectra of the synthesized samples, using λ_{exc}=400 nm and λ_{em}=800 nm, respectively. 98
Figure 3.8 - (**A**) External quantum efficiencies of samples with different Se/Cl ratios, using a 480 nm excitation. (**B**) Normalized emission spectra of all synthesized samples, exciting at 480 nm. 99
Figure 3.9 - Photoluminescence decay times (scatter) and respective fittings (solid line) of samples with different Se/Cl ratios, recorded with an λ_{exc}=445 nm and λ_{em}=750 nm. See residuals of the fittings in **Figure B.1**. 100
Figure 3.10 - Proposed illustration demonstrating the filling effect of sodalite cages according to Se/Cl ratios. Here, $[Se_2]^-$ species compete with chloride anions to occupy these cages. The blue circle has a radius of around 9 Å. 103
Figure 3.11 - Proposed double electron transfer mechanism illustrating the quenching phenomenon observed in these samples, attributed to interactions between $[Se_2]^-$ clusters. The diagram highlights the molecular orbitals involved in the $^2\Pi_g \leftrightarrow {}^2\Pi_u$ transitions of $[Se_2]^-$ species. 104
Figure 3.12 - Steady-state emission (λ_{exc}=480 nm) and excitation (λ_{em}=740 nm) spectra of sample Se/Cl=0.06 at 77 K (green) and at room temperature, RT (black). 105
Figure 3.13 - Steady-state emission (λ_{exc}=480 nm) and excitation (λ_{em}=740 nm) spectra of sample Se/Cl=4.5 at room temperature (RT) represented in black and at 77 K represented in green. 106

Figure 3.14 - Monitoring the disappearance of red emission of sample Se/Cl=4.5 through time-resolved measurements by varying the initial delay times in the nanosecond range, using an λ_{exc}=337 nm, at room temperature (RT) (**A**) and at 77 K (**B**). 107
Figure 3.15 - Normalized time-resolved emission spectra without a delay time (delay=0 ns) of sample Se/Cl=4.5 at room temperature (RT) represented in black and at 77 K represented in green. The red and brown arrows indicate the two wavelengths at which the photoluminescence decays were recorded, as presented in **Figure 3.16** and **Figure 3.17**. 107
Figure 3.16 - Photoluminescence decay times of sample Se/Cl=4.5 at liquid nitrogen temperature (77 K) and at room temperature (RT) monitoring the emission at 650 nm. The insets show the components resulting from the decay fittings (see the resulting residuals in **Figure B.3**) and the average decay time. In brackets is the relative amplitude of each component. Note that the average decay times were calculated using the pre-exponential factors. 108
Figure 3.17 - Photoluminescence decay times of sample Se/Cl=4.5 at liquid nitrogen temperature (77 K) and at room temperature (RT) monitoring the emission at 800 nm. The insets show the components resulting from the decay fittings (see the resulting residuals in **Figure B.3**) and the average decay time. In brackets is the relative amplitude of each component. Note that the average decay times were calculated using the pre-exponential factors. 109
Figure 3.18 - (**A**) External quantum efficiencies of samples with different Se/Cl ratios, using a 400 nm excitation. (**B**) Normalized emission spectra of all synthesized samples, exciting at 400 nm (**Figure 3.7.A** normalized). 110
Figure 3.19 - Photoluminescence decay times (scatter) and respective fittings (solid line) of samples with different Se/Cl ratios, recorded with an λ_{exc}=400 nm and λ_{em}=800 nm. See residuals of the fittings in **Figure B.4**. 111
Figure 3.20 - Spectra deconvolution of the emission steady-state present in **Figure 3.7.A** of red emission (**A**) and NIR emission (**B**). 112
Figure 3.21 - Steady-state emission (λ_{exc}=400 nm) and excitation (λ_{em}=800 nm) spectra of sample Se/Cl=4.5 at room temperature (RT) represented in black and at 77 K represented in green. 113
Figure 3.22 - Monitoring the disappearance of red emission and appearance of NIR emission of sample Se/Cl =4.5 through time-resolved measurements by varying the initial delay times (nanoseconds), using an λ_{exc}=337 nm, at room temperature (RT) (**A**) and at 77 K (**B**). 114

Figure 3.23 - Monitoring the disappearance of the NIR emission of sample Se/Cl =4.5 through time-resolved measurements by varying the initial delay times (microseconds), using an λ_{exc}=337 nm, at room temperature (RT) (**A**) and at 77 K (**B**). 114
Figure 3.24 - Normalized time-resolved emission spectra after applying 5 microseconds delay time (delay=5 μs) of sample Se/Cl=4.5 at room temperature (RT) represented in black and at 77 K represented in green. The red and brown arrows indicate the two wavelengths at which the photoluminescence decays were recorded, as presented in **Figure 3.25** and **Figure 3.26**. 115
Figure 3.25 - Photoluminescence decay times of sample Se/Cl=4.5 at liquid nitrogen temperature (77 K) and at room temperature (RT) monitoring the emission at 650 nm. The insets show the components resulting from the decay fittings (see the resulting residuals in **Figure B.6**) and the average decay time. In brackets is the relative amplitude of each component. Note that the average decay times were calculated using the pre-exponential factors. 116
Figure 3.26 - Photoluminescence decay times of sample Se/Cl=4.5 at liquid nitrogen temperature (77 K) and at room temperature (RT) monitoring the emission at 800 nm. The insets show the components resulting from the decay fittings (see the resulting residuals in **Figure B.6**) and the average decay time. In brackets is the relative amplitude of each component. Note that the average decay times were calculated using the pre-exponential factors. 117
Figure 3.27 - Electronic paramagnetic resonance (EPR) spectra of sample Se/Cl=0.06 recorded at different temperatures from 150 K to 30 K. 118
Figure 3.28 - Electronic paramagnetic resonance (EPR) spectra of samples Se/Cl=0.21 (**A**) and Se/Cl=0.75 (**B**) recorded at different temperatures from 150 K to 30 K. 119
Figure 3.29 - Electronic paramagnetic resonance (EPR) spectra of samples Se/Cl=4.5 (**A**) and Se/Cl=0 (**B**) recorded at different temperatures from 150 K to 30 K. 120
Figure 3.30 - (**A**) Comparison of all EPR signals recorded at 150 K (**B**) alongside their corresponding normalized signal areas. Note that the signals from samples Se/Cl=0 and 4.5 were not considered since their intensities are minimal. 120
Figure 3.31 - (**A**) Comparison of all EPR signals recorded at 30 K (**B**) alongside their corresponding normalized signal areas with the resonance at 150 K subtracted. Note that the signals from samples Se/Cl=0 and 4.5 were not considered since their intensities are minimal. 121

Figure 3.32 - Comparison between the experimental absorption of the NIR emitters and the simulated absorption spectra of $[Se_3]^{2-}$ (**A**) and $[Se_4]^{2-}$ (**B**) species. 124
Figure 3.33 - **Proof-of-concept of selenium-doped zeolites as anticounterfeiting and security tags –** (**A**) Representation of the depositions using three different mixtures; mixture 1 (non-emissive) containing a Hematite mineral and a non-reduced sodalite sample; mixture 2 (yellow-orange emission) with a Hematite mineral and sulfur-doped zeolites (sample S/Cl=0.06, from subchapter **2.3**); mixture 3 (yellow-orange and NIR emission) containing sulfur-doped zeolites and selenium-doped zeolites (sample Se/Cl=4.5, from this subchapter). **(B**, **C**, **D)** Photographs were taken by a standard photographic camera under (**B**) ambient light and under **(C**, **D)** 400 nm excitation, applying a 495 nm and 800 nm cutoff filter, respectively. 125
Figure 3.34 - **Proof-of-concept of selenium-doped zeolites as NIR pc-LEDs in veins imaging –** (**A**) Representation of the setup. (**B**, **C**) Veins photographs were taken by a standard photographic camera equipped with an infrared cutoff filter of (**B**) fingers and (**C**) hands. .. 126
Figure 4.1 - Examples of nanoparticles and their suitability as NIR emitters for *in vivo* applications. RE stands for rare-earth elements, Au for gold, IO for iron oxide, MSNs for mesoporous silica nanoparticles and CNTs for carbon nanotubes. Adapted from reference **131**. 130
Figure 4.1.1 - SEM image of sample Se_0 gel resulting from the sol-gel synthesis. 133
Figure 4.1.2 - PXRD diffractogram of sample Se0 gel and comparison with the simulated diffractogram of sodalite octahydrate, with the composition $[Na_6(H_2O)_8][Si_6Al_6O_{24}]$, according to reference **145**. 134
Figure 4.1.3 - (**A**) SEM images and (**B**) PXRD diffractograms of samples $Se_{0.1}$ gel and Se_1 gel. Note the comparison with the simulated diffractogram of sodalite octahydrate, with the composition $[Na_6(H_2O)_8][Si_6Al_6O_{24}]$ in black, according to reference **145**. 135
Figure 4.1.4 - SEM images of the samples submitted to high-temperature synthesis at 900 °C. 137
Figure 4.1.5 - SEM images of sample $Se_{0.1}$ - 900 °C using different magnifications. 138
Figure 4.1.6 - Dynamic light scattering (DLS) autocorrelation functions of non-thermally treated sample Se_0 gel (dashed, black) and thermally treated sample $Se_{0.1}$ - 900 °C (solid, gray). 139
Figure 4.1.7 - PXRD diffractograms of samples Se_0 gel - 900 °C, $Se_{0.1}$ gel - 900 °C and Se_1 gel - 900 °C. Comparison with the ICDD standard reference card of 01-086-1844 sodalite ($Na_8Si_6Al_6O_{24}Cl_2$), 00-035-0424 nepheline ($Na_4Si_4Al_4O_{16}$) and 00-011-0220 carnegieite ($Na_4Si_4Al_4O_{16}$) 141

Figure 4.1.8 - PXRD diffractograms of samples $Se_{0.1}$ - 900 °C and Se_1 - 900 °C. Comparison with the ICDD standard reference card of 01-086-1844 sodalite ($Na_8Si_6Al_6O_{24}Cl_2$), 00-035-0424 nepheline ($Na_4Si_4Al_4O_{16}$) and 00-011-0220 carnegieite ($Na_4Si_4Al_4O_{16}$). 142
Figure 4.1.9 - Diffuse reflectance spectra of the synthesized samples. The insets show the photos of the samples under ambient light. 143
Figure 4.1.10 - Diffuse reflectance spectral deconvolution of sample Se_1 - 900 °C. 144
Figure 4.1.11 - (**A**) Emission, λ_{exc}=400 nm, and (**B**) corresponding normalized spectra of the synthesized samples after the high-temperature synthesis at 900 °C. 145
Figure 4.1.12 - (**A**) Excitation, λ_{em}=800 nm, and (**B**) corresponding normalized spectra of the synthesized samples after the high-temperature synthesist at 900 °C 145
Figure 4.1.13 - (**A**) Emission, λ_{exc}=480 nm, and (**B**) corresponding normalized spectra of the synthesized samples after the high-temperature synthesist at 900 °C. The typical emission spectrum of $[Se_2]^-$ species found in the selenium-doped zeolites is represented in green, as discussed in **Figure 3.5.A-B**, chapter **3**. 146
Figure 4.1.14 - (**A**) Excitation, λem=740 nm, and (**B**) corresponding normalized spectra of the synthesized samples after the high-temperature synthesist at 900 °C. The typical excitation spectrum of $[Se_2]^-$ species found in the selenium-doped zeolites is represented in green, as discussed in **Figure 3.6**, chapter **3**. 147
Figure 4.1.15 - External quantum efficiencies of the synthesized samples exciting at 400 nm. 148
Figure 4.1.16 - Photoluminescence decay times of the synthesized samples at a nanosecond time scale, recorded with an λ_{exc}=445 nm and λ_{em}=750 nm. Comparing with the green line representing the photoluminescence decay times of $[Se_2]^-$ clusters excited at the same wavelength. 149
Figure 4.1.17 - Photoluminescence decay times (scatter) and corresponding fittings (line) of samples doped before (**A**) and during (**B**) high-temperature synthesis with respective average decay times, monitored at λ_{exc}=400 nm and λ_{em}=800 nm. The corresponding residuals of the fittings are present in **Figure C.1.3**. 150
Figure 4.1.18 - Comparison of the emission spectra of sample Se_0 gel - 900 °C (black line) with the $[S_3]^{2-}$ species (dark-red line) obtained in sulfur-doped zeolites, as discussed in subchapter **2.3**, λ_{exc}=350 nm. 150
Figure 4.1.19 - Time-resolved emission spectroscopy of sample $Se_{0.1}$ - 900 °C applying shorter delay times and using an λ_{exc}=337 nm. 152

Figure 4.1.20 - Time-resolved emission spectroscopy of sample $Se_{0.1}$ - 900 °C by applying longer delay times, with λ_{exc}=337 nm. 152
Figure 4.1.21 - Steady-state emission (λ_{exc}=400 nm) and excitation (λ_{em}=800 nm) spectra of sample $Se_{0.1}$ - 900 °C at room temperature (RT) represented in black and at 77 K represented in green. 153
Figure 4.1.22 - Photoluminescence decay times of sample $Se_{0.1}$ - 900 °C at liquid nitrogen temperature (77 K) and at room temperature (RT) monitoring the emission at 800 nm. The insets show the components resulting from the decay fittings (see the resulting residuals in **Figure C.1.5**) and the average decay time. In brackets is the relative amplitude of each component. Note that the average decay times were calculated using the pre-exponential factors. 154
Figure 4.2.1 - Dynamic light scattering (DLS) autocorrelation functions of non-doped nanosodalite in colloid form (**A**) after colloid drying and (**B**) following manual milling of the colloid (**C**)..... 158
Figure 4.2.2 - **Dynamic light scattering (DLS) analysis of selenium-doped nanosodalite (Se_7 gel)** - (**A**) Size distribution and (**B**) autocorrelation function. 160
Figure 4.2.3 - (**A**, **B**) SEM images of the produced Se_7 gel nanozeolite sample using two different magnifications. 161
Figure 4.2.4 - PXRD diffractograms of the produced selenium-doped Se_7 gel nanosodalite sample compared with the simulated diffractogram of sodalite octahydrate, with the composition $[Na_6(H_2O)_8][Si_6Al_6O_{24}]$ in black, according to reference **145**. 162
Figure 4.2.5 - Photographs of the synthesis alumina crucible filled with selenium-doped Se_7 gel nanosodalite before and after high-temperature synthesis at 700 °C, 800 °C and 900 °C..... 163
Figure 4.2.6 - Dynamic light scattering (DLS) autocorrelation function comparison of the colloid (**Figure 4.2.2.A-B**) with milled and non-milled selenium-doped Se_7 gel nanosodalite samples after high-temperature synthesis (**A**) at 700 °C and (**B**) 800 °C. 164
Figure 4.2.7 - Dynamic light scattering (DLS) autocorrelation function comparison of the colloid (**Figure 4.2.2.A-B**) with milled and non-milled selenium-doped Se_7 gel nanosodalite samples after high-temperature synthesis at 900 °C. 164
Figure 4.2.8 - (**A**, **B**) SEM images of the nanozeolite samples submitted to 700 °C using two magnifications. Note that this sample was milled before SEM analysis. 165
Figure 4.2.9 - (**A**, **B**) SEM images of the nanozeolite samples submitted to 900 °C using two magnifications. Note that this sample was milled before SEM analysis. 166

Figure 4.2.10 - PXRD diffractograms of the produced samples illustrating the impact of thermal treatment and milling. The samples were subjected to varying temperatures: 700 °C (gray), 800 °C (blue) and 900 °C (red). Non-milled samples exhibit lighter colors, while milled show darker colors. The ICDD standard reference card for comparison includes 01-086-1844 sodalite ($Na_8Si_6Al_6O_{24}Cl_2$), 00-035-0424 nepheline ($Na_4Si_4Al_4O_{16}$) and 00-011-0220 carnegieite ($Na_4Si_4Al_4O_{16}$)..... 167
Figure 4.2.11 - Diffuse reflectance spectra of the milled and non-milled selenium-doped Se_7 gel nanosodalite samples after the high-temperature synthesis at 900 °C. The insets show the photos of the samples under ambient light..... 168
Figure 4.2.12 - (**A**) Emission, λ_{exc}=400 nm, and (**B**) corresponding normalized spectra of the milled and non-milled selenium-doped Se_7 gel nanosodalite samples after the high-temperature synthesis at 900 °C..... 168
Figure 4.2.13 - (**A**) Excitation, λ_{em}=800 nm, and (**B**) corresponding normalized spectra of the milled and non-milled selenium-doped Se_7 gel nanosodalite samples after the high-temperature synthesis at 900 °C..... 169
Figure 4.2.14 - Diffuse reflectance (**A**) and excitation (λ_{em}=740 and 800 nm) and emission (λ_{em}=400 and 480 nm) spectra (**B**) of the produced sample. The inset shows the photos of the sample under ambient light. 170
Figure 4.2.15 - (**Above)** Photoluminescence decay time of reduced sodium selenite acquired at room temperature (RT). The insets show the components resulting from the decay fitting and the average decay time. In brackets is the relative amplitude of each component. Note that the average decay times were calculated using the pre-exponential factors. (**Below**) corresponding residuals. 171
Figure 4.2.16 - PXRD diffractograms of the produced selenium-doped Se_1 gel nanosodalite sample compared with with the composition $[Na_6(H_2O)_8][Si_6Al_6O_{24}]$ in black, according to reference **145**. 173
Figure 4.2.17 - (**A**) Strategies to obtain Na_2Se_2 starting from elemental selenium in solution. (**B**) Example of a reaction mechanism involving the use of Na_2Se_2. Adapted from reference **149**. 175
Figure 5.1 - (**A**) PXRD diffractograms of the synthesized samples according to the Te/Cl ratio and comparison with the ICDD standard reference card of 01-086-1844 sodalite ($Na_8Si_6Al_6O_{24}Cl_2$), 00-035-0424 nepheline ($Na_4Si_4Al_4O_{16}$) and 00-011-0220 carnegieite ($Na_4Si_4Al_4O_{16}$). (**B**) Corresponding crystalline phases calculated from the PXRD diffractograms. 180

Figure 5.2 - Diffuse reflectance spectrum of samples with different Te/Cl ratios. Inset: photos of the samples under ambient light. 182
Figure 5.3 - Spectra deconvolution presented in **Figure 5.2**, using bands peaking at 395 nm (**A**), 485 nm (**B**) and 600 nm (**C**) and their behavior according to the Te/Cl ratio. 182
Figure 5.4 - Diffuse reflectance spectral deconvolution of the sample with Te/Cl=4.5 183
Figure 5.5 - Emission spectra of the synthesized tellurium-doped zeolite samples with different Te/Cl ratios, exciting at 400 nm. 184
Figure 5.6 - Emission spectra of the synthesized samples with different Te/Cl ratios, exciting at (**A**) 475 nm and (**B**) 600 nm. 184
Figure 5.7 - Excitation spectra of the synthesized samples using different Te/Cl ratios at (**A**) λ_{em}=800 nm and (**B**) corresponding normalized spectra. 186
Figure 5.8 - (**A**) Time-resolved emission spectroscopy of sample with Te/Cl=4.5, excited at 337 nm, using short delay times on the nanosecond timescale. (**B**) An approximation of the decay time of this emission. 187
Figure 5.9 - (**A**) Time-resolved emission spectroscopy of sample with Te/Cl=4.5, excited at 337 nm, using long delay times on the microsecond timescale. (**B**) An approximation of the decay time of this emission. Note their respective components and amplitudes (in brackets) alongside the corresponding average decay times. 188
Figure 5.10 - Photoluminescence decay times in the microsecond timescale using the different Te/Cl ratios, with λ_{exc}=400 nm. 189
Figure 5.11 - Electronic paramagnetic resonance (EPR) spectra of sample Te/Cl=0.06 recorded at different temperatures from 150 K to 30 K. 190
Figure 5.12 - EPR spectrum of sample Te/Cl=0.06 acquired at 30 K (red line) and corresponding simulations (gray lines) depicting species A, B and C. The black line shows the sum of these three species according to their calculated relative contributions, summarized in **Table 5.3**. 191
Figure 5.13 - Electronic paramagnetic resonance (EPR) spectra of sample Te/Cl=0.21 recorded at different temperatures from 150 K to 30 K. 192
Figure 5.14 - EPR spectrum of sample Te/Cl=0.21 acquired at 30 K (blue line) and corresponding simulations (gray lines) depicting species A, B, C and D. The black line shows the sum of these three species according to their calculated relative contributions, summarized in **Table 5.3**. 193
Figure 5.15 - Electronic paramagnetic resonance (EPR) spectra of samples Te/Cl=0.75 (**A**) and Te/Cl=4.5 (**B**) recorded at different temperatures from 150 K to 30 K. 193

Figure 5.16 - (**A**) Comparison of all EPR signals recorded at 30 K (**B**) alongside their corresponding normalized signal areas. Note that the signal from sample Te/Cl=4.5 was not considered since its intensities is minimal. 194
Figure 6.1 - (**Above**) Photos of the produced chalcogen-doped zeolite samples synthesized in chapters **2**, **3** and **5** under ambient light and standard UV ligth (λ_{exc}=365 nm). (**Below**) Resume of the emission and excitation spectra of the chalcogen $[X_2]^-$ radicals. 200
Figure 6.2 - (**Above**) Photos of the produced chalcogen-doped zeolite samples synthesized in chapters **2**, **3** and **5** under ambient light and standard UV ligth (λ_{exc}=365 nm). (**Below**) Resume of the emission and excitation spectra of the new chalcogen emitters, tentatively triatomic diradical $[X_3]^{2-}$ species. 201
Figure 7.2.1 - Typical assembly of a double-beam spectrometer for absorption spectroscopy. Adapted from reference **156**. 210
Figure 7.2.2 - (**Above**) Typical set-up of a diffuse reflectance spectroscopy experiment. (**Below**) Example of a reflectance spectrum (black) and corresponding one after applying Kubelka-Munk transformation (red). Adapted from reference **157**. 212
Figure 7.2.3 - Jablonski diagram demonstrating the mechanistic processes of fluorescence (FL), phosphorescence (Phos) and delayed fluorescence (DL) after absorption (Abs). Adapted from reference **116**. 214
Figure 7.2.4 - Representation of a typical set-up for steady-state emission spectroscopy experiments. Adapted from reference **158**. 215
Figure 7.2.5 - Representation of five different photoluminescence decay times occurring at different timescales. 217
Figure 7.2.6 - **Basics of Time-Resolved Emission Spectroscopy (TRES) technique** - (**A**) Representation of a typical photoluminescence decay time exhibiting the entire temporal profile of the emitted photons, introducing important concepts like delay time and gate width (integration signal area) for TRES technique. (**B**) Representation of the signal acquisition of TRES technique based on the full photoluminescence decay time depicted in (A), applying different delay times while maintaining the gate widths constant. (**C**) Example of corresponding emission spectra acquired through TRES techniques, using the inputs in (B). 219
Figure 7.2.7 - Typical transient absorption (TA) set-up with the pump pulse photoexciting the sample, while the probe pulse is used to observe the absorption response of the sample at different times after photoexcitation. Adapted from reference **161**. 221
Figure 7.2.8 - (**A**) Jablonski diagram with possible states and pathways occurring after pump and probe pulses. (**B**) Example of a typical TA spectrum (gray) deconvoluted with positive and

negative ΔA contributions. Ground-state bleach (brown) and stimulated emission (pink) have negative contributions and excited-state absorption (black) exhibits a positive contribution to ΔA. Adapted from reference **161**. 222
Figure 7.2.9 - (**A**) Schematic representation of a simple continuous wave (CW)-EPR spectrometer, illustrating the key components involved in the experiment. (**B**) Typical EPR absorption line, depicted as a Gaussian absorption band. (**C**) Corresponding derivative-like signal. Adapted from reference **163**. 224
Figure 7.2.10 - (**Left**) Basic representation of Raman spectroscopy technique and (**Right**) Jablonski diagram showing Raman shifts. Adapted from reference **165**. 225
Figure 7.2.11 - (**A**) DLS principle representation, with an incident laser beam into a cuvette containing particles and with the light scattered by these particles detected under a defined angle, θ. (**B**) Variations of scattered light over time according to the particle size. (**C**) Respective correlation functions after signal processing. (**D**) Particle size distribution according to the Stokes-Einstein relationship. Adapted from reference **166**. 227
Figure 7.2.12 - Schematic representation illustrating the generation of X-rays in PIXE technique (**A**), along with typical X-ray transitions (**B**). Example of X-ray transitions of selenium element (**C**). Adapted from reference **167**. 228
Figure 7.2.13 - Experimental setup for a DSC experiment. The amount of heat required to increase the temperature by the same increment (ΔT) of a sample cell (q_s) is higher than that required for the reference cell (q_r) by the excess heat absorbed by the sample (Δq). The resulting DSC scans with the reference subtracted from the sample show how this excess heat changes as a function of temperature. ΔH stands for change in enthalpy and T_m for transition and melting point. Adapted from reference **168**. 230
Figure 7.2.14 - (**A**) Illustration of a typical powder X-ray crystallography apparatus, with a close-up of the sample and the crystal, showing Bragg's law. (**B**) Debye-Scherrer rings representation of several crystalline planes according to the angles. (**C**) Corresponding detected powder diffraction pattern (**D**) and powder diffractogram. Adapted from reference **169**. 231
Figure 7.2.15 - Schematic diagram of the core components of a SEM microscope. Adapted from reference **170**. 233
Figure 7.2.16 - Schematic diagram of the core components of a TEM microscope. Adapted from reference **170**. 234
Figure 7.4.1 - Decomposition of the experimental emission spectra of sample Se/Cl=0.21 with the two pure red emission and NIR emissions 237

Figure 7.4.2 - Comparison of the pure red (**A**) and the NIR (**B**) emission spectra with the corresponding decomposed fractions calculated from the experimental emission spectrum, where a mixture of these mentioned emissions was found. 238
Figure 7.4.3 - Decomposition of the experimental diffuse reflectance spectra of sample Se/Cl=0.21 with the species responsible for the red and NIR emissions. 239
Figure 7.5.1 - Differential scanning calorimetry analysis of sample S/Cl=0 (black) and Se_0 gel (blue). 241
Figure A.1.1 - EPR spectra (red lines) and respective simulations (grey lines) of the samples S/Cl=0, 0.21 and 4.5 and commercial ultramarine blue pigment (UBP), recorded at 120 K, 2 mW and 9.45 GHz; in some cases, a multiplication factor was applied; the individual components simulations are presented below each spectrum, and were added with the indicated percentages to obtain the full spectrum overlaid with the experimental one. 257
Figure A.1.2 - Corresponding residuals of the fittings presented in **Figure 2.3.17** and **Figure 2.3.18**. 258
Figure A.1.3 - (**A-C**) Overlap of the diffuse reflectance spectrum of sample S/Cl=4.5 (black) with the combined calculated spectra of calculated sulfur species with $[S_3]^-$ clusters (red). 260
Figure A.1.4 - Kohn-Sham molecular orbitals and their symmetries. 262
Figure B.1 - Residuals of the fittings performed in **Figure 3.9** 264
Figure B.2 - Molecular orbitals of ground and excited states of luminescent $[Se_2]^-$ species[175]. 266
Figure B.3 - Residuals of the fittings performed in **Figure 3.16** and **Figure 3.17** 267
Figure B.4 - Residuals of the fittings performed in **Figure 3.19**. 268
Figure B.5 - Time-resolved emission of the sample with Se/Cl=0, using a λ_{exc}=337 nm. 269
Figure B.6 - Residuals of the fittings performed in **Figure 3.25** and **Figure 3.26** 270
Figure B.7 - EPR spectra (red lines) and corresponding simulations (black lines) depicting species A (detected at lower temperatures) and B (detected at 150 K) in sample Se/Cl=0.06. 271
Figure C.1.1 - Diffuse reflectance spectral deconvolution of samples $Se_{0.1}$ gel - 900 °C (black), Se_1 gel - 900 °C (red) and $Se_{0.1}$ - 900 °C (blue). 275
Figure C.1.2 - (**A**) Emission spectra of the synthesized samples with λ_{exc}=350 nm and (**B**) corresponding normalized spectra, with the green line representing the emission spectra of $[Se_2]^-$ clusters excited at the same wavelength. 276
Figure C.1.3 - Corresponding residuals of the fittings of the photoluminescence decay times present in **Figure 4.1.17**. 277

Figure C.1.4 - Time-resolved emission spectroscopy of sample Se_0 gel - 900 °C applying shorter (**A**) and longer (**B**) delay times, λ_{exc}=337 nm. 278
Figure C.1.5 - Residuals of the fittings present in **Figure 4.1.22**. 279
Figure I.I - Comparison between the initial and final selenium compounds after sonochemical synthesis. (**A**) Photos taken under ambient light and (**B**) corresponding absorption spectra. 284
Figure I.II - Photos of the mixture during and after synthesizing the selenium-doped Se_1 gel nanosodalite sample. 285
Figure I.III - (**A**) Diffuse reflectance spectra and (**B**) PXRD diffractogram of the produced selenium-doped Se_1 gel nanosodalite sample compared with the non-doped nanosodalite Se_0 gel sample. 286
Figure I.IV - Absorption spectra of an aliquot of the products resulting from the reduction of sodium selenite (**A**) and sodium sulfite (**B**) salt in methanol, along with corresponding photos of the products in the insets. 286

List of Schemes

Scheme 1.4.1 - Schematic presentation of several synthesis routes of Na-LTA, Na-FAU and sodalite zeolites that undergo high-temperature synthesis. 22
Scheme 2.1.1 - Proposed synthesis scheme of the zeolite transformations starting from Na-LTA zeolite at high temperatures, adopted from crystallographic data[99–102]. 45
Scheme 2.4.1 - Resume of the high-temperature zeolite transformations observed in the three subchapters in this chapter..... 90
Scheme 4.2.1 - Synthetic pathways explored in this subchapter to achieve emissive selenium-doped nanosodalites. Strategies I.A and II.A involve high-temperature (Δ) synthesis in solid-state, while strategies I.B and II.B comprise room-temperature (RT) synthesis in solution. ... 157
Scheme 4.2.2 - Strategies adopted for selenium reduction in solid-state to produce emissive nanozeolites, encompassing strategies I.A and II.A, according to **Scheme 4.2.1**. 159
Scheme 4.2.3 - Strategies adopted for selenium reduction in solution to produce emissive nanozeolites, encompassing strategies I.B and II.B, according to **Scheme 4.2.1**..... 174
Scheme 6.1 - Resume of the NIR applications studied during this thesis that showed a good suitability for the produced chalcogen-doped NIR-emitting zeolites. 202

List of Tables

Table 1.3.1 - Current clinical fluorescence-guided surgery techniques of indocyanine green (ICG) contrast agent and respective structure. Adapted from reference **37**. 9

Table 1.4.1 - Experimental values of absorption and emission transitions of the luminescent diatomic radical chalcogen species confined in zeolites. Adapted from reference **78**. 27

Table 2.1.1 - Calculated crystalline phases of the synthesized samples after 1 hour at 900 °C with S/Cl=0.21 and 4.5, along with their corresponding pairs with a NaCl excess, based on the ICDD standard reference cards. 44

Table 2.2.1 - Crystalline phases calculated from PXRD diffractograms of samples starting from Na-LTA zeolite and from sodalite zeolite. 58

Table 2.3.1 - Molar percentage of each main element found in zeolite samples using the PIXE technique. 65

Table 2.3.2 - g-values, relative percentages and species assignment present in the samples S/Cl=0, 0.21 and 4.5 and commercial ultramarine blue pigment (UBP). 71

Table 2.3.3 - Decay times (t), relative amplitudes (A), and average decay times of all synthesized samples 73

Table 2.3.4 - Intersystem process in $[S_3]^{2-}$ between S1→T1, S3→T5, S5→T5 and S6→T8 transitions. 84

Table 3.1 - Molar percentage of each main element found in zeolite samples using the WDXRF technique. 94

Table 3.2 - External quantum efficiencies (EQEs), photoluminescence decay times with their respective components and amplitudes, alongside average decay times and corresponding radiative (k_r) and non-radiative (k_{nr}) 'averaged' constants of the red emission. 102

Table 3.3 - External quantum efficiencies (EQEs), photoluminescence decay times with their respective components and amplitudes, alongside average decay times and corresponding radiative (k_r) and non-radiative (k_{nr}) 'averaged' constants of the NIR emission. 112
Table 3.4 - g-values and corresponding g-iso values (average g-values) of the two selenium EPR active species detected in the samples Se/Cl=0.06, 0.21 and 0.75. Species A is observed at lower temperatures, while species B is detected from 150 K. The EPR simulated spectra are illustrated in **Figure B.7**. The relative contributions of both species were calculated in the spectra recorded at 30 K for all synthesized samples. 122
Table 4.1.1 - Molar percentage of the observed elements in zeolite samples using the WDXRF technique. 136
Table 4.1.2 - Elemental analysis of each main element found in nanozeolite samples submitted to high-temperature synthesis at 900 °C using the EDS technique. 138
Table 4.1.3 - Crystalline phases calculated by comparing the ICDD standards reference cards with the PXRD diffractograms. 140
Table 4.1.4 - External quantum efficiencies (EQEs), photoluminescence decay times with their respective components and relative amplitudes (A), alongside average decay times and corresponding radiative (k_r) and non-radiative (k_{nr}) 'averaged' constants of the NIR emission. 151
Table 4.2.1 - Elemental analysis of selenium-doped nanozeolite sample using EDS technique. 161
Table 4.2.2 - Mean z-average particle size values obtained from DLS measurements averaged over five scans. See **Figure 4.2.2**, **Figure 4.2.6.A-B** and **Figure 4.2.7**. 165
Table 4.2.3 - Summary of results comparing the presence of the desirable optical properties and dispersibility of the samples after thermal treatment at 700 °C, 800 °C and 900 °C. 169
Table 4.2.4 - Resume of decay components, their relative amplitudes and average decay times monitored at 800 nm room temperature, compared with the reduced salt sample (Na_2SeO_3). 172
Table 5.1 - Molar percentage of each main element found in zeolite samples using the PIXE technique. 181
Table 5.2 - Photoluminescence decay times of the NIR emission with the two components, their relative amplitudes and the average decay times 189
Table 5.3 - g-values and corresponding g-iso values (average g-values) of the species detected in samples Se/Cl=0.06 and 0.21. The relative contributions of each species were calculated in the spectra recorded at 30 K for these two synthesized samples 195

Table A.1.1 - Fractions of sodalite, nepheline and carnegieite phases found in all synthesized samples extracted from PXRD data. 255
Table A.1.2 - Oxide weight percentage (wt%) of the elements found in the produced zeolite samples using the PIXE technique. 256
Table A.1.3 - Vertical electronic excitation energies (above 300 nm), oscillator strengths and optimized structures of several sulfur species. 259
Table A.1.4 - Electronic configuration of the most important singlet and triplet states. The main molecular orbitals (MO), oscillator strength (f) and excitation energy (E) of every state are also shown. 261
Table B.1 - Elemental composition in weight percentage (wt%) of the produced zeolite samples using the WDXRF technique. 263
Table B.2 - Sodalite unit cell parameters of the synthesized samples with different Se/Cl ratios calculated from PXRD data illustrated in **Figure 3.1.A**, considering the diffraction plan [211]. 265
Table C.1.1 - Elemental analysis in weight percentage (wt%) of the synthesized nanozeolites using the WDXRF technique. 273
Table C.1.2 - Elemental analysis of the impurities detected using the EDS technique in nanozeolite samples submitted to high-temperature synthesis at 900 °C. 274
Table D.1 - Oxide weight percentage (wt%) of the elements found in the produced zeolite samples using the PIXE technique. 281
Table D.2 - Sodalite unit cell parameters of the synthesized samples with different Te/Cl ratios calculated from PXRD data illustrated in **Figure 5.1.A**, considering the diffraction plan [211]. 282

Abbreviation List

k_r	Radiative Constant
k_{nr}	Non-radiative Constant
λ_{em}	Emission Wavelength
λ_{exc}	Excitation Wavelength
τ	Emission Lifetime
V_{Cl}	Chloride Vacancy
V_O	Oxygen Vacancy
Wt%	Weight Percent
A. u.	Arbitrary Units
CNTs	Carbon Nanotubes
D4r	Double 4-Membered Rings
D6r	Double 6-Membered Rings
D-A-D	Donor-Acceptor-Donor
DDS	Drug Delivery Systems
DLS	Dynamic Light Scattering
DTA	Differential Thermal Analysis
EDS	Energy Dispersive X-ray Spectroscopy

EPR	Electron Paramagnetic Resonance
EQE	External Quantum Efficiency
FAU	Faujasite
FDA	Food and Drug Administration
GRPR	Gastrin-Releasing Peptide Receptors
ICG	Indocyanine Green
LEDs	Light-Emitting Diodes
LTA	Linde Type A
NIR	Near-Infrared
NUV	Near-Ultraviolet
PCa	Prostate Cancer
Pc-LEDs	Phosphor-Converted LEDs
PIXE	Particle-Induced X-ray Emission
PLQYs	Photoluminescence Quantum Yields
PXRD	Powder X-ray Diffraction
RENPs	Rare-Earth Nanoparticles
SEM	Scanning Electron Microscopy
SOD	Sodalite
TA	Transient Absorption
TD-DFT	Time-Dependent Density-Functional Theory
TEM	Transmission Electron Microscopy
TRES	Time-Resolved Emission Spectroscopy
UV-Vis	Ultraviolet-Visible
WDXRF	Wavelength Dispersive X-ray Fluorescence
WLEDs	White Light-Emitting LEDs

1

INTRODUCTION

1.1 Motivation and Aim of the Dissertation

1.1.1 Motivation

Over the past decade, near-infrared (NIR) emitters have gained significant interest, mainly due to this spectral area's non-invasive nature and high-range applicability. This region offers advantages that extend beyond the limitations of visible light and has captured significant attention for applications in optical communications, *in vivo* imaging and detection systems.

The inherently lower energy within the NIR electromagnetic region is generally believed to increase material stability and device durability[1]. Furthermore, the broad bandwidth of NIR signals, coupled with minimal attenuation in optical fibers, allows for extended transmission ranges without significant signal loss[2]. These mentioned features are crucial for optical communications. The potential for enhanced tissue penetration, reduced scattering and minimal environmental interference makes working in this spectral region highly desirable for *in vivo* imaging[3,4]. Moreover, the lack of detection by the human eye in this region is particularly attractive for anticounterfeiting and authentication systems in which these emitters can be used as optical tags[5,6], requiring instrumental verification and increasing security level.

However, the emitters in this region present their own limitations related to some photophysical properties once they usually show low photoluminescence quantum yields (PLQYs) that result from the increase of non-radiative pathways (energy gap law)[3,7]. Besides, they typically demonstrate poor availability and/or lack of stability[8–10].

Zeolites, crystalline aluminosilicates known for almost 250 years[11], offer high tunability, excellent thermal stability, non-toxicity, and widespread availability, making them

indispensable in several applications, such as molecular sieves and catalysis[12,13]. As hosting materials, zeolites can provide a promising solution to surpass the limitations of the NIR emitters by entrapping and stabilizing them[12,13], with several reports indicating an enhancement in their luminescence quantum yields[14–16]. In fact, NIR emission was already found in these matrices while using rare-earth elements and bismuth as dopants[17–20]. Additionally, chalcogen elements, especially sulfur and tellurium, may also emit within the same spectral zone. Notably, these elements are not listed as critical raw materials by the European Commission (2020)[21], which is an advantage when compared with rare-earth and heavy-metal elements. Sulfur, in particular, stands out due to its high availability and non-toxic traits, affording non-expensive synthesis with low environmental impact[22].

The most recent studies regarding the exploration of NIR-emitting chalcogen-doped zeolites were made by Ruivo et al.[20] in sulfur-doped aluminosilicates. However, the origin of this emission remained unclear when starting the research leading to this thesis.

1.1.2 Aim

This thesis is focused on three main objectives. The first entails the synthesis of sulfur-, selenium- and tellurium-doped zeolites, emitting in both the visible and near-infrared (NIR) regions, with a particular focus on the latter. The study involves an in-depth photophysical characterization of these materials, aiming to significantly advance the state-of-the-art in the NIR region (where knowledge is practically nonexistent) while addressing gaps in the visible region. The second objective involves the synthesis of nanozeolites that exhibit the photophysical properties observed in their micro-sized counterparts. Finally, the third objective seeks to evaluate the practical applicability of these chalcogen-doped materials in NIR-based applications, such as detection systems and sensors, and assess their potential use in bioimaging.

Chalcogen-doped zeolites can be produced using a solid-state synthesis method, starting with commercial Na-LTA zeolite. Among the chalcogens, sulfur is the most extensively studied, exhibiting emissions that vary with its concentration, displaying an emission in the visible region at low concentrations and in the NIR region at higher ones. This sets the initial background for the research work included in this thesis, aiming to address these fundamental questions:

1. What mechanism underlies the NIR emissions observed in sulfur-doped zeolites? Is this due to the presence of new species or a photophysical phenomenon?
2. Do similar emission behaviors occur in selenium and tellurium systems, i.e., can two different emissions be formed according to the chalcogen concentration?

3. Can the photophysical characteristics identified in micro-sized be effectively replicated in nanozeolites?
4. What are the NIR applications that suit these emissive materials?

The research methodology is firmly rooted in a systematic, consistent, and meticulous approach involving varying chalcogen concentrations to address these questions. This approach allows for the comprehensive investigation of these materials and fills gaps in the current scientific literature.

1.2 Thesis Layout

Chapter **1** serves as a background chapter, focusing on the potential and applicability of the near-infrared region and its key emitters. It introduces zeolites as chosen materials and outlines their advantages compared to other materials. The chapter concludes with a brief introduction to sodalite zeolite, outlining several synthesis methods and offering an overview of the reported optical properties of chalcogen-doped sodalites.

Chapters **2** to **5** comprise the results and discussion of the work conducted to achieve the objectives proposed in this thesis. Chapter **2** explores sulfur-doped zeolites, serving as the starting point for this thesis since sulfur is the best-known chalcogen due to its natural occurrence as sulfur-doped sodalite. This chapter is subdivided into three subchapters (**2.1** to **2.3**). Subchapters **2.1** and **2.2** focus on synthesis optimization to achieve NIR-emitting zeolites, studying the impact of the produced zeolite structure on the optical properties, involving different synthesis times and starting materials. Subchapter **2.3** explores the nature of the sulfur NIR emission, using various techniques and theoretical calculations. In chapter **3**, luminescent selenium-doped zeolites were explored, investigating the visible and NIR region emissions. Chapter **4** is divided into two subchapters (**4.1** and **4.2**) covering the different synthetic approaches used to achieve selenium-doped nanozeolites with the same optical properties as those explored in chapter **3**. In subchapter **4.1**, the same high-temperature synthesis as in chapter **3** was employed but starting from nanosodalite zeolite. Subchapter **4.2** encompasses various approaches involving solution and solid-state reducing methods. Finally, in chapter **5**, a reference to the optical properties of tellurium-doped zeolites is provided.

Chapter **6** provides a comprehensive overview of this thesis's main achievements, conclusions and future perspectives.

In chapter **7**, the materials and methods are summarized, offering essential information on synthesis and sample characterization while providing an overview of the experimental techniques used.

Finally, chapter **8** presents a compilation of publications, conference presentations, and other publications indirectly connected to this thesis (conducted over the entire PhD duration).

1.3 Near-infrared (NIR) region

In the electromagnetic spectrum, the near-infrared region is situated immediately after the red region of the visible spectrum. There is no unanimous consensus on the definition of this region, so here, the IUPAC recommendations will be followed, which state that it is comprehended between 780 and 2500 nm (see **Figure 1.3.1**)[23]. This region is characterized by its ability to penetrate tissues deeply, minimal susceptibility to environmental interference, such as autofluorescence, and reduced light scattering[3,4,10,24].

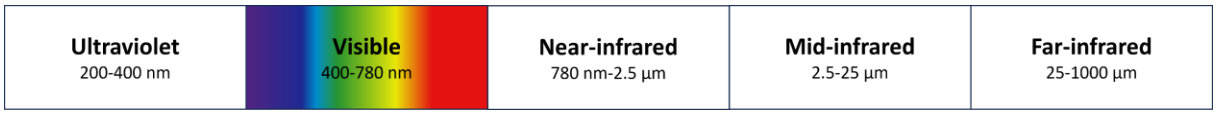


Figure 1.3.1 - Electromagnetic spectrum from UV to far-infrared regions, based on IUPAC recommendations[23].

However, there are several drawbacks pointed out while working in this spectral zone[25]: **i)** The increase of non-radiative pathways (energy gap law), resulting in low quantum yields (QYs)[3,7]; **ii)** Expensive and more complex detectors (when compared to the UV-Vis ones). NIR detectors need to be cooled down at cryogenic temperatures to have better signal-to-noise ratios; **iii)** Lack of detection by the human eye. This configures a critical requirement for some applications, given the need for immediate responses, such as in forensic analysis, environmental monitoring, or display technology.

Examples of highly explored NIR emitting molecules/materials are cyanine and cyanine-based molecules[25–27], rare-earth-doped materials[28,29], gold nanoclusters[7,30] and quantum dots[24,31,32], as depicted in **Figure 1.3.2**. These conventional NIR emitters face two main challenges: heavily reliant on rare-earth elements, listed as critical raw materials by the European Commission (2020)[21], and issues related to chemical and photostability, commonly found in organic-based compounds[9,10,33].

This led to the strategic decision to focus on studying NIR-emitting chalcogen species - sulfur, selenium and tellurium - in this thesis. Chalcogens, particularly sulfur, do not face availability issues, allowing more economical synthesis[22]. Furthermore, these emitters (highlighted in **Figure 1.3.2**) will be confined within zeolites, materials that have demonstrated enhanced photostability even under high temperatures up to 450 °C[20].

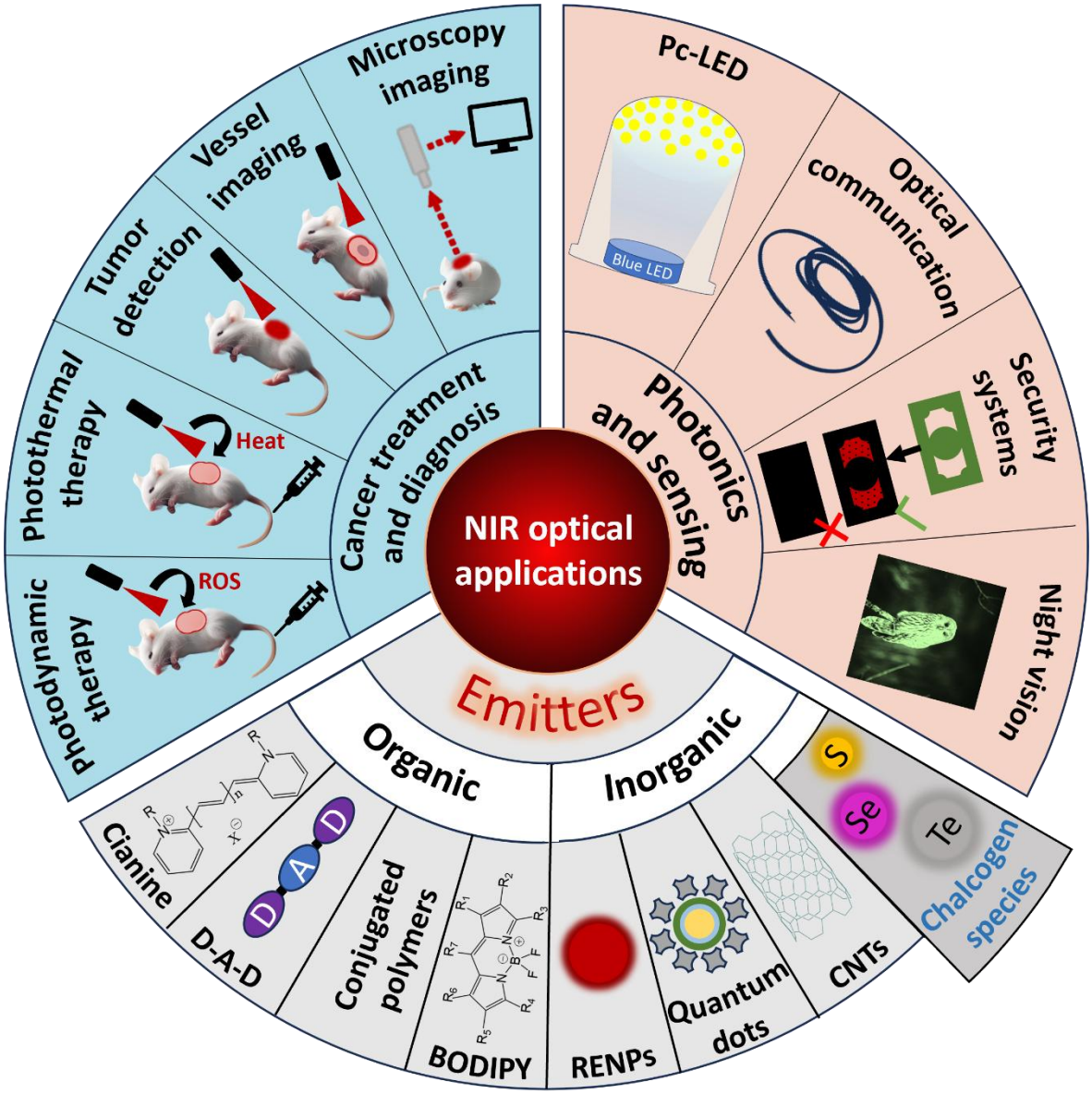


Figure 1.3.2 - Overview of the most commonly used NIR emitters (both organic and inorganic), with a particular emphasis on the chalcogen species that will be studied in this thesis. Additionally, some NIR applications are also referenced. D-A-D stands for donor-acceptor-donor molecules; RENPs stand for rare-earth nanoparticles and CNTs stand for carbon nanotubes. Adapted from reference **33**.

Additionally, established NIR applications, including cancer treatment and diagnosis, as well as photonics and sensing, will serve as a starting point for developing suitable applications for the chalcogen-doped zeolites.

1.3.1 NIR emitting applications

1.3.1.1 Tumor detection and removal

Nowadays, selecting a specific emitter tailored to interact with a particular cell or organelle is possible for precise sensing and imaging[34]. These tags are responsive to changes in biomolecular levels and the microenvironment, including variations in pH. This capability opens new avenues for targeting cancer cells with high precision and minimizing collateral damage.

Figure 1.3.3 illustrates an example of a D-A-D (donor-acceptor-donor) scaffold NIR emitting dye designed for targeting prostate cancer (PCa). Exploiting the overexpression of gastrin-releasing peptide receptors (GRPR) in this type of cancer, the authors[35] coupled the NIR emitter with a GRPR antagonist (RM26), as shown in the final structure in **Figure 1.3.3.A**. The absorption and emission spectra of the free NIR molecule (without the RM26) can be seen in **Figure 1.3.3.B**. This new molecule acts as a GRPR-targeted NIR probe, highlighting cancer cells.

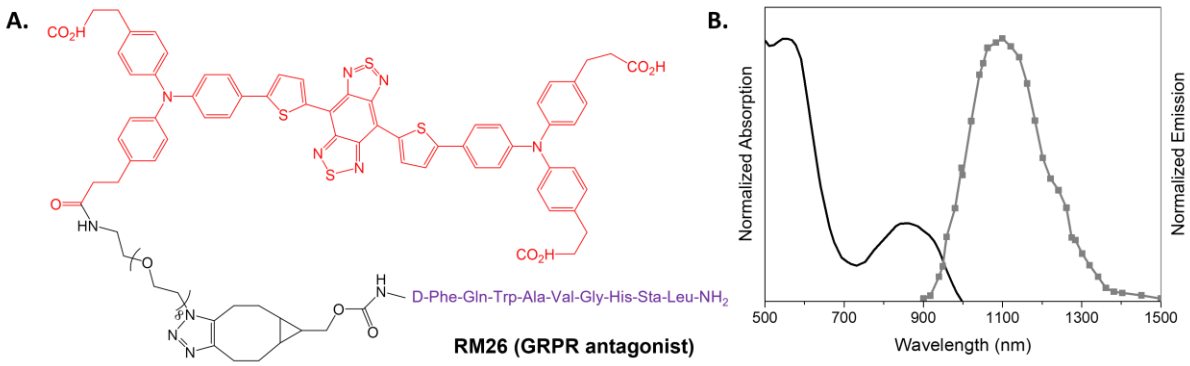


Figure 1.3.3 - (**A**) Structure of the GRPR-targeted NIR probe. (**B**) Absorption and emission spectra of the free-NIR probe (without the RM26). This probe is based on a D-A-D scaffold. Adapted from reference **35**.

After the probe is intravenously injected into PC3 tumor-bearing mice, tumors can be easily distinguished from the surrounding background tissue (**Figure 1.3.4**).

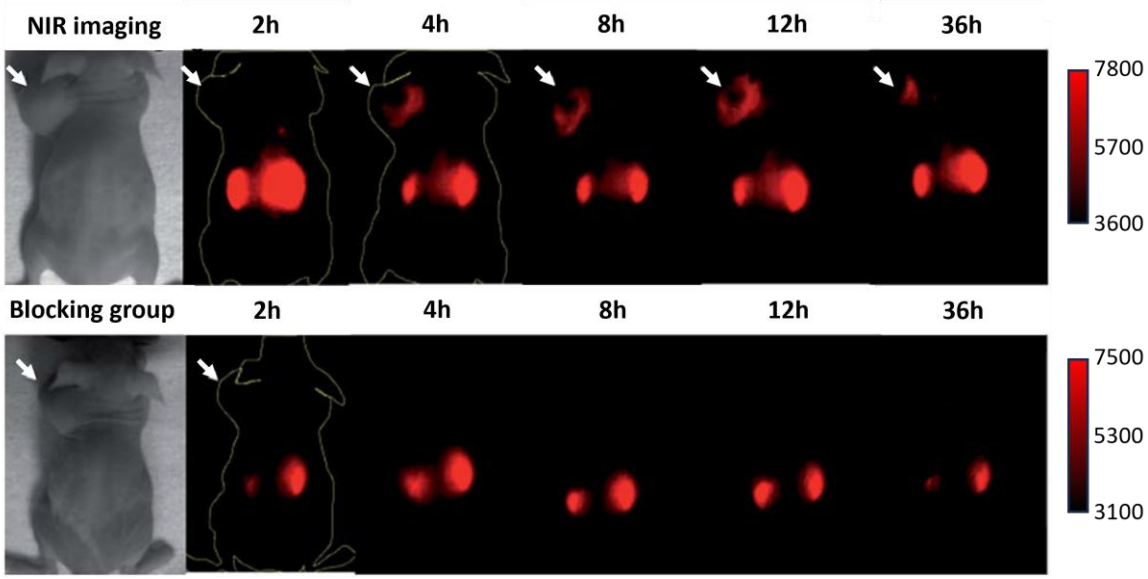
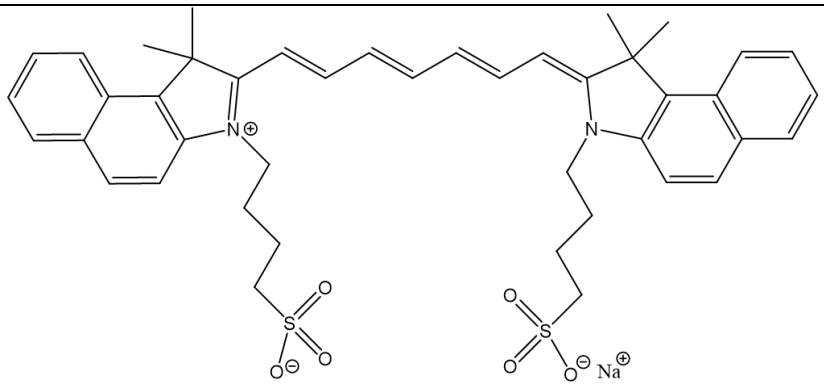


Figure 1.3.4 - NIR images of PC3 tumor-bearing mice (n=3 per group) at different times (2, 4, 8, 12 and 36h) after tail vein injection of GRPR-targeted NIR probe with or without blocking agent RM26 under 808 nm excitation. Note that the white arrows represent the site where the tumor is. Adapted from reference **35**.

Therefore, using a NIR probe for contrast can be extremely valuable in fluorescence image-guided surgery[36]. This targeted approach not only enhances the surgeon's ability to remove cancerous growths but also aids in identifying tiny or deeply situated tumors that might be challenging to distinguish with the naked eye alone. As a result, this advanced surgical strategy enables a high-precision and accurate tumor resection, significantly improving patient outcomes and a higher likelihood of long-term remission[37].

One of the most commonly used contract agents is indocyanine green (ICG), which is Food and Drug Administration (FDA)-approved and applicable in various fluorescence-guided surgery scenarios (**Table 1.3.1**). ICG has an excitation wavelength of 780 nm and an emission wavelength of 820 nm[37].

Table 1.3.1 - Current clinical fluorescence-guided surgery techniques of indocyanine green (ICG) contrast agent and respective structure. Adapted from reference **37**.

Applications	Types
Sentinel lymph node mapping	Breast, melanoma, head and neck and lung cancer
Tumor imaging	Hepatocellular carcinoma, liver metastases, lung and chest masses and ovarian cancer
Fluorescence endoscopy	Brain aneurysm, brain tumor, head and neck tumor
Marking tumor	Colonic tattooing
	

1.3.1.2 Single-Phase LED Phosphors

Phosphor-converted light-emitting diodes (pc-LEDs) represent a significant advancement in lighting technology and are known for their low energy consumption and extended device durability. These LEDs incorporate a phosphor layer - a luminescent material that emits light when stimulated by an external source of light or an electric field. This phosphor layer is positioned on top of an LED chip, and the LED excites the phosphor, causing it to emit light. While the primary application of pc-LED is in lighting, pc-NIR-LEDs exhibit potential in various other areas, including veins imaging and as an invisible light source, as demonstrated below.

An exemple of a NIR-emitting phosphor is $K_2NaInF_6:Cr^{3+}$, which was fabricated and excited by a 439 nm LED chip for veins imaging. This phosphor exhibits an emission spectrum peaking at 780 nm (see **Figure 1.3.5**)[38].

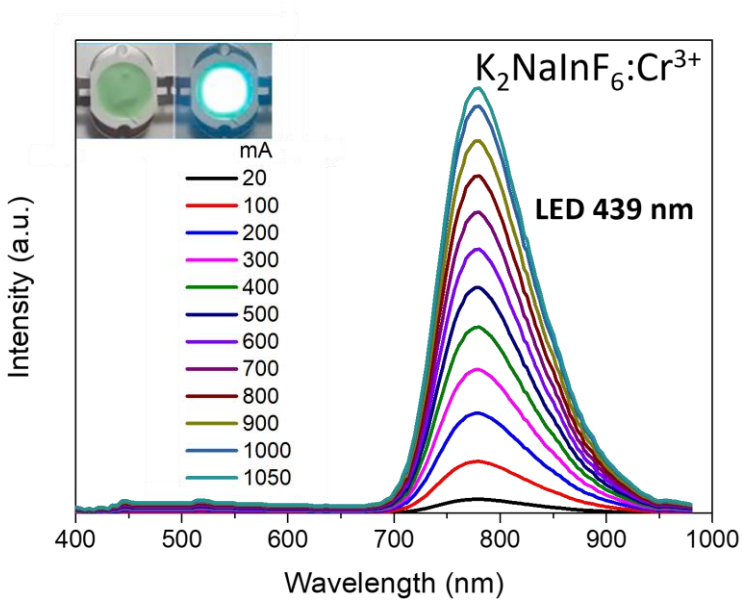


Figure 1.3.5 - Driven current-dependent electroluminescence spectra of the fabricated pc-NIR-LED with $K_2NaInF_6:Cr^{3+}$. The insets show photographs of the produced NIR LED. Adapted from reference **38**.

When fingers, palms and wrists are placed on top of this assembled device (as illustrated in **Figure 1.3.6.A**), veins are clearly distinguished and detected by a NIR CCD camera (**Figure 1.3.6.B**)[38]. This proof-of-concept demonstrates the deep tissue penetration capability of this NIR region.

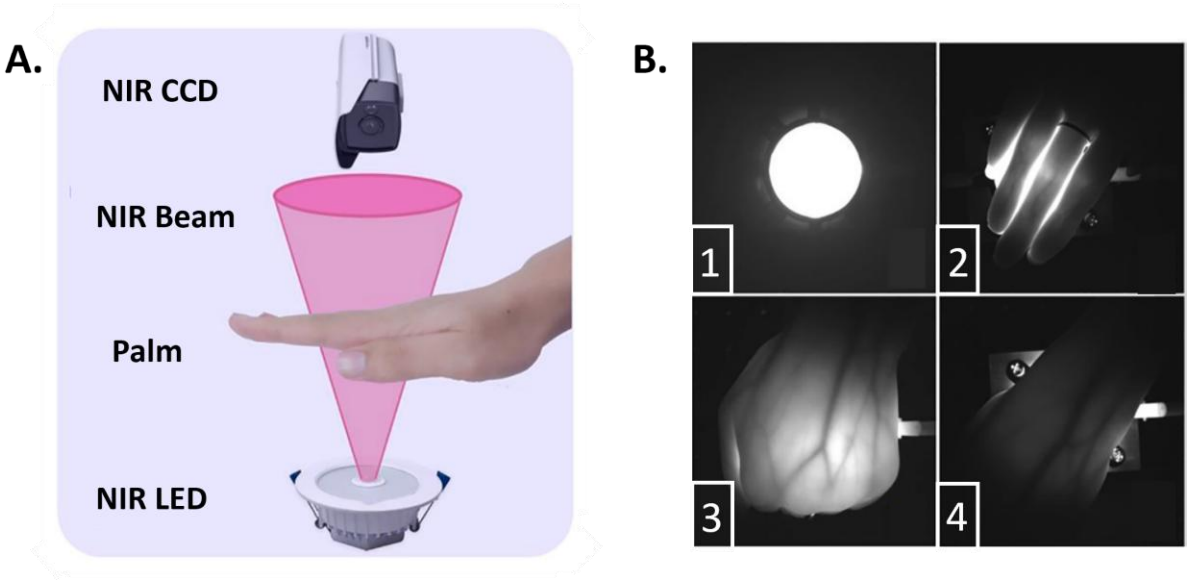


Figure 1.3.6 - **NIR application of pc-LED with $K_2NaInF_6:Cr^{3+}$ for veins imaging** - (**A**) Illustration of hand veins imaging using a high-power NIR LED device in its as-fabricated state. (**B**) Photographs of **1)** the illuminated NIR device and the transmission photographs of the veins in the **2)** fingers, **3)** palm and **4)** wrist taken with a NIR camera. Adapted from reference **38**.

Additionally, pc-NIR-LED can be used as a non-visible light source, particularly interesting in night vision technologies, security systems, and medical diagnostics where visible light may interfere or draw attention. These devices, exemplified by the rare-earth-based phosphor $K_3LuSi_2O_7:Eu^{2+}$, emit light centered around 730 nm when excited by a 460 nm LED chip (see **Figure 1.3.7**).

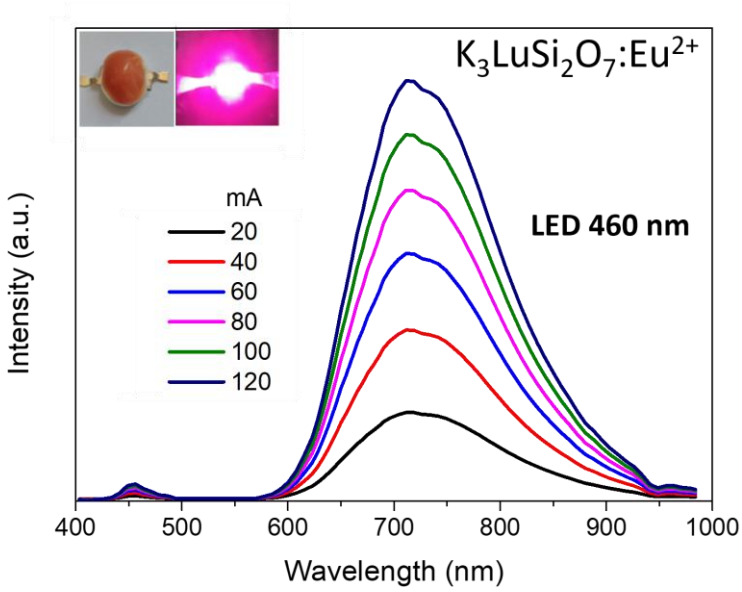


Figure 1.3.7 - Driven current-dependent electroluminescence spectra of the fabricated pc-NIR-LED with $K_3LuSi_2O_7:Eu^{2+}$. The insets show photographs of the produced NIR LED. Adapted from reference **39**.

A proof-of-concept for this application involves comparing the light output of the device when it is switched off and on. A near-infrared camera was used for this purpose. The experiment demonstrates that when the pc-LED is turned off, no signal is detected. However, when switched on, the device produces an image resembling natural light[39], as shown in **Figure 1.3.8**.



Figure 1.3.8 - **NIR application of pc-LED with $K_3LuSi_2O_7:Eu^{2+}$ for the non-visible light source -** Photographs under **1)** natural light, **2)** without light and **3)** under NIR pc-LED light, captured by the corresponding visible and NIR camera. Adapted from reference **39**.

1.3.1.3 Anticounterfeiting tags and security systems

NIR emitters can encode identification markers within products or packaging for security purposes. These markers are typically invisible under normal conditions but can be revealed and authenticated using specialized equipment, such as NIR sensors or scanners. By using these emitters, precise product authentication is enabled, offering manufacturers, regulators, and consumers an effective method for detecting counterfeit goods and ensuring the integrity of products throughout the supply chain.

An example of an anticounterfeiting tag is the emitting Sb^{3+}/Sm^{3+}-codoped $Cs_2NaLuCl_6$ perovskite. In this study, the authors[40] doped a blue-emitting Sb^{3+}-doped perovskite with samarium rare-earth element, producing emissive properties above 550 nm. This resulted in a material with emissions ranging from visible to NIR regions, as shown in **Figure 1.3.9**.

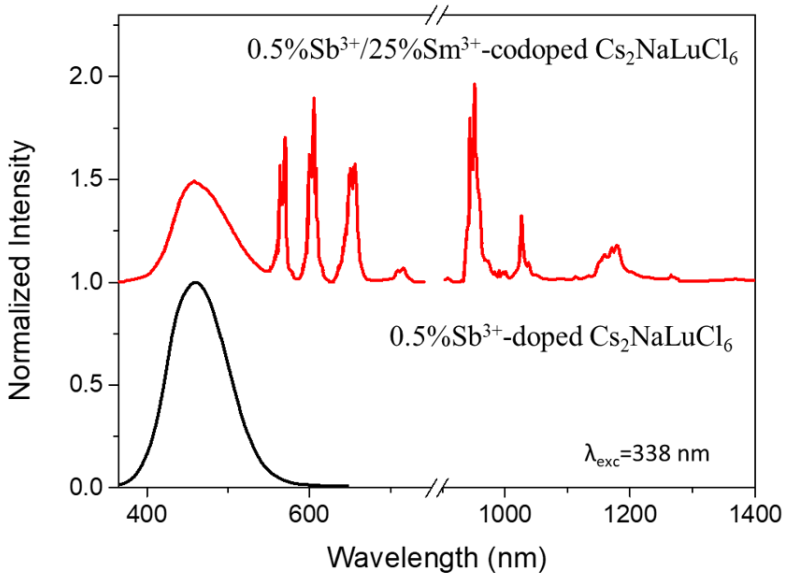


Figure 1.3.9 - Emission spectra of single-doped Sb^{3+}- $Cs_2NaLuCl_6$ perovskite and Sb^{3+}/Sm^{3+}-codoped $Cs_2NaLuCl_6$ perovskite. Adapted from reference **40**.

Additionally, the suitability of this double-doped perovskite was demonstrated for security systems. For this purpose, single-blue- and visible-NIR-emitting perovskites were deposited, forming different patterns. The former represented a '1' and the latter a '3', resulting in an '8' pattern indistinguishable under ambient light and UV light excitation of 254 nm. However, this changed when using a 365 nm excitation wavelength, where a blue '1' and a white '3' pattern were observed. This was due to the additional samarium excitation at this wavelength, resulting in a white emission. Furthermore, while using a 700 nm cutoff filter (that filters all shorter wavelengths), a single NIR '3' pattern was detected (**Figure 1.3.10**).

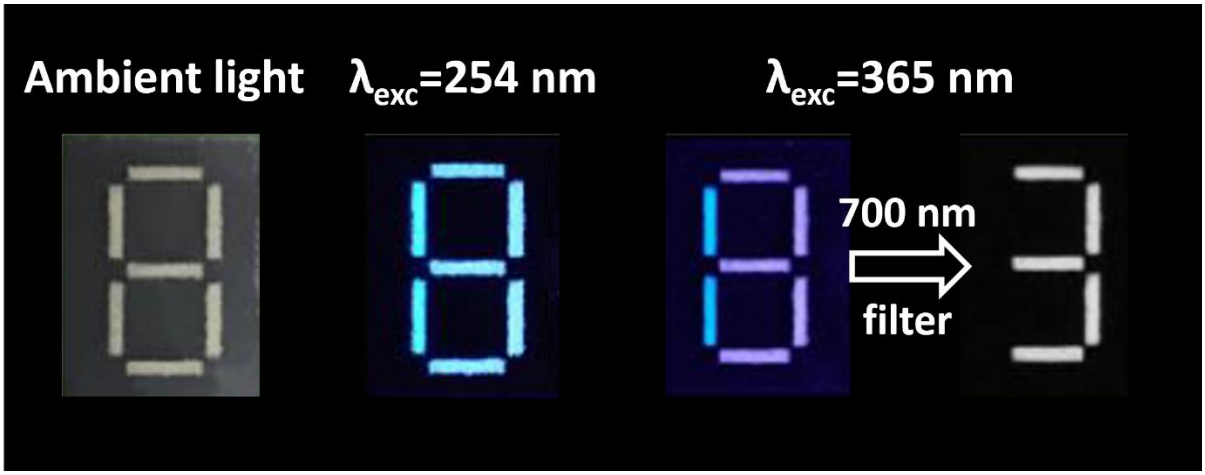


Figure 1.3.10 - Demonstration of the applicability of the NIR emitting material as an anticounterfeiting tag. Adapted from reference **40**.

1.3.1.4 Optical communications

Optical communications using NIR emitters involve transmitting data across an optical fiber using light signals within the NIR region. These emitters allow for high-speed and reliable data transmission over long distances with minimal signal loss and distortion. As they operate at wavelengths that are less susceptible to attenuation and dispersion, NIR emitters are less vulnerable to interception and electromagnetic interference.

Peng et al.[41] developed NIR-emitting Bi-doped germanium oxynitride fiber glasses with compositions varying as follows: $(55GeO_2\text{-}(20\text{-}x/2)Ga_2O_3\text{-}25BaO\text{-}xAlN\text{-}yBi_2O_3$, mol%, x=0-1, y=0-2). These glasses exhibit an ultrabroad emitting band exceeding 600 nm (**Figure 1.3.11**), covering key spectral regions relevant to biological tissue (bio-window) and optical communication (O-, E-, S-, C- and L-bands).

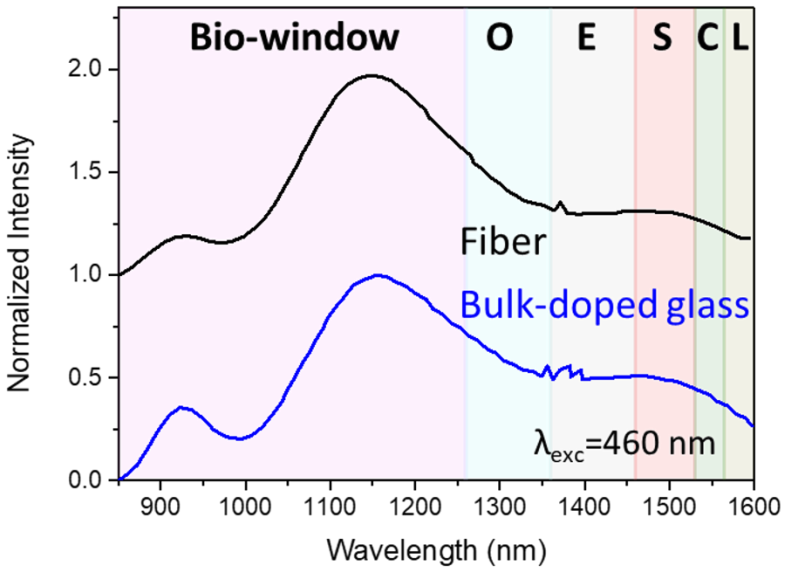


Figure 1.3.11 - Emission spectra of fiber and bulk-doped glass. Adapted from reference **41**.

Optical fibers were then fabricated using the rod-in-tube technique, employing a thin rod of bulk-doped glass and a thick rod of non-doped glass (**Figure 1.3.12**). The resulting fibers are visually transparent and maintain the emission properties of the doped glass, as illustrated in **Figure 1.3.11** and **Figure 1.3.12**.

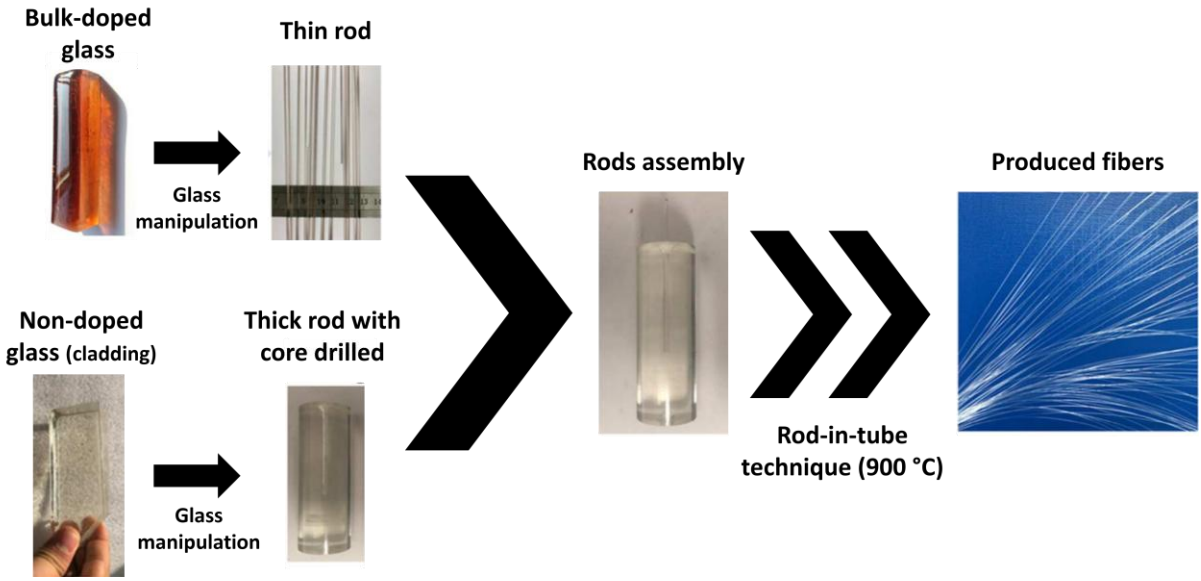


Figure 1.3.12 - Process of fiber fabrications through rod-in-tube technique. Adapted from reference **41**.

1.4 Sodalite zeolite

Zeolites typically present a basic structure composed of tetrahedrons of AlO_4 and SiO_4 (primary building), which are connected alternately through oxygens atoms to form their framework (secondary building). Some zeolites form interconnected cages and channels, providing them with unique catalytic activity and molecular sieving capabilities.

One example of their widespread application is in chemistry laboratories, where they serve as molecular sieves for drying solvents[42] due to their high sorption capacity and selectivity. Their regeneration process is also reasonably straightforward, e.g., through heating activation[43]. These materials also assume a prominent role in reducing the environmental footprint, offering important solutions, namely in treating and remediating contaminated sites, as well as in gas separation and greenhouse gas capture. Their sieving capacity and excellent ion-exchange ability make them ideal for wastewater treatment and environmental remediation, where a wide range of hazardous and toxic compounds can be removed from soil and aqueous systems. These treatments include the removal of heavy metal ions (Zn, Hg, etc.), radioactive species, ammonium, organic contaminants (phenol, cationic surfactants, etc.), or adjusting of salinity and acidity[44–46]. Harmful gases in the atmosphere can also be captured, particularly NO_2, CO_2 and CH_4[47–49]. Notably, these gases can be converted into energy sources afterward. For example, methane reaction to produce hydrogen can be catalyzed by zeolites, with certain synthetic routes generating CO_x-free H_2 gas[50,51].

Furthermore, their hosting capability is highly desirable for drug delivery systems (DDS), allowing for the incorporation and selective release of various agents, such as antibacterial and anticancer compounds, into their specific targets[52–54]. Besides, zeolites can entrap different compounds, including emitting chromophores. These optical materials hold potential for exploration in sensing scenarios, such as temperature, oxygen and humidity/water sensing[55–57]. **Figure 1.4.1** summarizes some of the applications in which zeolites are used.

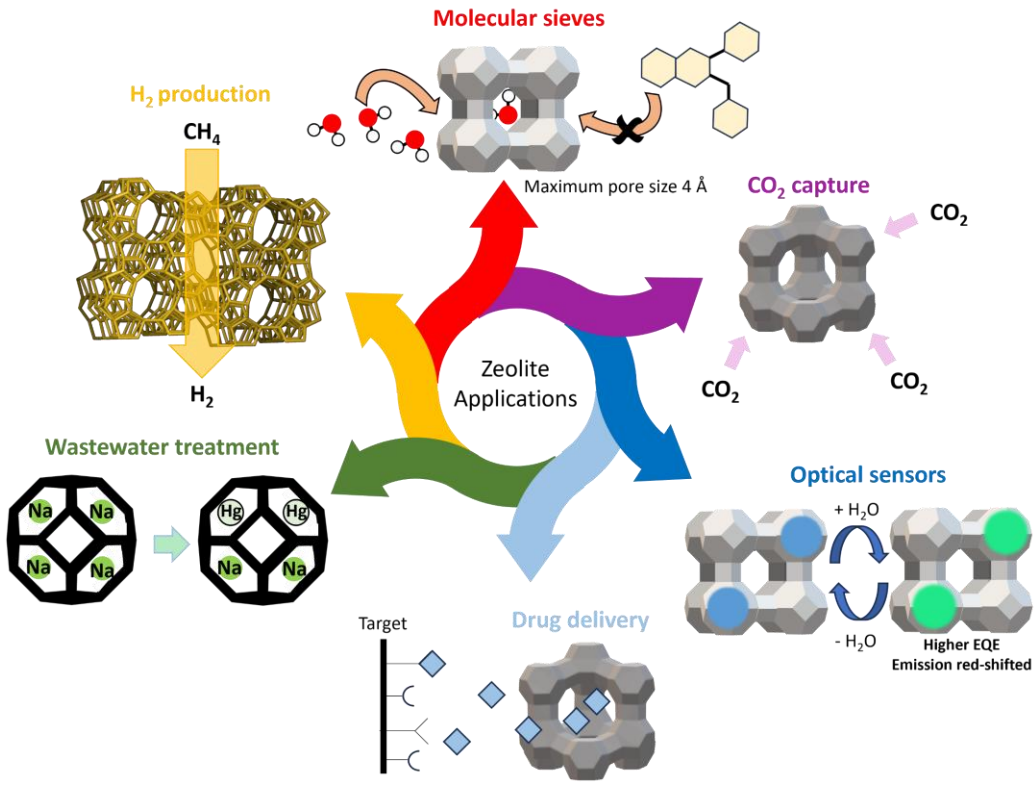


Figure 1.4.1 - Examples of applications in which zeolites are used.

Sodalite (SOD) zeolite, known for centuries, has recently been recognized as the ideal matrix for hosting chalcogen species. Depending on their nature, various optical properties can be achieved. The synthesis methods, optical properties and respective applications of this zeolite will be addressed next. Sodalite has a general composition of $Na_8[AlSiO_4]_6Cl_2$[58]. Its aluminosilicate matrix is composed of β-cages, also known as sodalite cages[59]. These cages are truncated octahedrals formed by the combination of six 4-membered rings and eight 6-membered rings[60] (**Figure 1.4.2**).

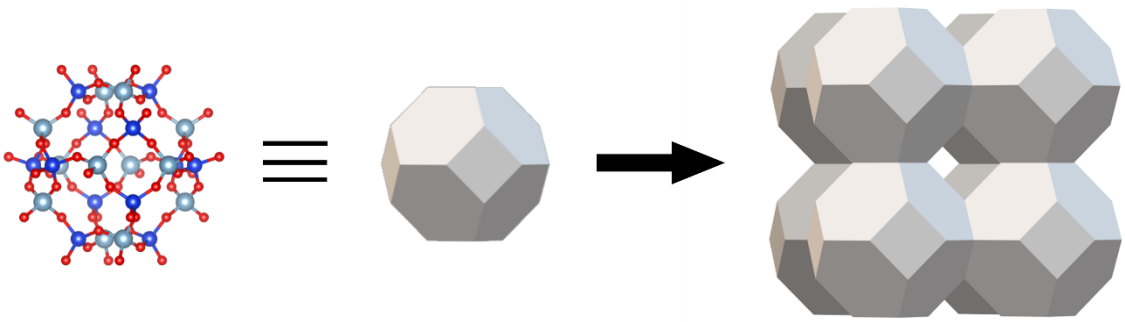


Figure 1.4.2 - Composition of β-cages (sodalite cages), which link together to form the sodalite zeolite structure.

Additionally, there is a $[Na_4Cl]^{3+}$ tetrahedron in the middle of the sodalite cages, where four sodium cations are coordinated tetrahedrally with a chloride anion (**Figure 1.4.3**). Each sodium is also coordinated with three oxygen atoms originating from the aluminum and silicon tetrahedrons[61].

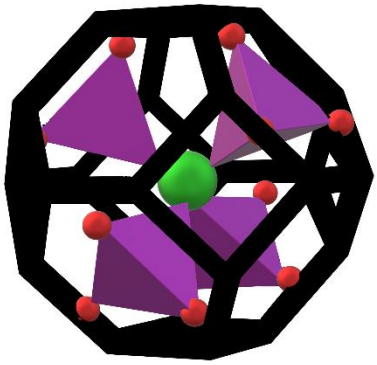


Figure 1.4.3 - Structures of $[Na_4Cl]^{3+}$ tetrahedron and the four $[NaO_3Cl]$ tetrahedrons inside the β-cage. Chloride is represented in green, sodium in pink and oxygen in red.

While sodalite naturally occurs as a mineral, it can be synthesized in the laboratory through several methods, including hydrothermal, sol-gel, and solid-state processes. Both hydrothermal and sol-gel synthesis involves mixing aluminum and silicon solution precursors in basic water. Hydrothermal synthesis typically involves elevated temperatures and pressure, while the sol-gel method occurs at atmospheric pressure and moderate temperatures[62–64]. In contrast, solid-state synthesis, as suggested by its name, involves only solid-state materials (reactants and products) and is usually conducted at high temperatures[65]. Starting materials similar to those mentioned earlier (excluding water) can be mixed and heated to obtain the sodalite structure[66]. An alternative approach involves zeolite transformation during the high-temperature synthesis, starting with Linde Type A (Na-LTA), Faujasite-X (Na-FAU-X) or Faujasite-Y (Na-FAU-Y)[67].

1.4.1 Solid-state synthesis of sodalite

Sodalite can be produced starting with Na-LTA, Na-FAU-X and Na-FAU-Y zeolites. Structurally, both zeolites are composed of β-cages. The differences lie in the way these cages are united to each other. In sodalite, they are directly linked to each other, whereas in LTA and FAU, they are connected through double 4-membered rings (d4r) and double 6-membered rings (d6r), respectively, consequently forming bigger cages, see **Figure 1.4.4**. In LTA, the α-cage, also

known as the LTA-cage, is a truncated cuboctahedron composed of twelve 4-membered rings, eight 6-membered rings and six 8-membered rings. In faujasite, the supercage is a truncated dodecahedron with four 12-membered rings, four 6-membered rings and eighteen 4-membered rings.

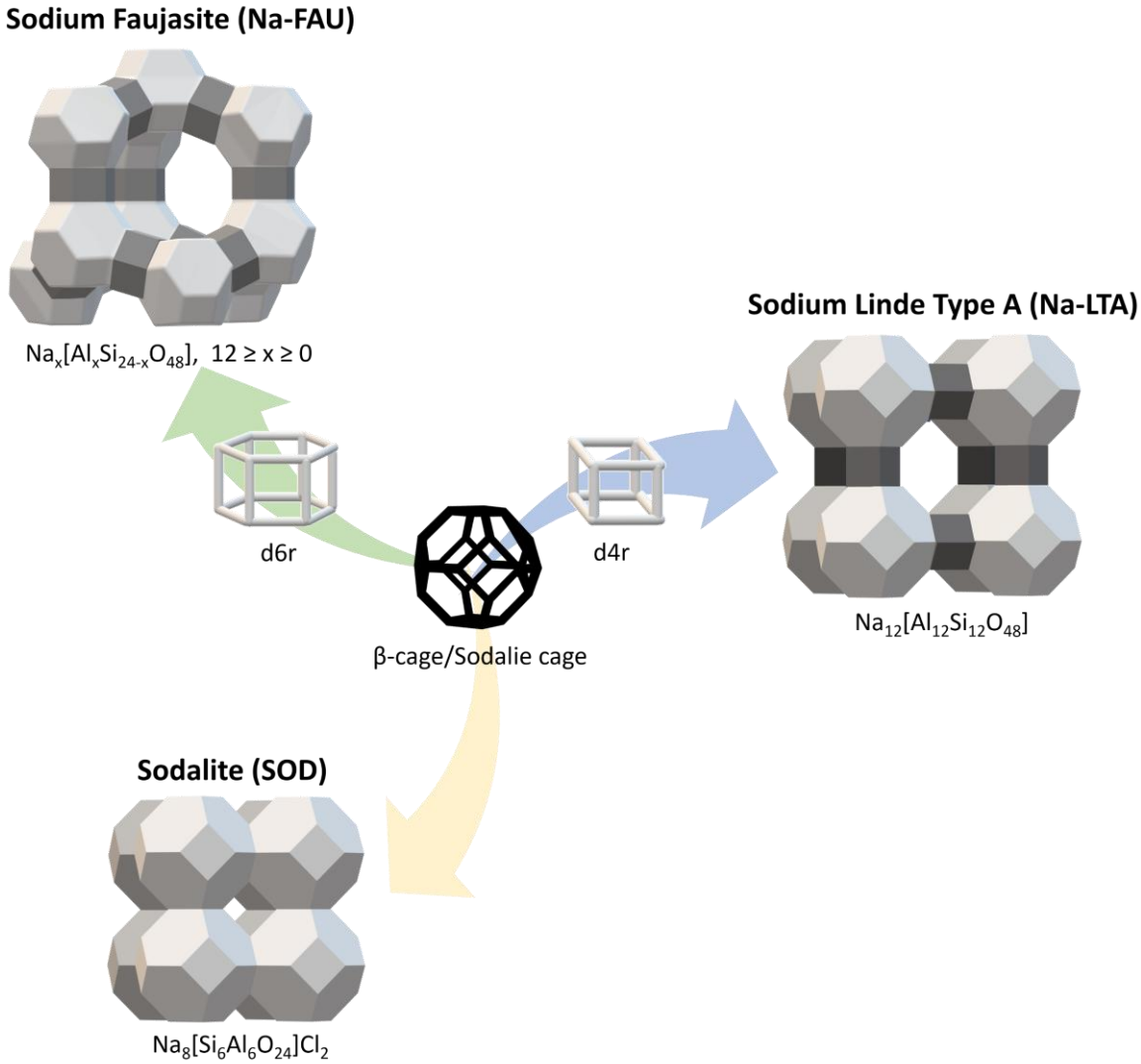


Figure 1.4.4 - Structures of Na-FAU, Na-LTA and sodalite zeolites and their building units.

The corresponding unit cells and largest pore size of SOD, LTA and FAU zeolites are $Na_8[Si_6Al_6O_{24}]Cl_2$ and 2.4 Å[60], $Na_{12}[Al_{12}Si_{12}O_{48}]$ and 4 Å[59] and $Na_x[Al_xSi_{24-x}O_{48}]$, with $12 \geq x \geq 0$ and 7.29 Å[68,69]. Additionally, faujasite-type zeolites can be labeled X or Y according to their silicon-to-aluminum ratios. FAU-X has lower values, typically around 1, and FAU-Y has higher values. The significant differences between their pore sizes make LTA and FAU more suitable for cation exchange and confinement of larger molecules[70]. On the other hand, sodalite is

more appropriate for encapsulating small clusters, particularly of anionic species (note that chloride anion is typically found entrapped inside the β-cages).

To successfully convert LTA or FAU into sodalite, it is necessary to work at least at 800 °C. The equation of solid-state synthesis that describes the conversion of zeolite Na-LTA into sodalite structure is given by equation (**1.4.1**)[20]:

$$Na_{12}[Al_{12}Si_{12}O_{48}] + NaCl \rightarrow 2\,Na_8[Si_6Al_6O_{24}]Cl_2 \quad (\mathbf{1.4.1})$$

According to Ding et al.[60], the addition of sodium chloride is crucial to obtaining the sodalite zeolite, otherwise, Na-LTA is completely converted into another aluminosilicate structure named nepheline, $Na_4[Si_4Al_4O_{16}]$. Furthermore, the authors propose a synthetic transformation mechanism where Na-LTA zeolite is first converted into carnegieite structure before it is finally converted into sodalite, as described by equation (**1.4.2**). Carnegieite is a polymorph of nepheline with the same composition, $Na_4[Si_4Al_4O_{16}]$.

$$Na - LTA \rightarrow Carnegieite \rightarrow Sodalite \quad (\mathbf{1.4.2})$$

The synthetic conversion of Na-LTA into sodalite zeolite is much faster at 850 and 900 °C than at 800 °C (with sodalite wt% formation of 93.7 and 99.7% against 29%, for the same synthesis time)[60]. This aligns with the phase transition detected at 820 °C by differential thermal analysis (DTA) above the melting point of sodium chloride. Notably, Na-LTA synthesis with lithium chloride (LiCl) produces the same wt% of sodalite. However, with potassium chloride (KCl), no sodalite is formed, with 100 wt% of (Na,K)-LTA zeolite remaining at the end of the synthesis[60].

No literature is available about the transformation of Na-FAU into sodalite zeolite. However, Dimitrijevic et al.[71] studied the behavior of Na-LTA and Na-FAU at temperatures ranging from 700 to 1500 °C. It was demonstrated that these starting zeolites and nepheline and carnegieite structures are intrinsically connected. Two different synthesis routes are proposed, see equations (**1.4.3**) and (**1.4.4**) for Na-LTA and Na-FAU, respectively[71].

$$Na - LTA \rightarrow Carnegieite \rightarrow Nepheline \rightarrow Carnegieite \quad (\mathbf{1.4.3})$$

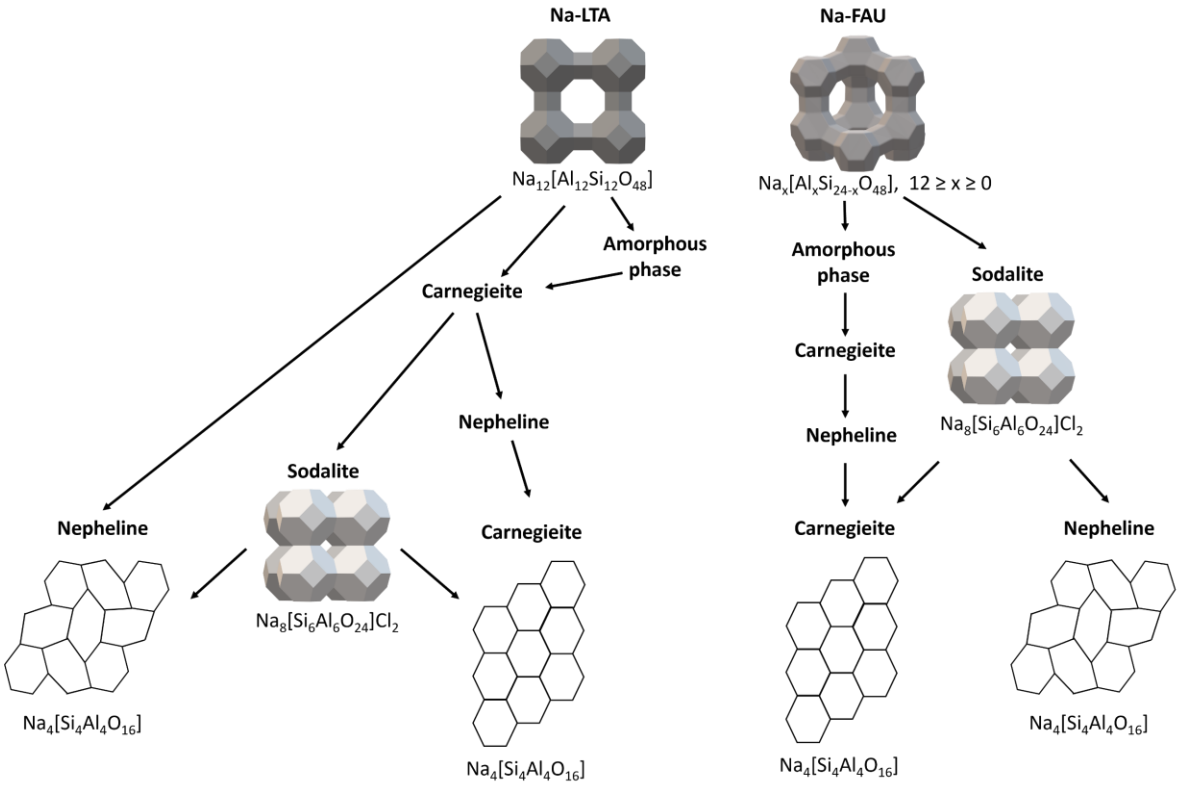
$$Na - FAU \rightarrow Amorphous\ phase \rightarrow Carnegieite \rightarrow Nepheline \rightarrow Carnegieite \quad (\mathbf{1.4.4})$$

Radulović et al.[72] also described Na-LTA transformations but at lower temperatures, from 750 to 1100 °C. The same structural differences were observed, with Na-LTA transforming into carnegieite at 800 °C, followed by the appearance of nepheline above 950 °C. Probably, the last transformation of nepheline into carnegieite was not detected since it should occur between 1100 and 1500 °C. Additionally, there was another synthetic route in which Na-LTA was converted into an amorphous phase before carnegieite and nepheline formation, similar to what happens in Na-FAU described in equation (**1.4.4**), see equation (**1.4.5**).

$$Na - LTA \rightarrow Amorphous\ phase \rightarrow Carnegieite \rightarrow Nepheline \quad (\mathbf{1.4.5})$$

Variations in composition are responsible for the distinct thermal behavior observed in these two Na-LTA samples, with compositions of $1.05Na_2O{:}1.06Al_2O_3{:}2.00SiO_2$ and $0.99Na_2O{:}1.00Al_2O_3{:}2.00SiO_2$, respectively.

The sodalite zeolite can also be converted into these two polymorph structures. Padilla et al.[73] studied the direct transformation of sodalite into nepheline, where the crystalline transition temperature varies according to the heating rate from 827 °C (at 10 °C/min) to 877 °C (at 50 °C/min). It is proposed that this transition occurs through a bulk nucleation mechanism with a constant number of nuclei and is controlled by interface reaction, resulting in a three-dimensional crystal growth. On the other hand, Schipper et al.[74] demonstrate through differential thermal analysis (DTA) the crystalline transition of sodalite into carnegieite at 740 °C. **Scheme 1.4.1** summarizes all these solid-state transformations.



Scheme 1.4.1 - Schematic presentation of several synthesis routes of Na-LTA, Na-FAU and sodalite zeolites that undergo high-temperature synthesis.

In summary, obtaining sodalite through zeolite transformation at high temperatures is not straightforward since both starting zeolites (Na-LTA and Na-FAU) and sodalite itself can suffer several structural transformations. Nonetheless, if operated within the appropriate temperature range (850-900 °C) and with excess sodium chloride, the sodalite structure can be stabilized, starting with Na-LTA zeolite[60].

Additionally, the small pore size of sodalite zeolite, 2.4 Å[60], prevents most molecules from fitting within its structure. However, species such as $[SO_4]^{2-}$ or $[SO_3]^{2-}$ can fit by replacing chloride anions in the β-cages[75], see **Figure 1.4.3**. These species can be further reduced during high-temperature synthesis, achieving different oxidation states. For instance, starting with $[SO_4]^{2-}$ can lead to the formation of $[S_2]^{-}$ or/and $[S_2]^{2-}$ clusters[20,75]. These sulfur species and their chalcogen analogs can confer multiple optical properties to sodalite, as discussed in the next section.

1.4.2 Optical properties of chalcogen-doped sodalite

The optical properties of sulfur are undoubtedly the most known and investigated of all chalcogens due to its natural occurrence as sulfur-doped sodalite mineral (previously known as

hackmanite) with the composition of $Na_8[Si_6Al_6O_{24}](Cl,S)_2$[58]. It can exhibit a handful of optical properties, including photochromism/tenebrescence and photoluminescence[76,77]. In the photochromic/tenebrescence mechanism, a pink color is obtained when irradiated with 254 nm due to the presence of $[S_2]^{2-}$ clusters[76]. Additionally, $[S_2]^-$ is responsible for the yellow-orange photoluminescence. These species have a high Stokes-shift, *ca.* 250 nm in the visible region, high external quantum efficiency (EQE) and stability at high temperatures[20]. Another photoluminescence mechanism may occur due to the presence of Ti^{3+}-V_o pairs, with long-lived emission in the blue/white region. These phenomena can also be generated through irradiation with electrons instead of light, i.e., cathodochromism and cathodoluminescence.

Selenium- and tellurium-doped sodalite may also be produced, giving rise to the same optical properties[78].

1.4.2.1 Photochromism or tenebrescence

Photochromism is a property of materials that change color upon exposure to light. As mentioned before, $[S_2]^{2-}$ species are responsible for this optical property in sodalite. Since these sulfur clusters have two negative charges, it implies that two chloride ions are substituted. Thereby, the charge balance is maintained in the sodalite matrix. Thus, in two adjacent sodalite cages, one has the $[S_2]^{2-}$ species and the other is left empty, originating a chloride vacancy (V_{Cl})[76] (**Figure 1.4.5**).

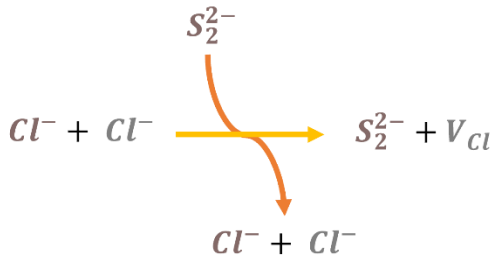


Figure 1.4.5 - Two chloride ions (in two adjacent β-cages) are substituted by one $[S_2]^{2-}$ cluster, creating a chloride vacancy (V_O).

The photochromic mechanism is expected to be as follows: **(1)** under UV light irradiation from 250-365 nm (3.4-5 eV), one electron of $[S_2]^{2-}$ cluster is transferred to a chloride vacancy (V_{Cl}), creating an F-center (a position in the lattice where an electron replaces a negatively charged ion). The electron stays trapped until there is enough energy to release it; **(2)** The purple-induced color appears because the F-center absorbs in the range 425-700 nm (1.8-2.9 eV). This is an allowed electronic transition; **(3)** when the system has enough energy through heat or exposure to sunlight, the trapped electron returns slowly to the $[S_2]^-$ cluster

(left in the adjacent β-cage). The purple color begins to fade, and the natural white color appears. See **Figure 1.4.6**, where the mechanism of photochromism is illustrated. This mechanism is reversible (tenebrescence) and can be repeated numerous times[76,79].

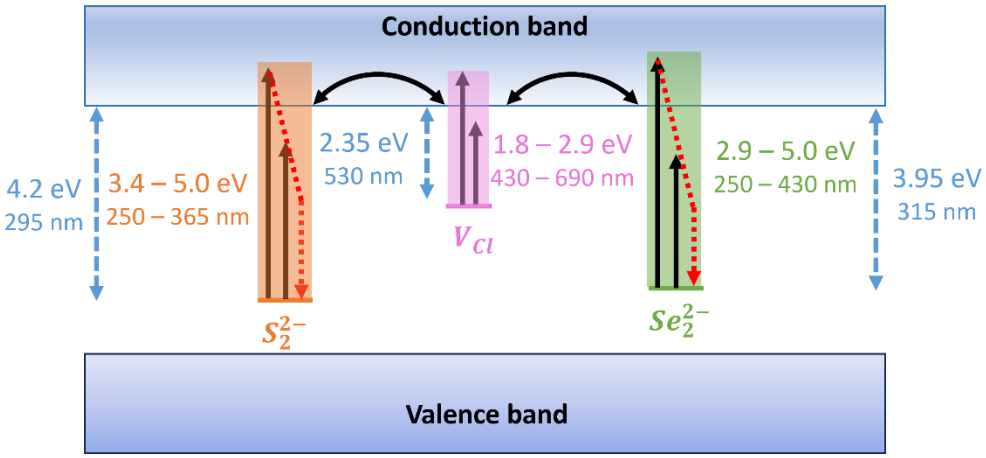


Figure 1.4.6 - Proposed photochromism mechanism of sulfur- and selenium-doped sodalites. Adapted from references **80** and **83**.

Recently, Byron et al.[80] have shown the tunability of induced colors in several types of sodalite, starting with the typical sulfur-doped sodalite, with the composition of $Na_8[Si_6Al_6O_{24}](S,Cl)_2$, and by changing sodium for other cations (Ca, K, and Rb), chloride for other anions (Br and I) and even replacing partially silicon for germanium, originating yellow to blue colors. In this study, selenium-chloride-doped sodalite was also produced, showing photochromism due to the presence of $[Se_2]^{2-}$ species. However, the maximum of the induced color is situated at around 500 nm instead of 550 nm, as in sulfur-chloride sodalite (**Figure 1.4.7**). Additionally, it can be excited in the visible region, contrary to the sulfur one. This can be particularly interesting for selective irradiation applications (see section **1.4.2.3.2**).

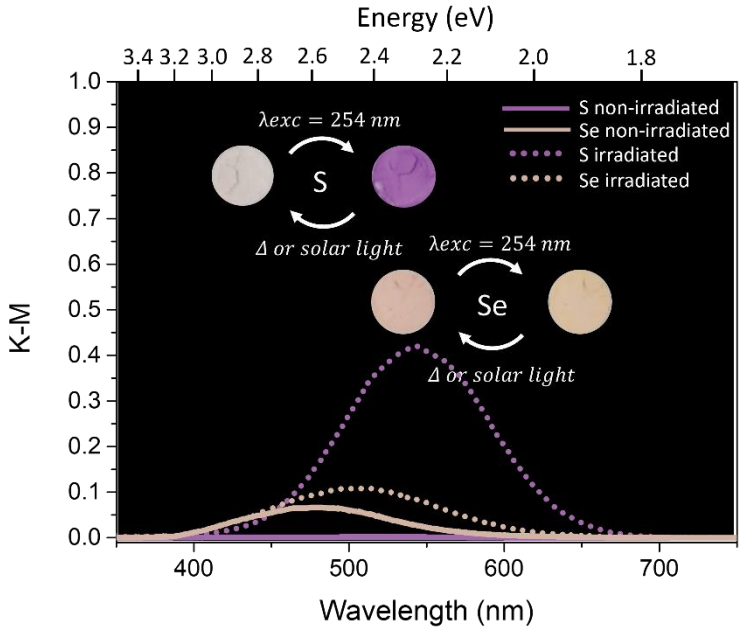


Figure 1.4.7 - Diffuse reflectance spectra of sulfur- and selenium-doped sodalites before and after UV irradiation. Δ symbol represents heat. Adapted from references **80** and **83**.

Beyond this photo-induced process, X-ray can also generate the same tenebrescence properties (cathodochromism). This phenomenon was observed in sulfur-sodalites, where similar X-ray- and UV-induced colors were found with the corresponding mechanism involving the $[S_2]^{2-}$ species and the chloride vacancy (V_{Cl})[82].

For tellurium-doped sodalites, it seems reasonable to suppose that $[Te_2]^{2-}$ clusters can also be incorporated inside sodalite, exhibiting the same tenebrescence properties[83].

1.4.2.2 Photoluminescence

When a molecule or material absorbs radiation of a specific energy, it can promote one of its valence electrons to a higher energy level (excited state), a phenomenon known as photoexcitation. If this excited electron emits light as it returns to its original energy level (ground state), the molecule or material exhibits photoluminescence. From the available information in the literature, these materials can exhibit two different photoluminescent mechanisms. One is assigned to the presence of diatomic chalcogen radical species, with emission with lifetimes in the range of nanoseconds and the second one is attributed to titanium and oxygen vacancies in the zeolite structure, showing persistent luminescence that can be detected in the seconds time scale.

1.4.2.2.1 Diatomic chalcogen radicals

In 1954, Kirk described for the first time the synthesis and photophysical characterization of sulfur-doped aluminosilicates, with emissions varying from visible (yellow-orange) to NIR region (peaking above 700 nm)[84]. After that, the yellow-orange emission has been extensively studied and assigned to the presence of $[S_2]^-$ clusters[85]. These diatomic radical species have thirteen valence electrons, with the corresponding ground and excited states of $^2\Pi_g$ and $^2\Pi_u$, respectively (**Figure 1.4.8**), resulting in absorption at *ca.* 390 nm and a characteristic emission spectrum centered at around 650 nm, with vibronic peaks separated by *ca.* 560 cm^{-1} (20-25 nm)[78,85]. It is a $\Pi \leftrightarrow \Pi^*$ transition and is allowed by symmetry, spin and parity.

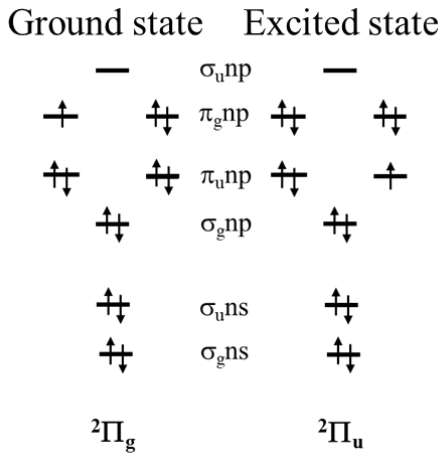


Figure 1.4.8 - General diagram of molecular orbitals of ground and excited states of the luminescent chalcogen diatomic radical species, where n = 3, 4 e 5 for S, Se e Te, respectively.

$[S_2]^-$ species exhibits photoluminescence decays of approximately 135 nanoseconds, external quantum efficiencies (EQEs) of around 53% and high-temperature stability of up to 450 °C[20,58]. The NIR emission, however, was only investigated later in 2009 by Gaft and coworkers, who reported a long-lived NIR emission spectrum in a sodalite mineral of natural origin with a decay time of 3.6 milliseconds[58]. In addition, Ruivo et al.[20] tackled the synthesis of NIR-emitting zeolites, varying the sulfur content in a systematic study. Although, the nature of the NIR emission still lacks consistent information.

Selenium- and tellurium-doped sodalites can also exhibit photoluminescent properties, where the emissive species are assigned to $[Se_2]^-$ and $[Te_2]^-$, respectively[78]. Compared with the sulfur-analogues radical, the emission of these diradical clusters changes from yellow-orange to the near-infrared region, with the increasing of the chalcogen size, i.e., from sulfur to

tellurium. **Table 1.4.1** summarizes the absorption and emission values of these chalcogen luminescent species[78].

Table 1.4.1 - Experimental values of absorption and emission transitions of the luminescent diatomic radical chalcogen species confined in zeolites. Adapted from reference **78**.

Species	Absoption $^2\Pi_g \rightarrow {}^2\Pi_u$		Emission $^2\Pi_u \rightarrow {}^2\Pi_g$	
	Energy (eV)	λ (nm)	Energy (eV)	λ (nm)
$[S_2]^-$	3.2	390	2.0	625
$[Se_2]^-$	2.5	500	1.7	715
$[Te_2]^-$	2.0	605	1.4	870

The vibronic bands in selenium-doped sodalite only appear while working at low temperatures (< 10 K), with a vibronic peak separation of 334 cm^{-1}[86]. Further characterization was made in $[Se_2]^-$-doped KI crystals[87], displaying a red emission with a photoluminescence decay time of around 14 nanoseconds and an excitation spectrum with two bands, at 515 nm (same as described above in **Table 1.4.1**, transition $^2\Pi_g \rightarrow {}^2\Pi_u$) and an additional one centered at 345 nm (transition $^2\Pi_g \rightarrow {}^2\Delta_u$), both ascribed to $[Se_2]^-$ clusters.

Tellurium-doped sodalites also contain the radical cluster, $[Te_2]^-$, which absorbs at around 600 nm and emits at 870 nm. This emission falls entirely in the near-infrared region and no vibronic bands are detected (even at low temperatures). However, the distances between the vibrational levels of the radical can be determined using the fundamental vibrational frequency provided by Raman spectroscopy, with values of *ca.* 230 cm^{-1}[19]. In **Figure 1.4.9**, the absorption and emission spectra of the mentioned diatomic chalcogen radicals are summarized[19,78,87,86].

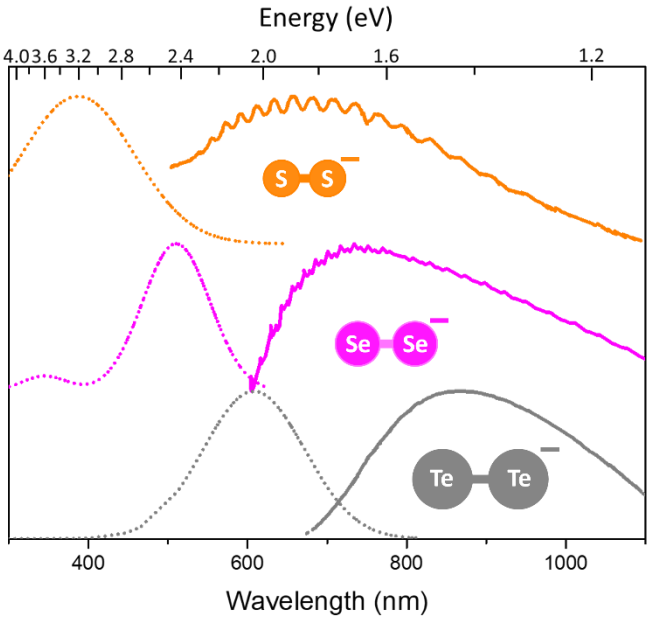


Figure 1.4.9 - Resume of the absorption (dotted) and emission (line) spectra of the diatomic chalcogen radicals. Adapted from references **19**, **78**, **87** and **86**.

1.4.2.2.2 Titanium and oxygen vacancies

Persistent luminescence is a phenomenon in which a material, after being exposed to a light source, continues to emit visible light for extended periods of time, often during hours or days (with the light source turned off). The mechanism involved is based on storing and trapping energy from an external source in charge carriers, with a slow release stimulated by thermal energy[75]. Phosphors containing rare-earth elements or heavy metals are commonly used and even find commercial applications. However, sulfur-doped sodalites can provide an alternative to these materials, showing persistent luminescence lasting for over four days.

This phenomenon is associated with the presence of titanium impurities. Zeolites typically contain several impurities, e.g. Fe, Mn and Ti[75]. In an aluminosilicate framework, Ti^{3+} species can replace aluminum and/or silicon in AlO_4 and SiO_4 tetrahedra, respectively, creating oxygen vacancies and V_O (holes in the zeolite structure where oxygen atoms are missing). Ti^{4+} might also be found in sodium sites. According to Norrbo et al.[81,88] the persistent luminescence mechanism is expected to be as follows: **(1)** the [Ti^{3+}-V_O] pair is excited with wavelengths lower than 365 nm (energies higher than 3.3 eV), creating a [Ti^{4+}-V_O^-] pair. **(2)** electrons can then move from these excited states to the conduction band and be trapped into the framework defects, V_O, and Ti^{4+} located in sodium sites, forming a vacancy populated with an electron (V_O^-) and Ti^{3+}, respectively. **(3)** when the system has enough energy (through thermal energy), the trapped electron returns slowly to the conduction band. **(4)** electrons reach the

excited states of the [Ti^{4+}-$V_O^{\cdot}$] pair, relaxing radiatively to the ground states emitting with a maximum of around 500 nm (2.5 eV). This mechanism is summarized in **Figure 1.4.10**.

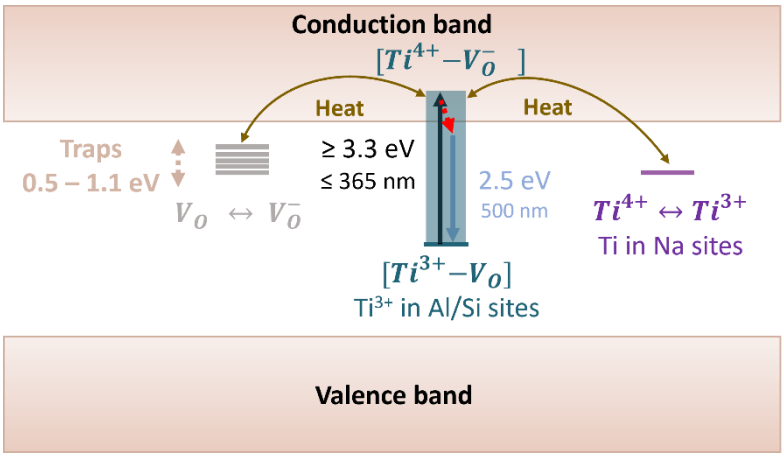


Figure 1.4.10 - Proposed mechanism of the persistent luminescence phenomenon found in sulfur-doped sodalites. Adapted from references **75**, **81** and **88**.

Additionally, **Figure 1.4.11** illustrates the corresponding persistent luminescent spectra of these sulfur-doped samples, acquired after a 1-minute delay and using two different excitation wavelengths (254 and 365 nm)[75].

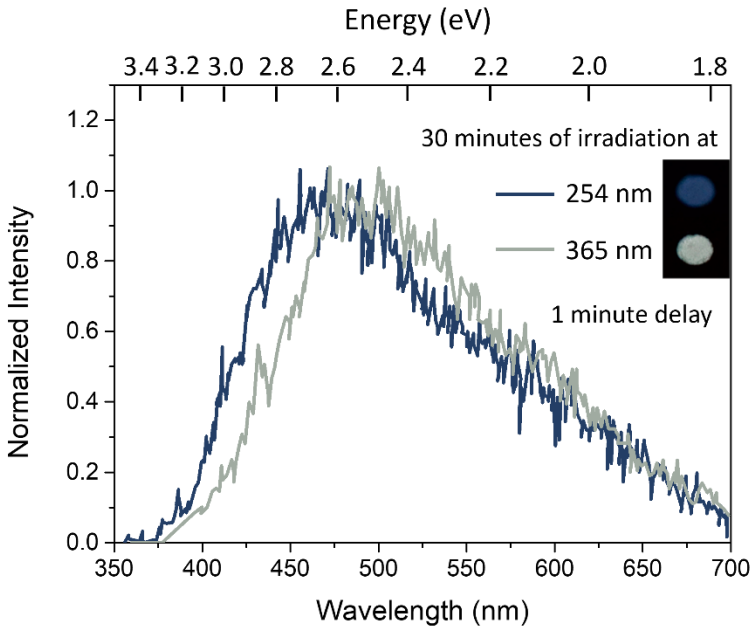


Figure 1.4.11 - Persistent luminescence spectra of sulfur-doped samples after applying a 1-minute delay using two different wavelengths (254 and 365 nm). The insets show photographs of the produced samples. Adapted from reference **75**.

Notably, both photo-induced mechanisms mentioned in this section, i.e., fluorescence, which arises from the presence of diatomic radical species, and persistent luminescence, assigned to the interaction of titanium and oxygen vacancies, can also be induced using an electron beam, a process known as cathodoluminescence[77].

1.4.2.3 Optical applications of sodalite

As stated above, sodalite can exhibit a wide range of optical properties when doped, making it suitable for several applications.

1.4.2.3.1 UV index detection with photochromic sodalite

In 2018, Norrbo et al.[22] demonstrated that photochromic sulfur-doped sodalite exhibits a color intensity dependency based on the UVC dose: higher doses induce higher color intensity (**Figure 1.4.12.A**). A couple of years later, Fang et al.[89] created UVC-sensing cellulose fibers with this material. Fibers containing 3.5% sulfur-doped sodalite were twisted together to create a single thread or yarn. Subsequently, a piece of jersey fabric was produced by knitting the yarn. This wearable fabric is UVC-sensitive, as shown in **Figure 1.4.12.B**, where a dependency between the UVC dose and color intensity is displayed (similarly to what happens with sodalite powder).

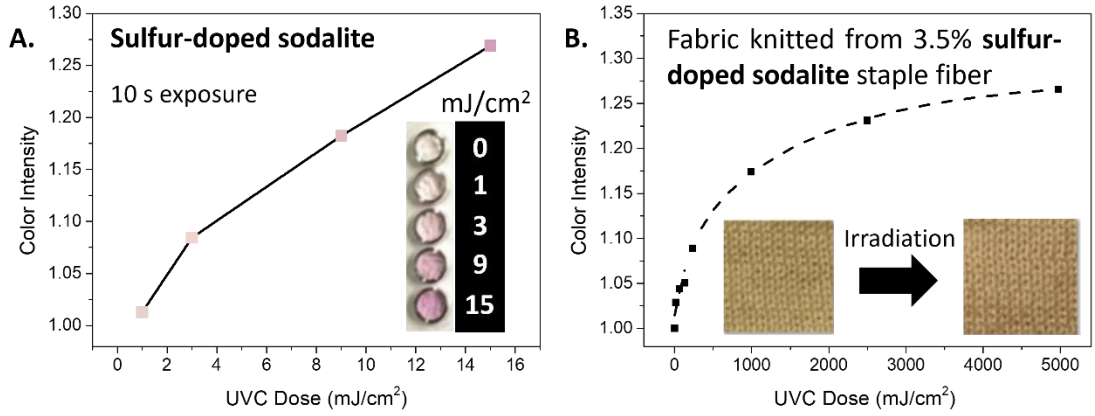


Figure 1.4.12 - (**A**) Color intensity of sulfur-doped sodalite after 10 seconds of exposure to different UVC doses. (**B**) Fabric knitted from 3.5% of sodalite in (A.) staple fibers and its color intensity dependency with UVC dose. Adapted from references **22** and **89**.

Laine et al.[90] developed a smartphone application for this sulfur-doped sodalite system. The application enables the user to estimate the UV index by comparing the non-induced and induced UV colors (**Figure 1.4.13**). This aims to increase accessibility to UV index detectors,

allowing individuals to make informed decisions about sun exposure and protect their skin from harmful UV radiation.

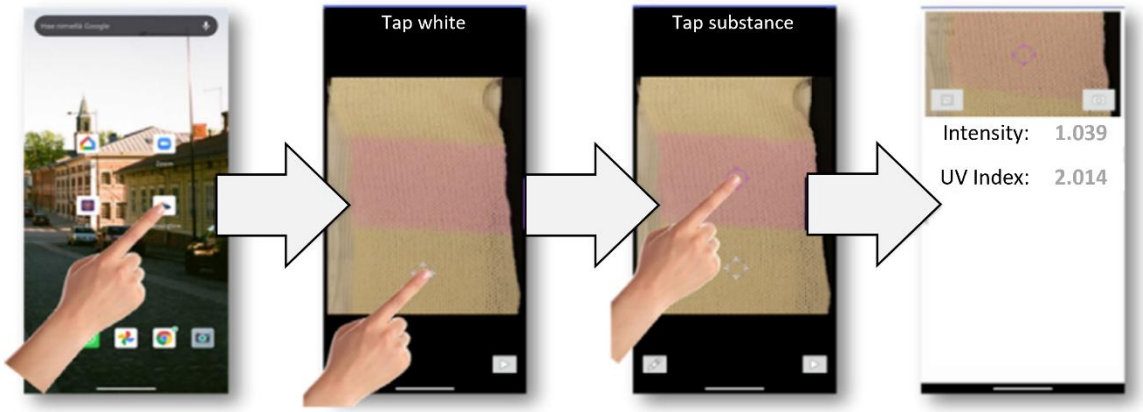


Figure 1.4.13 - Illustration of a smartphone application developed by Laine et al.[90] for this specific system, allowing the user to estimate the UV index. Adapted from references **22** and **89**.

1.4.2.3.2 Dosimetry of UV radiation

As described in section **1.4.2.1**, photochromic sodalites are highly tunable, showing a wide range of UV-induced colors, from yellow to blue. These differences lead to differences in the excitation threshold, ideal conditions for dosimetry applications. Byron et al.[80] developed a mixture containing two sodalites, a blue iodo-sodalite and a pink selenium-chloro-sodalite, with absorption maxima at 620 and 550 nm, respectively (**Figure 1.4.14.A**).

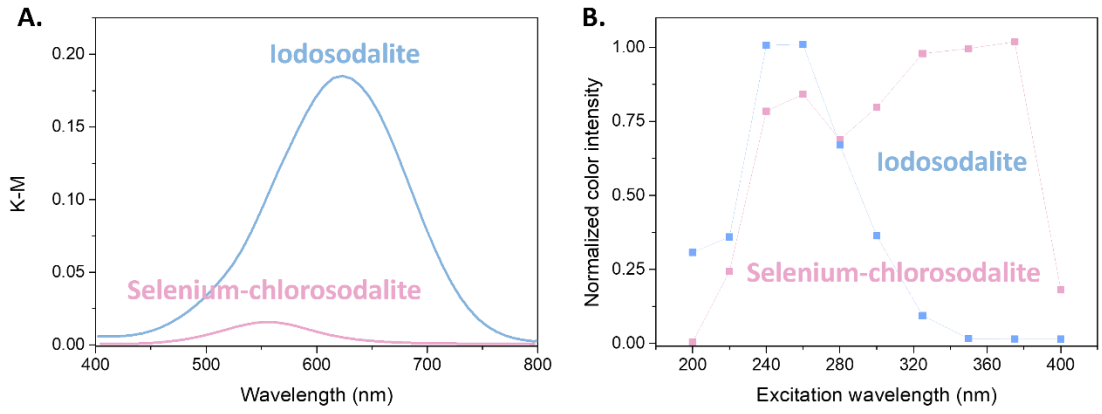


Figure 1.4.14 - (**A**) Diffuse reflectance spectra of two irradiated samples considered for wavelength-sensitive photochromism. (**B**) Corresponding induced-color intensities according to the excitation wavelength. Adapted from reference **80**.

The blue sodalite predominates under 280 nm, whereas only the pink variety is excited above 320 nm (**Figure 1.4.14.B**). This is evidenced in **Figure 1.4.15.A**, where a significant shift in

maximum absorption concerning the excitation wavelength of a similar mixture is visible. This phenomenon is further illustrated after applying the mixture in a film, as shown in the proof-of-concept in **Figure 1.4.15.B**. Notably, this material can distinguish between UVA, UVB and UVC radiation through color changes after exposure. Additionally, spectroscopic analysis of the induced UVA- and UVC-colors can be used to quantify the doses of both radiation types after simultaneous exposure.

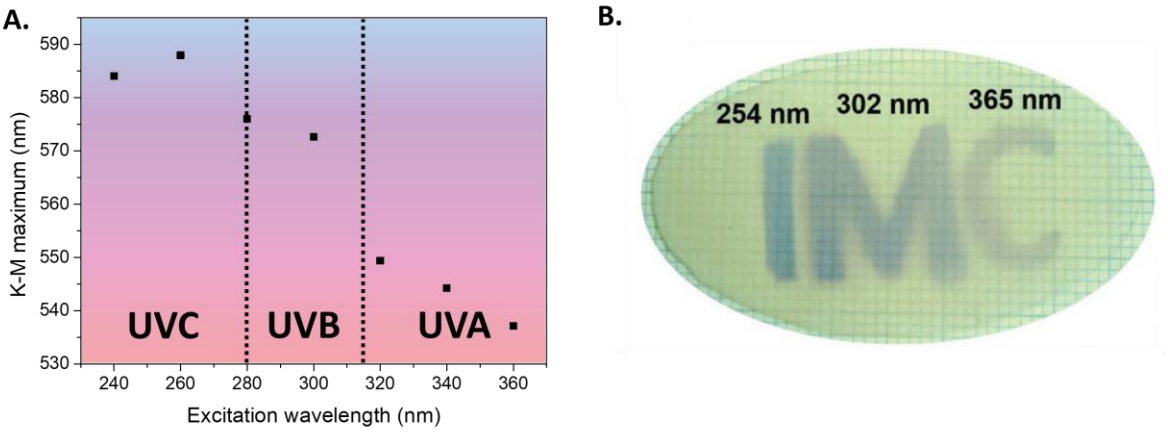


Figure 1.4.15 - (**A**) Diffuse reflectance maximum for a similar mix to that present in **Figure 1.4.14** concerning the excitation wavelength. (**B**) A film created from a sodalite mix, marked with the inscription 'IMC', after irradiation with different UV radiation. Adapted from reference **80**.

In summary, these materials have proven to function as optical sensors, detecting UVA, UVB, and UVC radiation. They also allow for quantifying radiation doses in the case of UVA and UVC energies. Such capabilities are particularly valuable for gaining insights into real-life scenarios and precise measurement and control of UV radiation exposure. For example, these materials can serve as UV sensors for evaluating the effectiveness of sunscreens.

1.4.2.3.3 Single-Phase LED Phosphors

Light-emitting diodes (LEDs) have become increasingly important compared to older lighting technologies, such as incandescent bulbs and fluorescent lights. This technology offers higher energy efficiency, longer lifespan and is environmentally friendly. Hence, white light-emitting LEDs (WLEDs) are now regarded as the evolution of traditional lighting sources, with remote phosphor-converted WLEDs (pc-LEDs) being the most common type. In pc-LEDs, a commercial LED is used, typically a blue one, and a phosphor is used on top. For instance, a

blue LED (InGaN) can be combined with a yellow Ce^{3+}-doped yttrium-aluminum garnet (YAG:Ce^{3+}) phosphor, resulting in WLEDs through merging blue and yellow colors.

Baekelant et al.[91] proved that a WLED can be achieved by using a silver-exchanged sulfur-doped sodalite. After ion exchanging sulfur-doped sodalite (which has $[S_2]^-$ as the emitting clusters, see section **1.4.2.2.1**) with a silver-containing solution, a new white emission was produced (**Figure 1.4.16.A**). As a proof-of-concept, a device was conceived in which a film composed of this ion-exchanged sample was placed on top of a (near-UV) NUV-LED, with an emitting wavelength of 340 nm, showing the same white emission, as illustrated in **Figure 1.4.16.B**.

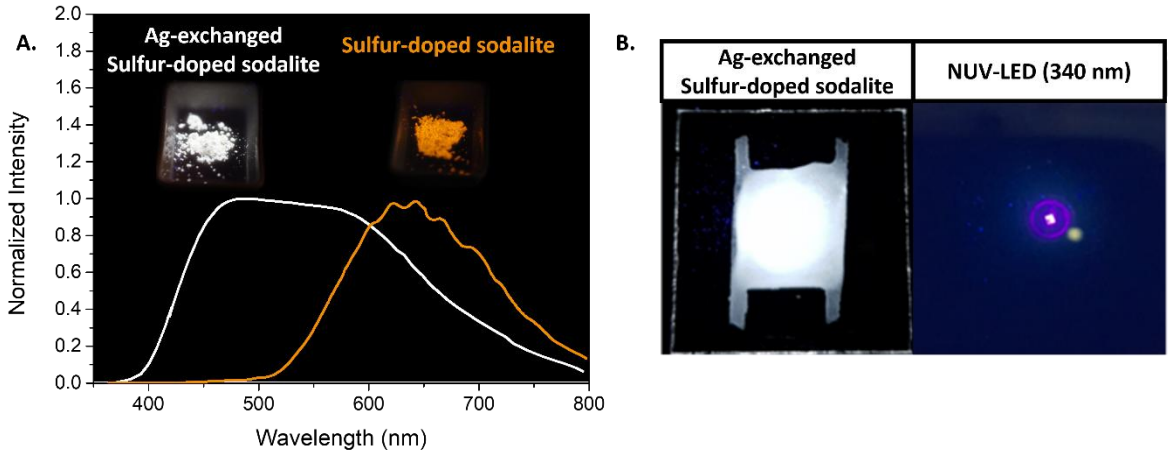


Figure 1.4.16 - (**A**) Emission spectra of starting sulfur-doped sodalite and Ag-exchanged sulfur-doped sodalite, with insets of photographs of samples under 350 nm excitation. (**B**) **Left -** Film of the Ag-exchanged sulfur-doped sodalite, excited by a NUV-LED (340 nm); **Right -** NUV-LED (340 nm). Adapted from references **20** and **91**.

Furthermore, Norrbo et al.[88] also demonstrated the feasibility of using this material for LEDs, with sodalites exhibiting persistent luminescence rather than shorter-lived emissions (as shown in the previous example). Here, a sodalite with the composition of $LiNa_7[Si_6Al_6O_{24}](S,Cl)_2$:2%Ti was used. When excited at 254 nm, this material shows an emission maximum at around 500 nm, which remains observable with a spectrometer for more than 100 hours. Additionally, it stays for 7 hours above the standard photopic luminance limit of 0.3 mcd/m^2, according to 2009 regulations[92] (**Figure 1.4.17.A**). The authors also performed some experiments to test the suitability of this material as a phosphor, with LED excitation of 310 nm, as illustrated in **Figure 1.4.17.B**.

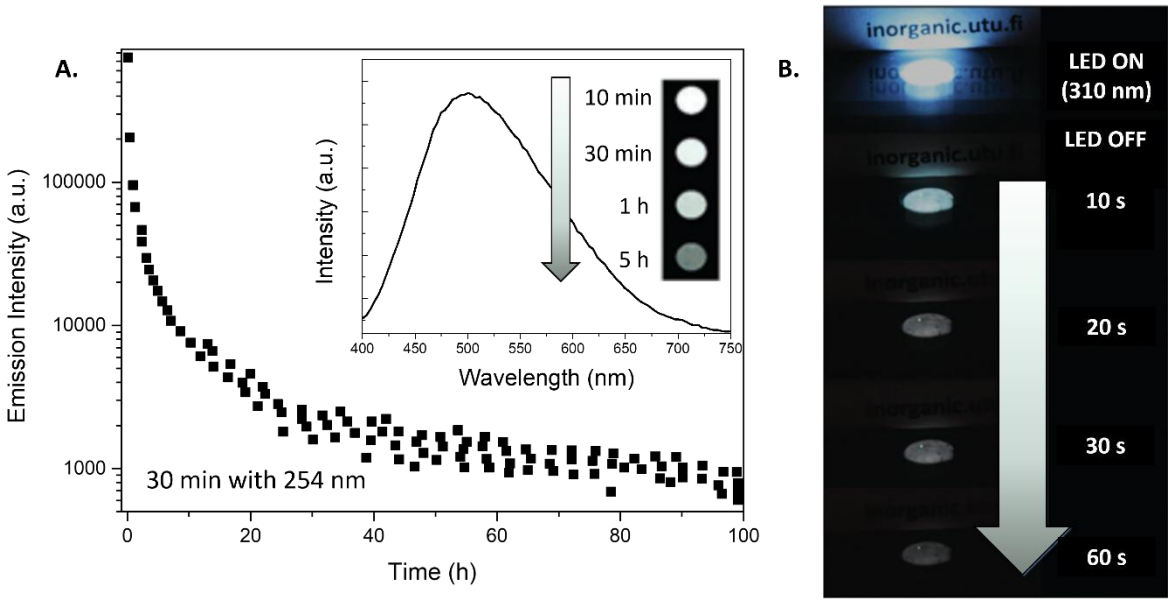


Figure 1.4.17 - (**A**) Fading of the persistent luminescence over time after 30 minutes of excitation at 254 nm. The inset shows the corresponding emission spectra of this emission and photographs of this material taken at different times. (**B**) Performance of this material as a phosphor with 310 nm LED excitation followed by glow in the dark. Adapted from reference **88**.

Besides surpassing rare-earth-doped materials in availability and raw material cost, sulfur-doped sodalites can outperform them by exhibiting white emission instead of single RGB colors (blue, green, and red) and longer persistent luminescence over time. For example, the commercial phosphor $Y_2O_2S:Eu^{3+},Mg^{2+},Ti^{4+}$ shows red emission and stays for around 4 hours above the standard photopic luminance limit of 0.3 mcd/m^2[88].

1.4.2.3.4 Bioimaging

Continuing with the last discussed samples and Norrbo et al.[88] study, further investigation was conducted on $LiNa_7[Si_6Al_6O_{24}](S,Cl)_2$:2%Ti sodalite. Both the bulk powder and aqueous suspension of these materials were analyzed, revealing the presence of micro-sized particles as well as smaller particles with an approximate size of 200 nm (**Figure 1.4.18**).

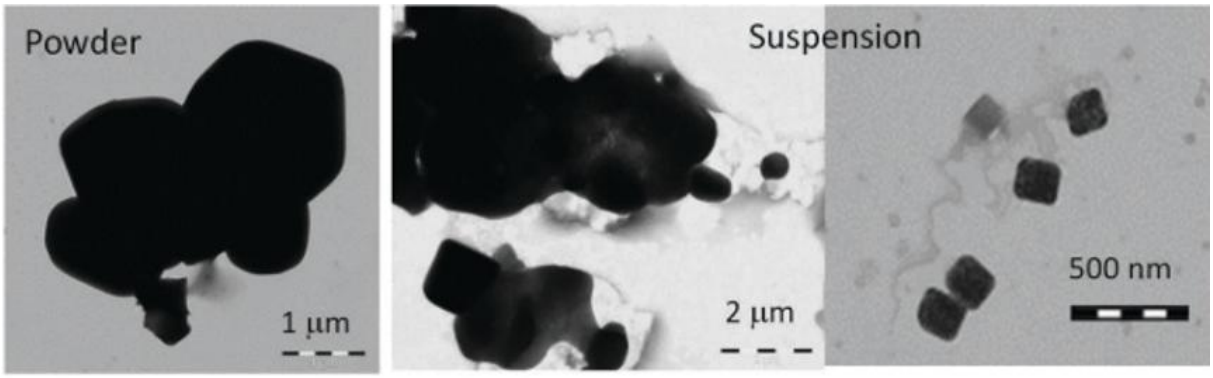


Figure 1.4.18 - Transmission Electron Microscopy (TEM) images of $LiNa_7[Si_6Al_6O_{24}](S,Cl)_2$:2%Ti sodalite particles in powder form and aqueous suspensions. Adapted from reference **88**.

Notably, similar photophysical properties were observed in both forms, as depicted in **Figure 1.4.17** for powder and **Figure 1.4.19** for solution. Even at low concentrations in the nanomolar range, persistent emission was detected in solution.

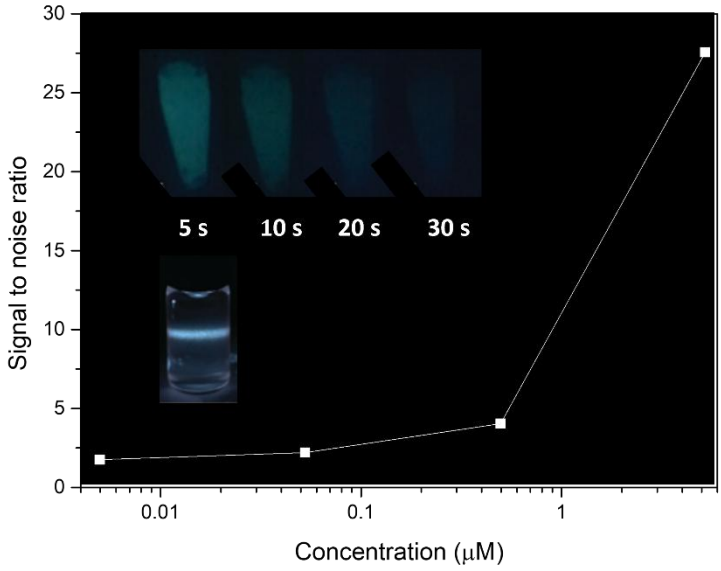


Figure 1.4.19 - **Graph:** Effect of $LiNa_7[Si_6Al_6O_{24}](S,Cl)_2$:2%Ti sodalite particle concentration on persistent luminescence intensity observed in aqueous suspension. **Top photograph:** Persistent luminescent in an aqueous suspension with a concentration of 5 mg/mL after 1 min irradiation by a solar simulator lamp (1000 W/m^2). **Bottom photograph:** aqueous suspension under excitation of a 310 nm LED. These photographs were captured using a standard cell phone camera (Nokia Lumia 520). Adapted from reference **88**.

Nevertheless, a drawback identified regarding the applicability of these materials in bioimaging systems is related to the material excitation wavelength, which falls into the UV region. Direct exposure to this energy can potentially induce cell apoptosis and death[93].

However, this can be easily overcome since the material presents persistent luminescence and excitation does not need to occur *in situ*. This allows the material to be excited for minutes outside the tissue, followed by its injection and subsequent detection, which can occur seconds, minutes, or even hours later.

In conclusion, this section has demonstrated the material's broad range of optical applications, depending on its distinct optical properties, such as photochromism and short-lived and long-lived photoluminescence. These applications vary from UV detection and dosimetry to remote phosphor-converted WLEDs (pc-LEDs) and bioimaging, primarily involving the visible region. Consequently, the following chapters will focus on developing and comprehending different near-infrared (NIR)-emitting chalcogen-doped zeolites for NIR applications.

2

NIR-EMITTING SULFUR-DOPED ZEOLITES

The third part of this chapter - subchapter **2.3** - is partly based on the paper "Viola, C. *et al.* Long-lived NIR emission in sulfur-doped zeolites due to the presence of $[S_3]^{2-}$ clusters. *Materials Today Chemistry* **30** (2023)".

The author contributed to the planning and execution of all the experiments presented in this paper, including the synthesis and mainly structural and photophysical experiments. The author was also involved in the interpretation and discussion of all results and in the preparation of the manuscript.

Sulfur is essential for life, serving as a crucial element in numerous biochemical processes, including the creation of amino acids, vitamins and coenzymes. This non-metallic element exhibits a wide range of forms, from elemental sulfur to sulfides, sulfates, and organosulfur compounds. Elemental sulfur, in particular, is exceptionally abundant on Earth and has been a valuable resource for human societies for millennia, finding extensive applications due to its natural abundance.

One example of sulfur's historical significance is lapis lazuli, known for approximately 5500 years and highly valued as a precious stone and pigment source (**Figure 2.1**). Lazurite mineral [$(Na,Ca)_8(Al_6Si_6O_{24})(SO_4,S,Cl)_2$] is responsible for the valued blue color of this gemstone due to sulfur radicals entrapment within zeolites[78,94]. These chromophores consist of yellow $[S_2]^-$ and blue $[S_3]^-$ species, with corresponding absorption peaks at 380-400 nm and 600 nm, respectively[95]. Adjusting the ratio of these two species yields different shades, ranging from violet-blue to steel-blue and green, in proportion to the increase of $[S_2]^-$ content[78,96]. However, these clusters present emissive properties, in contrast to the triatomic sulfur species, $[S_3]^-$.

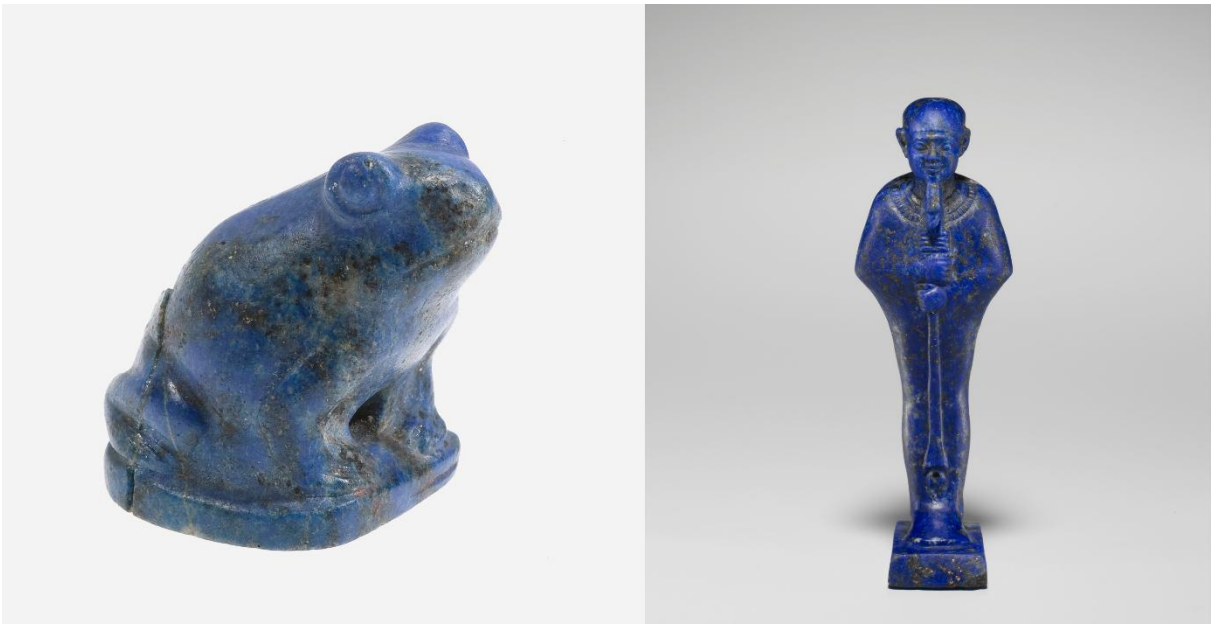


Figure 2.1 - Lapis lazuli art pieces present in The Metropolitan Museum of Art, New York - (**Left**) Frog Amulet and (**Right**) Amulet, Ptah[97].

The zeolite host for these sulfur species is sodalite, with the chemical formula $Na_8[Si_6Al_6O_{24}]Cl_2$, and can also be naturally found as sulfur-doped sodalite, $Na_8[Si_6Al_6O_{24}](S,Cl)_2$[58]. This material exhibits different optical properties, including photoluminescence, cathodoluminescence, photochromism, and cathodochromism[77,80,85], depending on the sulfur species present. Concerning photoluminescence, $[S_2]^-$ is responsible for emitting light

in the visible region, specifically in the yellow-orange zone, with a maximum at 650 nm. This emission spectrum displays vibronic bands at room temperature, with a peak separation of *ca.* 560 cm^{-1} (20-25 nm)[85]. These bands arise from electron transitions between vibrational levels of the excited and fundamental electronic states of $[S_2]^-$. The spacing between these vibronic levels reflects the fundamental vibrational frequency of this molecule's ground state. Additionally, these species have a photoluminescence lifetime of about 135 nanoseconds, with external quantum efficiencies (EQEs) reaching around 53% and stability at high temperatures, up to 450 °C[20,58]. An electron beam can also induce identical emission spectra, known as cathodoluminescence[77].

Besides the emission in the visible region, researchers such as Kirk[84] in 1954, and more recently, Gaft et al.[58] in 2008, have identified a new emission that falls in the near-infrared (NIR) region. This emission has been assigned to Fe^{3+} centers, showing a photoluminescence decay time at 77 K of 3.6 milliseconds. Furthermore, studies conducted by Ruivo et al.[20] revealed that varying the sulfur and chloride content within sodalite results in a change from visible to NIR emission at higher S/Cl ratios. This might indicate that different excited states of $[S_2]^-$ are populated or that a new sulfur species arises at these concentrations.

The development of a sulfur-based NIR emitter represents a significant advancement in the current state of the art. This element is abundant and non-toxic, allowing for inexpensive synthesis with minimal environmental impact[22], in contrast to common NIR emitters that suffer from poor photo and chemical stability and often rely significantly on rare-earth elements, considered critical raw-materials by the European Union[21].

2.1 Influence of NaCl and Synthesis Duration on Optical Properties

According to the knowledge produced by Ruivo et al.[20], the S/Cl ratios in sulfur-doped zeolites have been shown to affect their luminescent properties. Near-infrared (NIR) emission is observed at high S/Cl ratios during a 1-hour synthesis at 900 °C starting from commercial Na-LTA zeolite. Furthermore, variations in crystalline phases were detected depending on the S/Cl ratios used. The powder X-ray diffractograms demonstrated that Na-LTA zeolite was completely converted into sodalite and nepheline. Sodalite content decreased as S/Cl ratios increased, while nepheline exhibited the opposite behavior. This suggests that samples containing more

nepheline exhibit NIR-emitting properties. However, the potential influence of the produced crystalline phase on the optical properties was neither proposed nor studied.

The objective of this first study is to address this gap by conducting a synthesis systemization and optimization. It aims to elucidate any correlation between crystalline phases and the formation of NIR-emitting species and determine the optimal synthesis parameters for achieving these desired optical properties. For that, different synthesis durations and S/Cl ratios were studied. Additionally, the impact of NaCl content on the optical properties was also tested since studies show a relationship between the use of this salt and the sodalite crystalline phase stabilization[60].

2.1.1 Synthesis and structural characterization

In the previous study[20], thermally-treated sulfur-doped aluminosilicate zeolites with S/Cl nominal ratios of 0.21 and 4.5 exhibited the most distinct optical properties with the yellow-orange emission characteristic of $[S_2]^-$ clusters appearing at S/Cl=0.21 and the NIR emission at S/Cl=4.5. Therefore, this study focuses on investigating the properties of zeolites at these concentrations by mixing the appropriate amounts of Na-LTA zeolite, NaCl, and Na_2SO_3 and using S/Cl nominal ratios of 0.21 and 4.5, following the stoichiometry $Na_8Si_6Al_6O_{24}S_xCl_{2-2x}$. Each resulting mixture was divided into three portions, each undergoing heat treatment at 900 °C for one, four and eight hours under the same reducing atmosphere. See the experimental procedure in section **7.1.1**.

Two additional mixtures with S/Cl of 0.21 and 4.5 were also prepared using identical amounts of Na-LTA zeolite and Na_2SO_3 but with an excess of NaCl, further denominated as S/Cl=0.21 +NaCl and S/Cl=4.5 +NaCl, respectively. Afterward, these samples were subjected to the same high-temperature procedure for 1 hour. See the experimental procedure in section **7.1.1**.

The influence of synthesis time at 900 °C on the final crystalline phases was confirmed through powder X-ray diffraction (PXRD) analysis, see section **7.2.13** for more information about this technique. In all the produced samples, Na-LTA zeolite ($Na_{12}Si_{12}Al_{12}O_{48}$) was not detected and was transformed entirely into sodalite ($Na_8Si_6Al_6O_{24}Cl_2$), nepheline ($Na_4Si_4Al_4O_{16}$) and carnegieite ($Na_4Si_4Al_4O_{16}$) aluminosilicate structures (**Figure 2.1.1** and **Figure 2.1.2**), as described in equation (**2.1.1**).

$$Na - LTA \xrightarrow{\Delta} Sodalite + Nepheline + Carnegieite \qquad (2.1.1)$$

According to the literature, these three structures are typically formed at high temperatures from Na-LTA zeolite[60,72]. However, it is worth noting that while nepheline and carnegieite can be formed at high temperatures alone, sodalite formation additionally requires the presence of NaCl[60], see **Scheme 1.4.1** of the introduction section where solid-state transformations starting from Na-LTA zeolite are summarized. This suggests that the integrity of the sodalite cages (shared structural units in Na-LTA and sodalite zeolites) is preserved by incorporating chloride anions, ensuring stability. Additionally, sodium plays a pivotal role in maintaining charge balance within the structure[98].

PXRD diffractograms evidence variations when comparing the two concentrations following just 1 hour of synthesis at 900 °C (**Figure 2.2.1.A** and **Figure 2.1.2.A**). These differences are especially evident regarding the sodalite phase formation, varying from around 89% to 36%, from samples with S/Cl=0.21 to S/Cl=4.5 (**Figure 2.2.1.B** and **Figure 2.1.2.B**), respectively. This can be explained by decreasing the chloride amount when increasing the sulfur amount since the stoichiometry used was S_xCl_{2-2x}, confirming Ding et al.[60] observations regarding the importance of chloride in sodalite zeolite stabilization. Furthermore, longer synthesis times also demonstrated an impact on the produced crystalline phases according to the S/Cl ratios. Samples with S/Cl=0.21, initially consisting of 89% sodalite, decrease to 72% after an 8-hour synthesis. This reduction in sodalite led to the formation of nepheline, increasing from 9% to 26%. In contrast, carnegieite showed minimal changes, not exceeding 2% (**Figure 2.2.1.B**).

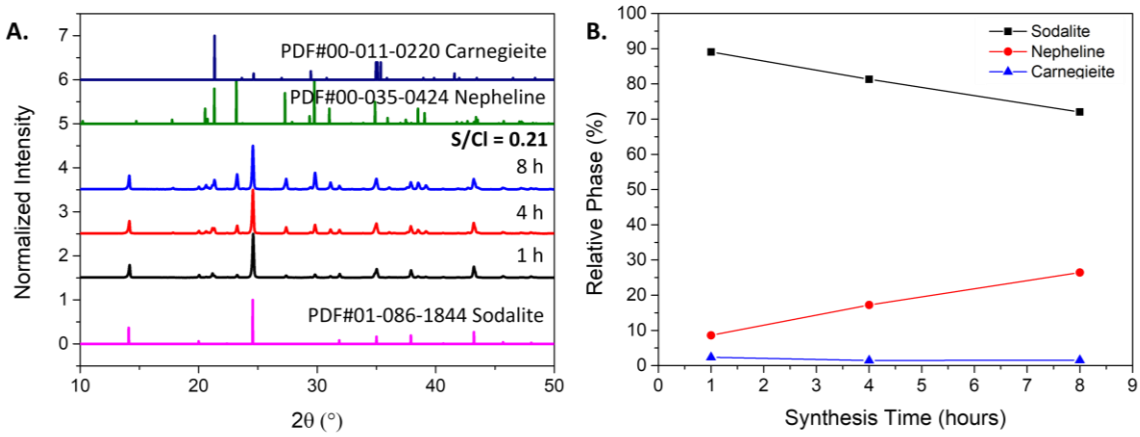


Figure 2.1.1 - (**A**) PXRD diffractograms of sample S/Cl=0.21 according to the synthesis time, comparing with the ICDD standard reference card of 01-086-1844 sodalite ($Na_8Si_6Al_6O_{24}Cl_2$), 00-035-0424 nepheline ($NaSiAlO_4$) and 00-011-0220 carnegieite ($NaSiAlO_4$). (**B**) Corresponding calculated relative phases.

Samples with S/Cl=4.5 started with just 36% of sodalite, decreasing to 4% after 8 hours. In this case, sodalite appears to transform into nepheline and carnegieite, respectively changing from 22% to 37% and from 42% to 59% (**Figure 2.1.2.B**).

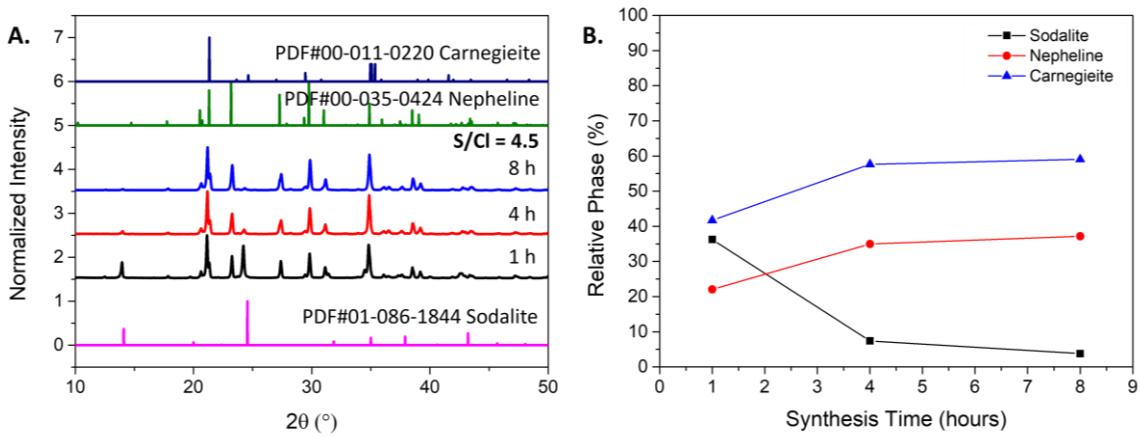


Figure 2.1.2 - (**A**) PXRD diffractograms of sample S/Cl=4.5 according to the synthesis time, comparing with the ICDD standard reference card of 01-086-1844 sodalite ($Na_8Si_6Al_6O_{24}Cl_2$), 00-035-0424 nepheline ($NaSiAlO_4$) and 00-011-0220 carnegieite ($NaSiAlO_4$). (**B**) Corresponding calculated relative phases.

In summary, the two studied concentrations exhibited distinct behaviors by varying the synthesis times. At low S/Cl ratios, the zeolite transformation is summarized in equation (**2.1.2**), while at high S/Cl ratios, it is represented by equation (**2.1.3**). Previous studies have described these zeolite transformations at high temperatures, starting from the sodalite zeolite[73,74].

$$Sodalite \xrightarrow{\Delta} Nepheline \text{ (low S/Cl ratios)} \quad (2.1.2)$$

$$Sodalite \xrightarrow{\Delta} Nepheline + Carnegieite \text{ (high S/Cl ratios)} \quad (2.1.3)$$

Additionally, considering the apparent effect of chloride in stabilizing the sodalite zeolite, samples based on S/Cl=0.21 and 4.5 containing the same amount of raw materials but with an excess of NaCl were also studied. The PXRD patterns of these two samples, denominated as S/Cl=0.21 + NaCl and S/Cl=4.5 + NaCl, are presented in **Figure 2.1.3**, along with the respective calculated contributions of crystalline phases summarized in **Table 2.1.1**. These results are compared with previously discussed ones from samples S/Cl=0.21 and 4.5 treated at 900 °C for 1 hour.

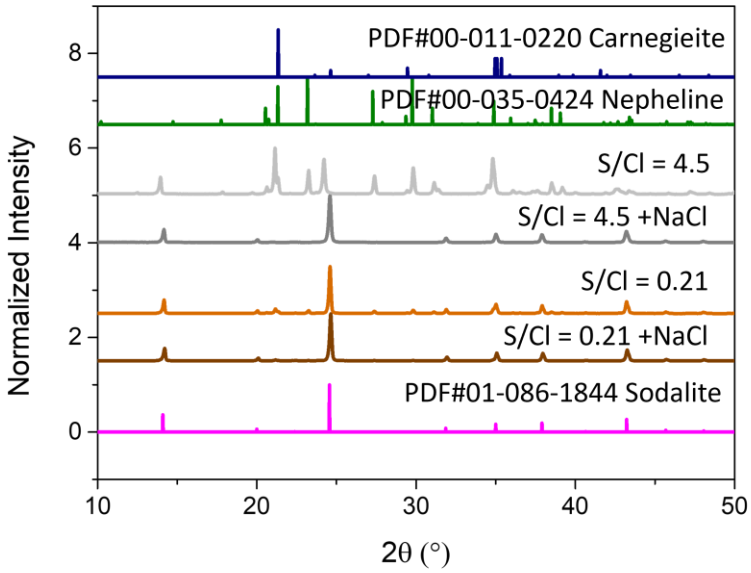


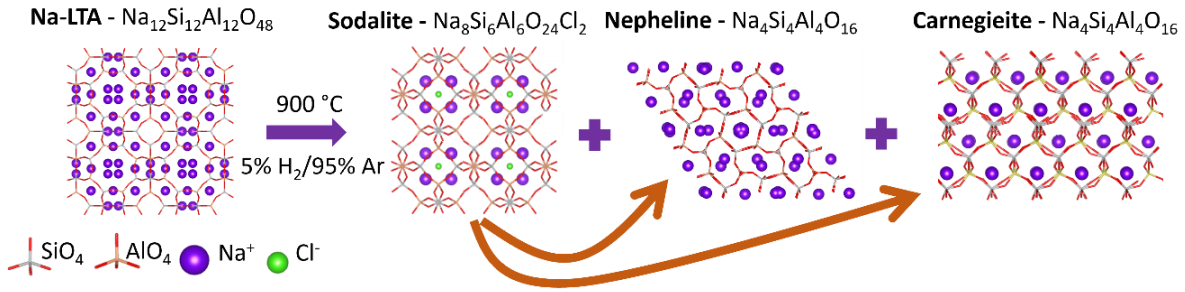
Figure 2.1.3 - PXRD diffractograms of synthesized samples after 1 hour at 900 °C using S/Cl=0.21 and 4.5 (lighter colors) and corresponding samples with a NaCl excess (darker colors) while comparing the ICDD standard reference cards of sodalite, nepheline and carnegieite phases.

It is evident that adding an excess of NaCl highly stabilizes the sodalite phase, reaching >94% in both samples. This may occur since it is believed that when confined within β-cages (shared structures of Na-LTA and sodalite zeolites), chloride occupies the center of these structures (see **Figure 1.4.3** in the introduction section). Consequently, this hinders the transformation of Na-LTA zeolite into other structures, such as nepheline and carnegieite aluminosilicates. Such an effect is more pronounced in the sample with a higher sulfur concentration, as the sample used as reference (S/Cl=4.5) starts with a sodalite percentage of 36%. In contrast, the sample with a lower sulfur concentration used for direct comparison (S/Cl=0.21) already begins with a high sodalite content of 89%, making the difference less impactful.

Table 2.1.1 - Calculated crystalline phases of the synthesized samples after 1 hour at 900 °C with S/Cl=0.21 and 4.5, along with their corresponding pairs with a NaCl excess, based on the ICDD standard reference cards.

Nominal S/Cl	Crystalline Phases (%)		
	Sodalite	Nepheline	Carnegieite
0.21	89	9	2
0.21 +NaCl	94	3	3
4.5	36	22	42
4.5 +NaCl	98	0	2

In summary, variations in synthesis times and chloride loading (more evident when using a NaCl excess) significantly impact the final crystalline phases. Longer synthesis times lead to a reduction in the sodalite crystalline phase, transforming it into nepheline and carnegieite phases. Additionally, chloride is observed to stabilize the sodalite phase. **Scheme 2.1.1** provides an overview of the transformations observed in these produced samples following a high-temperature treatment.



Scheme 2.1.1 - Proposed synthesis scheme of the zeolite transformations starting from Na-LTA zeolite at high temperatures, adopted from crystallographic data[99–102].

The implications of these structural differences in the optical properties were studied in the next section.

2.1.2 Optical properties

The powder samples were first analyzed using diffuse reflectance spectroscopy. After applying the Kubelka-Munk transformation[103], the spectra of samples with S/Cl=0.21 and samples with S/Cl=4.5 were obtained (see more details about this technique and Kubelka-Munk transformation in section **7.2.2**). The diffuse reflectance spectra of samples S/Cl=0.21 (1h, 4h, 8h and +NaCl-1h) exhibit the same profile (**Figure 2.1.4.A**), peaking at around 385 nm, consistent with the transition $^2\Pi_g \rightarrow {}^2\Pi_u$ of $[S_2]^-$ clusters[104], refer to **Figure 1.4.8** of the introduction chapter for more information about this transition. However, variations in intensities were observed, decreasing with increasing synthesis times and showing a slight increase in the sample with an excess of NaCl compared with the sample submitted to the same synthesis time - S/Cl=0.21 1h, (as discussed below).

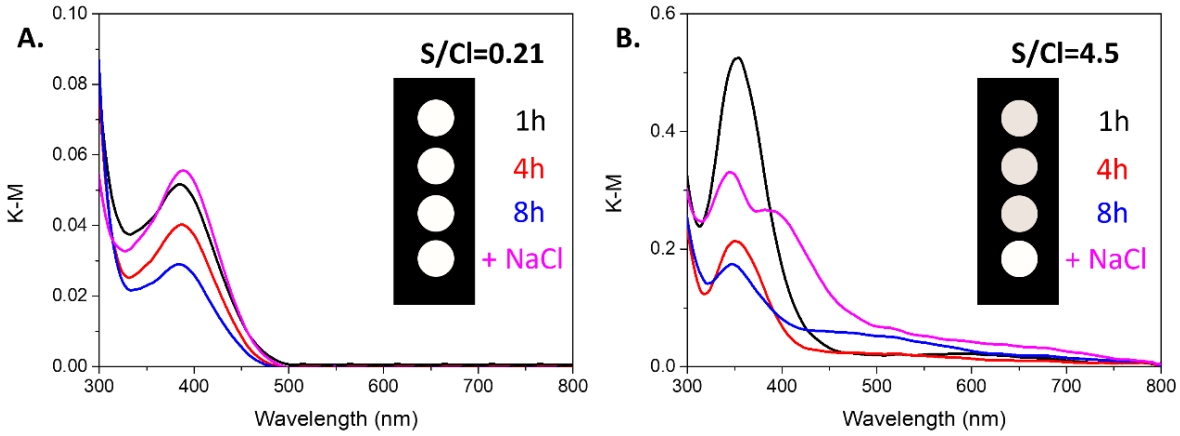


Figure 2.1.4 - Diffuse reflectance spectra of samples with S/Cl=0.21 (**A**) and S/Cl=4.5 (**B**) using different synthesis times and a NaCl excess. The insets show photos of the samples under ambient light.

In samples with S/Cl=4.5 (1h, 4h, 8h and +NaCl-1h), a main absorption band is observed, peaking at around 355 nm (**Figure 2.1.4.B**), indicative of the absorption of the NIR-emitting clusters[20]. The absorption intensities of these samples decrease once again with increasing synthesis time, i.e., from 1 to 8 hours. Additionally, sample S/Cl=4.5 with excess of NaCl exhibits an additional absorption band around 385 nm, confirming the presence of $[S_2]^-$.

These absorption spectra results, along with the PXRD data, suggest that $[S_2]^-$ species are related with the sodalite zeolite since its absorption is observed in samples presenting >70% of sodalite crystalline phase. On the other hand, the absorption at 355 nm, indicative of the NIR emitters, is detected in samples containing more carnegieite and nepheline phases (with sample S/Cl=4.5 8h containing just 4% of sodalite). The absorption at 355 nm is still observed in sample S/Cl=4.5 with an excess of NaCl, which only contains 2% of carnegieite. This suggests that NIR emitters can still be detected even at lower amounts of this crystalline phase. Besides the differences found in the crystalline phases, the variations in absorption intensity may also be attributed to the formation of other sulfur species at longer synthesis times, namely $[S_3]^-$ absorbing at 600 nm[67] (species detected in Ruivo et al.[20] work after thermal treatment), as illustrated in **Figure 2.1.4.B**.

Next, the photoluminescence of these samples under different wavelengths was evaluated (see section **7.2.3** for more details about this technique). When exciting the S/Cl=0.21 samples at the $[S_2]^-$ absorption wavelength, i.e., 380 nm, the emission spectra of these species were observed in all samples with its characteristic vibronic resolution ($^2\Pi_u \rightarrow {}^2\Pi_g$ transition)[85,105], peaking at around 625 nm (**Figure 2.1.5.A**). The excitation spectra corresponding to the emission at 650 nm revealed a band peaking at 385 nm, consistent with

the diffuse reflectance spectra and confirming the presence of $[S_2]^-$ (**Figure 2.1.5.B**). Intensity comparisons showed a similar behavior to diffuse reflectance spectroscopy, decreasing with synthesis times except for the sample with NaCl excess, which exhibited the highest intensity.

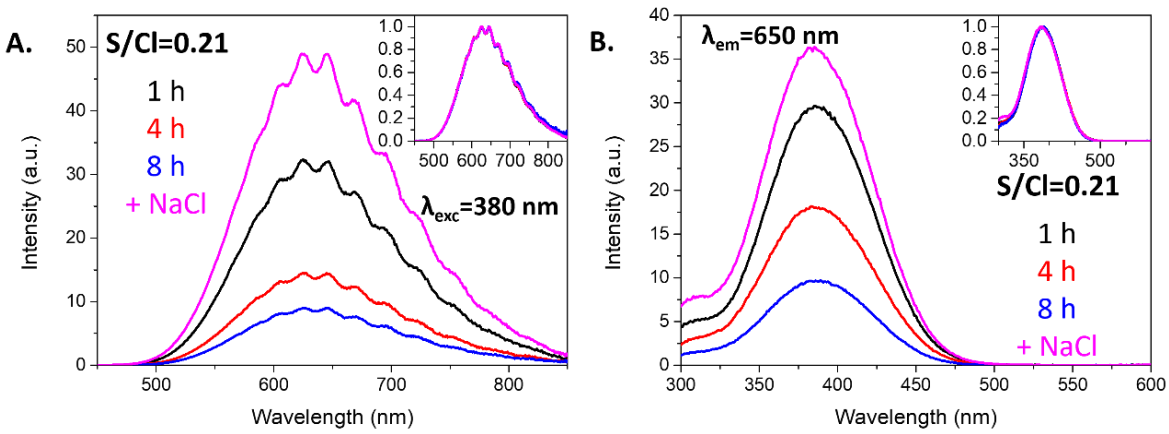


Figure 2.1.5 - Emission (**A**) and excitation (**B**) spectra of samples based on S/Cl=0.21, monitoring the $[S_2]^-$ species at λ_{exc}=380 nm and λ_{em}=650 nm. The insets show the corresponding spectra normalized.

When exciting these S/Cl=0.21 samples with the wavelength suggested by Ruivo et al.[20] for the absorption maximum of the NIR-emitting species (λ_{exc}=355 nm), a similar behavior, with a band centered at 625 nm, was observed in the resultant emission spectra, as depicted in **Figure 2.1.6.A**. However, the corresponding normalized spectra indicated a minimal contribution in the NIR region, especially in samples subjected to 900 °C for 8 hours (inset of **Figure 2.1.6.A**). The excitation spectra corresponding to the emission at 720 nm still showed a band centered around 380 nm, corresponding to $[S_2]^-$ species (**Figure 2.1.6.B**). Nonetheless, these bands are broader than the ones resulting from the excitation spectra corresponding to the emission at 650 nm (**Figure 2.1.5.B**), suggesting a minimal contribution of the NIR emission in these samples.

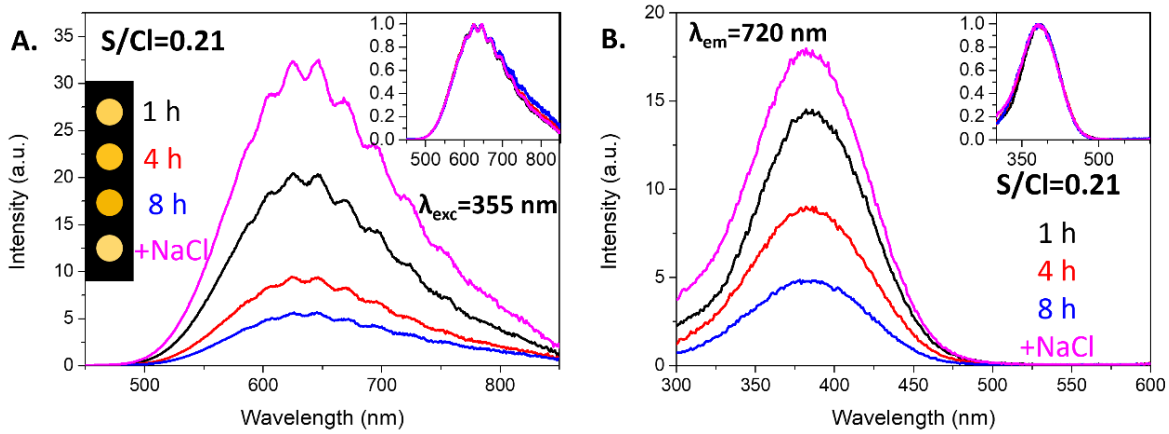


Figure 2.1.6 - Emission (**A**) and excitation (**B**) spectra of samples based on samples with S/Cl=0.21, monitoring the NIR-emitting species at λ_{exc}=355 nm and λ_{em}=720 nm. The insets show the corresponding spectra normalized and photos of the samples under UV light, λ_{exc}=365 nm.

Upon analyzing the S/Cl=4.5 samples, when exciting the $[S_2]^-$ species (λ_{exc}=380 nm), the yellow-orange emission characteristic of these clusters was only detected in the sample with a NaCl excess (**Figure 2.1.7.A**). This finding was further confirmed by the excitation spectra (λ_{em}=650 nm), revealing a band centered at 385 nm (**Figure 2.1.7.B**). In contrast, the remaining samples exhibited a NIR emission, peaking at 775 nm. The corresponding excitation spectra exhibited a band centered at 355 nm, consistent with the absorption bands found in these samples (**Figure 2.1.4.B**) and supported by existing literature[20]. This is the first report of the excitation spectrum of this NIR emission, suggesting that the absorbing species at 355 nm are responsible for this emission.

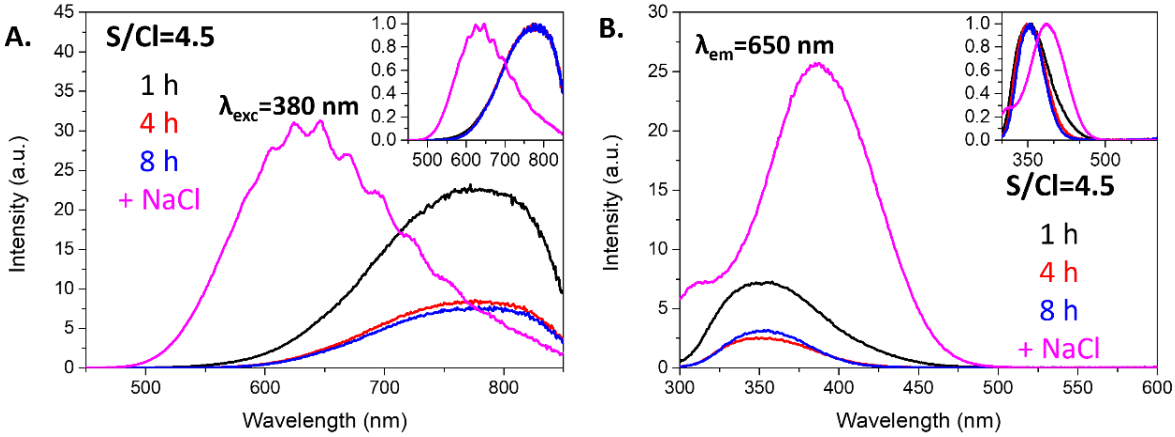


Figure 2.1.7 - Emission (**A**) and excitation (**B**) spectra of samples based on samples with S/Cl=4.5, monitoring the $[S_2]^-$ species at λ_{exc}=380 nm and λ_{em}=650 nm. The insets show the corresponding spectra normalized.

When exciting these S/Cl=4.5 samples using this wavelength (λ_{exc}=355 nm), the expected NIR emission spectra were observed in all samples except for the one with NaCl excess. Instead, this sample exhibited the emission spectra of $[S_2]^-$ with a contribution from the NIR emission (**Figure 2.1.8.A**). This behavior was also evident in the corresponding excitation spectra (λ_{em}=720 nm), with bands peaking at 355 nm and with the contribution of $[S_2]^-$ detected only in the sample with NaCl excess (**Figure 2.1.8.B**).

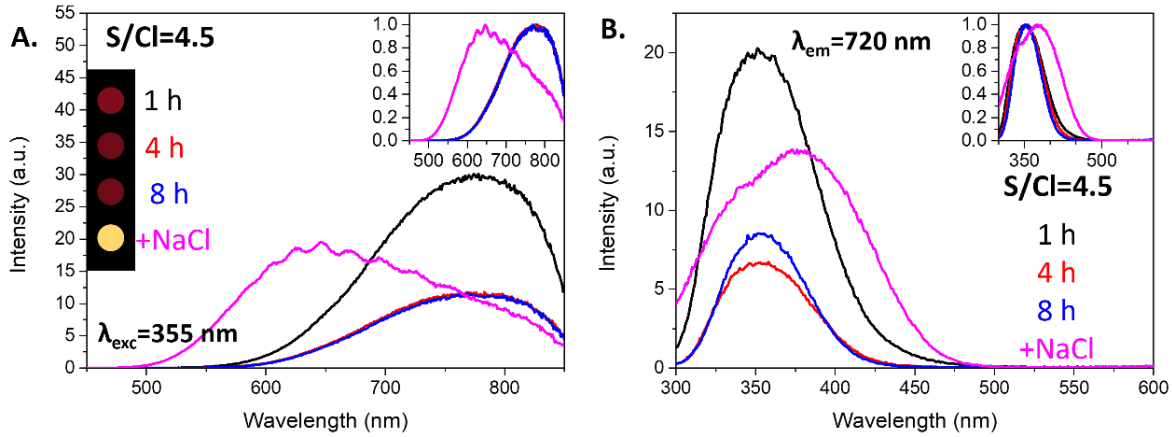


Figure 2.1.8 - Emission (**A**) and excitation (**B**) spectra of samples based on samples with S/Cl=4.5, monitoring the NIR-emitting species at λ_{exc}=355 nm and λ_{em}=720 nm. The insets show the corresponding spectra normalized and photos of the samples under UV light, λ_{exc}=365 nm.

The observed optical differences seem closely related to the structural findings outlined in section **2.2.1**, illustrating their interconnected relationship. For instance, chloride appears to stabilize the sodalite crystalline phase, promoting the formation of $[S_2]^-$ clusters. Consequently, this hinders the formation of the species responsible for the NIR emission.

This correlation is particularly evident when comparing the diffuse reflectance spectrum of sample S/Cl=4.5 (1h) with that of sample S/Cl=4.5 +NaCl (**Figure 2.1.4.B**). These samples exhibit significant differences in their structural composition, as evidenced above in **Table 2.1.1**, with sodalite zeolite relative percentages varying from 36% to 98%, respectively. Furthermore, their optical characterization reflects these variations accordingly. It appears that the absorption band intensity at 355 nm observed in sample S/Cl=4.5 (1h) halved in sample S/Cl=4.5 +NaCl. In this last-mentioned sample, $[S_2]^-$ absorption band with a similarly reduced intensity emerged. As a result, the emission spectra shifted from a single NIR-emitting sample to a dual-emitting sample in yellow-orange and NIR regions (**Figure 2.1.8.A-B**), respectively.

Moreover, it was demonstrated that the optimal intensity of NIR emission occurs at higher S/Cl ratios following a 1-hour synthesis, with this intensity decreasing thereafter. This

observation aligns with reduced sodalite zeolite formation and increased nepheline and carnegieite structures at such ratios.

2.1.3 Conclusions

This study revealed a relationship between the produced crystalline phases and the resulting optical properties. $[S_2]^-$ clusters are characterized by an absorption at 385 nm and emission at 625 nm ($^2\Pi_g \leftrightarrow {}^2\Pi_u$ transitions). It was observed that these species seem more present when the sodalite zeolite is obtained, as they were detected in samples with >70% of sodalite crystalline phase. Notably, chloride incorporation was found to play a crucial role in stabilizing this zeolite, with higher formation at lower S/Cl ratios (note that the stoichiometry used was S_xCl_{2-2x}). This effect was more pronounced when using a NaCl excess, resulting in a sodalite structure formation exceeding 94%.

On the other hand, a different species absorbing at 355 nm seems to be responsible for the NIR emission centered at around 775 nm. These species become more prevalent as the formation of nepheline and carnegieite crystalline phases increases, which may indicate an association with these structures. Reducing chloride content, for example, by using high S/Cl ratios and shorter synthesis durations, favors the formation of these desired NIR emitters.

2.2 Impact of Starting from Sodalite Zeolite Instead of Na-LTA Zeolite on Optical Properties

In this subchapter, a different synthesis methodology was adopted. Unlike the previous approach, where sulfur precursors were incorporated into commercial Na-LTA zeolite followed by high-temperature synthesis, the current method involves initially converting commercial Na-LTA into sodalite, with the sulfur precursors introduced subsequently. To the best of our knowledge, this is the first time such a procedure has been used to achieve photoluminescent sodalite.

Subchapter **2.1** provided important insights into the high-temperature transformation of sodalite into carnegieite and nepheline crystalline phases, which appear to be associated with the NIR-emitting species. Additionally, the investigation conducted in this subchapter will explore the impact of using another starting zeolite and two different sulfur precursors (sodium sulfite, the same species used earlier, and elemental sulfur) in the production of NIR-emitting zeolites. The interest in using elemental sulfur arises from its natural occurrence in volcanic regions, representing a readily available and significant sulfur source.

2.2.1 Synthesis and structural characterization

As demonstrated in the study conducted in subchapter **2.1**, the use of NaCl is fundamental to producing sodalite at high temperatures, otherwise, Na-LTA would be converted into nepheline and carnegieite. Thus, the first synthesis step consisted of converting commercial Na-LTA zeolite into sodalite at 900 °C for 1 hour without a reducing atmosphere, following equation (**2.2.1**).

$$3\ Na_2Al_2Si_2O_8 + 2\ NaCl \xrightarrow{\Delta} Na_8Al_6Si_6O_{24}Cl_2 \qquad (2.2.1)$$

Sodalite was initially synthesized and labeled as SOD-S_0, then divided into two batches. In one batch, Na_2SO_3 was introduced as a sulfur precursor, while elemental sulfur (S) was introduced in the other. Furthermore, each precursor was tested with two different sulfur concentrations, $S_{0.3}$ and $S_{0.9}$. These materials were mixed and submitted to a high-temperature synthesis at 900 °C for 1 hour under a reducing atmosphere of 5% H_2 / 95% Ar. Refer to section **7.1.1** for more information about the experimental procedure.

The PXRD diffractograms of the samples produced with Na_2SO_3 and elemental sulfur (S) are illustrated in **Figure 2.2.1** and **Figure 2.2.2**, respectively, alongside the calculated relative crystalline phases. In the initial synthesis involving the transformation of Na-LTA zeolite into sodalite according to the stoichiometric equation (**2.2.1**), approximately 86% of this crystalline phase was detected, with the remainder undergoing conversion into nepheline and carnegieite phases (SOD-S_0 sample). Upon doping this sample with sodium sulfite (Na_2SO_3), some changes were observed (**Figure 2.2.1.A**). At lower levels of sulfur doping ($S_{0.3}$), no differences in the crystalline phases were detected. However, with increased sulfur content ($S_{0.9}$), sodalite was partially transformed into carnegieite, increasing the latter phase from 8% to 23% (**Figure 2.2.1.B**). This effect agrees with the observations in the last subchapter, where sodalite was partially transformed into carnegieite when using higher sulfur loadings, as described in equation (**2.1.3**).

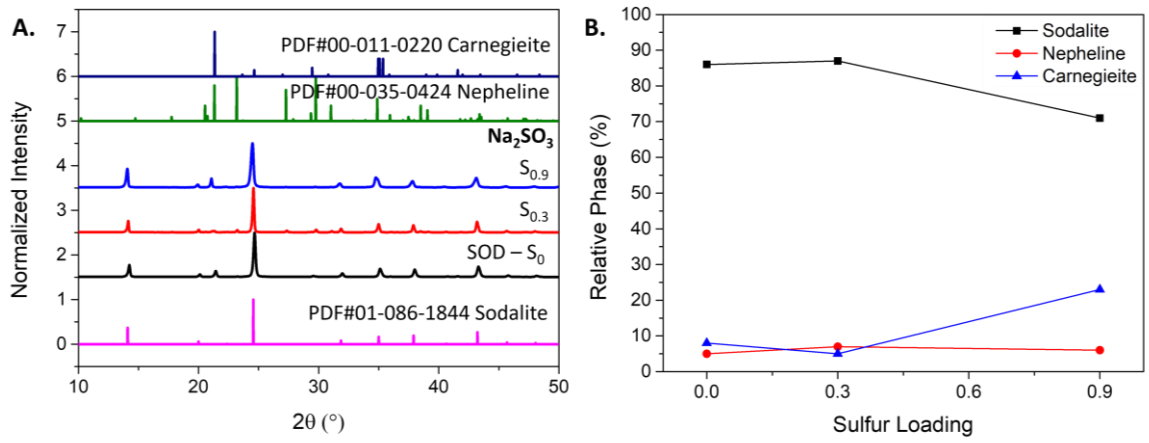


Figure 2.2.1 - (**A**) PXRD diffractograms of the synthesized samples using Na_2SO_3 as the sulfur precursor, along with the respective comparison with ICDD standard reference cards of sodalite, nepheline and carnegieite crystalline phases. (**B**) Corresponding calculated relative phases.

Notably, no changes were observed in the crystalline phases when elemental sulfur (S) was used as a sulfur precursor (**Figure 2.2.2.A**). These findings are supported by the calculated relative phases, as shown in **Figure 2.2.2.B**.

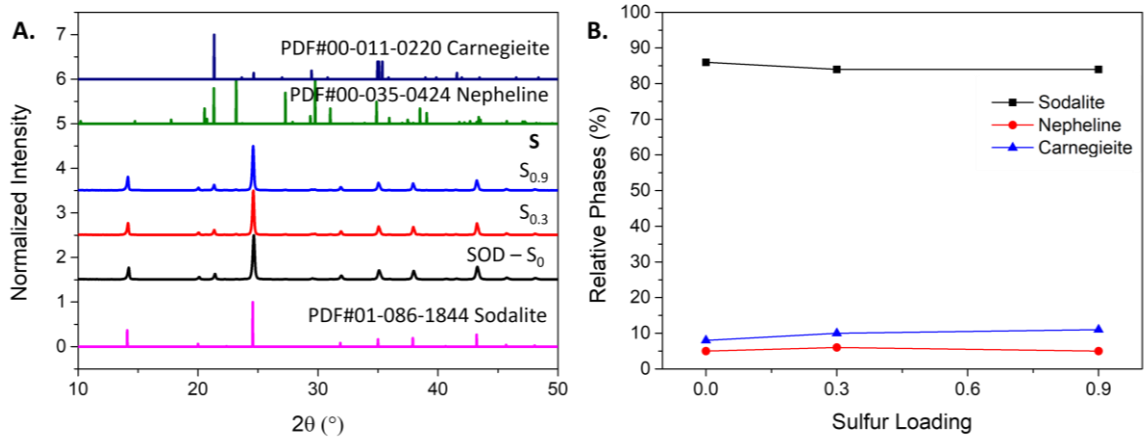


Figure 2.2.2 - (**A**) PXRD diffractograms of the synthesized samples using elemental sulfur (S) as the sulfur precursor, along with the respective comparison with ICDD standard reference cards of sodalite, nepheline and carnegieite crystalline phases. (**B**) Corresponding calculated relative phases.

Next, the impact of these structural differences on the optical properties was further analyzed.

2.2.2 Optical characterization

The diffuse reflectance spectra of these samples reveal significant differences. Samples doped with sodium sulfite exhibit the presence of chromophores, while those doped with elemental sulfur lack them (see **Figure 2.2.3**). The spectrum of sample $S_{0.3}$ Na_2SO_3 shows an absorption band with a maximum at 395 nm, assigned to $[S_2]^-$. In contrast, the spectrum of sample $S_{0.9}$ Na_2SO_3 displays an absorption band with a maximum at 355 nm, indicating the presence of the absorption band associated with the NIR-emitting species. These results are consistent with those obtained when starting with Na-LTA zeolite.

The absence of chromophores in samples using elemental sulfur as a sulfur precursor may be attributed to the fact that all sulfur species, including its main component, S_8, do not decompose in the required manner to be further reduced into the necessary sulfur emissive species. Additionally, the evaporation of sulfur could contribute to this phenomenon, given its boiling point of approximately 445 °C, significantly lower than the synthesis temperature at 900 °C.

The PXRD results and these absorption data suggest that successful sulfur incorporation into the zeolite matrix influences the resulting crystalline phases. Even after treatment at 900 °C for 1 hour, the PXRD diffractograms of samples using elemental sulfur remained unchanged

(**Figure 2.2.1.A-B**). In contrast, differences were detected in the crystalline phases of the samples using sodium sulfite (**Figure 2.2.2.A-B**).

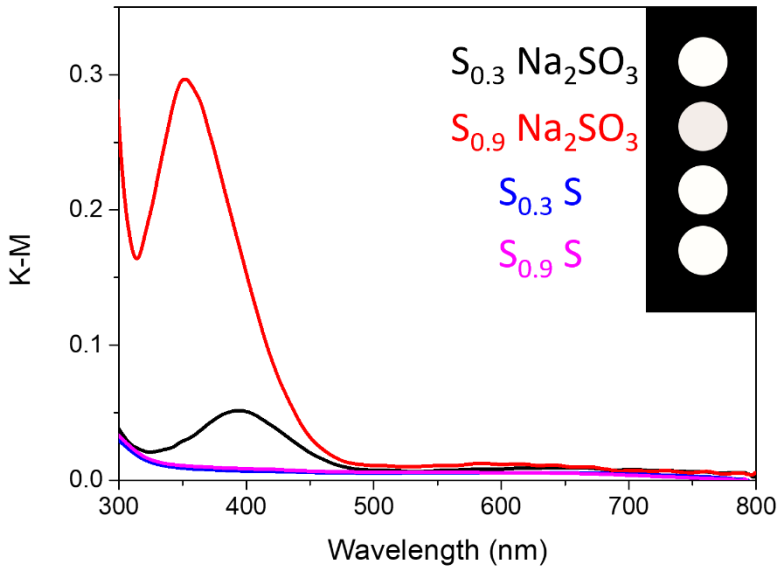


Figure 2.2.3 - Diffuse reflectance spectra of synthesized samples, using Na_2SO_3 and elemental sulfur as sulfur precursors. The insets show photos of the samples under ambient light.

The photoluminescent behavior of these samples was also evaluated by tracing their emission and excitation spectra. Starting with sample $S_{0.3}$ Na_2SO_3, the characteristic emission (**Figure 2.2.4.A**) and excitation (**Figure 2.2.4.B**) spectra of $[S_2]^-$ were detected, even when selecting the typical wavelengths of the NIR-emitting species (λ_{exc}=355 nm and λ_{em}=720 nm).

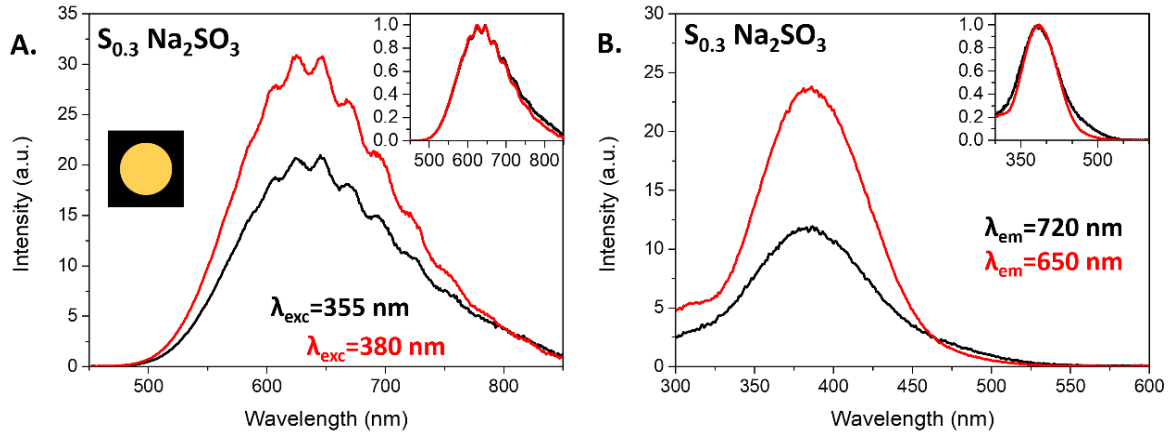


Figure 2.2.4 - Emission (**A**) and excitation (**B**) spectra of $S_{0.3}$ Na_2SO_3 sample, monitoring the behavior of $[S_2]^-$ (λ_{exc}=380 nm and λ_{em}=650 nm) and the NIR-emitting species (λ_{exc}=355 nm and λ_{em}=720 nm). The insets show the corresponding normalized spectra and a photo of the samples under UV light, λ_{exc}=365 nm.

In contrast, the NIR emission was detected in sample $S_{0.9}$ Na_2SO_3, although with $[S_2]^-$ still present (**Figure 2.2.5.A**), with its vibronic structure evident upon excitation at 355 nm. The corresponding excitation spectra (**Figure 2.2.5.B**) reflect this observation. The spectrum monitoring the $[S_2]^-$ emission (λ_{em}=650 nm) exhibits a band centered at 395 nm, with a minor contribution at 355 nm. Furthermore, the excitation spectrum corresponding to the NIR emission (λ_{em}=720 nm) reveals a broad band centered at 355 nm, with contributions from both $[S_2]^-$ and the NIR-emitting species, the latter being predominant.

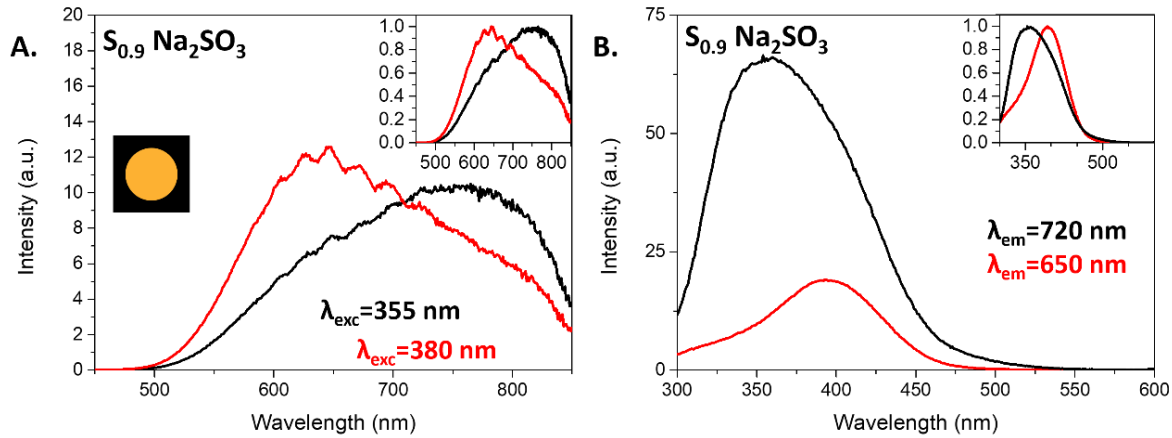


Figure 2.2.5 - Emission (**A**) and excitation (**B**) spectra of $S_{0.9}$ Na_2SO_3 sample, monitoring the behavior of $[S_2]^-$ (λ_{exc}=380 nm and λ_{em}=650 nm) and the NIR-emitting species (λ_{exc}=355 nm and λ_{em}=720 nm). The insets show the corresponding normalized spectra and a photo of the samples under UV light, λ_{exc}=365 nm.

These results corroborate the diffuse reflectance findings, where sample $S_{0.3}$ Na_2SO_3 displays a single $[S_2]^-$ absorption band, consequently detecting these species emission. On the other hand, the absorption spectrum of sample $S_{0.9}$ Na_2SO_3 exhibits a band at 355 nm, indicating the presence of the NIR-emitting species. However, the emission spectra reveal the presence of $[S_2]^-$. This discrepancy can be attributed to a minor amount of $[S_2]^-$ in sample $S_{0.9}$ Na_2SO_3, which is undetected in the diffuse reflectance spectra but becomes apparent in the emission spectra.

The photoluminescent properties of samples using elemental sulfur as the sulfur source were also studied despite the lack of chromophore formation revealed by diffuse reflectance spectroscopy. Indeed, both samples exhibit emissive properties, as illustrated in **Figure 2.2.6.A-B**, displaying the $[S_2]^-$ emission spectrum. The absence of absorption detection, combined with the low emission intensity, suggests that these species are present in minimal amounts. This may be attributed to sulfur impurities in commercial Na-LTA zeolite, as indicated in **Table A.1.2**, instead of resulting from incorporating sulfur from elemental sulfur.

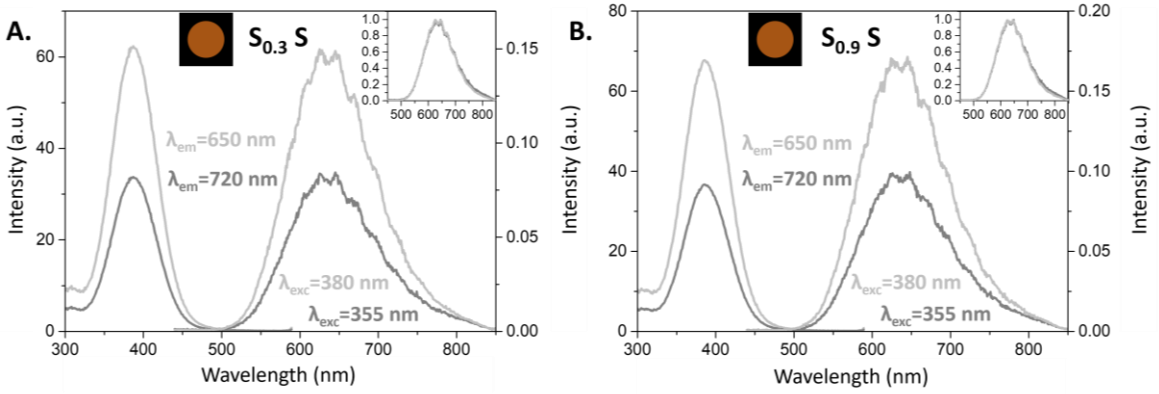


Figure 2.2.6 - Emission and excitation spectra of the samples prepared from elemental sulfur, using $S_{0.3}$ (**A**) and $S_{0.9}$ (**B**) concentrations. The behavior of $[S_2]^-$ was monitored using λ_{exc}=380 nm and λ_{em}=650 nm (light gray) and the NIR-emitting species using λ_{exc}=355 nm and λ_{em}=720 nm (dark gray). The insets show the corresponding normalized spectra photos of the samples under UV light, λ_{exc}=365 nm.

In summary, starting from sodalite zeolite and incorporating sodium sulfite results in either single yellow-orange emitting zeolites or dual-emitting zeolites in yellow-orange and NIR regions. This can be attributed to the high chloride content, which is necessary for synthesizing sodalite at high temperatures (according to equation (**2.2.1**). As discussed in subchapter **2.1**, the presence of high amounts of sodalite phase appears to promote the formation of $[S_2]^-$ species, consequently hindering the formation of the NIR-emitting species. However, the

NIR emission starts to be detected when sodalite decreases from 86% to 71%, while carnegieite increases from 8% to 23%. This may suggest a relationship between the NIR-emitting clusters and the carnegieite crystalline phase.

Additionally, elemental sulfur was found unsuitable as a sulfur precursor since the NIR photoluminescent properties were not achieved.

The following section compares the differences observed between samples produced from Na-LTA zeolite and those produced from sodalite zeolite.

2.2.3 Samples comparison starting from Na-LTA and from sodalite zeolites

In order to evaluate if the sulfur doping during high-temperature synthesis, starting with zeolite Na-LTA or sodalite, significantly influences the obtained photophysical properties, the results presented in these two subchapters were compared. For this purpose, two samples, starting from Na-LTA zeolite (subchapter **2.1**) and two from sodalite zeolite (current subchapter), were selected. Each sample underwent the same high-temperature procedure at 900 °C for 1 hour under a reductive atmosphere. Furthermore, they were doped using the same sulfur precursor, sodium sulfite (Na_2SO_3).

In the samples starting from commercial Na-LTA zeolite, sodium sulfite and sodium chloride were added following equation (**2.2.2**). These samples were studied and discussed in subchapter **2.1**, previously mentioned as S/Cl=0.21 1h and S/Cl=4.5 1h, and further denominated as $S_{0.3}$ (S/Cl=0.21) and $S_{0.9}$ (S/Cl=4.5).

$$3Na_2Al_2Si_2O_8 + xNa_2SO_3 + (2-x)NaCl \rightarrow 900\,°C, 1h; with\ x = 0.3\ and\ 0.9$$
$$\boldsymbol{S_{0.3}(S/Cl = 0.21)\ and\ S_{0.9}(S/Cl = 4.5)\ samples, from\ subchapter}\ 2.1 \quad (2.2.2)$$

Additionally, samples starting from sodalite zeolite, following equation (**2.2.3**), were selected from this subchapter. These samples were denominated as $S_{0.3}$ Na_2SO_3 and $S_{0.9}$ Na_2SO_3, further described as $S_{0.3}$ and $S_{0.9}$, respectively.

$$Na_8Al_6Si_6O_{24}Cl_2 + xNa_2SO_3 \rightarrow 900\,°C, 1h; with\ x = 0.3\ and\ 0.9$$
$$\boldsymbol{S_{0.3}\ and\ S_{0.9}\ samples, from\ this\ subchapter} \quad (2.2.3)$$

The XRD results of the four samples are summarized in **Table 2.2.1**, revealing identical behavior in samples with low sulfur content. However, differences emerge at higher sulfur

concentrations. Sample starting from Na-LTA zeolite led to a lower formation of sodalite crystalline phase (~36%) compared to the 71% found starting from sodalite zeolite. This difference seems to be due to the chloride content within the sodalite starting zeolite, which continues to stabilize this zeolite even after a second high-temperature synthesis.

Table 2.2.1 - Crystalline phases calculated from PXRD diffractograms of samples starting from Na-LTA zeolite and from sodalite zeolite.

Starting zeolite	Samples	Crystalline Phases (%)		
		Sodalite	Nepheline	Carnegieite
Na-LTA	$S_{0.3}$ (S/Cl=0.21)	89	9	2
	$S_{0.9}$ (S/Cl=4.5)	36	22	42
Sodalite	$S_{0.3}$	87	7	5
	$S_{0.9}$	71	6	23

Furthermore, **Figure 2.2.7.A** depicts the diffuse reflectance spectra of these samples, with $S_{0.3}$ (S/Cl=0.21) and $S_{0.3}$ samples presenting an absorption band centered at 390 nm, assigned to $[S_2]^-$. In contrast, $S_{0.9}$ (S/Cl=4.5) and $S_{0.9}$ samples display an absorption band at 355 nm related to the NIR-emitting species.

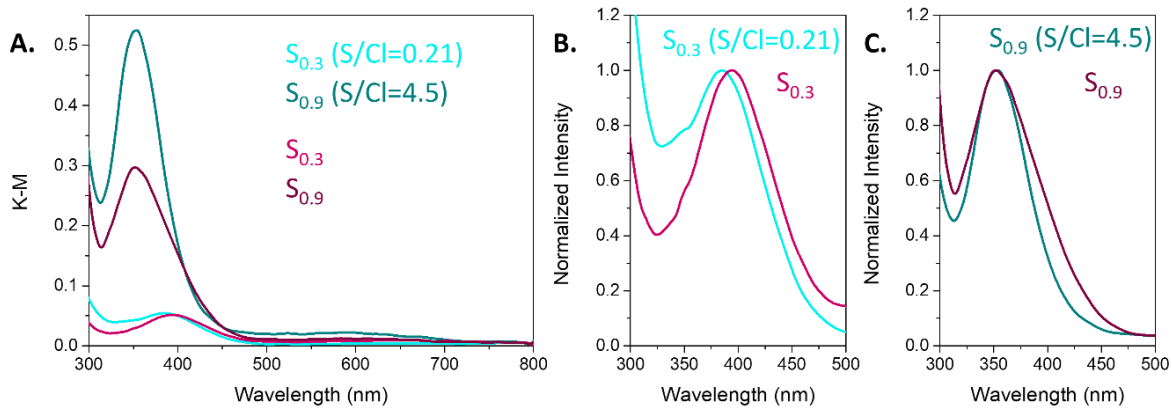


Figure 2.2.7 - (**A**) Diffuse reflectance spectra of the four samples, varying the sulfur amount and the starting zeolite. Normalized spectra of the main absorption band of samples $S_{0.3}$ (**B**) and $S_{0.9}$ (**C**).

Upon closer examination of the $[S_2]^-$ bands (**Figure 2.2.7.B**), a slight shift in the absorption maximum is observed, from 385 nm in sample $S_{0.3}$ (S/Cl=0.21) to 395 nm in sample $S_{0.3}$. Since these samples have the same crystalline phases, this can not explain the observed shift in the absorption spectra. This shift may be due to a higher amount of NIR-emitting species formation

in sample $S_{0.3}$ (S/Cl=0.21), evidenced by a higher intensity at 355 nm. Notably, both absorption bands exhibit similar intensities, indicating an equivalent amount of chromophore formation in both samples despite using different synthesis methods. Furthermore, the normalized NIR-emitting species bands (**Figure 2.2.7.C**) have the same maxima at 355 nm. However, sample $S_{0.9}$ exhibits a broader band, most likely due to the presence of $[S_2]^-$. Comparing the non-normalized spectra (**Figure 2.2.7.A**), sample $S_{0.9}$ shows approximately 2.5 times less intensity, supporting the idea of the formation of other chromophores, such as $[S_2]^-$.

The emission spectra of the assembled samples are illustrated in **Figure 2.2.8**. Sample $S_{0.3}$ (S/Cl=0.21) and sample $S_{0.3}$ display the $[S_2]^-$ emission spectrum (**Figure 2.2.8.A**), consistent with the PXRD and diffuse reflectance results. Finally, samples $S_{0.9}$ (S/Cl=4.5) and $S_{0.9}$ exhibit visible differences (**Figure 2.2.8.B**). Sample $S_{0.9}$ (S/Cl=4.5) displays a single NIR emission, while sample $S_{0.9}$ shows a predominant NIR emission but with an apparent contamination of $[S_2]^-$. Again, this may be attributed to the higher sodalite phase content in sample $S_{0.9}$, reaching up to 71%, compared to the 36% present in sample $S_{0.9}$ (S/Cl=4.5).

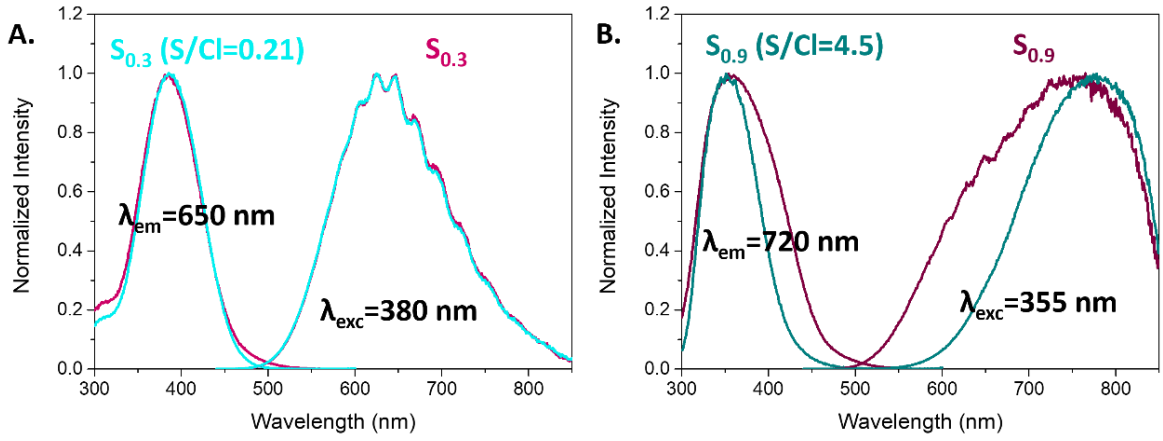


Figure 2.2.8 - Emission spectra of $S_{0.3}$ (**A**) and $S_{0.9}$ (**B**) samples, monitoring the behavior of $[S_2]^-$ species at λ_{exc}=380 nm and λ_{em}=650 nm and NIR-emitting species at λ_{exc}=355 nm and λ_{em}=720 nm.

In summary, using Na-LTA zeolite as the starting material yields optimal results, achieving the desired single NIR emission.

2.2.4 Conclusions

This study demonstrated that sulfur could be directly incorporated into sodalite zeolite, thereby exhibiting photophysical properties, without the necessity of using Na-LTA zeolite as a starting material. Additionally, the selection of the sulfur precursor was revealed to be important, as

the naturally available form of sulfur (elemental sulfur) did not display these optical properties. The exact reasons behind this phenomenon remain unclear. It could be due to potential reagent loss by evaporation and/or the high-temperature decomposition of the several sulfur forms present in this reagent, which may not lead to chromophore formation when in the presence of a reducing atmosphere. In contrast, using sodium sulfite as a sulfur precursor resulted in the same chromophore formation as those observed when starting with Na-LTA zeolite, as discussed in subchapter **2.1**.

The high-temperature transformation of Na-LTA zeolite into sodalite inherently required the use of chloride, which enhanced the stabilization of $[S_2]^-$ clusters, resulting in a yellow-orange emission. These findings further supported the observations discussed in subchapter **2.1**, emphasizing the correlation between the sodalite crystalline phase and the presence of $[S_2]^-$ species. Consequently, despite increasing sulfur loading, a single NIR emission was not observed. The sample in which this single emission was detected exhibited a higher amount of nepheline and carnegieite crystalline phases and a lower amount of sodalite. This highlights once again that the NIR emission appears to be associated not with the sodalite phase but with the nepheline and carnegieite crystalline phases.

A direct comparison between the two synthesis methods demonstrates that starting with Na-LTA zeolite produces the optimal optical properties, forming single NIR-emitting zeolites.

2.3 Unraveling NIR Emission and Applicability of Sulfur-Doped Zeolites

The information gathered in subchapters **2.1** and **2.2** served as the basis for improving the synthesis conditions to produce NIR-emitting zeolites. A 1-hour synthesis duration, starting from Na-LTA zeolite, while using high S/Cl ratios, yielded the optimal results. However, the exact nature of this emission is not yet fully understood.

To address this issue, a detailed and comprehensive investigation was conducted in this study. This involved covering a wide range of S/Cl ratios under optimal synthesis conditions, i.e., 1 hour of synthesis. Such an approach aims to understand better how sulfur influences the resulting optical properties. Once the optimal S/Cl ratio for achieving NIR-emitting zeolites is identified, this emission will be extensively studied using several techniques, including theoretical calculation.

2.3.1 Synthesis and structural characterization

Luminescent sulfur-doped aluminosilicate zeolites were synthesized by mixing Na-LTA zeolite, NaCl, and Na_2SO_3, followed by a heat treatment at 900 °C for one hour under a reducing atmosphere, following the stoichiometry $Na_8Si_6Al_6O_{24}S_xCl_{2-2x}$. Samples were produced with nominal molar ratios of S/Cl=0, 0.06, 0.13, 0.21, 0.33, 0.50, 0.75, 1.17, 2.0 and 4.5. See the experimental procedure in section **7.1.1**.

These samples were analyzed using powder X-ray diffraction, and the crystalline phase of the starting material Na-LTA zeolite was not detected. Instead, three different crystalline phases were identified: sodalite, nepheline and carnegieite (see **Figure 2.3.1.A**). These crystalline phases were already identified in subchapters **2.1** and **2.2** after high-temperature synthesis starting from Na-LTA zeolite. **Figure 2.3.1.B** and **Table A.1.1** summarize the calculated relative fractions of these three crystalline phases. As the S/Cl ratio increases, the sodalite phase decreases, while both nepheline and carnegieite phases become more prominent. This phenomenon can be explained by the decreasing amount of NaCl during the synthesis, considering the used stoichiometry, S_xCl_{2-2x}, which favors the formation of nepheline and carnegieite. This aligns with our previous observations regarding the importance of chloride in the stabilization of the sodalite crystalline phase.

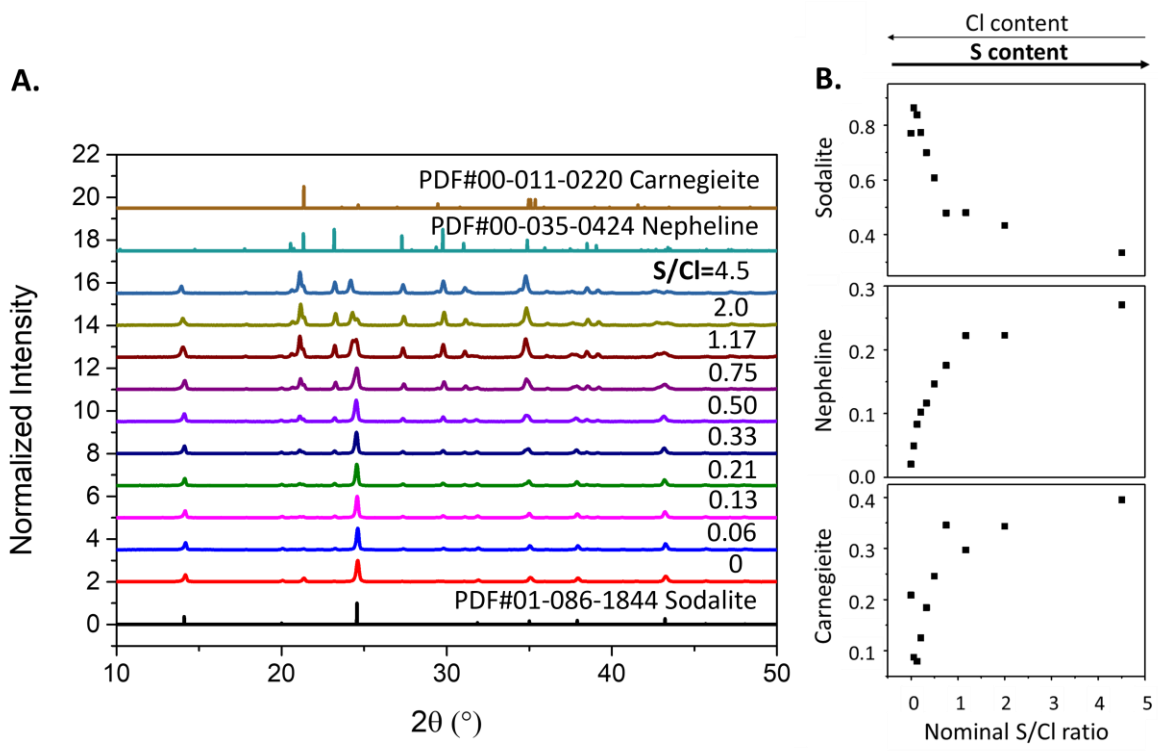


Figure 2.3.1 - **Structural analysis of sulfur-doped zeolites samples –** (**A**) PXRD diffractograms of the synthesized sulfur-doped zeolites samples with different S/Cl ratios and the ICDD standard reference card of 01-086-1844 sodalite ($Na_8Si_6Al_6O_{24}Cl_2$), 00-035-0424 nepheline ($NaSiAlO_4$) and 00-011-0220 carnegieite ($NaSiAlO_4$). (**B**) Sodalite, nepheline and carnegieite fractions calculated in the synthesized zeolite samples.

The changes observed in the diffractograms when varying the S/Cl ratios do not significantly impact the morphology of the samples, as shown by scanning electron microscopy (SEM). The SEM images (**Figure 2.3.2.A-F**) reveal highly heterogeneous agglomerates with sizes up to 6 µm, regardless of the S/Cl ratio used. These agglomerates consist of varying-sized particles forming larger clusters. High-temperature synthesis probably contributes to the fusion of these particles into cohesive structures. (For more information about this technique, see section **7.2.14**.)

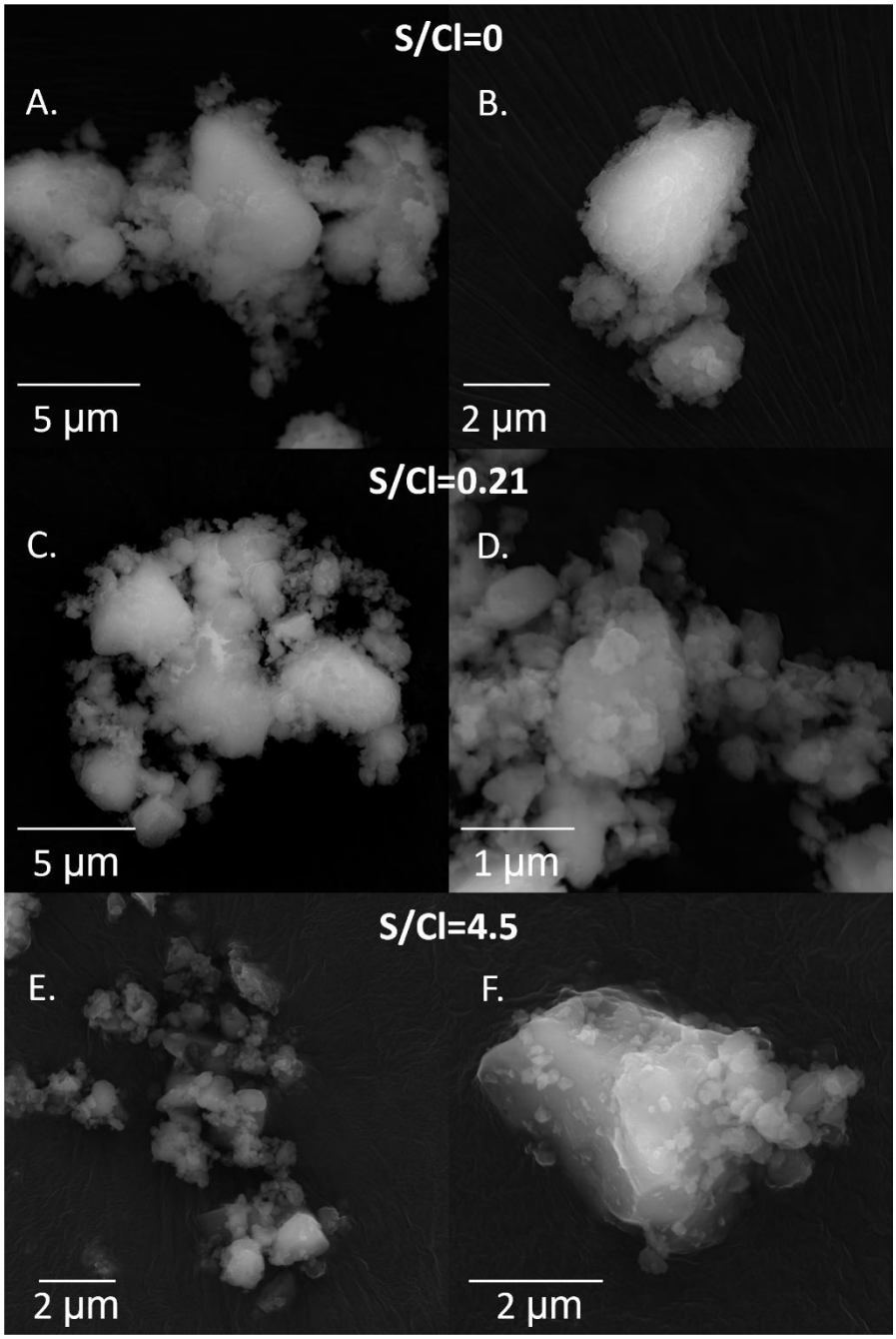


Figure 2.3.2 - SEM images of the samples with S/Cl=0 (**A, B**), 0.21 (**C, D**) and 4.5 (**E, F**).

Furthermore, transmission electron microscopy (TEM) confirms this heterogeneity, revealing dispersible agglomerates that contain distinguishable single particles. They display notably irregular and angular shapes (**Figure 2.3.3.A-D**). (See section **7.2.15** for more information about this technique.)

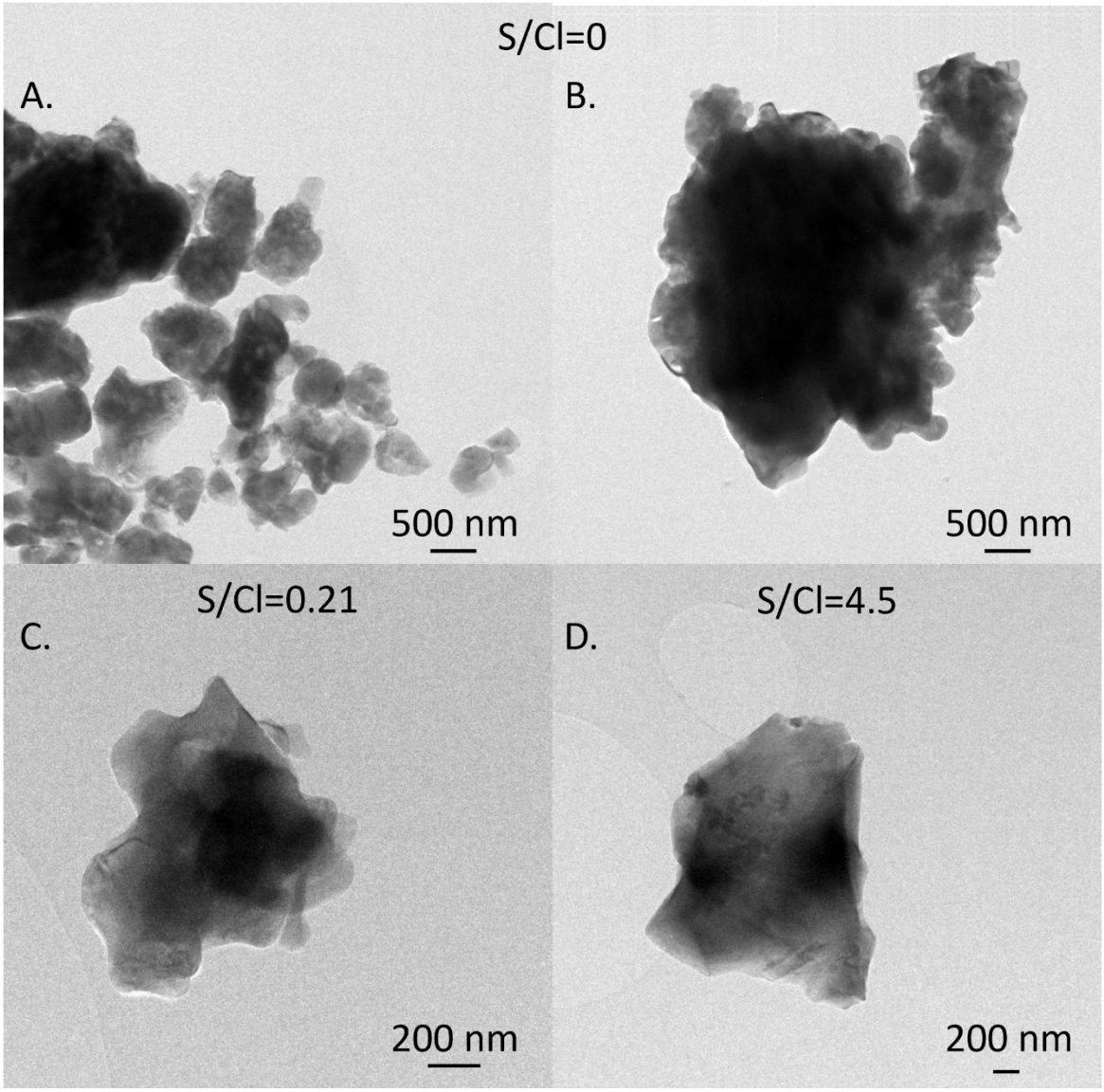


Figure 2.3.3 - TEM images of samples with S/Cl=0 (**A**, **B**), 0.21 (**C**) and 4.5 (**D**).

The elemental analysis of the synthesized materials was determined using the particle-induced X-ray emission (PIXE) technique (**Table A.1.2**). **Table 2.3.1** summarizes the concentration of the most relevant elements found in molar percentage for the samples with S/Cl=0, 0.21, and 4.5 and compares it with the theoretical values. (Refer to section **7.2.10** for additional information about this technique.)

Table 2.3.1 - Molar percentage of each main element found in zeolite samples using the PIXE technique.

Nominal S/Cl	Molar percentage composition (%)[a]						Obtained S/Cl
	Na	Si	Al	O	S	Cl	
0	15.69	13.37	13.01	54.33	0.00	3.26	0
0.21	15.75	13.39	13.01	54.77	0.12	2.62	0.05
4.5	15.55	13.66	13.15	56.54	0.50	0.27	1.82

[a]Calculated from the PIXE weight percentage (wt%) (**Table A.1.2**).

These results indicate that the sulfur-doping process was effective, as evidenced by the increasing percentage of sulfur as the starting sulfur precursor (Na_2SO_3) increased its concentration. Similarly, the chloride content decreased since less NaCl was added to the starting mixture. Furthermore, the Si/Al ratio remained largely unaffected by the high-temperature procedure and doping process, remaining *ca.* 1 in all samples[71].

2.3.2 Optical and NIR emission characterization

As shown in the last two studies, there seems to be a close relationship between the structural zeolite composition and the resulting optical properties. Therefore, this section includes a series of characterizations conducted on these samples. Starting with diffuse reflectance spectroscopy, **Figure 2.3.4** depicts the obtained spectra of the prepared zeolite samples following transformation using the Kubelka-Munk theory[103]. At low concentrations (S/Cl<0.33), a predominant band at 390 nm is observed, aligning with the $^2\Pi_g \rightarrow {}^2\Pi_u$ transition of the $[S_2]^-$ clusters[104]. As the sulfur content increases, the 390 nm band disappears and is replaced by two new absorption bands at approximately 355 nm and 600 nm. The latter is attributed to $[S_3]^-$ clusters in sodalite, known for their absorption around 600 nm[104], commonly recognized as the ultramarine blue pigment. The presence of both $[S_2]^-$ and $[S_3]^-$ species was confirmed by Raman and electron paramagnetic resonance (EPR) spectroscopies (**Figure 2.3.8** and **Figure 2.3.9**, respectively)[106–109], as discussed below. However, the identity of the species causing absorption at 355 nm remained unknown.

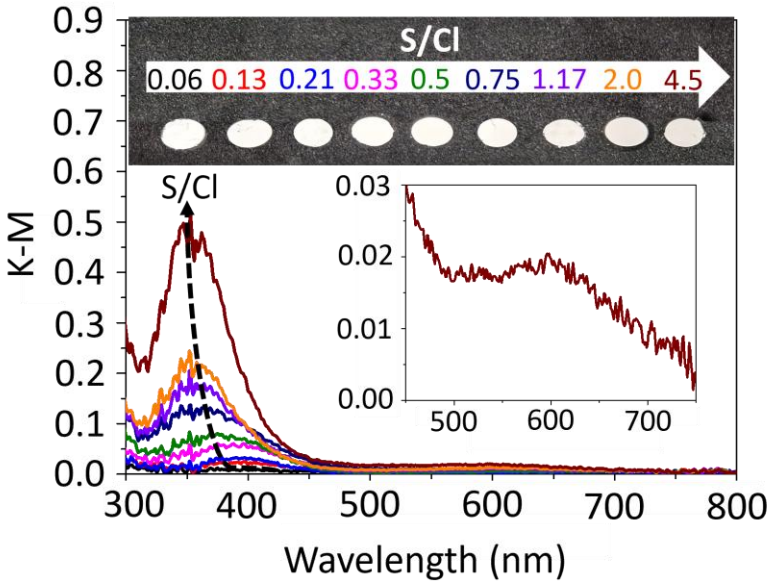


Figure 2.3.4 - Diffuse reflectance spectrum of samples with different S/Cl ratios. The inset on top depicts photos of the samples under ambient light. The inset on the right shows a close-up of the S/Cl=4.5 sample in the 450-750 nm region.

Next, the photoluminescence of these samples was evaluated upon UV-light excitation, with the resulting emission spectra depicted in **Figure 2.3.5.A**. In samples with low sulfur content (S/Cl<0.33), the characteristic band with a vibronic resolution of $[S_2]^-$, centered at around 625 nm, was detected, increasing in intensity with sulfur concentration[85,105].

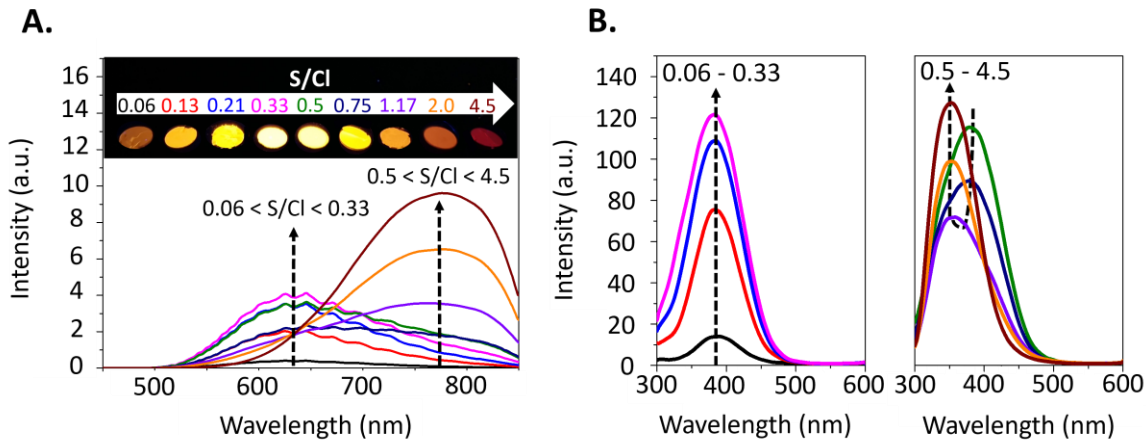


Figure 2.3.5 - (**A**) Steady-state emission spectra of samples with different sulfur content (λ_{exc}=355 nm). The inset on top depicts photos of the samples under UV light, with λ_{exc}=365 nm. (**B**) Excitation spectra of synthesized samples 0.06<S/Cl<0.33 **(left)** and 0.5<S/Cl<4.5 **(right)**, using λ_{em}=725 nm.

At higher sulfur content (S/Cl>0.5), a new emission band emerged centered at 775 nm, lacking vibronic resolution, and became dominant at S/Cl=4.5. Additionally, the excitation spectra of these samples revealed that these two emissions arise from different species (**Figure 2.3.5.B**). The band at 625 nm corresponds to the species absorbing at 390 nm, $[S_2]^-$, while the NIR-emitting species is responsible for the absorption at 355 nm. It is worth noting that the excitation spectrum of sample S/Cl=4.5 exclusively displayed the band at 355 nm, which overlapped with the diffuse reflectance spectrum of this sample (**Figure 2.3.6**).

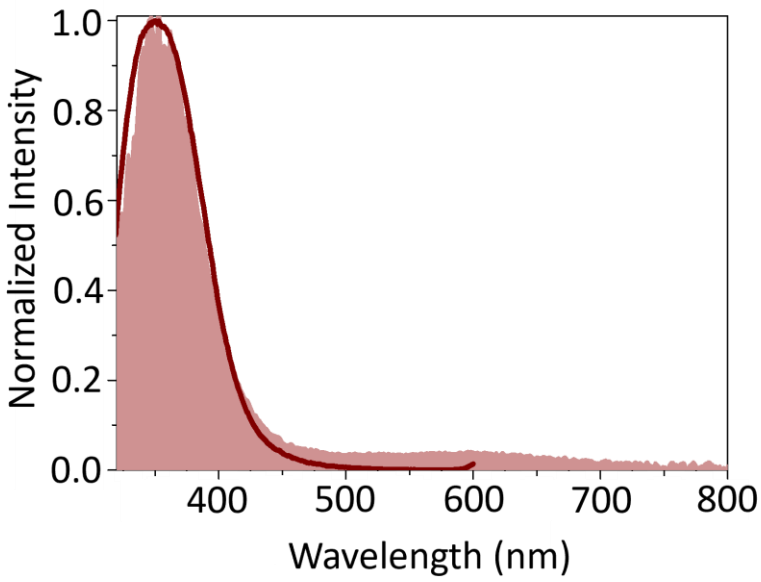


Figure 2.3.6 - Overlap of the diffuse reflectance spectrum (light-brown) with the excitation spectrum (dark-brown) of sample S/Cl=4.5.

These findings corroborate previously discussed observations, relating $[S_2]^-$ clusters to the absorption band at 390 nm and the respective emission centered at 625 nm. Moreover, the absorption band at 355 nm is associated with the NIR emission, peaking at 775 nm. Furthermore, these results suggest that sulfur is responsible for the observed differences in diffuse reflectance and emission spectra, contradicting the previous assignment of Fe^{3+} impurities[58]. Notably, the PIXE results revealed identical iron concentrations in sulfur-doped samples (**Table A.1.2**), which do not explain the variation in the optical properties.

The same NIR emission was observed in the Na-LTA zeolite sample subjected to the same experimental procedure conditions (temperature and reductive atmosphere) as the sulfur-doped samples (**Figure 2.3.7.A**). This emission can be assigned to the presence of small traces of sulfur in the Na-LTA zeolite (**Table A.1.2**). Furthermore, analysis of PXRD data revealed that

this sample exclusively consists of nepheline and carnegieite crystalline phases, with no trace of sodalite (**Figure 2.3.7.B**). The lack of NaCl during the synthesis can explain the absence of the sodalite crystalline phase. This further reinforces previous observations in subchapters **2.1** and **2.2**, suggesting that the NIR emission originates not from sulfur species within sodalite but rather from sulfur present in the nepheline and/or carnegieite phases.

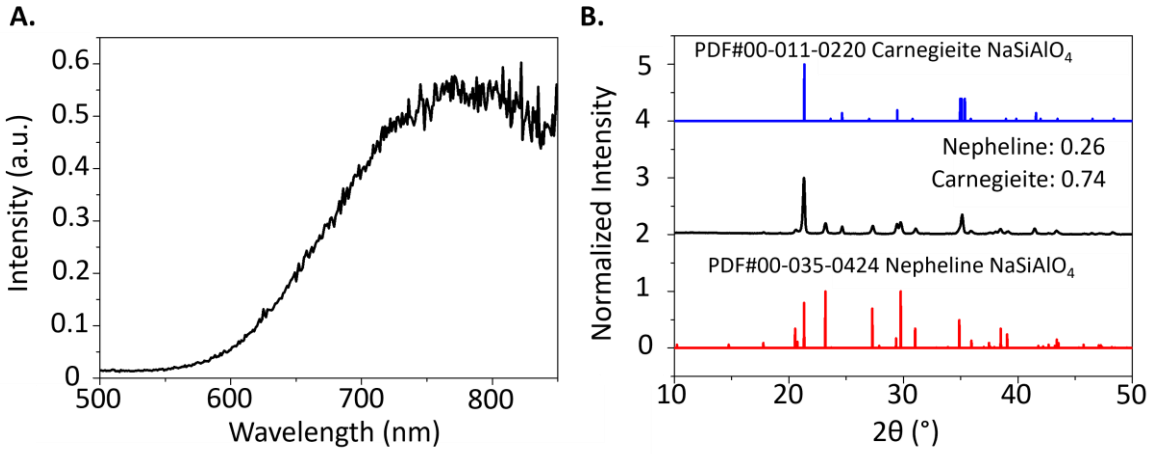


Figure 2.3.7 - Characterization of zeolite Na-LTA sample after 1 hour at 900 °C, under reductive atmosphere – (**A**) Emission spectra (λ_{exc}=355 nm). (**B**) PXRD diffractogram and relative crystalline phases and comparison with the ICDD standard reference card of 00-035-0424 nepheline ($NaSiAlO_4$) and 00-011-0220 carnegieite ($NaSiAlO_4$).

Further characterization was conducted using Raman spectroscopy for samples S/Cl=0, 0.21 and 4.5 to identify the vibrational modes and to determine if the band peaking at 600 nm, observed in the diffuse reflectance spectrum of sample S/Cl=4.5 (**Figure 2.3.4**), is indeed due to $[S_3]^-$ species. Therefore, a commercial ultramarine blue pigment (UBP) was used as a reference for these $[S_3]^-$ clusters. The Raman band at 550 cm^{-1} is ascribed to the vibrational modes v_1 of $[S_3]^-$ clusters[106,109] (**Figure 2.3.8**). Remarkably, $[S_2]^-$ vibrational modes were not detected in sample S/Cl=0.21, despite their presence being previously confirmed by absorption and emission spectroscopies. According to Ledé et al.[109], these clusters should be detected at around 590 cm^{-1}. Their detection further demonstrated an energy dependency, with maximal sensitivity using a 457.9 nm laser, becoming undetected with lower-energy lasers[109]. This may explain the lack of detection of $[S_2]^-$, since the 632.8 nm laser is not sufficient to induce the resonance of these clusters. Besides, vibrations between 400 to 500 cm^{-1} are attributed to the framework of sodalite, nepheline and carnegieite[110–112]. The vibration around 460 cm^{-1} can be assigned to the sodalite crystalline phase, as its relative intensity decreases from sample S/Cl=0 to sample S/Cl=4.5, consistent with behavior confirmed by X-ray diffraction. On the other hand,

vibrations between 400 and 450 cm^{-1} show an increase in relative intensity, which is in agreement with the behavior observed in the nepheline and carnegieite phases. However, assigning specific vibrations to each phase was not possible due to their similar relative phase contributions and vibrational modes[72]. (See section **7.2.8** for further information about this technique.)

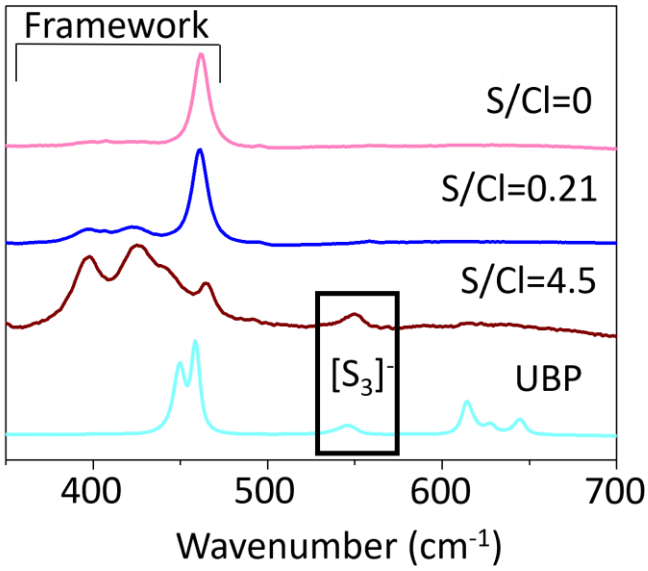


Figure 2.3.8 - Raman spectra of samples S/Cl=0, 0.21 and 4.5 and commercial ultramarine blue pigment (UBP), used as a reference for $[S_3]^-$ cluster.

In the same way, these four mentioned samples were also studied by electron paramagnetic resonance (EPR), with the corresponding spectra recorded at 120 K depicted in **Figure 2.3.9**. These spectra underwent deconvolution to identify the present species (**Figure A.1.1**), and the obtained results are summarized in **Table 2.3.2**. Sample S/Cl=0.21 shows two rhombic signals corresponding to two different species, $[S_2]^-$ and $[SO_2]^-$, with identical contributions. They were simulated with g-values of 2.002, 2.012 and 2.032, and 2.002, 2.008 and 2.019, respectively. (Section **7.2.7** contains supplementary information about this technique.)

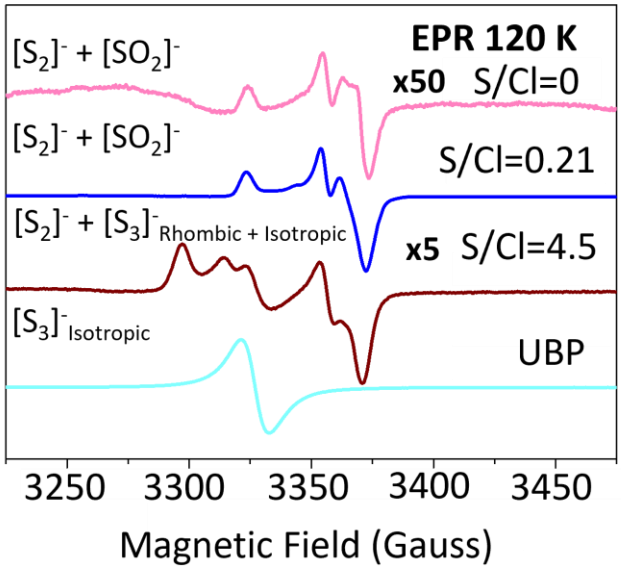


Figure 2.3.9 - Electron paramagnetic resonance (EPR) spectra of samples S/Cl=0, 0.21 and 4.5 and commercial ultramarine blue pigment (UBP), used as a reference for $[S_3]^-$ cluster. Note the multiplication factors applied in S/Cl=0 and 4.5 samples. For EPR spectra deconvolution, see **Figure A.1.1**.

Absorption and emission spectroscopies supported the assignment of $[S_2]^-$, which undoubtedly confirmed its presence in sample S/Cl=0.21. It should be noted that the parameters found in the literature for this radical anion are very divergent[106,108,113]. On the other hand, the g-values obtained for $[SO_2]^-$ are compatible with those previously described by Schneider and co-workers in KCl crystals doped with sulfur[114]. The presence of these species in this sample is presumably associated with the synthesis process, where $[SO_3]^{2-}$ was not fully reduced to $[S_2]^-$. This last-mentioned species is also present in the samples S/Cl=0 and 4.5, with essentially the same g-values. The blank sample presents the same two species, $[S_2]^-$ and $[SO_2]^-$, identified in the sample S/Cl=0.21 but with slight differences in their individual contribution to the spectrum, 50/50%.

Table 2.3.2 - g-values, relative percentages and species assignment present in the samples S/Cl=0, 0.21 and 4.5 and commercial ultramarine blue pigment (UBP).

Sample S/Cl	Species assignment	g_1	g_2	g_3	Relative contribution (%)
0	$[S_2]^-$	2.000	2.013	2.031	50
	$[SO_2]^-$	2.000	2.005	2.012	50
0.21	$[S_2]^-$	2.002	2.012	2.032	40
	$[SO_2]^-$	2.002	2.008	2.019	60
4.5	$[S_2]^-$	2.002	2.012	2.031	40
	$[S_3]^-$ rhombic	2.003	2.034	2.048	35
	$[S_3]^-$ isotropic	2.029	2.029	2.029	25
UBP	$[S_3]^-$ isotropic	2.029	2.029	2.029	100

In contrast, in sample S/Cl=4.5, alongside the contribution of $[S_2]^-$ species at 40%, two additional species account for 35% and 25%, respectively. The first one was simulated with g-values of 2.003, 2.034 and 2.048, consistent with the presence of an $[S_3]^-$ species, similar to previous literature descriptions[106,107]. This data also agrees with the results obtained by absorption and Raman spectroscopies (**Figure 2.3.4** and **Figure 2.3.8**). Contrary to the previously described species, the second species exhibits an isotropic signal with g = 2.029, corresponding to $[S_3]^-$. This is similar to the one described by Chukanov and coworkers[108], where $[S_3]^-$ is in a homogeneous environment in the sodalite cages. These species were also observed in the spectrum obtained for the commercial ultramarine blue pigment (UBP), used as a reference for $[S_3]^-$, which contains this radical species. Therefore, both species can be attributed to the presence of $[S_3]^-$ radical but in different local environments.

In summary, EPR spectroscopy reveals that the increase in sulfur concentration leads to a *ca.* 5-fold reduction in the intensity of the EPR signals (see multiplication factors in **Figure 2.3.9**), indicating a lower concentration of paramagnetic species in sample S/Cl=4.5 compared to sample S/Cl=0.21. This corroborates the absorption and emission data collected from sample S/Cl=4.5, which suggests the presence of both $[S_2]^-$ and $[S_3]^-$ (paramagnetic) in low concentrations. Moreover, it indicates that a non-paramagnetic species is responsible for the absorption band at approximately 355 nm and the NIR emission.

The upcoming characterizations will focus on better understanding this unknown NIR emission. Initially, the lifetimes were measured in all samples using photoluminescence decay times, monitoring at the emission maxima (λ_{em}=800 nm). The measured decays were fitted with the following bi-exponential equation (**2.3.1**).

$$y = A_1 \times e^{\frac{-x}{\tau_1}} + A_2 \times e^{\frac{-x}{\tau_2}} + y_0 \quad (2.3.1)$$

Figure 2.3.10 depicts the obtained photoluminescent decay time of sample S/Cl=4.5. (Refer to section **7.2.4** for more information about this technique.)

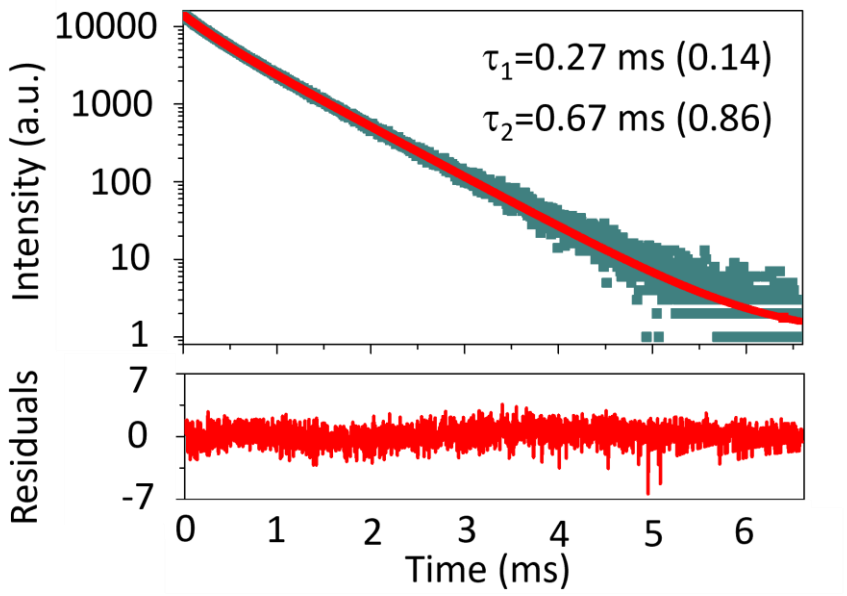


Figure 2.3.10 - (**Above)** Photoluminescence decay of sample with S/Cl=4.5 (dotted line) and respective bi-exponential fitting (solid line) at 800 nm (λ_{exc} = 402.9 nm) and (**Below**) corresponding residuals. Note the decay components and respective relative amplitudes in brackets.

Notably, the same decay time was obtained for all samples at room temperature, revealing an average decay time of 0.54 ± 0.027 milliseconds (**Table 2.3.3**).

Table 2.3.3 - Decay times (t), relative amplitudes (A), and average decay times of all synthesized samples.

Sample S/Cl	t_1(ms)	t_2 (ms)	A_1	A_2	$t_{Average}$ (ms)[a]	Q^2
0.06	0.27	0.67	0.14	0.86	0.56	1.14
0.13	0.27	0.67	0.13	0.87	0.56	1.03
0.21	0.27	0.67	0.10	0.90	0.58	1.13
0.33	0.27	0.67	0.14	0.86	0.56	1.11
0.50	0.27	0.67	0.18	0.82	0.52	0.97
0.75	0.27	0.67	0.23	0.77	0.50	1.13
1.17	0.28	0.67	0.24	0.76	0.50	1.15
2.0	0.28	0.67	0.21	0.79	0.52	1.06
4.5	0.27	0.67	0.14	0.86	0.55	1.14

[a]The pre-exponential factors were used for the calculations.

Further characterization demonstrated that the intensity of this long-lived emission constantly increased with the S/Cl ratios, as illustrated in the emission spectra in **Figure 2.3.11**. This suggests that this NIR emission arises from a spin-forbidden transition of a sulfur species.

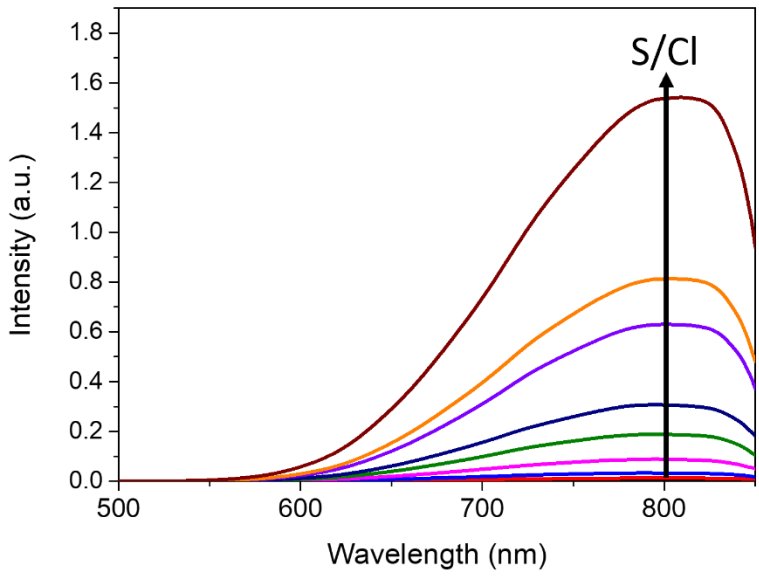


Figure 2.3.11 - Emission spectra after applying a delay time of 0.1 ms to samples with different S/Cl ratios, with λ_{exc}=380 nm.

The same bi-exponential decay was found in the sample with just nepheline and carnegieite crystalline phases (**Figure 2.3.12**), confirming previous assumptions that this NIR emission is not associated with sodalite zeolite.

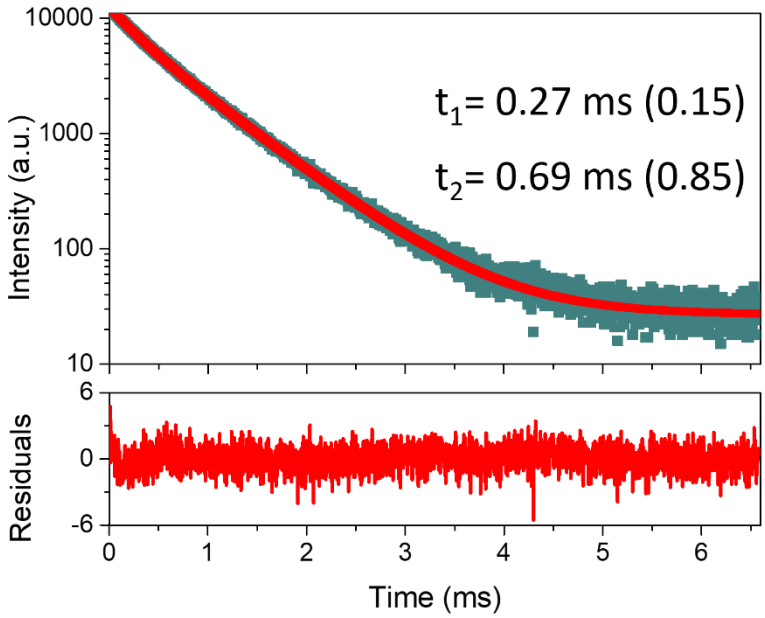


Figure 2.3.12 - **(Above)** Photoluminescence decay (dotted line) and respective bi-exponential fitting (solid line) at 800 nm (λ_{exc} = 402.9 nm) of zeolite Na-LTA sample after 1h at 900 °C, under reductive atmosphere. **(Below)** Corresponding residuals.

The time evolution of the emission characteristics of sample S/Cl=4.5 was studied in more detail by acquiring the spectra at different time delays (**Figure 2.3.13**) after excitation. (Section **7.2.5** contains additional information about the time-resolved emission spectroscopy - TRES - technique.) At shorter times, $[S_2]^-$ characteristic emission was registered (**Figure 2.3.13.A**), while the NIR emission dominates at longer times (**Figure 2.3.13.B**) (centered at around 780 nm). Note that the steady-state emission spectrum of this sample exhibits the same NIR emission (**Figure 2.3.5.A**), suggesting that a fraction of $[S_2]^-$ is present at these higher sulfur concentrations. This further aligns with the EPR analysis, where the presence of this cluster was found (**Figure 2.3.9**). The relationship established between the sodalite crystalline phase and the $[S_2]^-$ cluster formation, as demonstrated in subchapters **2.1** and **2.2**, supports this finding. Given that this sample contains approximately 33% of this phase (**Figure 2.3.1.B**), it can explain the presence of these clusters, even that in small amounts.

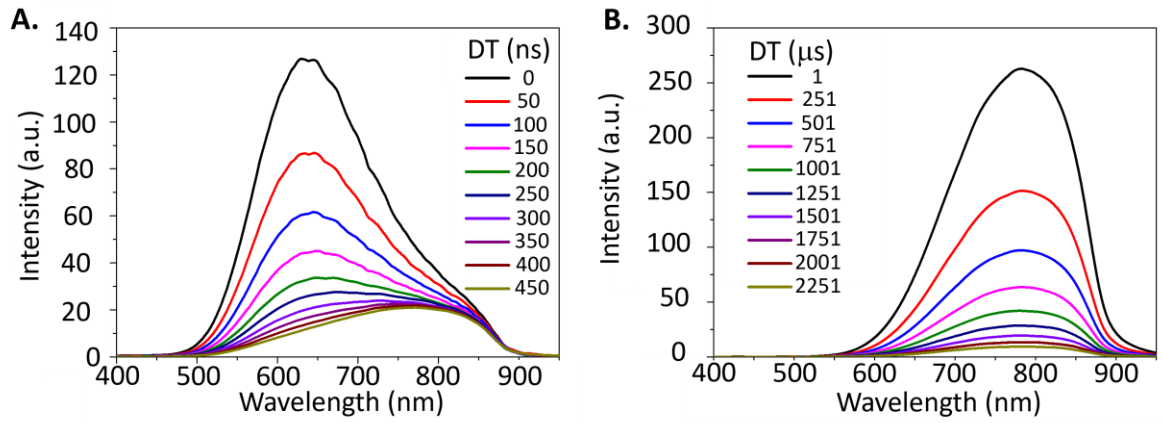


Figure 2.3.13 - (**A** and **B**) Time-resolved emission spectroscopy of sample S/Cl=4.5 at different delay times, DT, (λ_{exc}=337 nm)

In terms of external quantum efficiency (EQE) measurements, these NIR emissive species exhibited a value of 17%, surpassing the more common photoluminescence quantum yields (PLQYs) of around 10%, typically observed in the region of ~750 to 1000 nm[115].

Given that these species present a high Stokes-shift of *ca.* 1.90 eV and a long-lived emission, this can indicate the presence of triplet states. To explore this possibility, the transient diffuse reflectance spectroscopy technique was used. (Refer to section **7.2.6** for further information about this technique.) The obtained transient absorption spectra revealed long-lived species centered at approximately 580 nm (**Figure 2.3.14**). This observation is consistent with a triplet-triplet absorption band, providing additional support for the hypothesis that the long-lived emission arises from the presence of a long-lived triplet state.

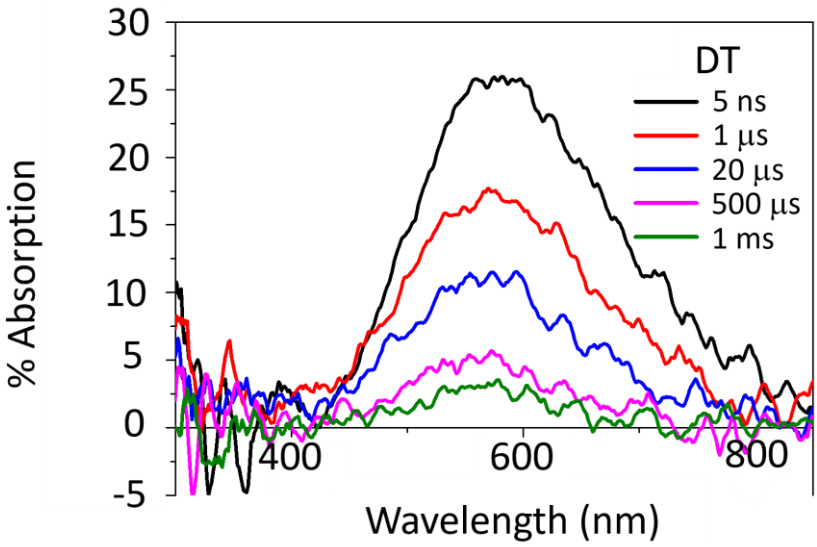


Figure 2.3.14 - Transient absorption spectra at different delay times (λ_{exc}=266 nm) of sample S/Cl=4.5.

The next section will study the behavior of the yellow-orange and the NIR emissions at different temperatures.

2.3.2.1 Temperature studies

The emission of samples S/Cl=0.21 and 4.5 was first evaluated under two different temperatures: room temperature (RT) at around 298 K and liquid nitrogen temperature at 77 K. **Figure 2.3.15** illustrates the emission and excitation spectra of sample S/Cl=0.21 under these two temperatures. The spectrum produced at low temperatures exemplifies the Franck-Condon principle[116] (see section **7.2.3** for supplementary information about this principle), exhibiting a high-resolution vibrational spectrum compared to the room temperature one, with a vibrational peak separation of 550 cm^{-1}. These values are compatible with the ones previously described for $[S_2]^-$ species, with values of 560 cm^{-1} (*ca.* 20-25 nm)[85].

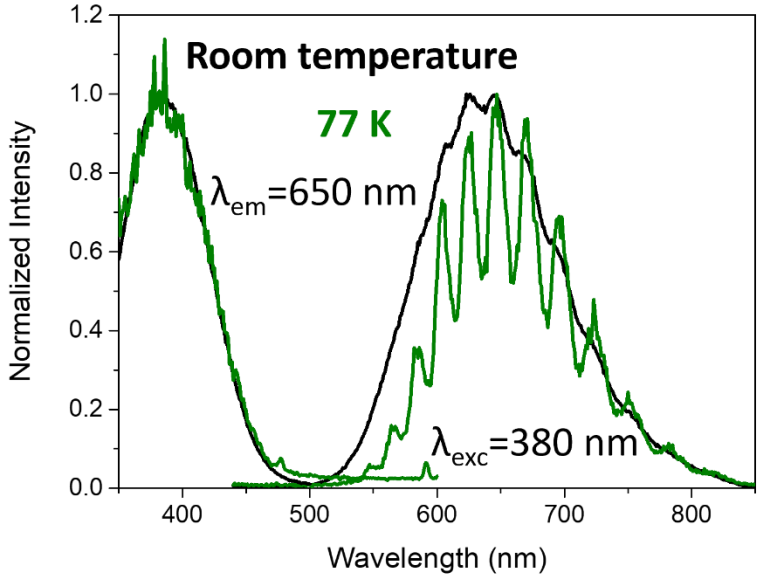


Figure 2.3.15 - Emission and corresponding excitation spectra of sample S/Cl=0.21 at 77 K (green) and at room temperature (black).

A different behavior was observed when analyzing sample S/Cl=4.5, revealing an emission spectrum broadening with temperature. The maximum shifts from around 810 nm to 785 nm, as depicted in **Figure 2.3.16**. To better understand these spectral differences, the decay times were recorded at these two temperatures, monitoring the emission at two different wavelengths, 600 nm and 800 nm. These wavelengths were chosen based on the behavior of the steady-state spectra at these wavelengths (see the red and brown arrows in **Figure 2.3.16**). The choice of 600 nm was motivated by the fact that at 77 K, its emission is practically nonexistent, in contrast to room temperature and 800 nm was selected as it represents almost the maximum in both temperatures.

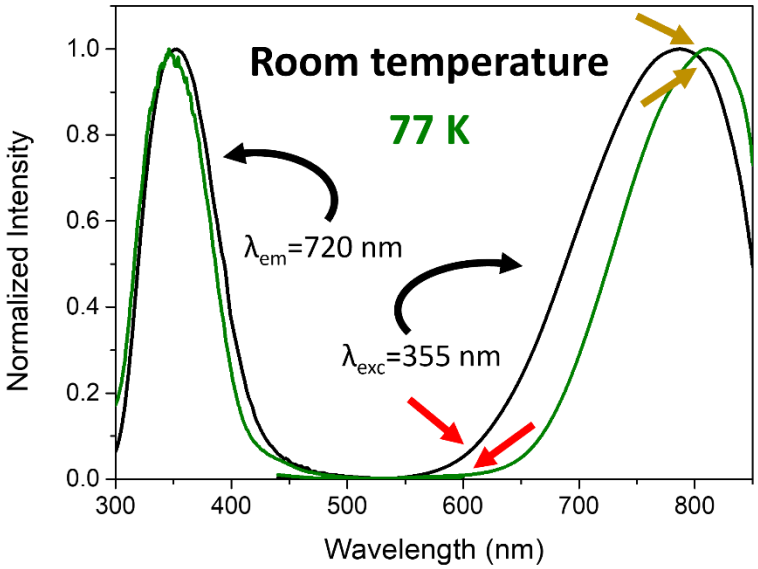


Figure 2.3.16 - Normalized steady-state emission and excitation spectra of sample S/Cl=4.5 acquired at liquid nitrogen temperature (77 K) and at room temperature (RT). The red and brown arrows indicate the two wavelengths at which the photoluminescence decays were recorded, as presented in **Figure 2.3.17** and **Figure 2.3.18**.

While monitoring the emission decay at 800 nm (near the emission maximum at each temperature), it is evident that when increasing the temperature, both decay components and decay time become faster (**Figure 2.3.17**), with the decay assuming a more bi-exponential behavior. This corresponds to the expected behavior since increasing the temperature typically enhances non-radiative pathways, for example, by increasing the molecule vibrations. Consequently, the excited state persists for shorter times before returning to the ground state, resulting in faster lifetimes.

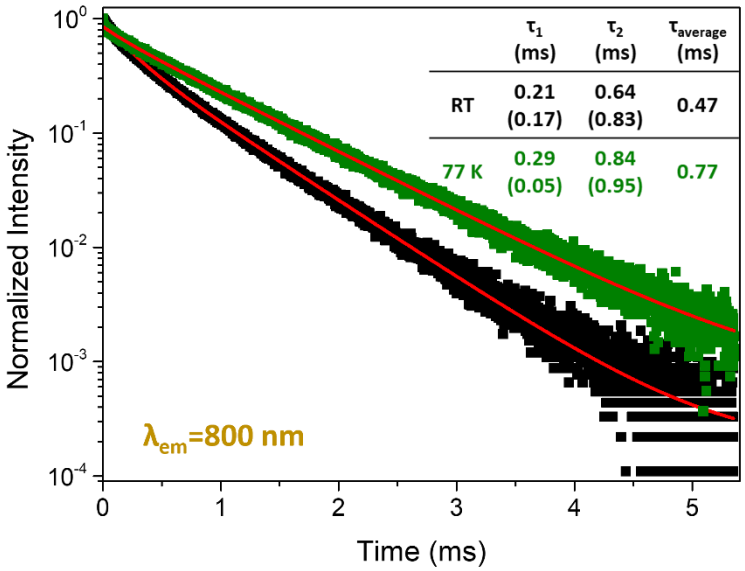


Figure 2.3.17 - Photoluminescence decay times of sample S/Cl=4.5 at liquid nitrogen temperature (77 K) and at room temperature (RT) monitoring the emission at 800 nm. The insets show the components resulting from the decay fittings (see the resulting residuals in **Figure A.1.2**) and the average decay time. In brackets is the relative amplitude of each component. Note that the average decay times were calculated using the pre-exponential factors.

At this point, there is no evidence suggesting the involvement of more than one emissive species in this NIR emission. This is supported by the absorption and excitation spectra, which reveal a single band centered at 355 nm. Therefore, the observed bi-exponential behavior seems to be related with different surrounding environments of these clusters within the aluminosilicate matrix. These differences may cause different relaxation times to the ground-state, thereby exhibiting different decay components.

EPR spectroscopy findings gave some insights into the presence of different local environments in this particular sample. At 120 K, two distinct signals were observed for the same non-emissive $[S_3]^-$ chromophores: one isotropic and the other rhombic (see **Table 2.3.2** and deconvoluted spectra in **Figure A.1.1**). Kowalak et al.[113] attributed the isotropic signal to rotating $[S_3]^-$, while the rhombic one was assigned to non-rotating species. Additionally, Hassan et al.[100] demonstrated that temperature-dependence may also occur within the aluminosilicate framework itself, affecting rotation angles and bond elongation, as observed in the case of sodalite.

Therefore, the more pronounced mono-exponential decay behavior observed at 77 K (**Figure 2.3.17**), as explained in equation (**2.3.2**), may be assigned to more homogeneous local

environments of these NIR-emitting species. The presence of slower decay components aligns with the decrease of non-radiative pathways at this low temperature.

$$A \rightleftarrows B, \downarrow T \tag{2.3.2}$$

with A being the fast decay component, B the slow decay component and T the temperature.

This may also affect the observed steady-state emission spectrum, which broadens with temperature (**Figure 2.3.16**), due to a different population distribution of the energy levels of these species.

Additionally, following the emission at 600 nm (**Figure 2.3.18**) at 77 K, faster decay components and decay time were observed compared to those observed at 800 nm. However, with increasing temperature, similar values to those at 800 nm were found, resulting in an average decay time approximately 10 times slower than at 77 K.

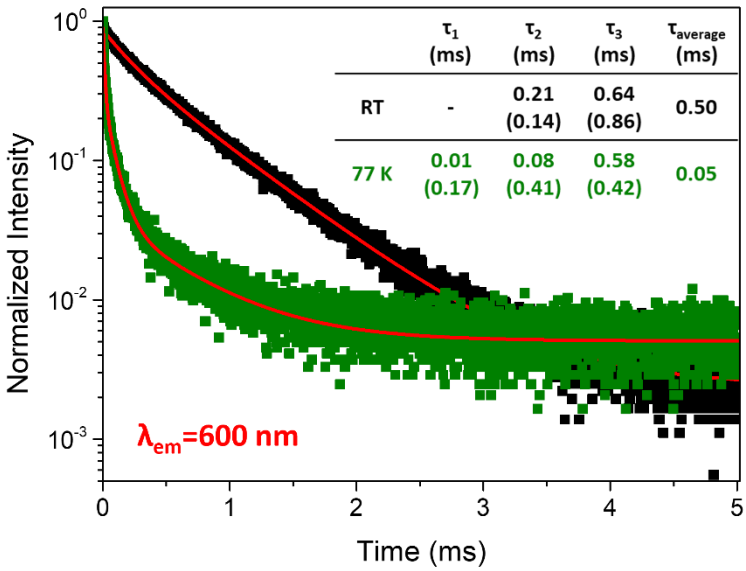


Figure 2.3.18 - Photoluminescence decay times of sample S/Cl=4.5 at liquid nitrogen temperature (77 K) and at room temperature (RT) monitoring the emission at 600 nm. The insets show the components resulting from the decay fittings (see the resulting residuals in **Figure A.1.2**) and the average decay time. In brackets is the relative amplitude of each component. Note that the average decay times were calculated using the pre-exponential factors.

It should be noted that the normalized emission spectra at low temperatures exhibit reduced intensity at this wavelength (**Figure 2.3.16**), which may explain these differences since this NIR emission seems not to be detected. Furthermore, once slower decay components were found

at room temperature, it was not possible to determine if such fast decay components were also present at this temperature.

Having established that there is an emission temperature-dependance, further temperatures were studied using a temperature ramp varying from 77 K to 348 K (75°C). In this experiment, a phosphorometer was used, yielding the time-resolved emission spectra depicted in **Figure 2.3.19**. Consistent with previous findings, the emission spectra exhibited a broadening and blue-shift as the temperature increased.

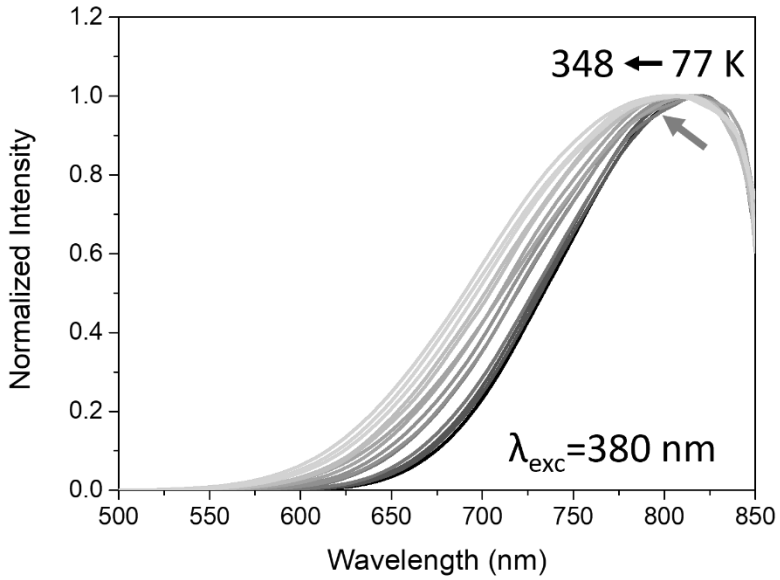


Figure 2.3.19 - Time-resolved emission spectra using a 0.2 millisecond delay time of S/Cl=4.5 sample, varying the temperature from 77 K to 348 K.

The photoluminescence decay times were also obtained by monitoring the emission at 800 nm, with an initial delay of 0.1 milliseconds. **Figure 2.3.20** illustrates the most relevant results, indicating faster lifetimes at higher temperatures.

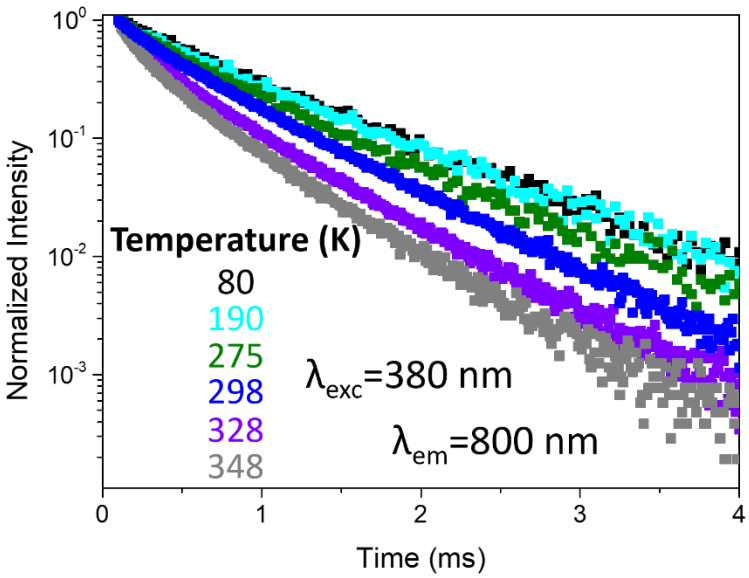


Figure 2.3.20 - Photoluminescence decay time of selected temperatures monitoring the emission at 800 nm of S/Cl=4.5 sample, using a 0.1 millisecond delay, varying the temperature from 77 K to 348 K.

These photoluminescence decays were fitted using two exponential functions, with the relative amplitudes, decay components and average decay times, presented in **Figure 2.3.21.A** and **Figure 2.3.21.B**, respectively. Once again, the decay components become faster with increasing temperature, resulting in faster average decay times. The relative amplitudes of the fast decay component also increase with temperature. These results support the previously proposed mechanism, suggesting that a specific matrix environment becomes predominant at lower temperatures.

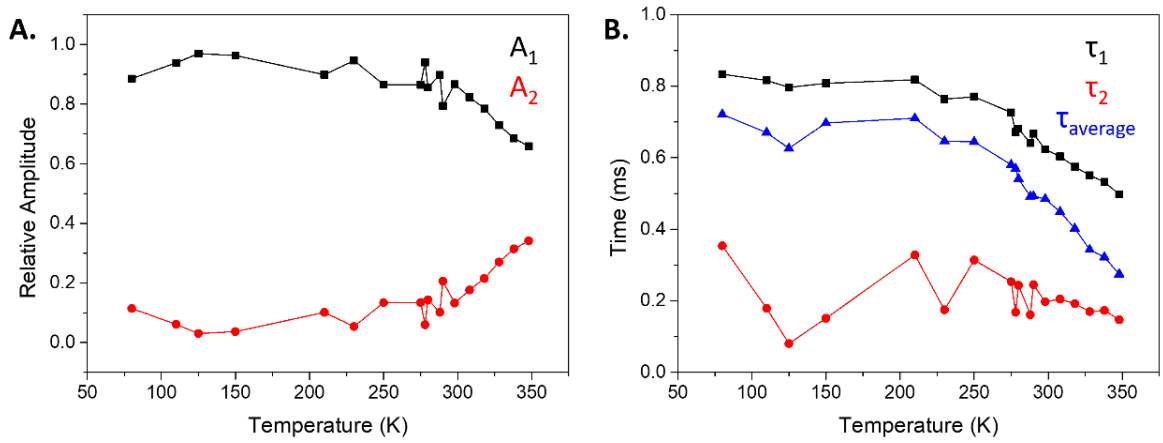


Figure 2.3.21 - Relative amplitudes (**A**), decay time components and average decay times (**B**) of the fitted photoluminescence decay time present in **Figure 2.3.20**.

It seems that a phosphorescence mechanism is responsible for this NIR emission. Another emission mechanism that can arise from triplet states is thermally activated delayed fluorescence (TADF). However, a sigmoidal behavior should be observed when plotting the temperature against the decay times. Considering the used temperature range, the decay times vary almost linearly with temperature. Therefore, a TADF mechanism was discarded. (See section **7.2.3** for more information about this mechanism.)

The humidity/water and oxygen sensitivity were also tested, and no significant changes were observed (see sections **7.5** and **7.6**). This further confirms that this is not a TADF mechanism and that these species are well confined within the aluminosilicates, not being susceptible to environmental changes such as humidity.

2.3.3 Computational studies

The experimental results were combined with theoretical calculations in an attempt to identify the species responsible for the NIR emission. In accordance with prior findings, which have identified absorptions around 350 nm, the origin of this specific emission is attributed to polysulfide ($[S_x]^{2-}$) species, such as $[S_2]^{2-}$, $[S_3]^{2-}$, $[S_4]^{2-}$ or $[S_5]^{2-}$[117–119]. Thus, several absorption spectra were calculated and simulated using time-dependent density functional theory TD-DFT (**Table A.1.3**) for $[S_3]^{-}$ (C_{2v}), $[S_3]^{2-}$ (C_{2v}), $[S_4]^{2-}$ (C_2), $[S_4]^{2-}$ (C_{2h}) and $[S_4]^{2-}$ (C_{3v}), selected due to the small sulfur molecules already reported in these type of aluminosilicate materials. The optimal results were obtained with $[S_3]^{2-}$ (with a minor contribution of $[S_3]^{-}$) species. **Figure 2.3.22.A** depicts the diffuse reflectance spectrum of sample S/Cl=4.5 superimposed with the simulated absorption spectrum that best fits the experimental results. These findings align with the EPR data, which suggests a reduction in the relative abundance of paramagnetic species in the sample S/Cl=4.5, indicating that the dominant species is non-paramagnetic. **Figure A.1.3** illustrates the comparison of the combined spectra of the other calculated species with the experimental results. (Section **7.2.16** contains more information about computational studies techniques.)

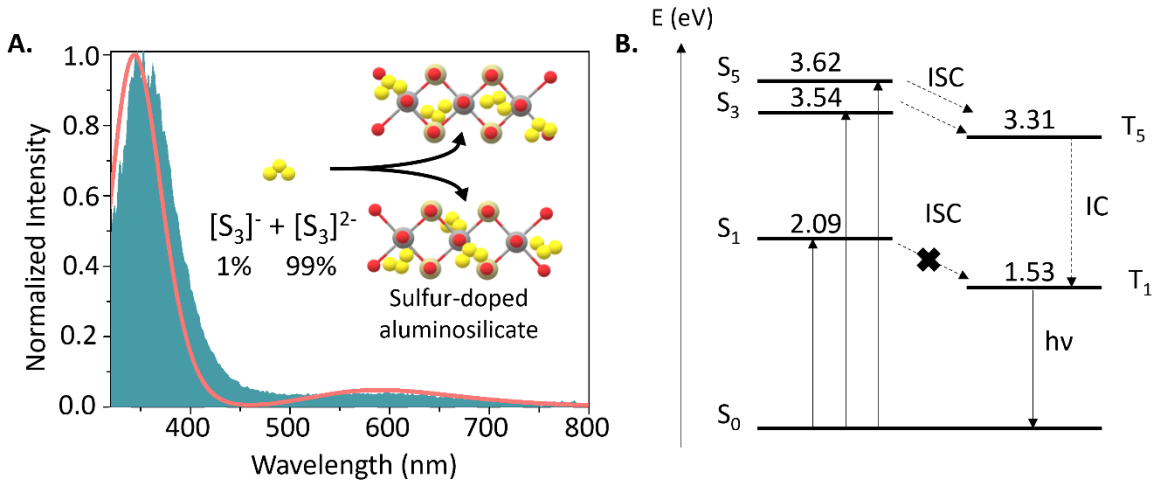


Figure 2.3.22 - **Computational studies –** (**A**) Overlap of the Kubelka-Munk spectrum of sample S/Cl=4.5 (green) and the combined calculated spectra of $[S_3]^{2-}$ and $[S_3]^{-}$ species (orange). (**B**) Proposed energy diagram of $[S_3]^{2-}$ clusters.

Figure 2.3.22.B displays a schematic representation of the relative energy of the calculated singlet and triplet states of $[S_3]^{2-}$. Detailed information on state symmetries and orbitals is summarized in **Table A.1.4** and **Figure A.1.4**. The experimental transition observed in the diffuse reflectance spectrum, centered at 355 nm (3.49 eV), is in good agreement with the calculated energies for the $S_0 \rightarrow S_3$ and $S_0 \rightarrow S_5$ transitions. **Table 2.3.4** illustrates the intersystem crossing mechanism between $S_1 \rightarrow T_1$, $S_3 \rightarrow T_5$ and $S_5 \rightarrow T_5$ transitions. Notably, transitions $S_3 \rightarrow T_5$ and $S_5 \rightarrow T_5$ involve simultaneous spin and orbital changes, preserving total angular momentum and allowing non-radiative transitions. In contrast, the conservation of orbital in the $S_1 \rightarrow T_1$ transition results in a forbidden transition, according to El-Sayed rules[120]. On the other hand, the energy gap (ΔE_{ST}) is considerably smaller in $S_3 \rightarrow T_5$ and $S_5 \rightarrow T_5$ compared to $S_1 \rightarrow T_1$, leading to significantly higher rates of intersystem crossing $k_{ISC}^{S_3 \rightarrow T_5}, k_{ISC}^{S_5 \rightarrow T_5} \gg k_{ISC}^{S_1 \rightarrow T_1}$.

Table 2.3.4 - Intersystem process in $[S_3]^{2-}$ between S1→T1, S3→T5, S5→T5 and S6→T8 transitions.

$$k_{ISC} \propto \left(\frac{\langle S_n | \hat{H}_{SO} | T_m \rangle}{\Delta E_{ST}} \right)^2$$

$S_1 \xrightarrow{ISC} T_1$	$\Delta E_{ST} = 0.56\ eV$	$\langle (H, L) \vert \hat{H}_{SO} \vert (H, L) \rangle$	No orbital change
$S_3 \xrightarrow{ISC} T_5$	$\Delta E_{ST} = 0.22\ eV$	$\langle (H-2, L) \vert \hat{H}_{SO} \vert (H-3, L) \rangle$	Orbital change
$S_5 \xrightarrow{ISC} T_5$	$\Delta E_{ST} = 0.30\ eV$	$\langle (H-1, L) \vert \hat{H}_{SO} \vert (H-3, L) \rangle$	Orbital change
$S_6 \xrightarrow{ISC} T_8$	$\Delta E_{ST} = 0.27\ eV$	$\langle (H-1, L+1) \vert \hat{H}_{SO} \vert (H-3, L+1) \rangle$	Orbital change
$k_{ISC}^{S_3 \rightarrow T_5}, k_{ISC}^{S_5 \rightarrow T_5}, k_{ISC}^{S_6 \rightarrow T_8} \gg k_{ISC}^{S_1 \rightarrow T_1}$			

The calculated oscillator strength of S_1 can explain the lack of fluorescence through the natural radiative lifetime. The natural radiative lifetime occurs in the absence of any non-radiative processes involved. This constant can be calculated through the oscillator strength by equation (**2.3.3**) (where f denotes the oscillator strength and v_{max} represents the frequency of absorption in cm^{-1}). It sets an upper boundary to the lifetime of an excited molecule[121].

$$\tau_N = \frac{1.5}{\bar{\upsilon}^2_{máx} \times f} \qquad (2.3.3)$$

Thus, the calculated $\tau_N^{S_1}$ using the theoretical values from **Table A.1.4** is approximately 2.92 x 10^{-6} s, corresponding to a k_N of 3.4 x 10^5 s^{-1}. Typically, the kinetic constant for internal conversion (k_{IC}) is on the order of 10^{12} s^{-1}[121]. Consequently, $k_{IC}^{S_1 \rightarrow S_0} \gg k_N^{S_1}$, providing an explanation for the lack of fluorescence. Given that singlet states S_3 and S_5 can undergo intersystem crossing to T_5 state, it is expected that $k_{ISC}^{S_3 \rightarrow T_5} + k_{ISC}^{S_5 \rightarrow T_5} \gg k_{IC}$, so that phosphorescence is possible by population of the triplet manifold from higher lying Singlet States. This El-Sayed allowed transition to the triplet manifold can occur by exciting at 266 nm (**Table 2.3.4**). At this wavelength the performed transient absorption experiment revealed a long-lived state which can be assigned to $T_1 \rightarrow T_n$ transition (**Figure 2.3.14**), which is also in good agreement with the calculated transitions (**Table A.1.4**). Additionally, the predicted energy of the triplet state T_1 is at 1.53 eV (809 nm), corresponding closely to the long-lived emission values in the NIR region of 1.59 eV (780 nm), as depicted in **Figure 2.3.13.B**.

2.3.4 Suitable applications for these materials

The observed luminescent properties highlight the potential applications of sulfur-doped zeolites in anticounterfeiting and authentication systems, as well as in NIR phosphor-convert light emitting diodes (NIR pc-LEDs), as illustrated in **Figure 2.3.23**. Here, proof-of-concepts are demonstrated for both applications.

Firstly, two zeonex films, one coated with sample S/Cl=0.21 (yellow-orange emission) and the other with S/Cl=4.5 (NIR emission), were deposed in the 'O' of the 'NOVA' logo, printed in an acetate sheet, creating a well-defined pattern (the internal 'O' with the NIR emission and the external 'O' with the yellow-orange emission, see **Figure 2.3.23.B**). These coated films are indistinguishable under ambient light (**Figure 2.3.23.A**), only becoming observed when excited by UV light. In a second experiment, a commercial UV-LED with an excitation wavelength of

approximately 365 nm was coated with a zeonex film containing sample S/Cl=4.5, as shown in **Figure 2.3.23.E** under ambient light and **Figure 2.3.23.F** under UV light.

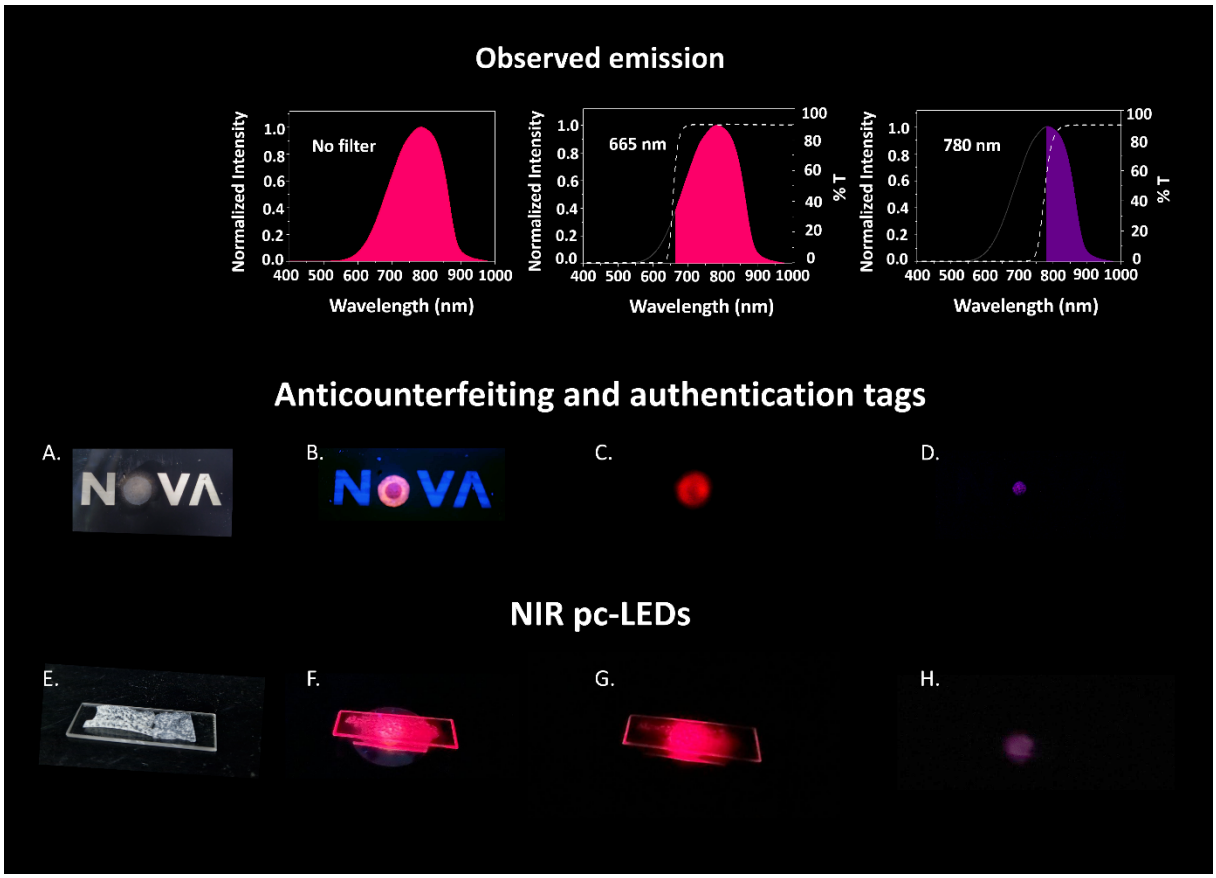


Figure 2.3.23 - Prototypes using sulfur-doped zeolites as authentication and anticounterfeiting tags (Middle) and as NIR pc-LEDs (Below). Photos were taken by a smartphone under ambient (**A, E**) and under UV illumination, around λ_{exc}=365 nm (**B-D** and **F-H**). Without any cutoff filter (**B**, **F**) and using a 665 nm (**C, G**) and a 780 nm (**D**, **H**) cutoff filters. **(Top).** Note the overlap between the emission spectra of the NIR-emitting sample and the transmission spectra of the cutoff filters used. The filled area under the curve represents the emission detected by the smartphone.

In both cases, a smartphone camera was equipped with various cutoff filters with different wavelengths (665 and 780 nm), as presented in **Figure 2.3.23.C** and **Figure 2.3.23.G** for 665 nm, and **Figure 2.3.23.D** and **Figure 2.3.23.H** for 780 nm. Remarkably, the luminescence from the NIR-emitting samples persisted and remained detectable, even with the use of a 780 nm cutoff filter, while remaining entirely invisible to the human eye.

2.3.5 Conclusions

Nowadays, there is a growing need for alternatives to conventional near-infrared (NIR) emitters due to issues related to availability and stability. This study demonstrates the feasibility of

creating a zeolite-based luminescent material, exhibiting emission peaking at 780 nm and external quantum efficiency of 17%. This material can be easily prepared using sustainable and non-toxic sources, starting with widely available Na-LTA zeolite. By adjusting the sulfur content in the initial materials, materials with emissions ranging from orange-yellow to NIR were produced.

Through the analysis of spectroscopy and computational data, it was shown that the $[S_2]^-$ species, responsible for the orange-yellow emission of sulfur-doped zeolites at low sulfur concentrations are replaced by triatomic sulfur clusters $[S_3]^-$ and $[S_3]^{2-}$ when sulfur concentration increases. Additionally, with the characterization and calculation results, the NIR emission was assigned to $[S_3]^{2-}$ clusters. These species exhibit an absorption band around 355 nm, displaying a remarkable Stokes shift of 1.90 eV. The long emission lifetime and a detected transient absorption confirmed the prepared materials are phosphorescent.

The XRD data demonstrated that the NIR-emitting clusters are present in nepheline and/or carnegieite crystalline phases, which replace the sodalite phase at high sulfur concentrations. The same emission and decay time were also found in samples composed only by nepheline and carnegieite crystalline phases (see **Figure 2.3.7** and **Figure 2.3.12**).

The optical properties of these materials, with absorption in the UV region and emission mainly in the NIR, along with an EQE of around 17% and an average decay time of 0.54 milliseconds, make them particularly interesting for various photonic applications such as anticounterfeiting and authentication tags, light-based communication technologies or as phosphors in the preparation of NIR-LEDs.

2.4 General Chapter Conclusions

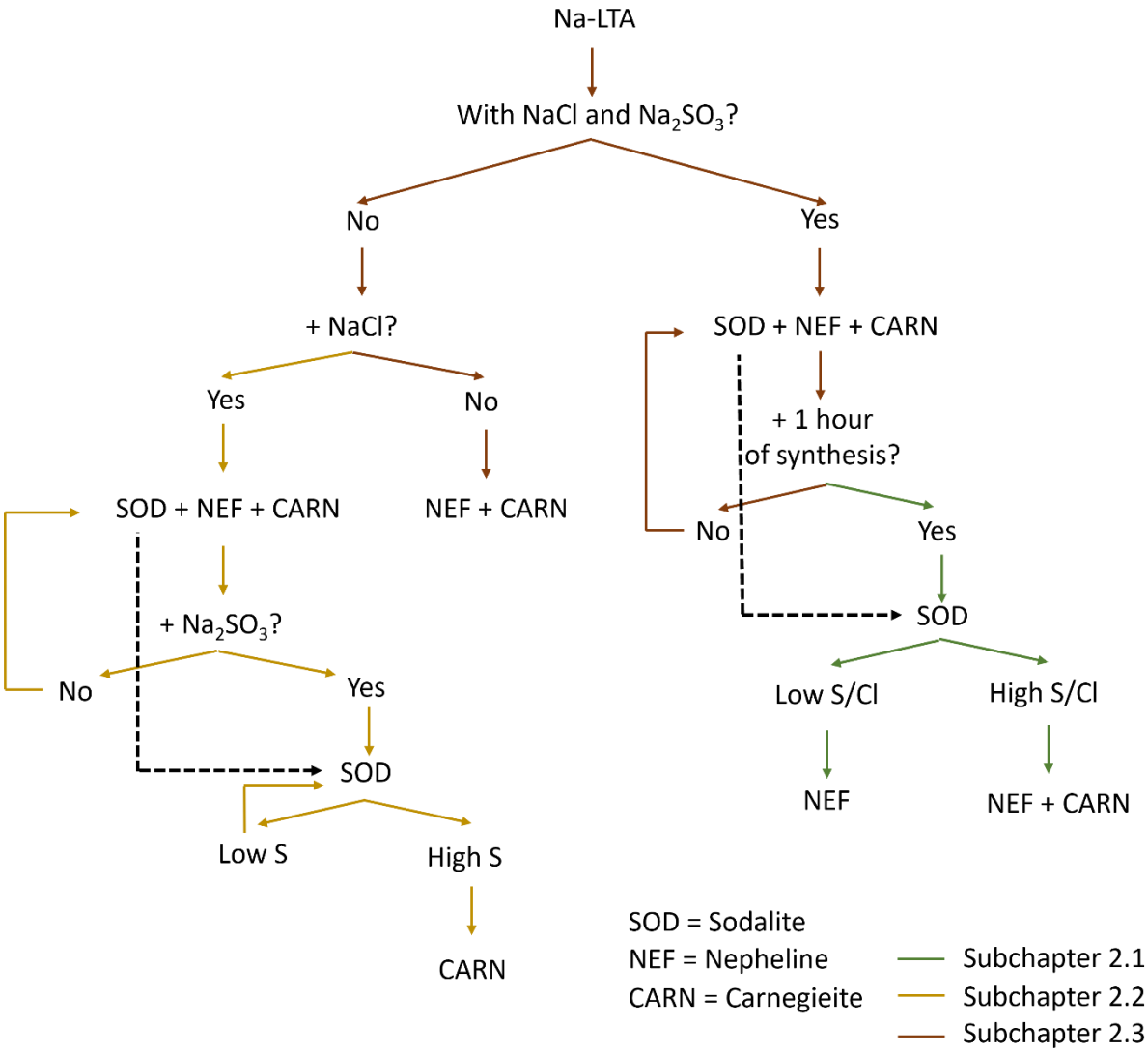
The three sections of this chapter focus on understanding the optical properties of luminescent sulfur-doped zeolites, particularly the NIR emission. Several synthesis parameters were analyzed, including different sulfur precursors, sulfur and chloride concentrations, and synthesis times. Consequently, an intrinsic relationship between the obtained crystalline phases and optical properties was demonstrated, revealing the presence of two different emissive species:

1) $[S_2]^-$, absorbing at 385 nm and emitting at 625 nm ($^2\Pi_g \leftrightarrow {}^2\Pi_u$ transitions). These species are associated with sodalite zeolite and samples with S/Cl=0.21 and S/Cl=0.33 exhibit the highest emission intensities. Previous studies demonstrated external quantum efficiencies (EQEs) of 53% and photoluminescence decay times of about 135 nanoseconds for this emission[20,58].

2) The second emissive species was assigned to a phosphorescence mechanism of $[S_3]^{2-}$ species, which absorbs at 355 and emits around 780 nm. This new species increases with the S/Cl ratios and is related with nepheline and/or carnegieite structures. An EQE of 17% and an average decay time of 0.54 milliseconds were observed.

These produced sulfur-doped zeolites demonstrated promissing results for use in authentication and anticounterfeiting tags, as well as in NIR pc-LEDs. This potential was illustrated through proof-of-concept examples for each NIR application.

Structurally, this sulfur chapter also provided important insights into the high-temperature zeolite transformations. **Scheme 2.4.1** summarizes these transformations according to the studies presented in each subchapter. Note that the black dashed line is related to transformations that happen exclusively in the sodalite phase present in the initial mixture of sodalite, nepheline and carnegieite (SOD+NEF+CARN). Afterward, this sodalite phase was only partially transformed into the mentioned phases, as this phase was consistently detected.



Scheme 2.4.1 - Resume of the high-temperature zeolite transformations observed in the three subchapters in this chapter.

Overall, the comprehensive study developed here, relating the structural characterization of these materials to their optical properties, was crucial for understanding this chalcogen and for the work developed in the following chapters.

3

Selenium-Doped Zeolites: Exploring Red and NIR Emissions and Their Applicability

Selenium is renowned not only for its vital role in essential functions within the human body[122] but also for its versatile optical properties that extend across a broad spectrum, covering from ultraviolet (UV) to near-infrared (NIR) regions.

However, the behavior of this chalcogen, when confined within zeolites, remains limited at this point. Several studies indicate that photochromism or photoluminescence mechanisms may occur depending on the species present. Byron et al.[80] recently demonstrated that selenium-doped sodalite, when containing $[Se_2]^{2-}$ species, exhibits photochromic properties upon irradiation with 254 nm light. The resulting color change is characterized by an absorption band peaking at *ca.* 500 nm. Furthermore, in the presence of $[Se_2]^{-}$ radical clusters, a photoluminescence mechanism emerges, characterized by an absorption at 490 nm and emission at 740 nm due to the transitions $^2\Pi_g \leftrightarrow {}^2\Pi_u$[86]. This red emission displays vibronic bands at low temperatures (< 10 K), with a peak separation of 334 cm^{-1}. Further investigation into $[Se_2]^{-}$-doped KI crystals[87] revealed similar emission properties. The corresponding excitation spectrum showed two bands at 515 nm (transition $^2\Pi_g \rightarrow {}^2\Pi_u$) and an additional one centered at 345 nm (transition $^2\Pi_g \rightarrow {}^2\Delta_u$), both ascribed to $[Se_2]^{-}$ clusters. Moreover, photoluminescence decay times of approximately 85 nanoseconds and 14 nanoseconds were observed at 2 K and 77 K, respectively, in these crystals.

In the following study, a detailed investigation into the photophysical properties of selenium-doped zeolites was conducted. Different loadings of chalcogen and chloride were used to assess whether similar behavior to that observed in the sulfur case occurs. This investigation

aimed to address significant gaps in the existing literature regarding red region emission and to explore the potential appearance of a novel emission at higher chalcogen amounts. Furthermore, the evaluation of these materials for NIR applications was also explored.

3.1 Synthesis and structural characterization

Emissive selenium-doped aluminosilicate zeolites were synthesized by mixing Na-LTA zeolite, NaCl, and Na_2SeO_3, followed by heat treatment at 900 °C for one hour under a reducing atmosphere, according to the stoichiometry $Na_8Si_6Al_6O_{24}Se_xCl_{2-2x}$. Samples with nominal molar ratios of Se/Cl=0, 0.06, 0.21, 0.75 and 4.5 were produced. Refer to section **7.1.1** for more information about the experimental procedure.

The crystallinity of the final synthesized materials after the high-temperature treatment was analyzed using powder X-ray diffraction (see section **7.2.13** for more information about this technique), revealing the presence of three different crystalline phases: sodalite, nepheline and carnegieite (**Figure 3.1**). All these phases are known to be directly converted from Na-LTA zeolite[60,71]. However, the modifications involved can be more complex than initially perceived. Sodalite $Na_8[Si_6Al_6O_{24}]Cl_2$ can also be transformed into nepheline and carnegieite[73,74,123], structures that have the same composition, $Na_4[Si_4Al_4O_{16}]$. Additionally, interconversion between these polymorphs may also occur[71,72]. Based on the acquired knowledge from sulfur-doped zeolites, the following synthesis scheme is proposed, as illustrated in equation (**3.1**).

$$\begin{aligned} Na-LTA \xrightarrow{\Delta} Sodalite + Nepheline + Carnegieite \\ \Delta \not\rightarrow Nepheline + Carnegieite \end{aligned} \qquad (3.1)$$

Two different structural mechanisms were considered: **i)** Na-LTA being completely converted into sodalite, nepheline and carnegieite phases, and **ii)** Sodalite being converted into nepheline and carnegieite. The interconversion from nepheline into carnegieite and vice versa was discarded since it is reported to occur at temperatures equal to or higher than 900° C[71,72] and was not detected in the previous synthesis discussed in chapter **2**.

The relative fractions of the identified phases were calculated by fitting the experimental PXRD data with the corresponding ICDD standards reference cards (**Figure 3.1.A**). This analysis revealed a decrease in the sodalite phase, reaching 60%, and an increase in both nepheline and carnegieite phases, each accounting for approximately 20%, with the Se/Cl ratio increase,

as illustrated in **Figure 3.1.B**. However, it is evident that the sodalite relative phase stabilizes and even increases slightly, from sample Se/Cl=0.75 to sample Se/Cl=4.5.

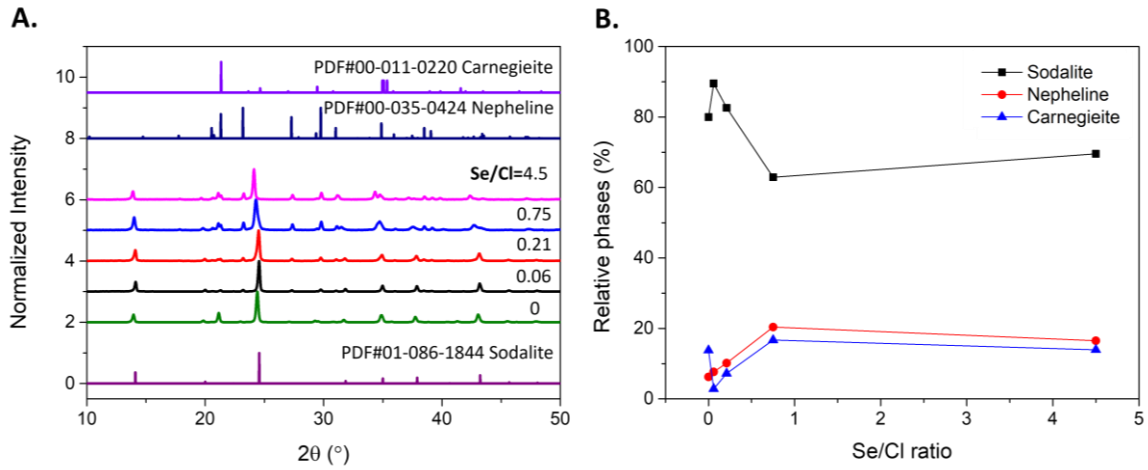


Figure 3.1 - **Structural analysis of selenium-doped zeolite samples –** (**A**) PXRD diffractograms of the synthesized selenium-doped zeolite samples with different Se/Cl ratios and the ICDD standard reference card of 01-086-1844 sodalite ($Na_8Si_6Al_6O_{24}Cl_2$), 00-035-0424 nepheline ($Na_4Si_4Al_4O_{16}$) and 00-011-0220 carnegieite ($Na_4Si_4Al_4O_{16}$). (**B**) Sodalite, nepheline and carnegieite relative phases calculated in the synthesized zeolite samples.

This behavior contrasts with the one found in sulfur-doped zeolites prepared under similar conditions in subchapter **2.3**, where the sodalite phase consistently decreased while the nepheline and carnegieite phases increased with the increase of S/Cl ratio. This resulted in a sodalite phase of almost 30%, with 30% nepheline and 40% carnegieite in sample S/Cl=4.5 (**Figure 2.3.1.B**).

Thus, selenium appears to exhibit a more stabilizing effect on the sodalite phase than sulfur. This phenomenon may be assigned to the larger size of the chalcogen, resulting in a higher occupancy of the sodalite cages when using selenium. As previously reported by Ding et al.[60] and highlighted in chapter **2**, the use of chloride in high-temperature synthesis starting from Na-LTA zeolite stabilizes the sodalite phase, otherwise, Na-LTA is completely converted into nepheline and carnegieite. In this sense, it seems that selenium exhibits a similar effect to chloride, preventing the formation of both nepheline and carnegieite phases.

The element analysis, conducted using wavelength dispersive X-ray fluorescence (WDXRF), corroborates the efficacy of the synthesis process by revealing an increase in selenium content and a reduction in chloride loading according to the Se/Cl ratios (**Table 3.1**). However, the observed selenium values are slightly lower than initially expected. This discrepancy could potentially be attributed to evaporation losses during the high-temperature synthesis at 900 °C. These molar percentages were calculated from the weight percentage of the

corresponding elements in their oxide form (**Table B.1**). Furthermore, the Al/Si ratio is preserved, remaining *ca.* 1. (Refer to section **7.2.11** for further information about this WDXRF technique.)

Table 3.1 - Molar percentage of each main element found in zeolite samples using the WDXRF technique.

Nominal Se/Cl	Molar percentage composition (%)[a]						Obtained Se/Cl
	Na	Si	Al	O	Se	Cl	
0.06	13.88	14.14	12.84	55.03	0.15	3.55	0.04
0.21	14.59	13.66	12.83	54.86	0.36	3.28	0.11
0.75	14.45	13.54	13.11	55.92	0.81	1.69	0.48
4.5	14.15	13.69	13.07	56.92	1.29	0.45	2.86

[a]Calculated from the WDXRF weight percentage (wt%) (**Table B.1**).

3.2 Absorption spectra

Selenium doping seems to impact the optical properties of the produced zeolite samples, displaying a pink coloration. Therefore, these samples were first analyzed using diffuse reflectance spectroscopy (see section **7.2.2** for more details about this technique). Following the application of the Kubelka-Munk theory[103], the resulting spectra are presented in **Figure 3.2**. For low Se/Cl ratios (<0.21), two distinct absorption bands emerge at 350 and 490 nm, respectively. These bands closely correspond to those reported by Hiroshi et al.[87] for the $[Se_2]^-$ center in KI crystals, where the 350 nm band is associated with the $^2\Pi_g \rightarrow {}^2\Delta_u$ transition and the one at 490 nm band with the $^2\Pi_g \rightarrow {}^2\Pi_u$ transition (see **Figure 1.4.8** of the introduction chapter). However, at higher Se/Cl ratios (>0.75), a new band at 400 nm becomes evident. The same study also mentioned this band, though no further characterization was performed.

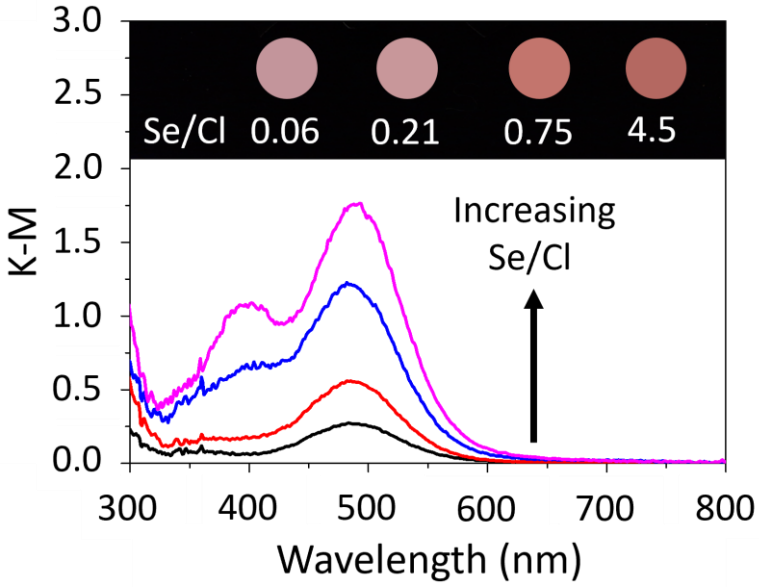


Figure 3.2 - Diffuse reflectance spectrum of samples with different Se/Cl ratios. Inset: photos of the samples under ambient light.

To better understand the differences in the diffuse reflectance spectra, a spectral deconvolution was performed. The experimental spectra were possible to recreate (**Figure 3.2**), combining the 350 and 490 nm bands (**Figure 3.3.A**) with the 400 nm band (**Figure 3.3.B**). Additionally, the areas of both simulated and experimental absorption bands consistently increase with the Se/Cl ratios (see the insets of **Figure 3.3.A-B**), confirming the elemental analysis results and indicating the progressive formation of selenium chromophores.

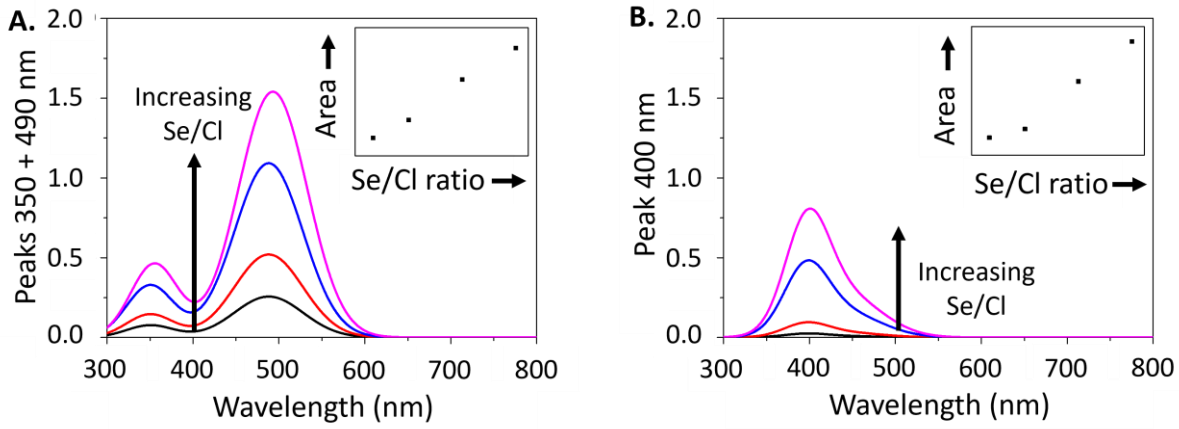


Figure 3.3 - **Spectral deconvolution of the experimental diffuse reflectance spectra –** (**A**) Combination of 350 and 490 nm absorption bands, assigned to $[Se_2]^-$ clusters. (**B**) Absorption band peaking at 400 nm. The insets show the calculated peak areas.

Figure 3.4 illustrates the deconvoluted spectrum of the sample with Se/Cl=0.75 using the two absorption bands depicted in **Figure 3.3.A-B**.

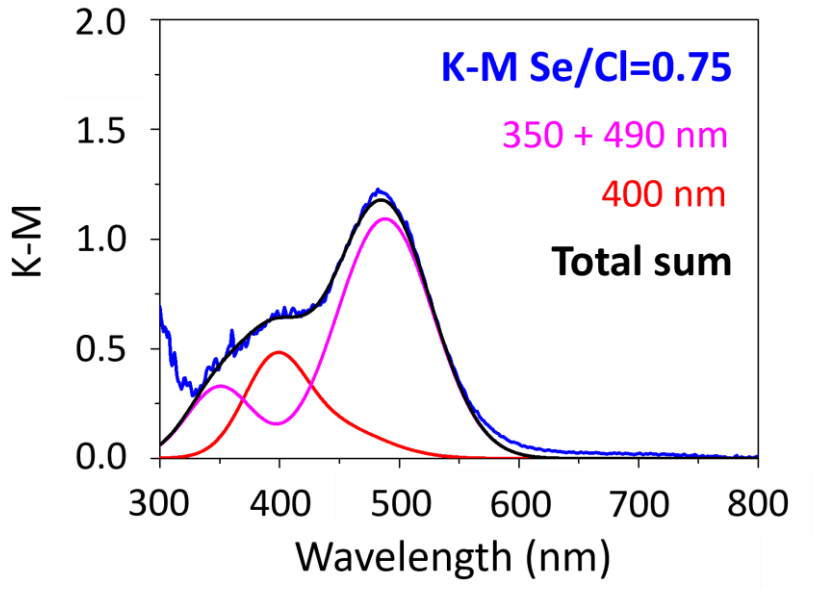


Figure 3.4 - Diffuse reflectance spectral deconvolution of the sample with Se/Cl=0.75.

3.3 Emission and excitation spectra

In this section, the photoluminescent properties of these samples were studied (see section **7.2.3** for more details about this technique). For that purpose, different wavelengths were used to excite the samples, matching the three absorption band maxima - 350, 400 and 490 nm. Excitation at 350 and 490 nm produces identical emission spectra, with a band maximum at around 740 nm (**Figure 3.5.A-B**). This observation is consistent with the reported literature on the emission spectra of $[Se_2]^-$ clusters in zeolites[86].

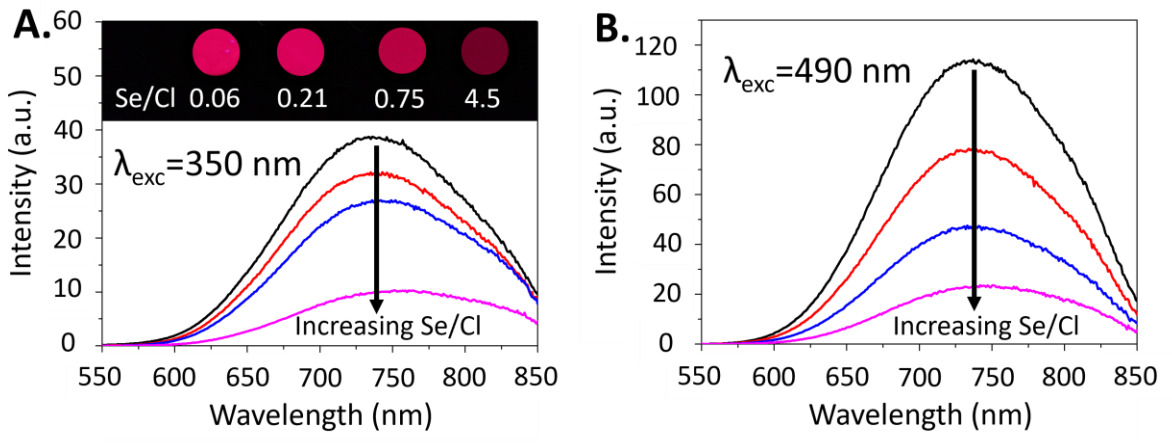


Figure 3.5 - Steady-state emission spectra of samples with different Se/Cl ratios using different excitation wavelengths, λ_{exc}=350 nm (**A**) and λ_{exc}=490 nm (**B**). Inset: photos of the samples under UV light (λ_{exc}=365 nm).

Accordingly, the corresponding excitation spectra for this emission (**Figure 3.6**) reveal two bands at 350 and 490 nm at low Se/Cl ratio, in conformity with the $^2\Pi_g \rightarrow {}^2\Delta_u$ and $^2\Pi_g \rightarrow {}^2\Pi_u$ transitions, respectively, of $[Se_2]^-$ species[87]. At Se/Cl=4.5 (pink lines), a new band at 400 nm emerges, suggesting that a new emissive species is formed at this ratio.

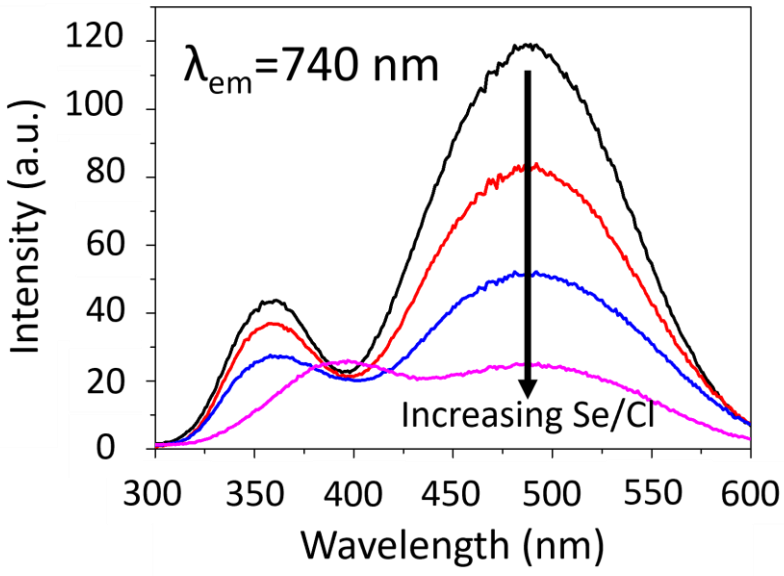


Figure 3.6 - Excitation spectra of the synthesized samples monitoring the emission at 740 nm.

However, when these materials are excited at 400 nm, a change in the emission spectra is observed (**Figure 3.7.A**), with the maximum progressively shifting to *ca.* 800 nm with increasing Se/Cl ratio. The corresponding excitation spectra (**Figure 3.7.B**) follow the same behavior

as the one already discussed, with the distinction that the band at 400 nm takes on a more prominent role. This suggests that the absorbing species at 400 nm are responsible for the NIR emission.

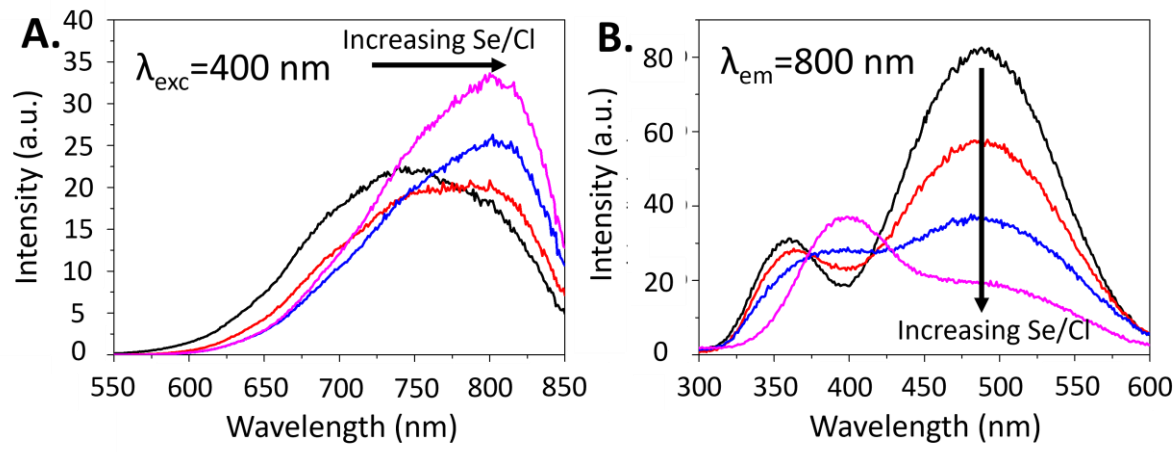


Figure 3.7 - Emission (**A**) and excitation (**B**) spectra of the synthesized samples, using λ_{exc}=400 nm and λ_{em}=800 nm, respectively.

The emission and excitation spectra reveal two distinct emissive species: one absorbs at 350 and 490 nm and emits in the red region (peaking at 740 nm), characteristic of $[Se_2]^-$ clusters; the other absorbs at 400 nm and emits in the NIR region (with a maximum at 800 nm). However, the nature of these species remains unclear, as only the absorption spectra have been previously reported[87].

Notably, similar to the sulfur system discussed for $[S_2]^-$, it appears that $[Se_2]^-$ species are located inside the sodalite zeolite, contributing to its stabilization. In contrast, the species responsible for the NIR emission seem to be associated with nepheline and carnegieite crystalline structures, as they are predominantly found in samples with higher amounts of these phases. Consequently, the significant stabilization of sodalite, which consistently remains the majority phase, may explain the presence of both emitting species even at high Se/Cl ratios.

Furthermore, the observed decrease in intensity in both emission and excitation spectra of the red emission, combined with the increased formation of $[Se_2]^-$ detected in diffuse reflectance with varying Se/Cl ratios, suggests the occurrence of emission quenching. To determine this phenomenon conclusively, the upcoming sections will explore the photophysical properties of red and near-infrared (NIR) emissions.

3.4 Red emission

To clarify the existence of a quenching effect, the external quantum efficiencies (EQEs) and photoluminescence decay times of this red emission (λ_{exc}=350 or 490 nm and λ_{em}=740 nm) were measured in all samples. (See additional information about EQE in section **7.2.3** and photoluminescence decay times in section **7.2.4**.) It was observed that both parameters exhibit a decrease with an increase in the Se/Cl ratios.

For EQE calculations, the 'absorption measured' values obtained by the absolute method using an integrating sphere were corrected, according to equation (**3.2**), since the species responsible for the NIR emission also absorbs at this wavelength.

$$Abs_{Corrected} = Abs_{Measured} \times \frac{Abs\ intensity\ at\ 480\ nm\ of\ [Se_2]^-\ species}{Total\ abs\ intensity\ at\ 480\ nm} \quad (3.2)$$

The 'absorption intensity at 480 nm of $[Se_2]^-$ species' was taken from the deconvoluted spectrum illustrated in **Figure 3.3.A** and the 'total absorption intensity at 480 nm' from the diffuse reflectance spectra depicted in **Figure 3.2**. Therefore, the EQE values range from 23% to 3% according to the Se/Cl ratio, as shown in **Figure 3.8.A** and summarized in **Table 3.2**. These values suggest a possible quenching effect, as initially assumed in the steady-state measurements of the emission spectra (**Figure 3.5.A-B**) and the excitation spectra (**Figure 3.6**).

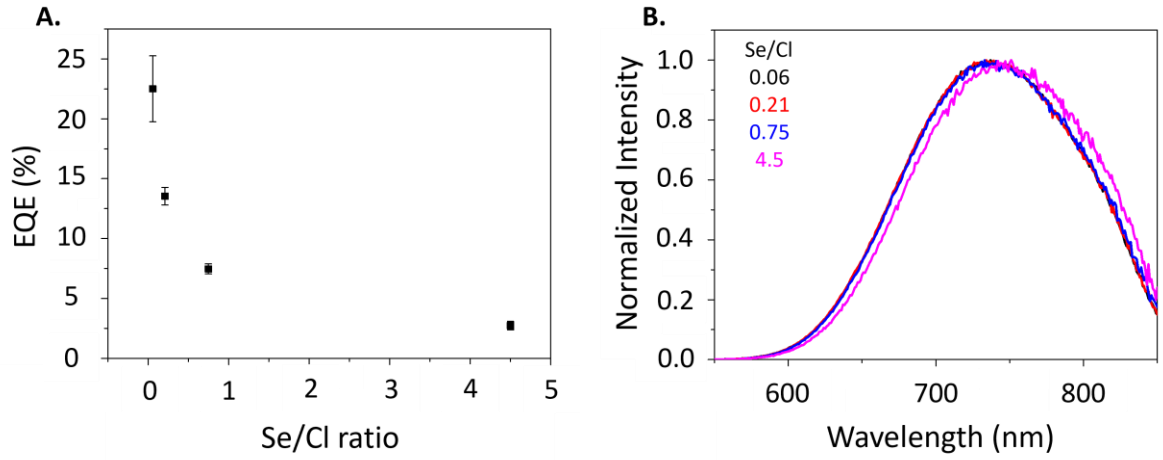


Figure 3.8 - (**A**) External quantum efficiencies of samples with different Se/Cl ratios, using a 480 nm excitation. (**B**) Normalized emission spectra of all synthesized samples, exciting at 480 nm.

Figure 3.8.B depicts the normalized emission spectra, using the same excitation wavelength as in the EQE measurements. Noticeably, the sample with a higher Se/Cl ratio exhibits a slight red-shift originating from the presence of NIR-emitting species.

Additionally, the photoluminescence decay times were analyzed using a bi-exponential decay model, which identified a fast component exhibiting a minimal variation (only 3 ns) and a slow one showing higher variation (decreasing by approximately 25 ns with increasing Se/Cl ratio). To better understand the impact of selenium concentration, the fast component was fixed using its average value of 18 nanoseconds. Consequently, the slow component decreased from 110 to 88 nanoseconds with increasing Se/Cl ratio, resulting in average decay times ranging from 96 to 56 nanoseconds, respectively (see **Figure 3.9** and **Table 3.2**).

Note that the photoluminescence decay time of the sample with Se/Cl=4.5 (illustrated in pink, **Figure 3.9**) is depicted on a secondary scale due to a significant contribution of a long-lived emission, which will be discussed in the next section. This emission persists well beyond the 800-nanosecond measuring window, making it challenging to fully capture its decay. Consequently, the signal from this emission merges with the baseline, making it unfeasible to accurately fit the data while considering these long-lived species.

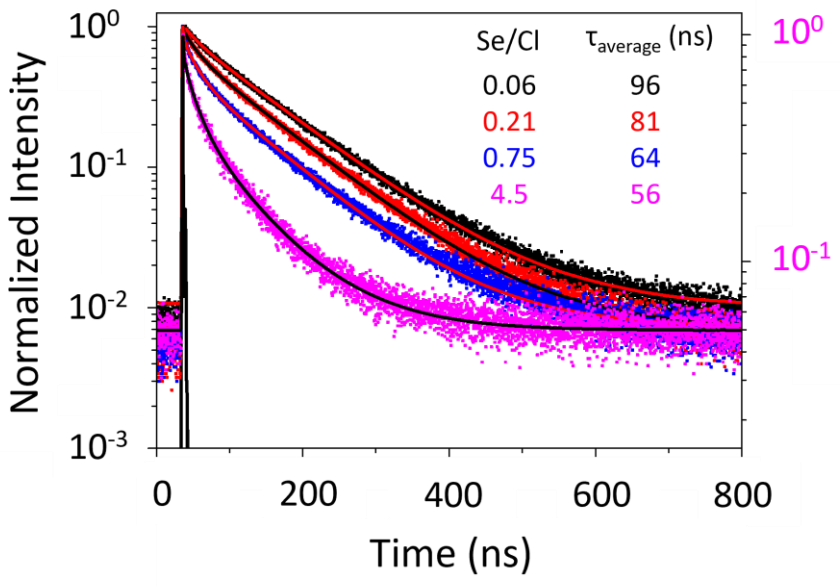


Figure 3.9 - Photoluminescence decay times (scatter) and respective fittings (solid line) of samples with different Se/Cl ratios, recorded with an λ_{exc}=445 nm and λ_{em}=750 nm. See residuals of the fittings in **Figure B.1**.

Similarly to what was discussed in sulfur systems (subchapter **2.3**), this bi-exponential behavior might be due to the different local environments of these $[Se_2]^-$ species. In fact,

Schlaich et al.[86] propose that these species may exhibit two different coordination environments within sodalite cages due to their comparatively larger size relative to chloride anion. One environment is composed of $[Se_2]^-$ in a tetrahedral $[Na_4]^{4+}$ coordination, while the other involves a trigonal $[Na_3]^{3+}$ coordination, which is preferentially present (see **Figure 1.4.3** of the introduction section, illustrating the typically $[Na_4Cl]^{3+}$ tetrahedron found in the center of sodalite cages).

Considering that each of these $[Se_2]^-$ environments is responsible for each observed decay component. The photoluminescence decay times demonstrate that one is more susceptible than the other, varying with selenium loading (**Figure 3.9**). Furthermore, the differences detected in the decay times of $[Se_2]^-$ when confined within KI crystals are also indicative of the influence of the matrix nature. If surrounded by an octahedron of K^+, mono-exponential decays yielding values of 85 and 14 nanoseconds were observed at temperatures of 2 K and 77 K, respectively[87].

Table 3.2 summarizes the external quantum efficiencies (EQEs) and photoluminescence decay times values observed with varying Se/Cl ratios. They demonstrate a more pronounced decrease in external quantum efficiencies than in photoluminescence decay times. These discrepancies may arise if shorter-lived species than the laser pulse duration used of 1.3 nanoseconds are present, leading to incomplete detection of photoluminescence decay times. Alternatively, a quenching effect involving the presence of non-emissive selenium species can also explain these results. Note that the EQEs are calculated based on the ratio of the number of emitted photons to the number of absorbed photons, while photoluminescence decay times focus on monitoring the emitting species.

As previously discussed, the diffuse reflectance spectra of the synthesized samples were deconvoluted, considering different contributions from the same absorption spectra (350 nm and 490 nm, assigned to $[Se_2]^-$ species and depicted in **Figure 3.3.A**, and 400 nm, ascribed to NIR-emitting species and illustrated in **Figure 3.3.B**). Consequently, no evidence of a new species was observed. Thus, a self-quenching effect caused by $[Se_2]^-$ species seems to be the most straightforward explanation for the decrease in EQE values. This phenomenon maintains the shape of the absorption spectra unchanged (varying only in intensity) and significantly impacts EQEs more than photoluminescence decay times. This hypothesis will be further explored in the following paragraphs.

Table 3.2 - External quantum efficiencies (EQEs), photoluminescence decay times with their respective components and amplitudes, alongside average decay times and corresponding radiative (k_r) and non-radiative (k_{nr}) 'averaged' constants of the red emission.

Nominal Se/Cl	EQE (%) at 480 nm	τ_1 (ns)	Relative amplitude (A_1)	τ_2 (ns)	Relative amplitude (A_2)	$\tau_{average}$ (ns)*	$k_{r\,(Av.)}$ (s^{-1}) x10^6	$k_{nr\,(Av.)}$ (s^{-1}) x10^6
0.06	23	18	0.03	110	0.97	96	2.35	8.10
0.21	14	18	0.06	105	0.94	81	1.67	10.69
0.75	7	18	0.12	98	0.88	64	1.16	14.36
4.5	3	18	0.15	88	0.85	56	0.49	17.42

*Values calculated using the pre-exponential factors.

Additionally, to better understand the alterations caused by selenium doping, radiative (k_r) and non-radiative (k_{nr}) 'averaged' constants were calculated[124], following equations (**3.3**) and (**3.4**), respectively. Note that the presented equations were slightly modified for materials analysis. In solution, the quantum yield (ϕ) term is used instead of external quantum efficiency (EQE), and typically a mono-exponential decay time (τ) is used instead of $\tau_{Average}$.

$$k_{r\,(Average)} = \frac{EQE}{\tau_{Average}} \quad (3.3)$$

$$k_{nr\,(Average)} = \frac{1}{\tau_{Average}} - k_r \quad (3.4)$$

As illustrated in **Table 3.2**, radiative 'averaged' constants decrease while non-radiative 'averaged' constants increase with Se/Cl ratios. These variations are studied below.

As previously mentioned, a self-quenching produced by $[Se_2]^-$ clusters may explain all the findings presented and discussed. Considering that these species are mainly located within sodalite cages, they compete with chloride anions to fill these zeolite structures, as illustrated in **Figure 3.10**. At higher Se/Cl ratios, the amount of $[Se_2]^-$ species increases, as demonstrated by diffuse reflectance spectroscopy (**Figure 3.2**) and corroborated by X-ray diffraction, showing an increase in sodalite unit cells from 8.88 to 9.03 Å (**Table B.2**) with selenium loading. A unit cell refers to the smallest repeating structure within a crystal lattice, consisting of a sodalite cage in this zeolite[125]. Furthermore, since it is a cubic system, all three axes present the same length, which, in this case, is around 9 Å.

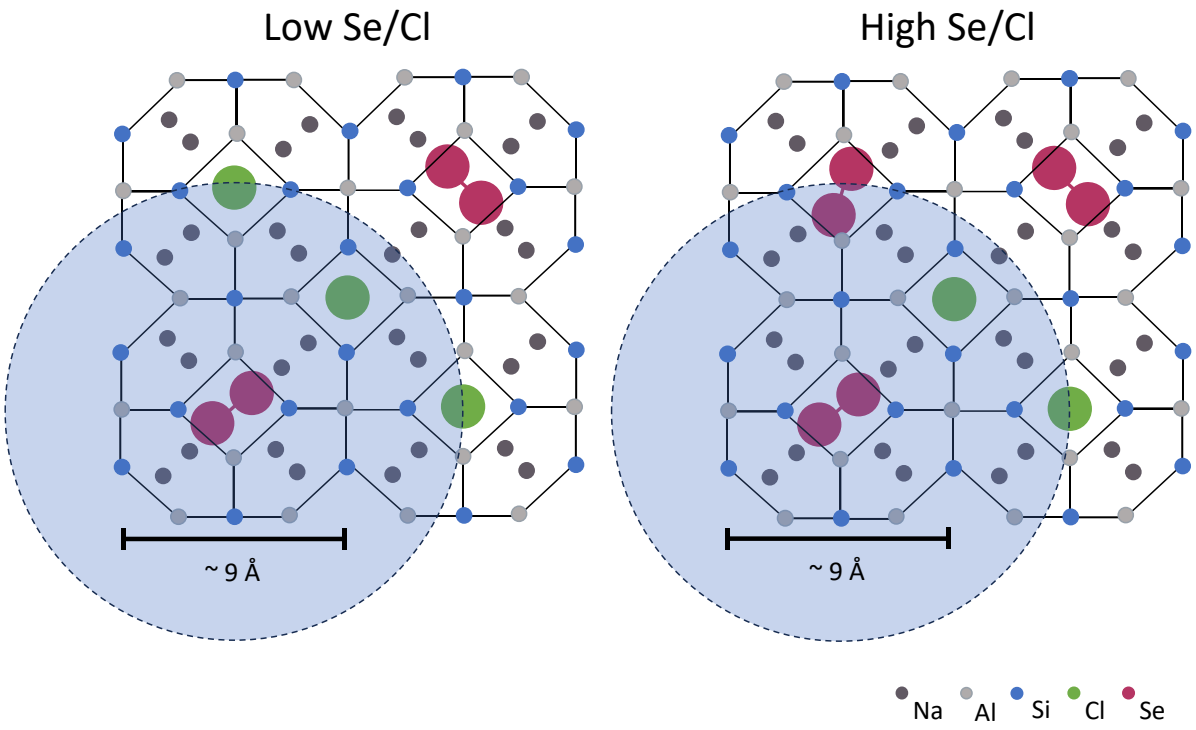


Figure 3.10 - Proposed illustration demonstrating the filling effect of sodalite cages according to Se/Cl ratios. Here, $[Se_2]^-$ species compete with chloride anions to occupy these cages. The blue circle has a radius of around 9 Å.

When the selenium loading is significantly high, $[Se_2]^-$ species may be present in adjacent cages at the same distances (~ 9 Å), see **Figure 3.10**. At such close proximities, they can strongly interact with each other, such as through Dexter energy transfer (DET). This mechanism typically occurs at distances up to 10 Å as the wavefunction overlap of electron clouds dictates the exchange interactions[126,127]. In **Figure 3.11**, the proposed double electron transfer mechanism between one excited selenium diatomic species, $[Se_2]^{-*}$, and one species in the ground state, $[Se_2]^-$, is proposed. It is worth noting that **Figure 3.11** only illustrates the transition $^2\Pi_g \leftrightarrow {}^2\Pi_u$ of $[Se_2]^-$ species, corresponding to the absorption at 490 nm and red emission. For additional information about the molecular orbitals and corresponding ground and excited states of $[Se_2]^-$ clusters, refer to **Figure B.2**.

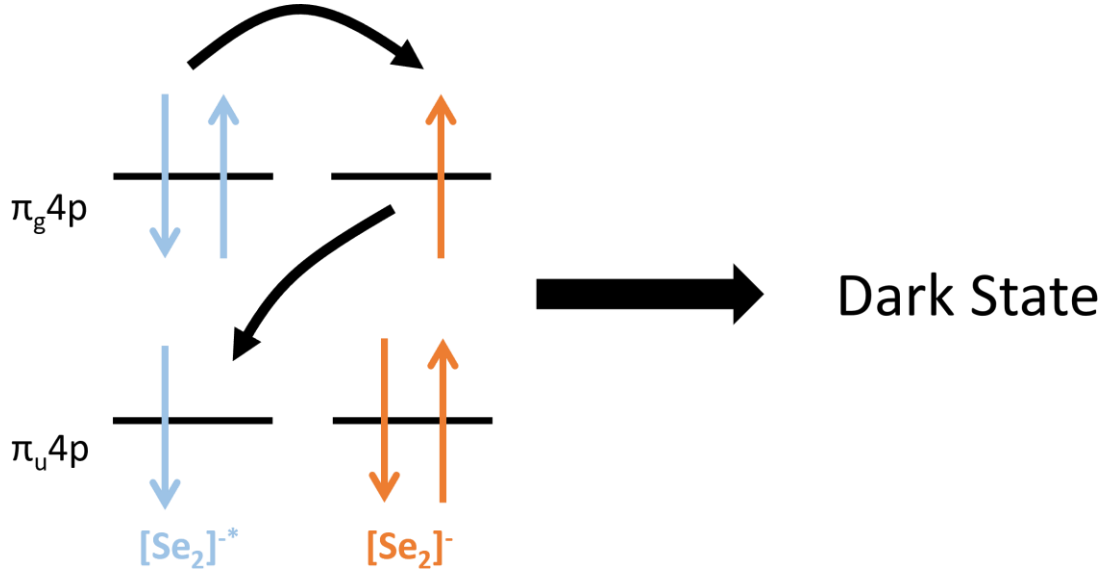


Figure 3.11 - Proposed double electron transfer mechanism illustrating the quenching phenomenon observed in these samples, attributed to interactions between $[Se_2]^-$ clusters. The diagram highlights the molecular orbitals involved in the $^2\Pi_g \leftrightarrow {}^2\Pi_u$ transitions of $[Se_2]^-$ species.

Therefore, the enhancement in non-radiative 'averaged' constants with the Se/Cl ratios (**Table 3.2**) is in good agreement with the increased proximity of different $[Se_2]^-$ species within the aluminosilicate matrix, thereby favoring electron transfer. This hypothesis also supports the EPR spectroscopy findings, as discussed in the following section **3.6**, which indicates an anti-ferromagnetic coupling in these samples. This results in a decrease in EPR intensity signals with selenium content, favored by closer proximity between paramagnetic species (such as $[Se_2]^-$).

3.4.1 Temperature studies

The red emission was further characterized under liquid nitrogen temperature (77 K) to establish if this emission is temperature-sensitive. The steady-state of the samples with lower selenium loading (Se/Cl=0.06) and with a higher amount of selenium (Se/Cl=4.5) were initially investigated. As previously mentioned, the sample with Se/Cl=0.06 presents the highest red emission intensity and lower NIR emission contamination. Observing its behavior at 77 K reveals a sharpening of the emission spectrum of $[Se_2]^-$ clusters, resulting in a shift of the emission maximum from 740 to 765 nm (**Figure 3.12**). Notably, no vibronic structure is detected, contrary to the behavior found in sulfur regarding the $[S_2]^-$ species. This aligns with the previous observations that this structure is only evident at lower temperatures (< 10 K). Additionally, the corresponding excitation spectra do not show differences with temperature.

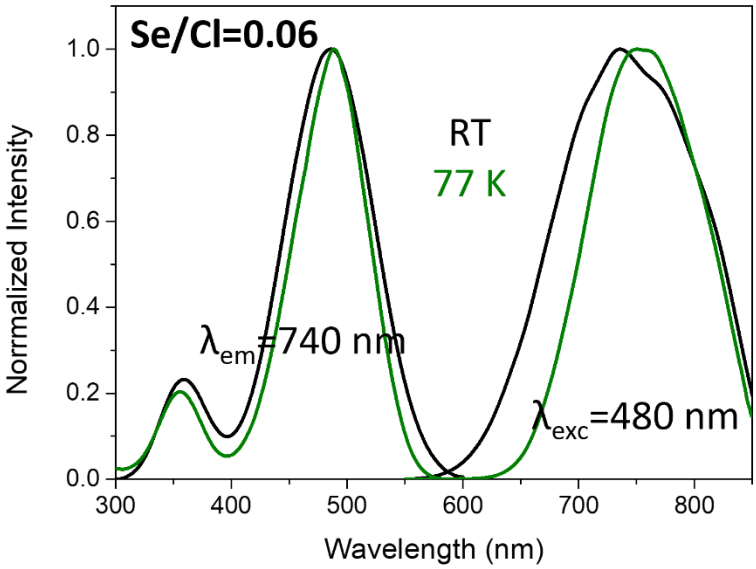


Figure 3.12 - Steady-state emission (λ_{exc}=480 nm) and excitation (λ_{em}=740 nm) spectra of sample Se/Cl=0.06 at 77 K (green) and at room temperature, RT (black).

The harmonic oscillator model of diatomic molecules can explain the necessity of using temperatures below 10 K[86] to detect vibronic bands in $[Se_2]^-$. This model demonstrates the relationship between molecular mass and vibrational energy. Heavier molecules exhibit vibrational levels that are closer to each other, resulting in less distinct vibronic peaks. A comparison between the vibronic peak separation observed in $[S_2]^-$ clusters (550 cm^{-1}) (subchapter **2.3**) and those reported in $[Se_2]^-$ (334 cm^{-1})[86] illustrates this difference. Consequently, while vibronic bands can be detected at room temperature in sulfur, lower temperatures are necessary to detect selenium ones.

Furthermore, sample with higher selenium concentration (Se/Cl=4.5) was also studied under the same conditions, with the emission spectra revealing a similar behavior, as illustrated in **Figure 3.13**. However, some differences are observed in the corresponding excitation spectra. At 77 K, the spectrum exhibits the main band of $[Se_2]^-$ at 490 nm and a second one with lower intensity at around 385 nm. This suggests a mixture involving the second band of $[Se_2]^-$ at 350 nm and the band at 400 nm associated with the NIR emission. At room temperature, the band at 400 nm becomes the majority, while the band at 490 nm is still observed.

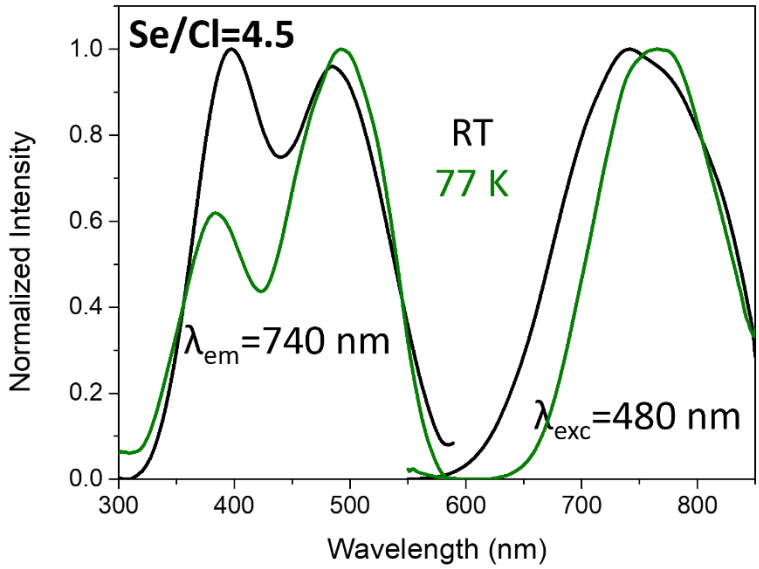


Figure 3.13 - Steady-state emission (λ_{exc}=480 nm) and excitation (λ_{em}=740 nm) spectra of sample Se/Cl=4.5 at room temperature (RT) represented in black and at 77 K represented in green.

Next, the time evolution of the emission characteristics of sample Se/Cl=4.5 was studied in more detail by acquiring the spectra at different time delays after excitation. (Section **7.2.5** contains additional information about the time-resolved emission spectroscopy - TRES - technique.) At short delay times, the produced spectra closely resemble the ones recorded in the steady-state, peaking at 755 nm at room temperature (**Figure 3.14.A**) and at 770 nm at 77 K (**Figure 3.14.B**). Once more, a spectra broadening is observed with temperature. Notably, the intensity of the spectra decreases similarly, regardless of the lower temperature used, contrary to initial expectations.

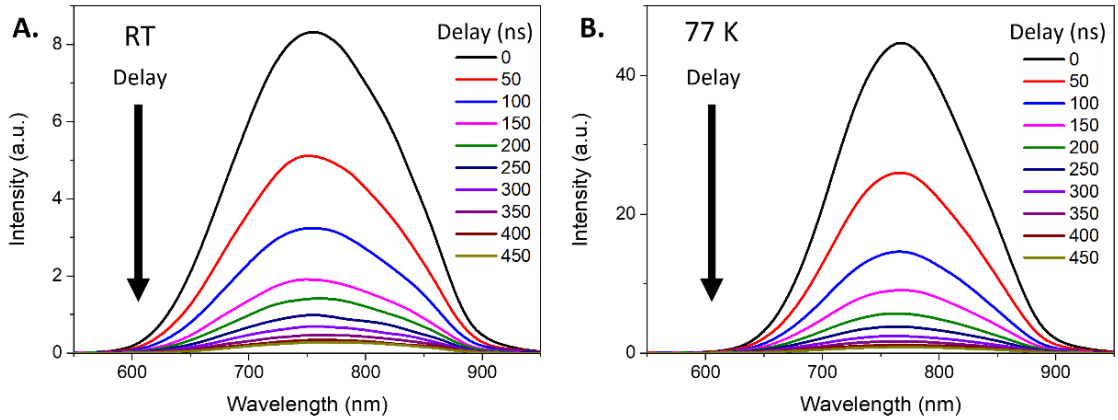


Figure 3.14 - Monitoring the disappearance of red emission of sample Se/Cl=4.5 through time-resolved measurements by varying the initial delay times in the nanosecond range, using an λ_{exc}=337 nm, at room temperature (RT) (**A**) and at 77 K (**B**).

A comprehensive study of the decay times was conducted to further investigate this effect by monitoring the emission at two different wavelengths, specifically at 650 nm and 800 nm. These wavelengths were selected since at 650 nm, the emission is low and experiences a significant reduction at 77 K, while at 800 nm, it is nearly at its maximum intensity at both temperatures (**Figure 3.15**).

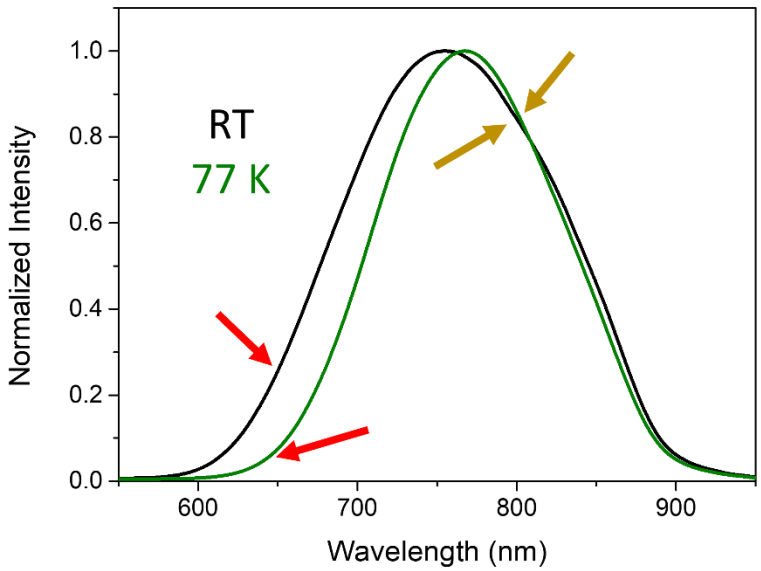


Figure 3.15 - Normalized time-resolved emission spectra without a delay time (delay=0 ns) of sample Se/Cl=4.5 at room temperature (RT) represented in black and at 77 K represented in green. The red and brown arrows indicate the two wavelengths at which the photoluminescence decays were recorded, as presented in **Figure 3.16** and **Figure 3.17**.

While monitoring the emission decay at 650 nm, two different decay times were observed: a fast one at 12 ns and a slow one at 78 ns. resulting in an average decay time of around 45 nanoseconds (**Figure 3.16**). Notably, no changes were found with temperature, as the decay components and average decay time remained consistent at 77 K and at room temperature.

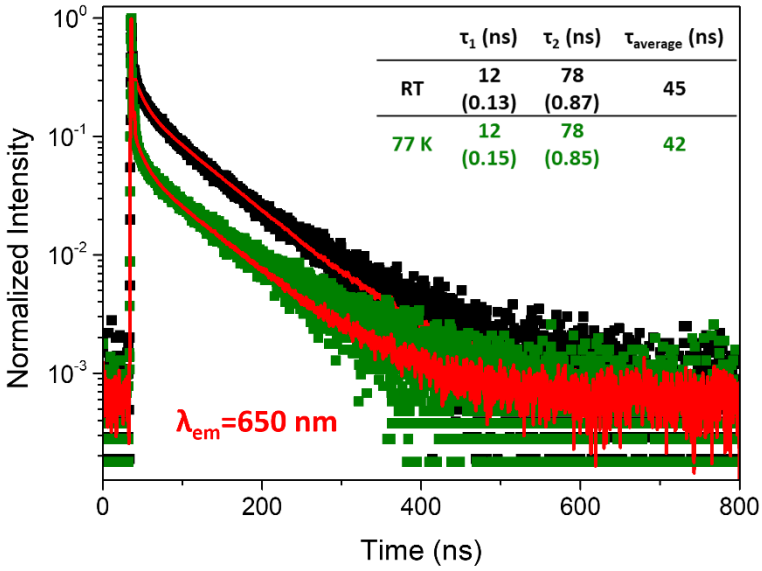


Figure 3.16 - Photoluminescence decay times of sample Se/Cl=4.5 at liquid nitrogen temperature (77 K) and at room temperature (RT) monitoring the emission at 650 nm. The insets show the components resulting from the decay fittings (see the resulting residuals in **Figure B.3**) and the average decay time. In brackets is the relative amplitude of each component. Note that the average decay times were calculated using the pre-exponential factors.

Following the emission at 800 nm, similar decay components were observed: a fast one of 19 ns and a slow one of 87 ns, regardless of the temperature (**Figure 3.17**). However, as the temperature increased, there was a slight change in the relative amplitudes of these decay components, leading to a more bi-exponential behavior and a faster average decay time, changing from 68 to 56 nanoseconds. The same behavior was found in sulfur-doped zeolites, with these differences assigned to more homogeneous local environments of the emitting species at 77 K.

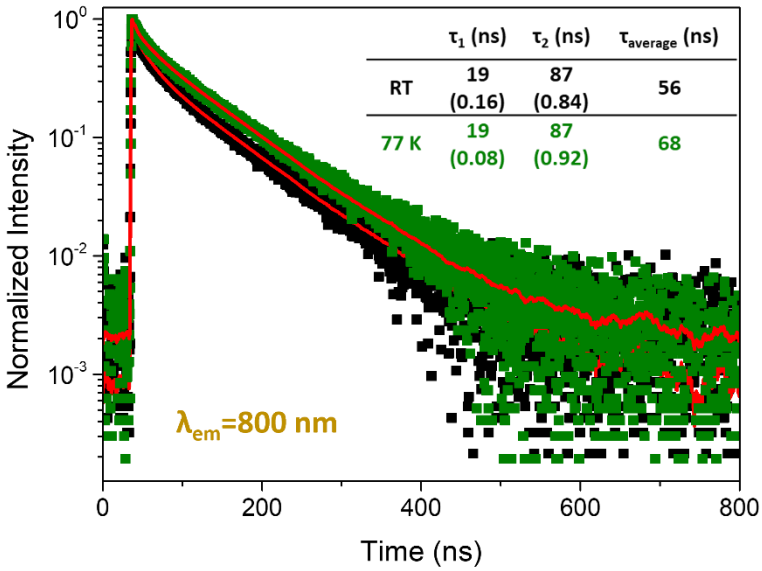


Figure 3.17 - Photoluminescence decay times of sample Se/Cl=4.5 at liquid nitrogen temperature (77 K) and at room temperature (RT) monitoring the emission at 800 nm. The insets show the components resulting from the decay fittings (see the resulting residuals in **Figure B.3**) and the average decay time. In brackets is the relative amplitude of each component. Note that the average decay times were calculated using the pre-exponential factors.

In summary, this study suggests that this red emission is sensitive to temperature, as evidenced by a broadening of the emission spectrum and variations in decay times.

Further measurements indicate that this emission is unaffected by oxygen and humidity/water, presenting a similar behavior to sulfur NIR emission (see sections **7.5** and **7.6**). This may be attributed to the confinement of the emissive clusters within the zeolite matrix, which protects these species from environmental factors.

Overall, this section provides important insights into the red emission of selenium-doped zeolites. It represents the first study relating the impact of different selenium loading in this emission and its photophysical properties. Analysis of emission and excitation spectra revealed a decrease in intensity with concentration. The differences observed in external quantum efficiencies and photoluminescence decay times further confirmed this quenching effect.

3.5 NIR emission

Similarly to the analysis conducted for the $[Se_2]^-$ emission, this section will investigate this novel NIR emission. According to the optical characterization conducted in sections **3.2** and **3.3**, the selenium-absorbing species at 400 nm seems to be responsible for this emission (peaking at around 800 nm). Based on this information, further photophysical characterization was

conducted, involving the measurement of external quantum efficiencies (EQE) and photoluminescence decay times.

The EQE values of these samples were measured, exciting the samples at 400 nm, however, at this wavelength, a significant contribution from the red emission is still observed, as evidenced in **Figure 3.18.B**. This may result in a high inaccuracy in calculating the EQE values using the full signal resulting from the emission spectra. Therefore, an approximation excluding the red emission was used, resulting in the EQE values present in **Figure 3.18.A** and summarized in **Table 3.3**. These values do not vary according to the Se/Cl ratios, considering the approximations used, with an average value of 6%. (The calculation method is explained in section **7.4**.)

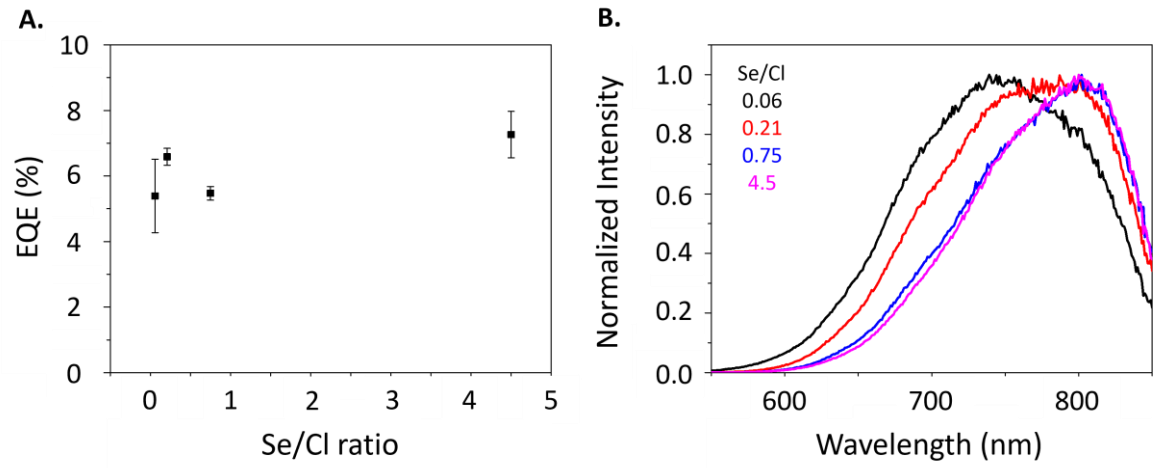


Figure 3.18 - (**A**) External quantum efficiencies of samples with different Se/Cl ratios, using a 400 nm excitation. (**B**) Normalized emission spectra of all synthesized samples, exciting at 400 nm (**Figure 3.7.A** normalized).

Furthermore, the photoluminescence decay times reveal the presence of long-lived emissive species decaying in the microsecond timescale. This contrasts with the short-lived $[Se_2]^-$ clusters responsible for the red emission, which exhibit lifetimes on the order of nanoseconds. The decay times were fitted with a bi-exponential function, fixing the fast decay component of 40 µs, with the slow component varying from 110 to 78 µs with the Se/Cl ratio, resulting in average decay times from 75 to 56 microseconds when comparing all synthesized samples (**Figure 3.19** and **Table 3.3**).

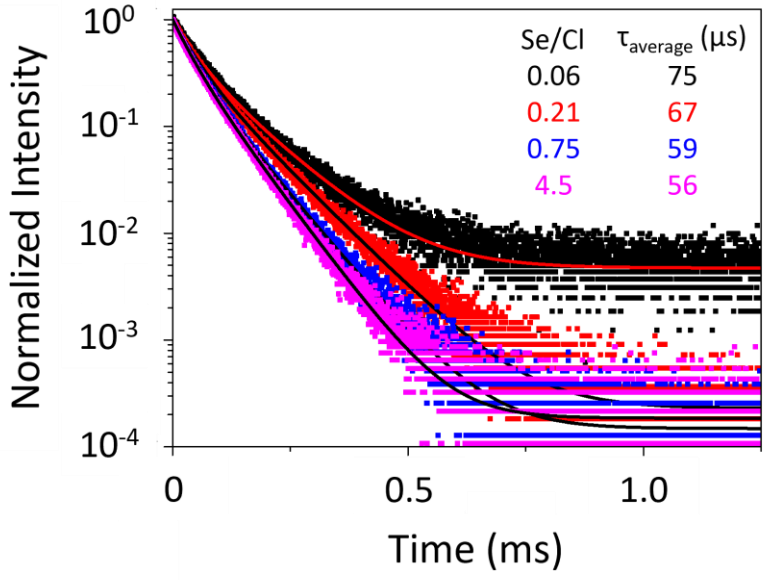


Figure 3.19 - Photoluminescence decay times (scatter) and respective fittings (solid line) of samples with different Se/Cl ratios, recorded with an λ_{exc}=400 nm and λ_{em}=800 nm. See residuals of the fittings in **Figure B.4**.

Notably, the species present in sample Se/Cl=0.06 (depicted in black, **Figure 3.19**) seem to not be fully decayed, showing an intensity approximately 100 times higher than the other samples. This may be due to the presence of sulfur NIR-emitting impurities. These sulfur species display slower decay components (approximately 270 and 670 μs) and are present in the blank sample (Se/Cl=0), as illustrated in the time-resolved emission spectroscopy (TRES) measurements shown in **Figure B.5**. Low concentrations of sulfur were detected in commercial Na-LTA zeolite reagent (**Table A.1.2**), meaning that all synthesized samples must have a sulfur contamination. However, the resulting emission of this impurity was only detected in sample Se/Cl=0.06. This could be attributed to the low intensity of the selenium NIR emission in this particular sample, making the presence of sulfur impurities stand out.

The emission spectra of these selenium-doped samples, acquired exciting the NIR species at 400 nm (**Figure 3.7.A**, with corresponding normalized spectra illustrated in **Figure 3.18.B**) were deconvoluted into the red (**Figure 3.20.A**) and NIR (**Figure 3.20.B**) emissions. The intensity of this selenium NIR emission demonstrates an increase with the Se/Cl ratio, further supporting the previous observation made for the sample Se/Cl=0.06.

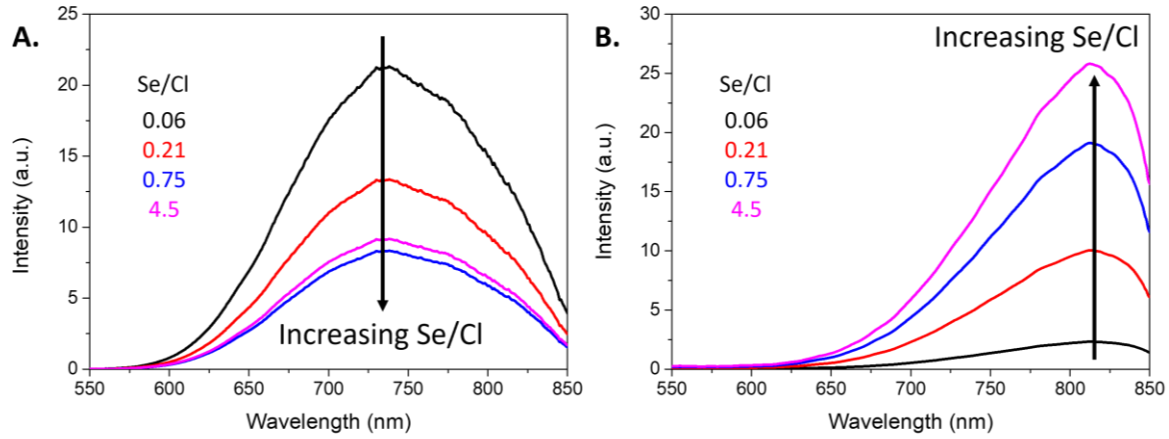


Figure 3.20 - Spectra deconvolution of the emission steady-state present in **Figure 3.7.A** of red emission (**A**) and NIR emission (**B**).

Table 3.3 summarizes the external quantum efficiencies and photoluminescence decay times of this NIR emission. Significant differences were only detected in the decay times, which decreased slightly with Se/Cl ratios. To better understand the processes responsible for these differences, radiative (k_r) and non-radiative (k_{nr}) 'averaged' constants were calculated using the equations (**3.3**) and (**3.4**), respectively. Both constants increase according with selenium loading (**Table 3.3**), with non-radiative 'averaged' constants showing values *ca.* 100 times higher. This behavior contrasts with that observed in red emission, however, some form of energy transfer may also occur here, increasing the non-radiative pathways.

Table 3.3 - External quantum efficiencies (EQEs), photoluminescence decay times with their respective components and amplitudes, alongside average decay times and corresponding radiative (k_r) and non-radiative (k_{nr}) 'averaged' constants of the NIR emission.

Nominal Se/Cl	EQE (%) at 400 nm	τ_1 (µs)	Relative amplitude (A_1)	τ_2 (µs)	Relative amplitude (A_2)	$\tau_{average}$ (µs)*	$k_{r\ (Av.)}$ (s^{-1}) x10^2	$k_{nr\ (Av.)}$ (s^{-1}) x10^4
0.06	5	40	0.26	110	0.74	75	7.17	1.26
0.21	7	40	0.32	100	0.68	67	9.78	1.39
0.75	6	40	0.40	85	0.60	59	9.34	1.61
4.5	7	40	0.40	78	0.60	56	12.89	1.65

*Values calculated using the pre-exponential factors.

Next, this novel NIR emission will be investigated at lower temperatures to assess its potential temperature sensitivity.

3.5.1 Temperature studies

In this section, the photophysical properties of this NIR emission were characterized at liquid nitrogen temperature (77 K) following the same approach as in the red emission. The steady-state of the sample with Se/Cl=4.5 demonstrated differences in emission and excitation spectra when comparing the results at 77 K and at room temperature (RT). A broadening in the emission spectra was detected when increasing the temperature, as illustrated in **Figure 3.21**. Furthermore, the corresponding excitation spectrum exhibited a slight increase in the contribution of $[Se_2]^-$ species, characterized by the band at around 490 nm. This latter evidence can be due to a lesser selectivity of the NIR emission when monitoring it (λ_{em}=800 nm) at room temperature.

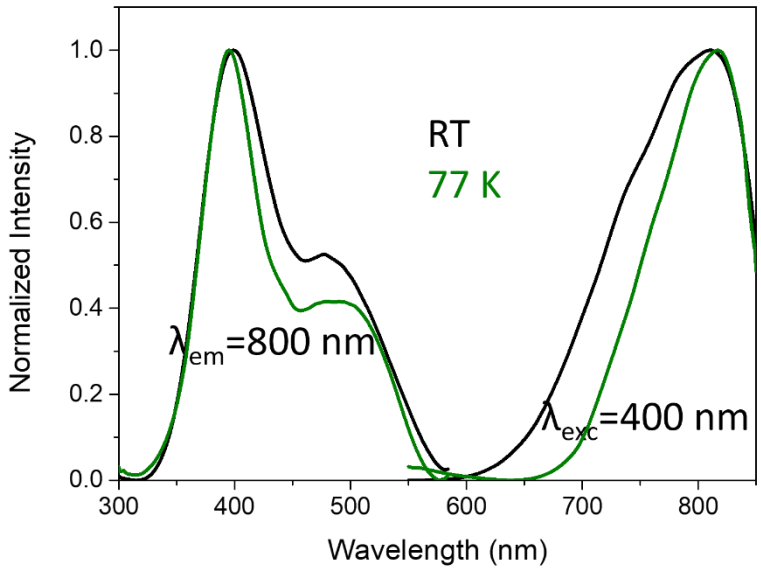


Figure 3.21 - Steady-state emission (λ_{exc}=400 nm) and excitation (λ_{em}=800 nm) spectra of sample Se/Cl=4.5 at room temperature (RT) represented in black and at 77 K represented in green.

Time-resolved emission spectroscopy measurements, applying longer delay times than those used in monitoring the red emission discussed in section **3.4** (see **Figure 3.14**), enable for the detection of this NIR emission. By incrementally extending the delay times, it becomes possible to observe a decrease in the predominance of fluorescence originating from $[Se_2]^-$ clusters (**Figure 3.22.A-B**). Notably, temperature-dependent differences were noted, with the

NIR emission becoming detectable at longer delay times at 77 K compared to room temperature. This phenomenon is assigned to the slower photoluminescence decay times found in $[Se_2]^-$ clusters at 77 K (section **3.4**, **Figure 3.17**).

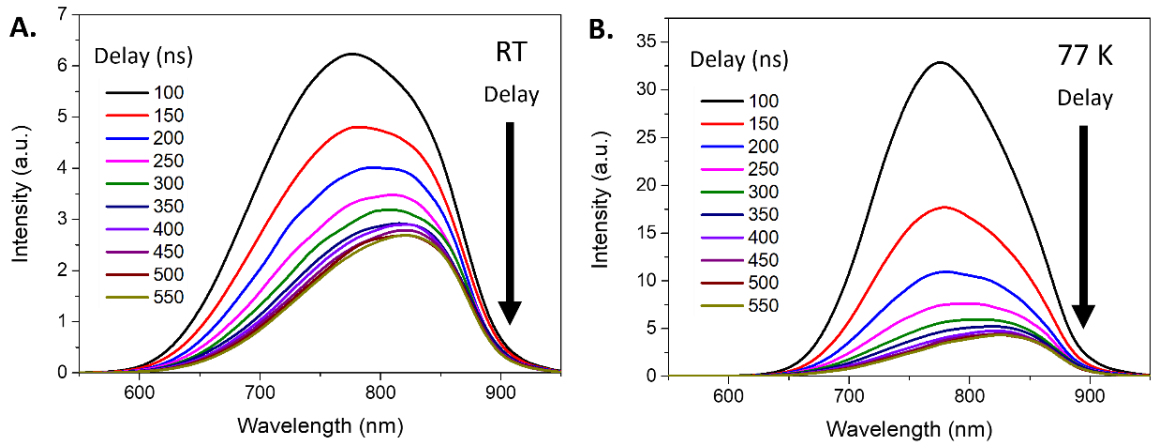


Figure 3.22 - Monitoring the disappearance of red emission and appearance of NIR emission of sample Se/Cl =4.5 through time-resolved measurements by varying the initial delay times (nanoseconds), using an λ_{exc}=337 nm, at room temperature (RT) (**A**) and at 77 K (**B**).

This NIR emission becomes then fully evident when longer starting delays are employed (**Figure 3.23.A-B**). Under these conditions, these species seem to decay similarly at both temperatures.

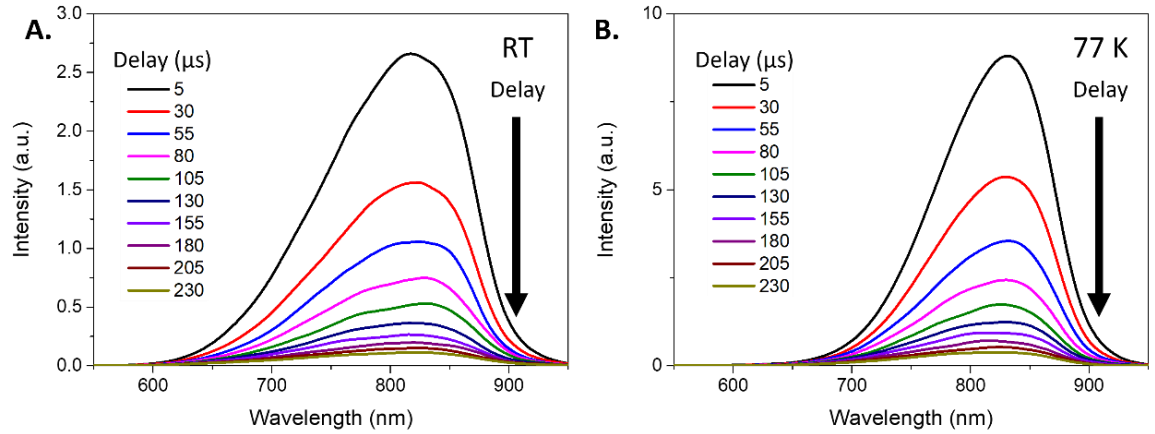


Figure 3.23 - Monitoring the disappearance of the NIR emission of sample Se/Cl =4.5 through time-resolved measurements by varying the initial delay times (microseconds), using an λ_{exc}=337 nm, at room temperature (RT) (**A**) and at 77 K (**B**).

Additionally, consistent with the steady-state experiments conducted on these species (**Figure 3.21**), the TRES spectra broaden with increasing temperature, as evidenced in **Figure 3.24**. Similar behavior was also observed and discussed in the sulfur NIR-emitting species (**Figure 2.3.16**, subchapter **2.3**) and in the selenium red emission (**Figure 3.15**).

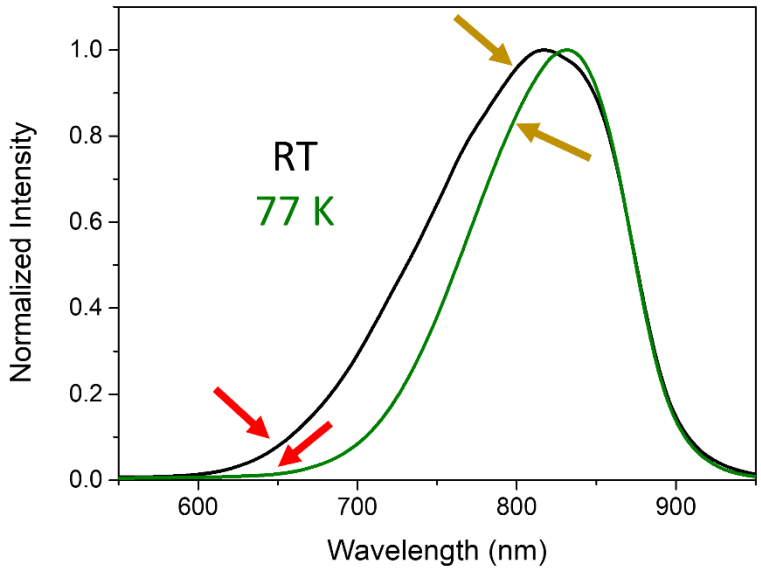


Figure 3.24 - Normalized time-resolved emission spectra after applying 5 microseconds delay time (delay=5 µs) of sample Se/Cl=4.5 at room temperature (RT) represented in black and at 77 K represented in green. The red and brown arrows indicate the two wavelengths at which the photoluminescence decays were recorded, as presented in **Figure 3.25** and **Figure 3.26**.

To better understand these spectral differences, the photoluminescence decay times were studied. The emission at 650 nm and 800 nm was monitored at 77 K and room temperature. Following the emission at 650 nm (**Figure 3.25**), two decay components were identified at 77 K: a fast one of 64 µs and a slow one at 160 µs, resulting in an average decay time of 109 microseconds. However, with increasing temperature, two faster decay components were observed: a fast one of 34 µs and a slow one at 77 µs, leading to a much faster average decay time of 54 microseconds. This bi-exponential behavior was already found in chalcogen-doped zeolites and was assigned to the presence of two different local environments of the emitters. Similarly, the differences with temperature were attributed to a decrease in non-radiative mechanisms at lower temperatures, probably due to the reduction of molecule rotations and/or vibrations.

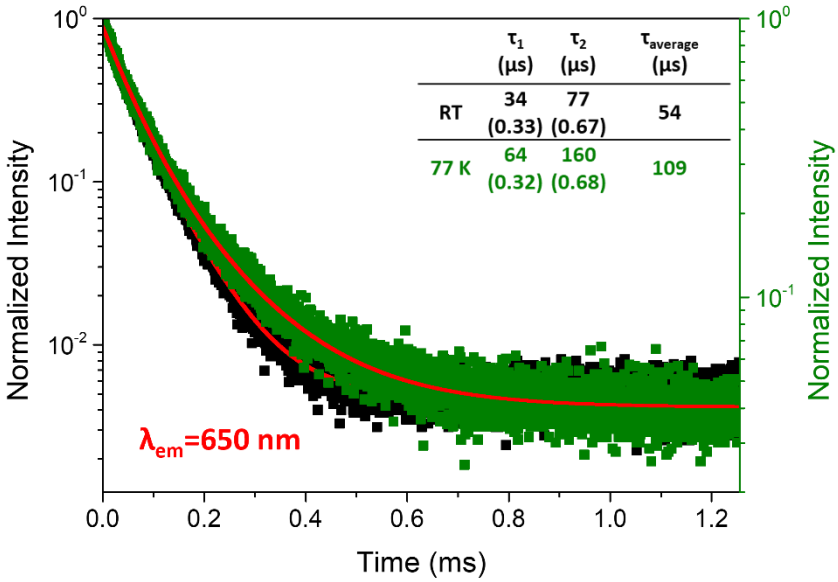


Figure 3.25 - Photoluminescence decay times of sample Se/Cl=4.5 at liquid nitrogen temperature (77 K) and at room temperature (RT) monitoring the emission at 650 nm. The insets show the components resulting from the decay fittings (see the resulting residuals in **Figure B.6**) and the average decay time. In brackets is the relative amplitude of each component. Note that the average decay times were calculated using the pre-exponential factors.

Additionally, while monitoring the emission at 800 nm (**Figure 3.26**), the same decay components were observed to those at 650 nm. However, a notable distinction arises in the relative amplitudes of these components at 77 K, where the fast component (64 μs) predominates over the slow one (160 μs). Nevertheless, this still results in a slower decay time at lower temperatures.

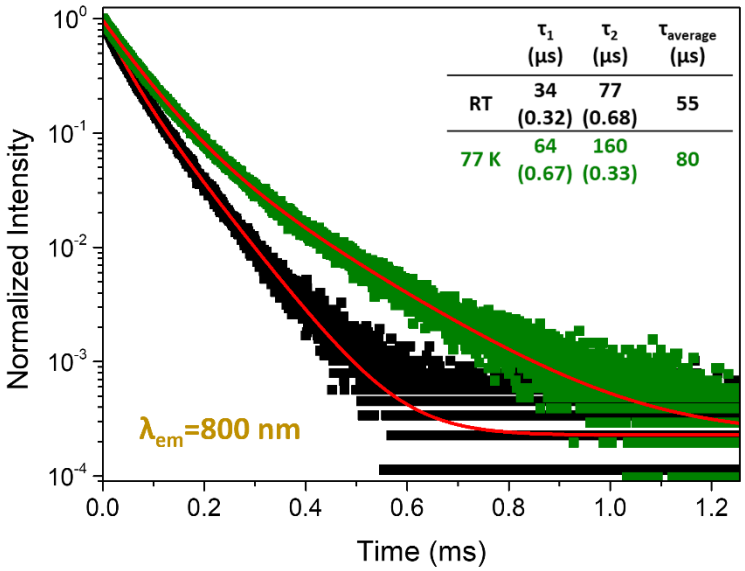


Figure 3.26 - Photoluminescence decay times of sample Se/Cl=4.5 at liquid nitrogen temperature (77 K) and at room temperature (RT) monitoring the emission at 800 nm. The insets show the components resulting from the decay fittings (see the resulting residuals in **Figure B.6**) and the average decay time. In brackets is the relative amplitude of each component. Note that the average decay times were calculated using the pre-exponential factors.

In summary, it was possible to conclude that this emission varies with temperature, resulting in a broader emission spectra and faster decay at higher temperatures.

Further experiments demonstrate that the NIR emission once again is not affected by oxygen and humidity/water (see sections **7.5** and **7.6**), with a behavior consistent with sulfur NIR emission and selenium red emission.

Overall, this section significantly contributes to the existing literature by comprehensively characterizing the photophysical properties of this novel NIR emission. Previous studies on selenium-doped KI crystals had only reported the absorption spectra of these species[87], leaving their identification unclear. The following section will delve deeper into this aspect, giving additional insights into the nature of these NIR-emitting species.

3.6 NIR-emitting species and their location in the aluminosilicate matrix

To better understand the responsible species for this NIR emission and considering the lack of available information in the literature, the first approach involved comparing these samples with the sulfur-doped zeolites discussed in chapter **2**. Notably, these systems exhibit several

similarities. Starting with the diatomic radical species, $[S_2]^-$ and $[Se_2]^-$, both characterized by nanosecond lifetimes and association with sodalite zeolite. In contrast, the NIR-emitting species (detected at higher chalcogen loadings) display long-lived emissions in the microsecond timescale and appear to be related with the nepheline and carnegieite structures. Further analysis assigned the sulfur NIR-emitting species to phosphorescence from $[S_3]^{2-}$ clusters. Consequently, based on the resemblances, it is inferred that triplet states from $[Se_3]^{2-}$ species may be involved in the selenium NIR emission. Electronic paramagnetic resonance (EPR) spectroscopy and theoretical calculations were used to assess this hypothesis.

In EPR spectroscopy, all synthesized selenium-doped samples were analyzed, revealing a dependence on temperature and selenium concentration. (Refer to section **7.2.7** for additional information about this technique.) The sample with Se/Cl=0.06 proved important for understanding this system. As illustrated in **Figure 3.27**, the EPR spectrum of this sample recorded at 150 K exhibits a single quasi-isotropic EPR signal. However, a new rhombic signal is detected when cooling the sample from 120 K to 30 K.

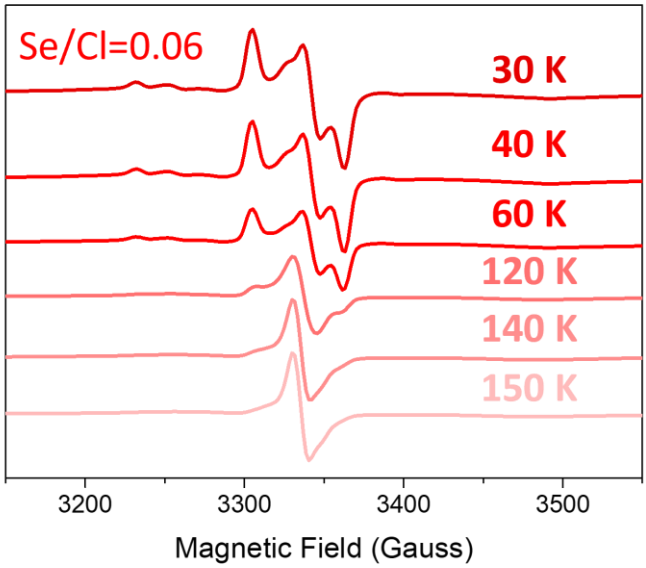


Figure 3.27 - Electronic paramagnetic resonance (EPR) spectra of sample Se/Cl=0.06 recorded at different temperatures from 150 K to 30 K.

Such observations suggest the presence of at least two different selenium paramagnetic species in this sample. Additionally, these species show different relaxation temperatures, with one remaining stable at 150 K, while the other is detectable only at temperatures lower than 120 K. This means that one of the signals can be easily isolated at higher temperatures.

When increasing the selenium loading, significant changes were detected in the EPR signal recorded at 150 K in samples Se/Cl=0.21 and 0.75 (**Figure 3.28.A-B**). As depicted in **Figure 3.30.A** below, this phenomenon is attributed to a decrease in signal intensity. Consequently, the spectra acquired at lower temperatures are also affected, leading to differences in signal relative intensities.

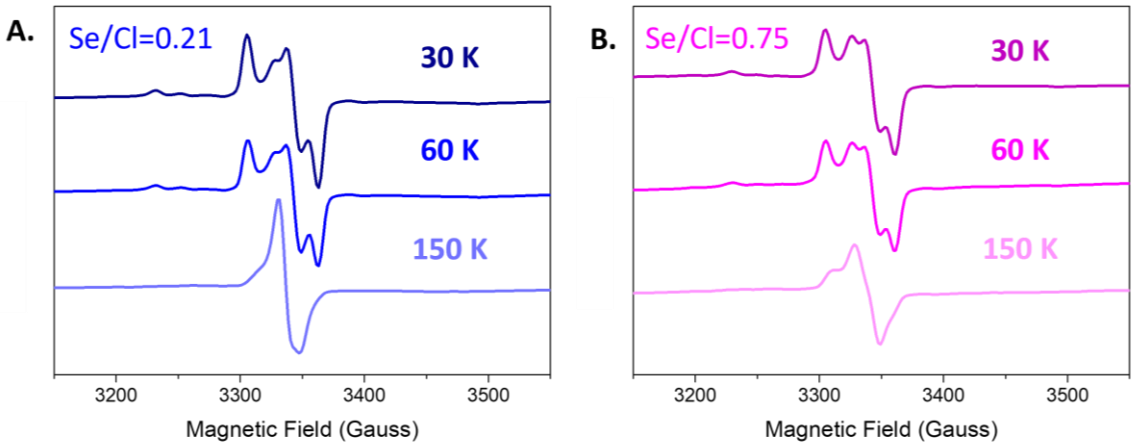


Figure 3.28 - Electronic paramagnetic resonance (EPR) spectra of samples Se/Cl=0.21 (**A**) and Se/Cl=0.75 (**B**) recorded at different temperatures from 150 K to 30 K.

These differences become even more evident in the sample with a higher Se/Cl ratio, where the presence of this radical is practically nonexistent at 150 K (**Figure 3.29.A**). The signals observed in this sample are entirely distinct from those found in sample Se/Cl=0.06 (**Figure 3.27**). However, they closely resemble those detected in the blank sample Se/Cl=0 (**Figure 3.29.B**), which, as previously discussed, contains sulfur impurities from Na-LTA zeolite. The signals found in this latter sample were assigned to a combination of $[S_2]^-$ and $[SO_2]^-$ species (see **Figure 2.3.9** and **Table 2.3.2** of section **2.3**). This indicates that small traces of sulfur paramagnetic species are present in all synthesized samples.

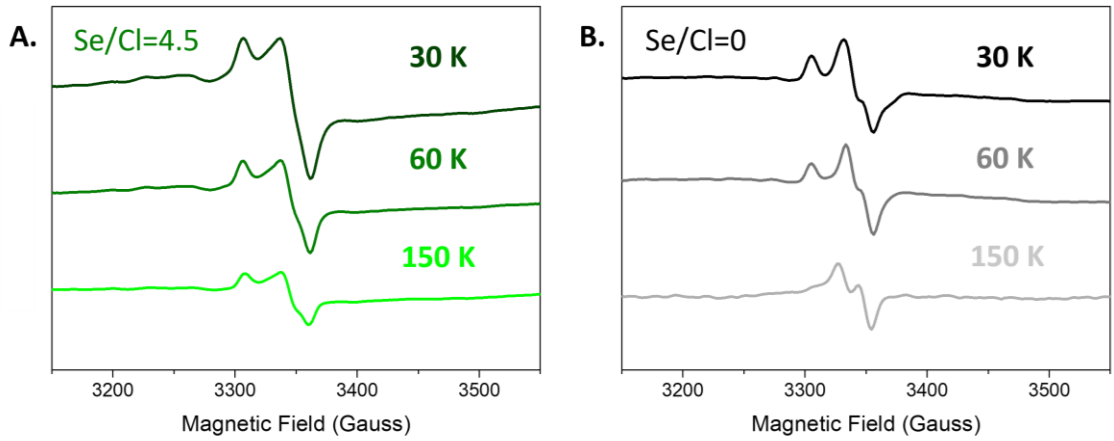


Figure 3.29 - Electronic paramagnetic resonance (EPR) spectra of samples Se/Cl=4.5 (**A**) and Se/Cl=0 (**B**) recorded at different temperatures from 150 K to 30 K.

A comparison of all signals recorded at 150 K (**Figure 3.30.A**) reveals a decrease in EPR signal intensity according to the increase in selenium loading, with Se/Cl ratios of 0.06>0.21>0.75 (**Figure 3.30.B**). Moreover, the intensities of samples Se/Cl=0 and 4.5 are similar, suggesting a comparable amount of paramagnetic species in sample Se/Cl=4.5 as in the blank sample.

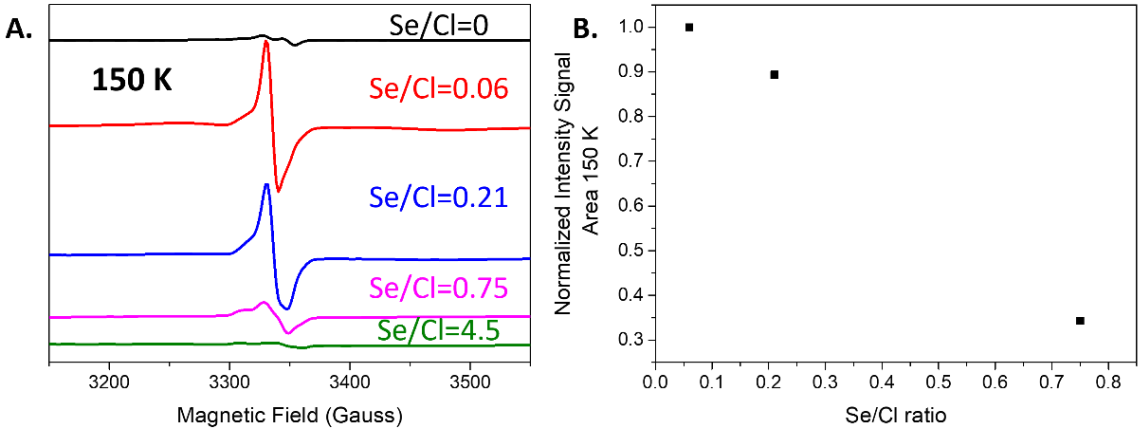


Figure 3.30 - (**A**) Comparison of all EPR signals recorded at 150 K (**B**) alongside their corresponding normalized signal areas. Note that the signals from samples Se/Cl=0 and 4.5 were not considered since their intensities are minimal.

The temperature-dependence studies demonstrated that the optimal detection temperature is 30 K, as both paramagnetic signals are observed. Lower temperatures were also tested, revealing a decrease in intensity due to EPR signal saturation. **Figure 3.31.A** summarizes the

signals acquired at this temperature for all synthesized samples. Upon subtracting the corresponding resonances detected at 150 K, a decrease in signal intensities was once again observed with increasing selenium loading (**Figure 3.31.B**). Furthermore, the signal intensity and shape of sample Se/Cl=4.5 once again resemble those detected in blank sample Se/Cl=0.

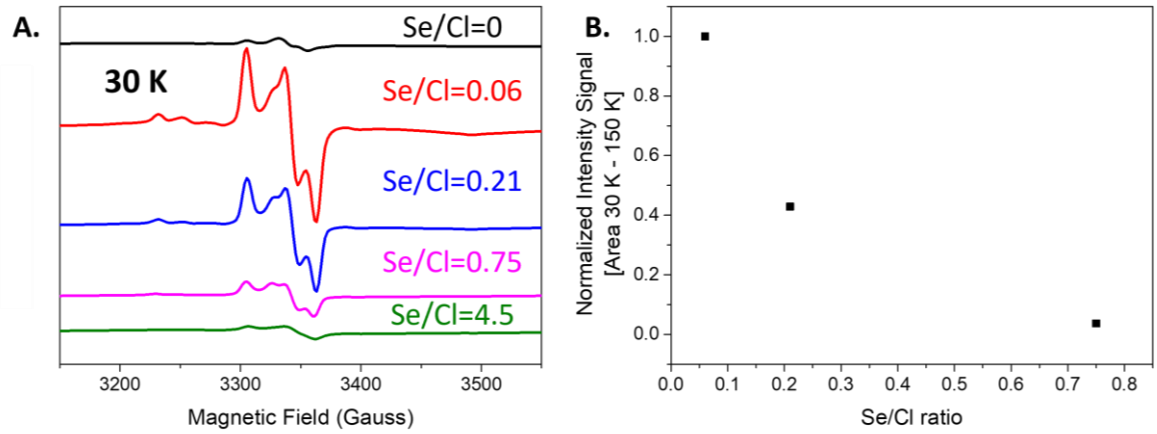


Figure 3.31 - (**A**) Comparison of all EPR signals recorded at 30 K (**B**) alongside their corresponding normalized signal areas with the resonance at 150 K subtracted. Note that the signals from samples Se/Cl=0 and 4.5 were not considered since their intensities are minimal.

Overall, at least two different selenium EPR active species were identified. One species (species A) was observed at lower temperatures from 120 K to 30 K. The second one (species B) was detected at all temperatures measured and was observed isolated at 150 K. The g-values corresponding to these species were obtained by theoretical simulation and are summarized in **Table 3.4** for samples with Se/Cl=0.06, 0.21, and 0.75. **Figure B.7** compares the experimental and simulated EPR spectra of sample Se/Cl=0.06 (which exhibits the highest EPR signal intensities).

Similar g-iso values (average g-values) of around 2.012 were calculated for both simulated species (**Table 3.4**). This similarity does not exclude the possibility that the same species in two different environments may be present, giving rise to two different EPR signals with the same g-iso values. Relating again sulfur to selenium, Kowalak et al.[113] demonstrated that in sulfur-doped zeolites, $[S_3]^-$ species may exhibit two distinct local environments when confined within these materials - one isotropic and another rhombic - each showing different relaxation temperatures. Both environments were also detected in the produced sulfur samples in **Table 2.3.2**, subchapter **2.3**.

Further simulations performed in the EPR spectra acquired at 30 K demonstrated similar relative contributions of species A and B in these three synthesized samples. Species A has a major contribution of ~75%, while species B contributes around ~25% (**Table 3.4**).

Table 3.4 - g-values and corresponding g-iso values (average g-values) of the two selenium EPR active species detected in the samples Se/Cl=0.06, 0.21 and 0.75. Species A is observed at lower temperatures, while species B is detected from 150 K. The EPR simulated spectra are illustrated in **Figure B.7**. The relative contributions of both species were calculated in the spectra recorded at 30 K for all synthesized samples.

Nominal Se/Cl ratio	Selenium EPR active species	g_1	g_2	g_3	g_{iso}	Relative contribution at 30 K (%)
0.06	A	1.998	2.010	2.034	2.014	75
	B	2.003	2.015	2.015	2.011	25
0.21	A	1.997	2.008	2.032	2.012	75
	B	2.004	2.014	2.014	2.011	25
0.75	A	1.997	2.009	2.032	2.013	70
	B	2.004	2.014	2.014	2.011	30

Although the literature on EPR active selenium species is quite limited, selenium analogs of the three species previously observed using EPR spectroscopy in sulfur-doped zeolites (as listed in **Table 2.3.2**, section **2.3**) - namely, $[Se_2]^-$, $[SeO_2]^-$ and $[Se_3]^-$ radicals - have been identified in selenium-doped crystals[114,128]. Unfortunately, given that these characterizations were made in single crystals (aligned with specific crystalline planes) and not in polycrystalline samples, such as these produced zeolites, a direct signal comparison was not possible.

Previously discussed optical characterization only confirmed the presence of $[Se_2]^-$ clusters. Furthermore, $[Se_3]^-$ clusters were discarded since, as noted by Reinen et al.[78], they have never been identified in sodalite zeolite, with their expected absorption occurring around 800 nm. The obtained absorption spectra of these samples do not exhibit bands in this spectral zone (**Figure 3.2**), making their presence unlikely. Another possibility is that the absorbing species responsible for the NIR emission may not be $[Se_3]^{2-}$ as inferred from sulfur systems, but rather another EPR active species. However, according to the simulations conducted in the diffuse reflectance spectra (**Figure 3.3.A-B**), the ratios of the absorption areas between NIR-emitting species and the $[Se_2]^-$ clusters constantly increase with the Se/Cl ratios, contrasting with the behavior found in the simulated species A and B, according to the **Table 3.4**. In summary, the most straightforward explanation for these EPR findings is the presence of two local

environments of $[Se_2]^-$ clusters. This can be attributed to $[Se_2]^-$ being coordinated in both a tetrahedral $[Na_4]^{4+}$ and a trigonal $[Na_3]^{3+}$ environment. This hypothesis was previously explored in photoluminescence decay times of $[Se_2]^-$ emission (**Figure 3.9**), where these two coordination environments were used to explain the bi-exponential behavior of this emission. It is important to note that the experimental findings leading Schlaich et al.[86] to suggest the presence of two different environments of selenium inside sodalite zeolites were based on detecting two vibronic progressions of $[Se_2]^-$ emission. However, detecting such phenomena only occurs at extremely low temperatures, i.e., below 10 K. Therefore, it is not expected that an absorption spectrum acquired at room temperature would reflect the presence of these two environments.

In addition, the increase in chromophore formation observed in diffuse reflectance spectroscopy (**Figure 3.2**) contrasts with the EPR findings. This is especially evident since at least one of these chromophores, i.e., $[Se_2]^-$ clusters, is EPR active. Therefore, the decrease in the EPR signals' intensity at 30 K and 150 K, with the increase of the Se/Cl ratio, can indicate the presence of an antiferromagnetic coupling between two paramagnetic species. This phenomenon is characterized by the antiparallel coupling of the two S=1/2 spins, resulting in a diamagnetic S=0 ground state, thus resulting in a system that is not EPR active.

Sodalite zeolite can exhibit an antiferromagnetic coupling between F-centers (electrons situated within the β-cages)[129,130]. This mechanism may occur due to interactions between F-centers situated in adjacent cages. Therefore, the model suggested in **Figure 3.10**, section **3.4**, to explain the quenching of red emission due to close proximity with different $[Se_2]^-$ species within sodalite zeolite might explain these results. By increasing the selenium loading, more radicals will be closer to each other, promoting this coupling and decreasing the EPR intensity. These $[Se_2]^-$ radicals should be located in the same position as the mentioned F-centers, with distances around 9 Å.

In contrast, since the absorbing species responsible for the NIR emission are associated with nepheline and carnegieite structures, even if they are EPR active, they are not expected to cause this coupling effect due to their distance.

Further characterization to understand the responsible species for the NIR emission involved TD-DFT theoretical calculations. (See section **7.2.16** for additional information about these calculations.) The absorption spectra of several selenium species were simulated and compared with the experimental data. These species were selected based on their size since, typically, small molecules are found in these aluminosilicates. Therefore, $[Se_2]^-$, $[Se_2]^{2-}$, $[Se_3]^-$ (C_{2v}) and $[Se_3]^{2-}$ (C_{2v}) and $[Se_4]^{2-}$ (C_{3v}) clusters were found to be suitable molecules. However, only the last two mentioned species were considered in this study. $[Se_2]^-$ was excluded since its

presence was confirmed by diffuse reflectance and emission spectroscopies. Additionally, both $[Se_2]^{2-}$ and $[Se_3]^{-}$ (C_{2v}) were dismissed since their optical properties were not detected in the produced selenium-doped samples[78,80]. Despite this, the simulated absorption spectra of $[Se_3]^{2-}$ (C_{2v}) and of $[Se_4]^{2-}$ (C_{3v}) did not match the experimental data, as illustrated in **Figure 3.32.A** and **Figure 3.32.B**, respectively.

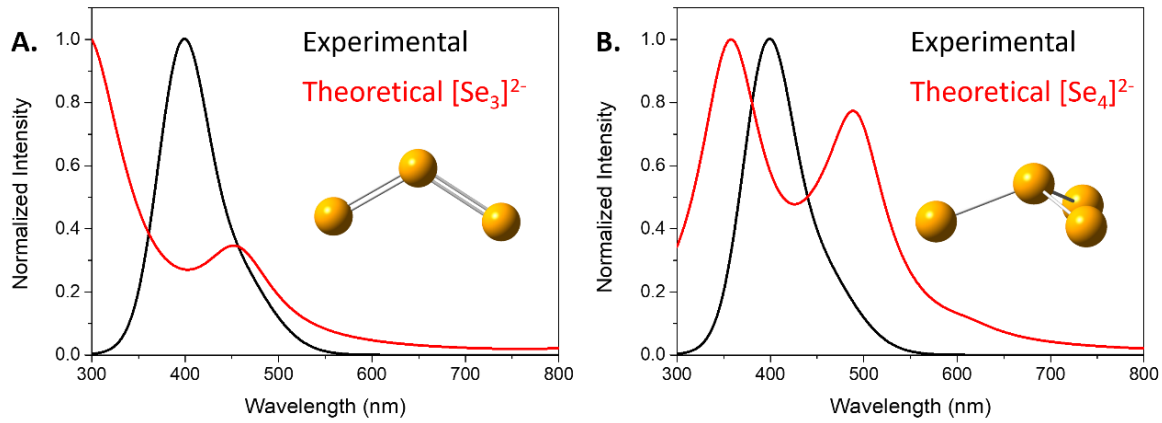


Figure 3.32 - Comparison between the experimental absorption of the NIR emitters and the simulated absorption spectra of $[Se_3]^{2-}$ (**A**) and $[Se_4]^{2-}$ (**B**) species.

Despite these results, it is important to consider whether the theoretical bases used in these calculations (identical to those for sulfur) are the most suitable before excluding these species as responsible for the absorption at 400 nm and NIR emission. Note that as the simulated element becomes heavier, the calculations become increasingly complex. Utilizing conditions identical to those in the sulfur system might introduce inaccuracies in the calculations, especially when dealing with heavier elements like selenium.

In summary, neither EPR spectroscopy nor theoretical calculations could conclusively demonstrate whether $[Se_3]^{2-}$ species or another polyselenide species were responsible for the NIR emission, nor could they dismiss these possibilities. Therefore, given the lack of further information and drawing from knowledge gained in the sulfur system, they will be tentatively assigned to the $[Se_3]^{2-}$ species.

3.7 Applications of the NIR emitters

The materials produced were tested in two different proofs of concept: in anticounterfeiting and security tags and as NIR phosphor-converted LEDs (NIR pc-LEDs) for veins imaging.

To evaluate the suitability of selenium-doped zeolites in anticounterfeiting and security tags, three different mixtures were dispersed in a 10% polyvinyl alcohol in water solution (**Figure 3.33.A**). They were subsequently deposited in a quartz glass, forming an '8' pattern under ambient light (**Figure 3.33.B**). Upon 400 nm excitation, two distinct patterns emerge: '7' using a 495 nm cutoff filter (**Figure 3.33.C**) and '1' using an 800 nm cutoff filter (**Figure 3.33.D**). The sulfur-doped zeolites sample with S/Cl=0.06 (characterized in subchapter **2.3**) emits in a different spectral region from the selenium-doped zeolites, adding an extra layer of security. This allows for specific exclusion of sulfur-doped zeolites emission, detecting only the NIR emission when using an 800 nm cutoff filter (that filters all shorter wavelengths).

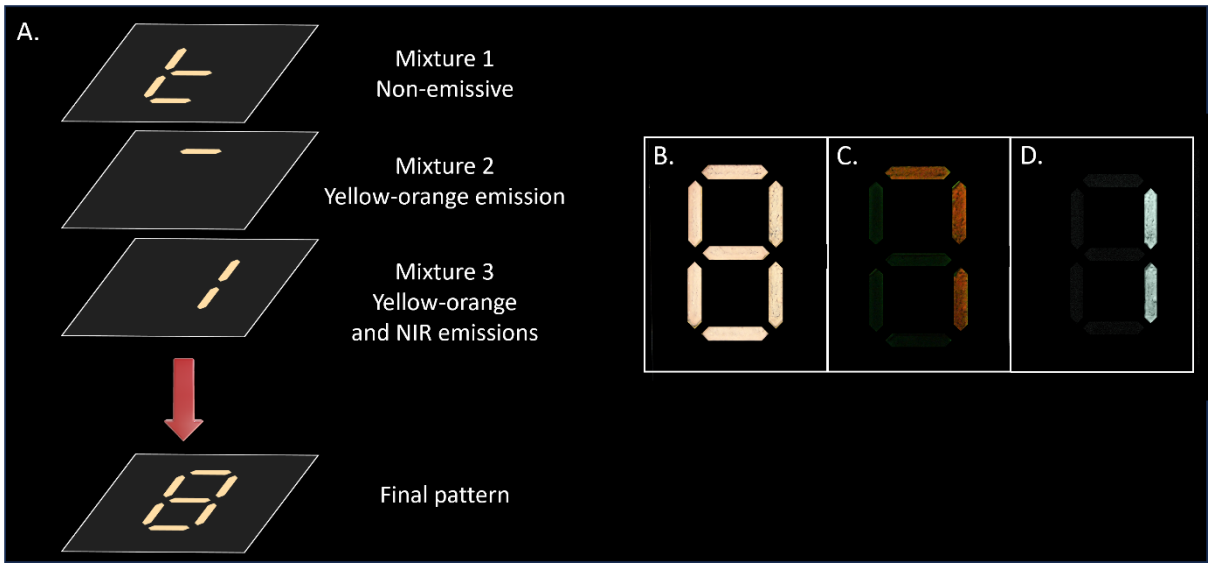


Figure 3.33 - Proof-of-concept of selenium-doped zeolites as anticounterfeiting and security tags – (**A**) Representation of the depositions using three different mixtures; mixture 1 (non-emissive) containing a Hematite mineral and a non-reduced sodalite sample; mixture 2 (yellow-orange emission) with a Hematite mineral and sulfur-doped zeolites (sample S/Cl=0.06, from subchapter **2.3**); mixture 3 (yellow-orange and NIR emission) containing sulfur-doped zeolites and selenium-doped zeolites (sample Se/Cl=4.5, from this subchapter). **(B**, **C**, **D)** Photographs were taken by a standard photographic camera under (**B**) ambient light and under **(C**, **D)** 400 nm excitation, applying a 495 nm and 800 nm cutoff filter, respectively.

These produced materials were also tested as NIR pc-LEDs in veins imaging. A commercial LED chip with a 400 nm excitation wavelength was coated with the Se/Cl=4.5 sample using an epoxy resin. Subsequently, the assembled phosphor-converted LEDs underwent testing for veins imaging. The experimental setup is schematically depicted in **Figure 3.34.A**, with fingers and hands covering the NIR pc-LED, while a standard photographic camera equipped with an infrared cutoff filter captured the resulting photographs in **Figure 3.34.B-C**, respectively.

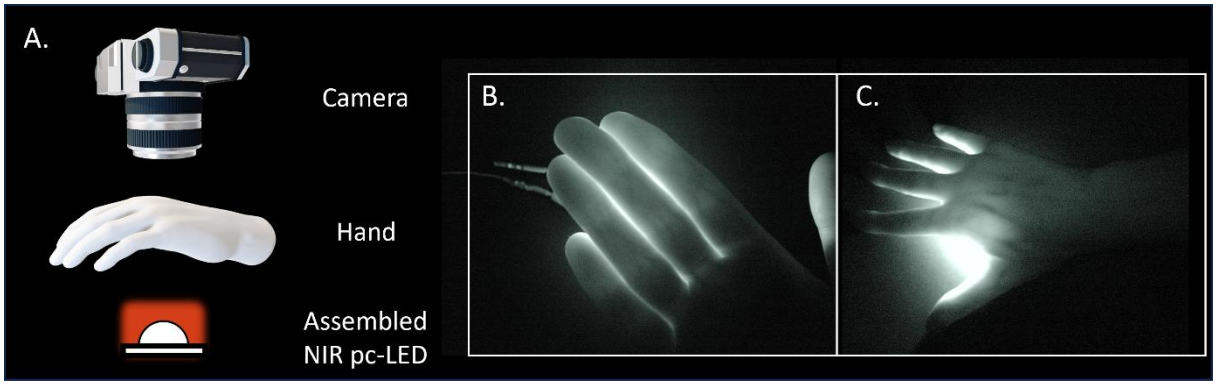


Figure 3.34 - **Proof-of-concept of selenium-doped zeolites as NIR pc-LEDs in veins imaging –** (**A**) Representation of the setup. (**B**, **C**) Veins photographs were taken by a standard photographic camera equipped with an infrared cutoff filter of (**B**) fingers and (**C**) hands.

3.8 Conclusions

This study significantly advances the understanding of selenium-doped zeolites, offering fundamental insights and exploring their practical applications. Two different emissive selenium species were observed:

1) $[Se_2]^-$, which absorbs at 350 and 490 nm and is responsible for the red emission centered at approximately 755 nm. These species are associated with sodalite zeolite, promoting its stabilization and preventing the formation of nepheline and carnegieite structures. Furthermore, emission quenching was observed, supported by decreasing external quantum efficiencies (EQEs) and photoluminescence decay times with Se/Cl ratios. Therefore, lower selenium loading demonstrated optimal values, with sample Se/Cl=0.06 displaying EQE of 23% and an average decay time of around 96 nanoseconds. This quenching phenomenon may be attributed to a double electron transfer mechanism, possibly due to close proximity between $[Se_2]^-$ clusters within different sodalite cages;

2) The second emissive species was tentatively assigned to $[Se_3]^{2-}$ clusters, absorbing at 400 nm and emitting in the NIR region around 820 nm. These new species were detected at higher Se/Cl ratios and are related with nepheline and carnegieite structures. Contrary to the red emission, no quenching effect was detected in this emission, with an EQE of 6% and an average decay of approximately 75 microseconds. However, presumably due to the stabilization effect of selenium in sodalite zeolite, single NIR-emitting samples were not produced. Thus, based on the knowledge gathered in this chapter and chapter **2**, two different methods are expected to promote such materials. The first involves using low selenium loadings without chloride, which is expected to form nepheline and carnegieite structures, lacking sodalite

zeolite. Conversely, ratios higher than Se/Cl=4.5 may induce complete quenching of the red emission, even in the presence of high amounts of sodalite zeolite. These hypotheses will be explored in the next chapter.

Additionally, two proofs of concept applications highlight the versatility of these selenium-doped zeolites in anticounterfeiting and security systems, as well as in NIR phosphor-converted LEDs for veins imaging. The ability to create complex, detectable patterns under visible light and specific circumstances emphasizes the potential of these materials for innovative security features. The successful integration of NIR phosphor-converted LEDs for veins imaging further highlights the real-world applicability of these synthesized zeolites. This non-invasive technology holds promise for enhancing medical diagnostics.

4

SELENIUM-DOPED EMITTING NANOZEOLITES

This chapter focuses on synthesizing nano-sized zeolites, aiming to replicate the near-infrared (NIR)-emitting properties discussed in the preceding chapters. In addition to the previously explored fields of photonics and sensing, nanoparticles offer potential for various other NIR applications, including *in vivo* imaging. Ranging typically from 1 to 100 nm (**Figure 4.1**), these materials exhibit enhanced surface areas that can significantly modify their properties compared to their bulk counterparts. Furthermore, their diverse shapes and morphologies, spanning from spheres to more complex structures such as rods, tubes and quantum dots, impact their physicochemical properties and functionalities. For example, spherical nanoparticles typically offer greater stability and uniformity in cellular uptake, while elongated or rod-shaped ones may enhance targeting capabilities. **Figure 4.1** summarizes examples of common nanoparticles[131].

The widespread use of nanoparticles in medical applications is mainly driven by their ability to easily interact with and be absorbed by cells. Nanoparticles can penetrate cell membranes through endocytosis or direct membrane fusion mechanisms, enabling targeted drug delivery, gene therapy, and imaging within specific cells or tissues (**Figure 4.1**)[132,133]. Factors such as surface chemistry, size, morphology and surface charge influence their cellular uptake efficiency[134]. Ensuring biocompatibility and low toxicity is vital to safely and effectively utilizing nanoparticles in biological systems. Although many demonstrate favorable characteristics, these materials may elicit adverse effects, such as cellular apoptosis, when exposed to sharply shaped nanoparticles[135].

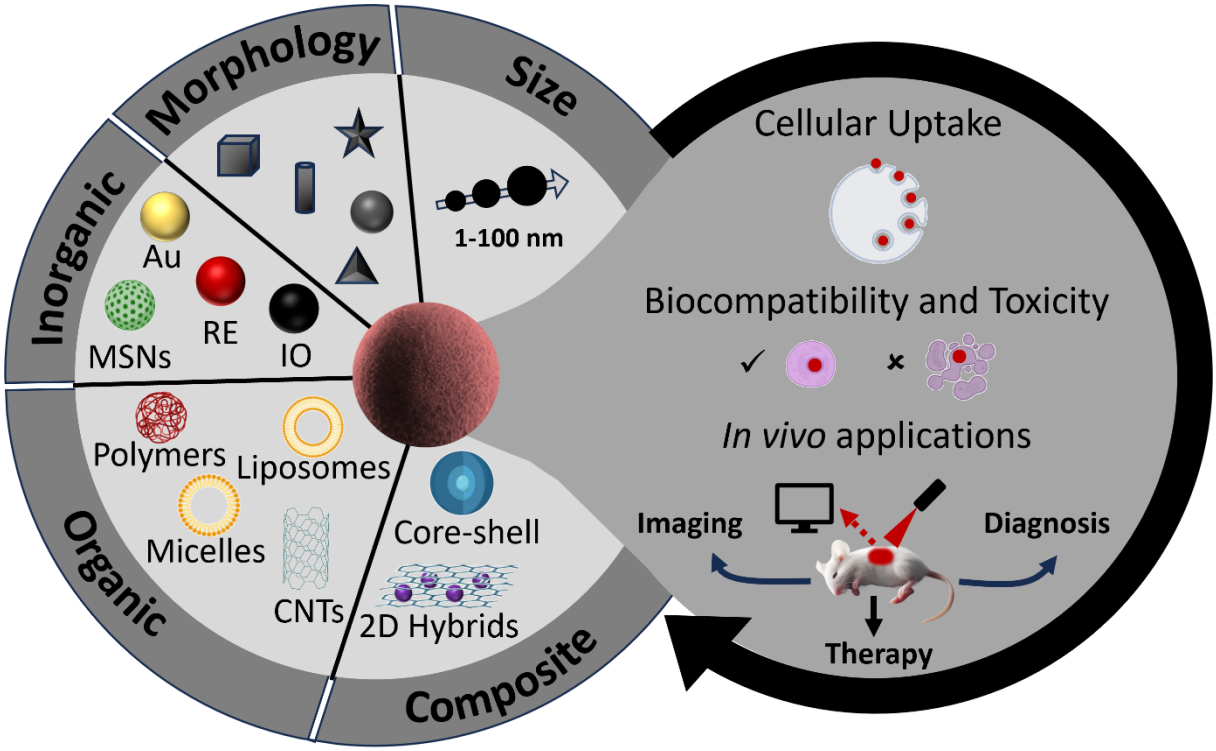


Figure 4.1 - Examples of nanoparticles and their suitability as NIR emitters for *in vivo* applications. RE stands for rare-earth elements, Au for gold, IO for iron oxide, MSNs for mesoporous silica nanoparticles and CNTs for carbon nanotubes. Adapted from reference **131**.

This NIR spectral region is particularly interesting due to its high tissue-penetrating capability and minimal susceptibility to environmental interference[3]. NIR-emitting and/or -absorbing nanoparticles are particularly explored in imaging, therapy, and diagnosis. Fluorescence and photoacoustic imaging enable high-resolution visualization of biological structures and processes deep within living organisms[136]. The contrast that these emissive materials provide aids in diagnosis, enabling the distinction between healthy and cancerous structures. This capability can enhance surgical precision by allowing the targeted removal of malignant tissue while preserving healthy structures and reducing tumor recurrence[137]. Moreover, NIR-responsive nanoparticles can be coupled with photothermal or photodynamic therapy for precise and controlled therapeutic interventions, exploiting the localized heating or generation of reactive oxygen species upon NIR irradiation to destroy unhealthy cells selectively[138,139].

The three chalcogen-doped zeolites explored within the scope of this thesis - sulfur and selenium, already discussed in chapters **2** and **3**, respectively, and tellurium, discussed in the following chapter **5** - can exhibit NIR emission. Selenium is a particularly promising candidate when compared with sulfur due to its photophysical characteristics within this region. Selenium NIR-emissive species absorb in the visible region at *ca.* 490 nm, contrasting with sulfur NIR-emitting species that absorb in the UV region, around 350 nm. Consequently, sulfur species

are considered unsuitable for *in vivo* applications due to the severe cellular damage induced by exposure to high-energy UV radiation[93].

Furthermore, selenium stands out from tellurium not for its photophysical properties but due to its greater availability and biocompatibility once tellurium NIR-emitting can also be excited in the visible region. Selenium is more abundant on Earth's core and crust than tellurium, offering a more reliable and sustainable source[140.141]. Moreover, selenium is widely recognized for its biocompatibility and important role in biological contexts. Its functions include preventing redox reactions, highlighting its significance in maintaining cellular integrity. These attributes enhance the attractiveness of selenium for biomedical applications. Conversely, tellurium is generally acknowledged as toxic to humans and many other organisms (even at low concentrations), lacking participation in essential reactions within the human body.

Thus, this study aims to synthesize selenium NIR-emitting nanozeolites with small and homogeneous sizes and to explore their potential for *in vivo* imaging. Producing these nano-sized materials minimizes the heterogeneity and impurities present in commercially available ones. Additionally, to avoid using organic structure-directing agents, commonly known as "templates" and considered unsustainable, nanosodalite zeolite was chosen as the target material. This choice is due to the high reliance on such templates in the synthesis of nano Na-LTA zeolite[142,143]. Subchapter **2.1** provided important insights into the high-temperature transformations of sodalite zeolite, resulting in the formation of nepheline and/or carnegieite. These two aluminosilicates are believed to be related with the desired selenium NIR-emitting species. Subsequently, subchapter **2.2** demonstrated the ability of sodalite zeolite to directly incorporate chalcogen precursors, thereby conferring emissive properties.

Several synthetic strategies were explored to achieve NIR-emitting nano-sized zeolites. Based on these approaches, this chapter is divided into two parts. The first part focuses on studying the high-temperature transformation of nanozeolites and their corresponding optical properties, similar to the study conducted in chapter **3**. The second part investigates alternative synthesis strategies, such as selenium precursor salt reduction in solution and solid-state, followed by its incorporation during nanozeolite synthesis.

4.1 Single NIR-Emitting Selenium-Doped Zeolites Starting From Nanozeolites

The nature of the selenium NIR emission was tentatively assigned to $[Se_3]^{2-}$ species present in nepheline and/or carnegieite structures, as discussed in chapter **3**. It was also demonstrated in subchapter **2.1** that these aluminosilicates can be formed through the high-temperature transformation of sodalite zeolite at 900 °C. However, high selenium concentrations seem to stabilize sodalite zeolite itself, hindering the formation of nepheline and carnegieite. Consequently, another selenium emissive center, $[Se_2]^-$, associated with this zeolite, was identified. Photophysical characterization revealed an emission quenching of these $[Se_2]^-$ radical clusters. The proposed mechanism involves self-quenching due to a double electron transfer mechanism promoted by their closeness within sodalite cages. Therefore, despite the high amount of sodalite zeolite, it is expected that this emission can be completely quenched at high selenium loadings.

Based on this information, two different strategies were adopted in this subchapter to produce single NIR-emitting selenium-doped nano-sized zeolites starting from nanosodalites: **1)** Using low selenium loadings and no sodium chloride to promote the formation of high amounts of nepheline and carnegieite structures; **2)** Using high selenium loadings to completely quench the emission of $[Se_2]^-$ species, resulting in the formation of sodalite, nepheline and carnegieite structures. Following the treatment at 900 °C, structural and optical characterization analyses were conducted for strategies **1)** and **2)**. To the best of our knowledge, this is the first time that such high-temperature zeolite conversion routes have been explored, starting from nanosodalite zeolite.

4.1.1 Synthesis and structural characterization

In this study, nanosodalites were synthesized using a sol-gel synthesis method and subsequently used as raw materials in a high-temperature synthesis. This differs from previous approaches, such as in chapter **3**, where zeolite transformations at 900 °C of commercial Na-LTA zeolite were studied instead. This apparent subtle difference proves crucial in achieving zeolites with enhanced purity.

Nanosodalite was synthesized following the protocol developed by Yang et al.[144], where these nano-sized zeolites were successfully produced. Refer to section **7.1.2** for more information about the experimental procedure. Thus, a generic gel composition of $18Na_2O:5SiO_2:1Al_2O_3:240H_2O$ was used. This non-doped sample will be further denominated

as Se_0 gel. Analysis by scanning electron microscopy (SEM) revealed nano-sized materials ranging from 50 to 70 nm (**Figure 4.1.1**). (For more information about this technique, see section **7.2.14**.)

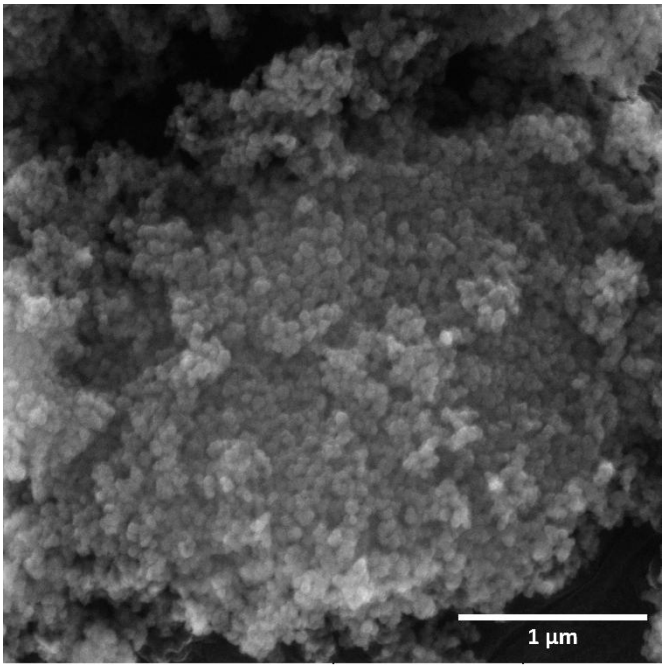


Figure 4.1.1 - SEM image of sample Se_0 gel resulting from the sol-gel synthesis.

Additionally, powder X-ray diffraction (PXRD) confirmed a pure sodalite crystalline phase (**Figure 4.1.2**), matching the simulated diffractogram of sodalite octahydrate, with the composition $[Na_6(H_2O)_8][Si_6Al_6O_{24}]$[145]. (Refer to section **7.2.13** for more information about this technique.)

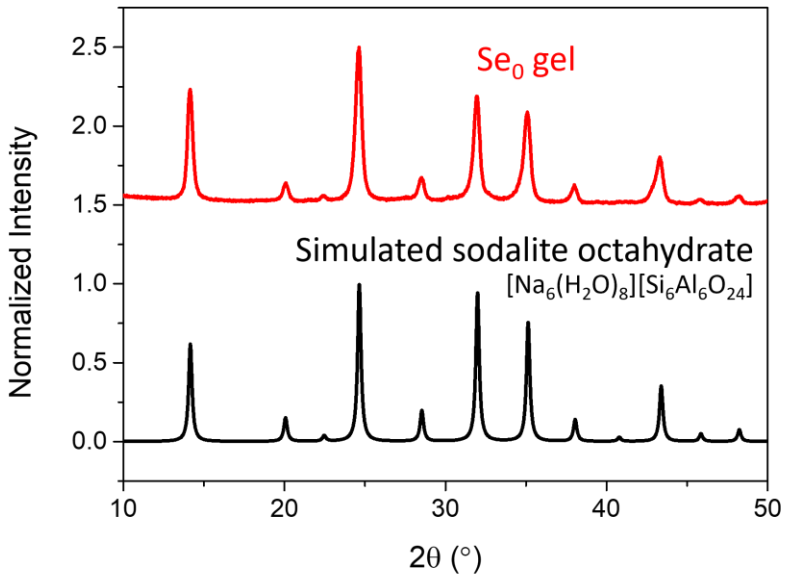


Figure 4.1.2 - PXRD diffractogram of sample Se0 gel and comparison with the simulated diffractogram of sodalite octahydrate, with the composition $[Na_6(H_2O)_8][Si_6Al_6O_{24}]$, according to reference **145**.

The first selenium doping method tested involved incorporating selenium (as selenium selenite, Na_2SeO_3) into the initial gel composition during the nanozeolite sol-gel synthesis. Two samples were synthesized with initial ratios corresponding to Al/Se=60 and 6, resulting in gel compositions of $18Na_2O:5SiO_2:1Al_2O_3:240H_2O:\underline{0.03SeO_2}$ and $18Na_2O:5SiO_2:1Al_2O_3:240H_2O:\underline{0.34SeO_2}$, respectively. These samples have ideal compositions of $[Na_6(H_2O)_8][Si_6Al_6O_{24}]\underline{Se_{0.1}}$ and $[Na_6(H_2O)_8][Si_6Al_6O_{24}]\underline{Se_1}$, further denominated as $Se_{0.1}$ gel and as Se_1 gel, respectively. Section **7.1.2** contains additional information about the experimental procedure. The produced samples revealed the presence of nano-sized materials

(**Figure 4.1.3.A**) and a single-sodalite phase (**Figure 4.1.3.B**), showing that this doping method does not affect the resulting samples.

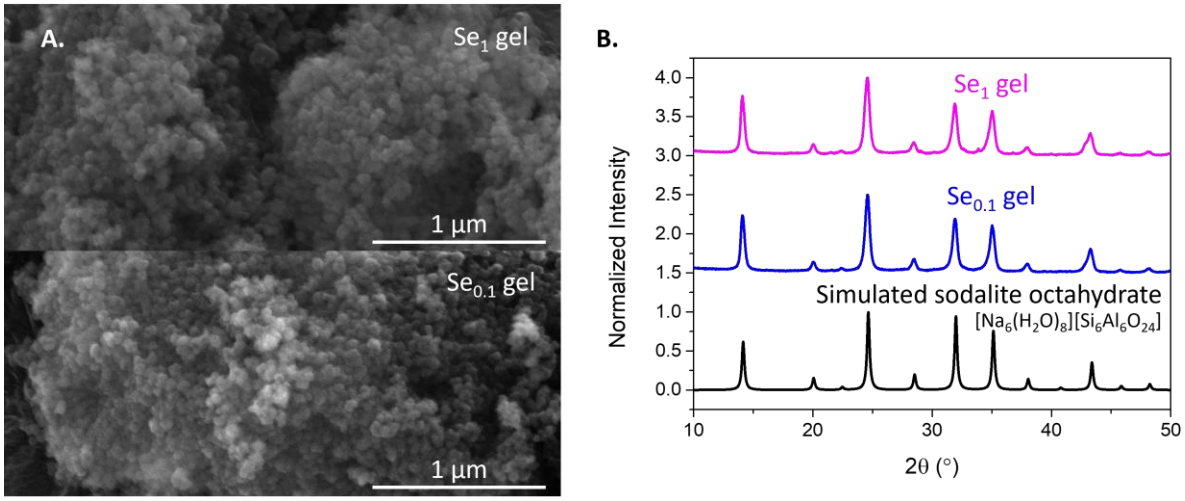


Figure 4.1.3 - (**A**) SEM images and (**B**) PXRD diffractograms of samples $Se_{0.1}$ gel and Se_1 gel. Note the comparison with the simulated diffractogram of sodalite octahydrate, with the composition $[Na_6(H_2O)_8][Si_6Al_6O_{24}]$ in black, according to reference **145**.

Element analysis conducted using wavelength dispersive X-ray fluorescence (WDXRF) revealed an increase in selenium content from sample $Se_{0.1}$ gel to sample Se_1 gel, as summarized in **Table 4.1.1**. However, these measured values are substantially lower than expected, resulting in significantly higher Al/Se ratios than the nominal ratios used in gel compositions during sol-gel synthesis. These differences suggest that the selenium doping method employed may not be as efficient as the one used in the previous study conducted in chapter **3**, where the selenium precursor was directly introduced to the zeolite at 900 °C during high-temperature synthesis, exhibiting higher selenium loadings (**Table 3.1**). Sulfur and chloride were also detected in these samples at molar percentages similar to selenium. Their origin may arise from raw material impurities or contaminated material used during synthesis. Note that these molar percentages were calculated from the weight percentage of the corresponding elements in their oxide form (**Table C.1.1**). (See section **7.2.11** for additional information about this WDXRF technique.)

Table 4.1.1 - Molar percentage of the observed elements in zeolite samples using the WDXRF technique.

Sample	Nominal Al/Se	Molar percentage composition (%)[a]							Obtained Al/Se
		Na	Si	Al	O	Se	S	Cl	
$Se_{0.1}$ gel	60	10.85	16.26	13.91	58.91	0.01	0.03	0.03	2366
Se_1 gel	6	10.14	16.54	13.92	59.26	0.05	0.04	0.04	294

[a]Calculated from the WDXRF weight percentage (wt%) (**Table C.1.1**).

To achieve the desired NIR emissive properties, these samples were subjected to a high-temperature synthesis at 900 °C for 1 hour under a reductive atmosphere of 5% H_2 / 95% Ar, resulting in samples $Se_{0.1}$ gel - 900 °C and Se_1 gel - 900 °C, respectively, according to equation (**4.1.1**). Refer to section **7.1.3** for more information about the experimental procedure.

$$[Na_6(H_2O)_8][Si_6Al_6O_{24}]Se_x \rightarrow [Na_6(H_2O)_8][Si_6Al_6O_{24}]Se_x$$
$$(\mathbf{Se_x\ gel} \rightarrow \mathbf{Se_x\ gel - 900\ °C}), with\ x = 0.1\ and\ 1 \quad (4.1.1)$$

Besides, considering that the first selenium-doping method was not as efficient as initially expected, as shown by the WDXRF results, a second one was tested. This method involved mixing non-doped nanosodalite (Se_0 gel) with desirable amounts of sodium selenite and placing the resulting mixture at 900 °C under a reductive atmosphere (similar to the method used in chapter **3**). Here, two amounts of selenium precursor were used, maintaining the initial ratios of Al/Se=60 and 6, corresponding to 0.1 and 1 moles of selenium. These samples are denominated as $Se_{0.1}$ - 900 °C and Se_1 - 900 °C, respectively. Equation (**4.1.2**) defines the expected transformations for this method. Section **7.1.3** contains additional information about the experimental procedure.

$$[Na_6(H_2O)_8][Si_6Al_6O_{24}] + x\ Na_2SeO_3 \rightarrow [Na_{6+2x}(H_2O)_8][Si_6Al_6O_{24}]Se_x$$
$$(\mathbf{Se_0\ gel} + Na_2SeO_3 \rightarrow \mathbf{Se_x - 900\ °C}), with\ x = 0.1\ and\ 1 \quad (4.1.2)$$

Note that sodium chloride was not used in the high-temperature syntheses described in equations (**4.1.1**) and (**4.1.2**), contrary to the experimental procedure discussed in chapter **3** above. Typically, this salt is used to stabilize sodalite zeolite during high-temperature synthesis, as demonstrated in subchapter **2.2**. However, in this study, sodalite was synthesized through a sol-gel synthesis. Consequently, free-NaCl sodalite is expected to convert into

carnegieite and nepheline during the temperature treatment, aluminosilicates which are associated with selenium NIR emission, as discussed in chapter **3**.

After the high-temperature treatment at 900 °C, significant structural differences were found in the synthesized zeolites, produced by using the two different methods. SEM images illustrate the role of this treatment in the integrity of nano-sized zeolites, with nanoparticles no longer visible, as demonstrated in **Figure 4.1.4**. It becomes evident that the once homogeneous small nanoparticles fused with each other, giving rise to heterogeneous large agglomerates.

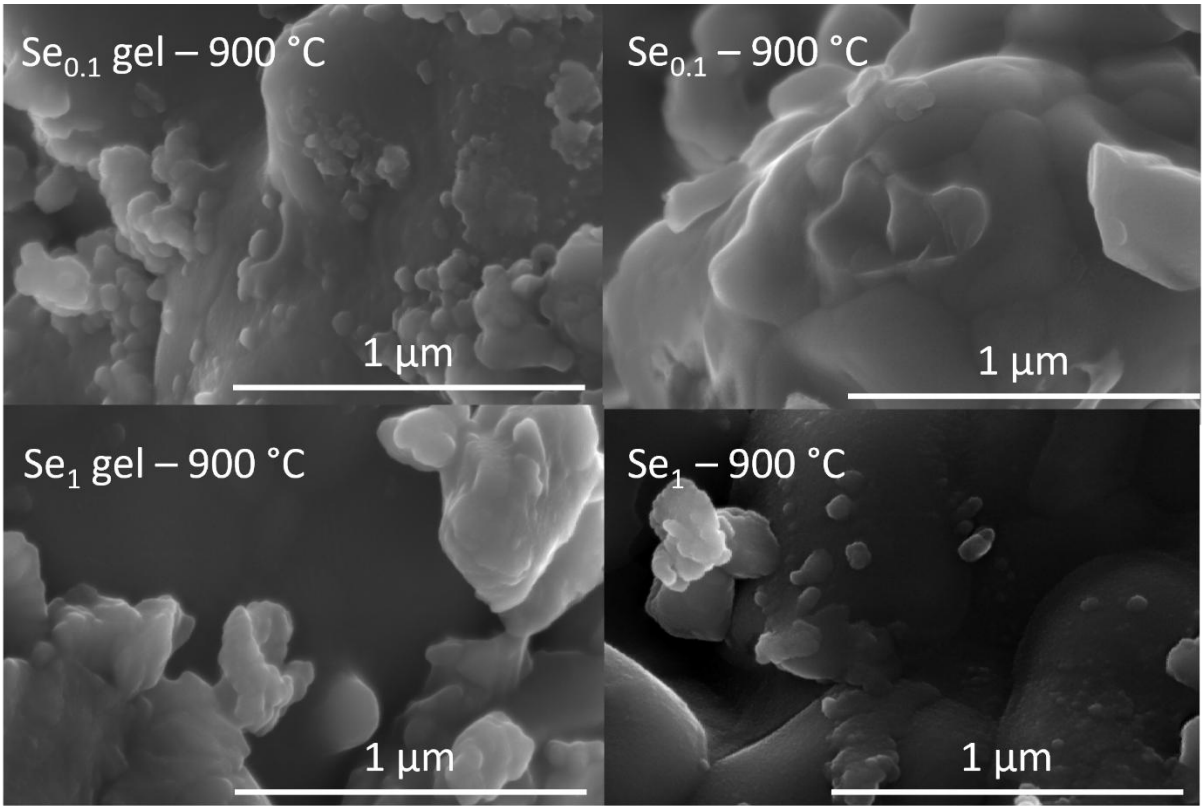


Figure 4.1.4 - SEM images of the samples submitted to high-temperature synthesis at 900 °C.

SEM images of sample $Se_{0.1}$ - 900 °C, captured at various magnifications (**Figure 4.1.5**), revealed that these agglomerates range from 2 to 35 μm.

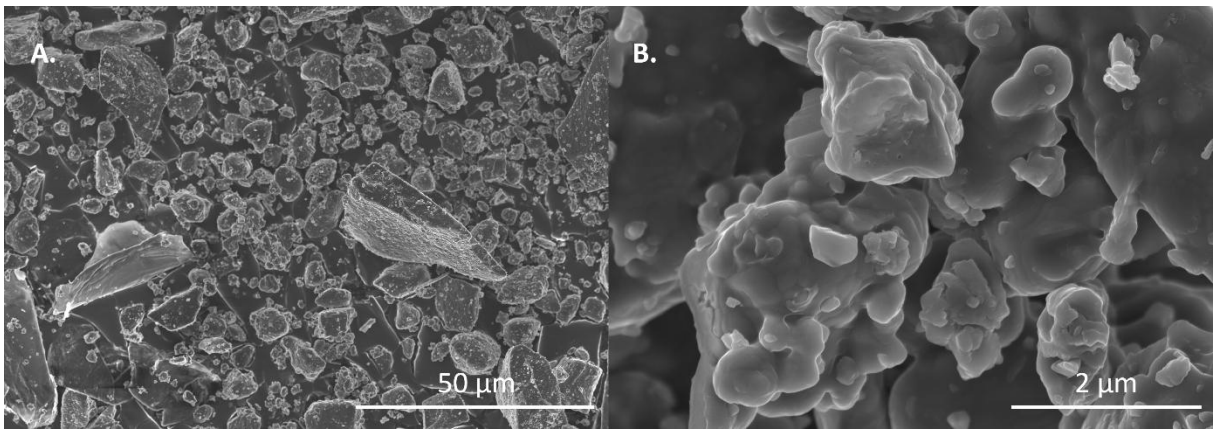


Figure 4.1.5 - SEM images of sample $Se_{0.1}$ - 900 °C using different magnifications.

Elemental analysis was conducted on the produced samples during SEM analysis, using energy dispersive X-ray spectroscopy (EDS), as summarized in **Table 4.1.2**. The values from sample Se_1 gel - 900 °C stand out, particularly due to the lack of selenium detection. This element was previously detected in this sample before high-temperature synthesis (**Table 4.1.1**) using the WDXRF technique. It is worth noting that the main elemental results of sample $Se_{0.1}$ gel - 900 °C are consistent across both analytic techniques. Therefore, the absence of selenium detection in sample Se_1 gel - 900 °C could be attributed to an analysis error. **Table C.1.2** depicts the impurities found in these samples, with chloride being the only common impurity detected by both techniques, although, in EDS analysis, it was only detected in sample Se1 - 900 °C.

Table 4.1.2 - Elemental analysis of each main element found in nanozeolite samples submitted to high-temperature synthesis at 900 °C using the EDS technique.

Sample	Nominal Al/Se	Molar percentage composition (%)[a]					Obtained Al/Se
		Na	Si	Al	O	Se	
$Se_{0.1}$ gel - 900 °C	60	13.91	14.47	13.93	57.53	0.04	348
Se_1 gel - 900 °C	6	9.05	25.57	16.55	48.25	-	-
$Se_{0.1}$ - 900 °C	60	13.07	13.61	13.65	58.27	0.14	98
Se_1 - 900 °C	6	15.07	14.15	13.93	55.38	1.24	11

[a]Experimental values extracted using the EDS technique. See **Table C.1.2** for additional information about the impurities found in these samples.

Furthermore, the second selenium doping method (samples $Se_{0.1}$ - 900 °C and Se_1 - 900 °C) proved more efficient in incorporating selenium, presenting higher selenium values (similar to those found in **Table 3.1**, chapter **3**). This efficiency is particularly evident when comparing the nominal Al/Se ratios with those obtained.

Dynamic light scattering (DLS) analysis also confirms the SEM observations, illustrating the agglomeration of these materials after the thermal treatment. An average particle size distribution (z-average) of approximately 9 µm was detected in sample $Se_{0.1}$ - 900 °C (**Figure 4.1.6**). In contrast, as-synthesized non-thermally treated sample Se_0 gel exhibits high dispersibility and nano-sized particles with a z-average of around 90 nm. (Refer to section **7.2.9** for additional information about this technique).

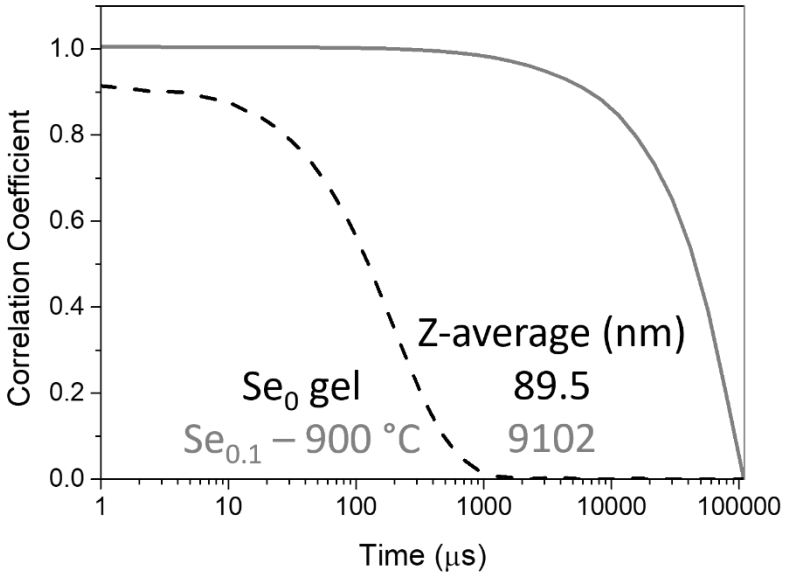


Figure 4.1.6 - Dynamic light scattering (DLS) autocorrelation functions of non-thermally treated sample Se_0 gel (dashed, black) and thermally treated sample $Se_{0.1}$ - 900 °C (solid, gray).

PXRD analysis also demonstrates significant differences, the first being related to the full width at half maximum (FWHM), which sharpens after the thermal treatment. This suggests that the final crystallite size of the materials is larger than those synthesized through the sol-gel method, as described by the Scherrer formula[146] in equation (**4.1.3**). These findings are in good agreement with the SEM images (**Figure 4.1.4**).

$$D = \frac{K.\lambda}{\beta.\cos(\theta)} \qquad (4.1.3)$$

where D is the average crystallite size, K is the shape factor of the crystallites, λ is the wavelength of the X-ray source, β is the FWHM of the diffraction peak and θ is the Bragg angle at which the diffraction peak occurs.

The diffractograms produced also reveal differences in the crystalline phases, as summarized in **Table 4.1.3**. Starting from the blank, non-doped Se_0 gel - 900 °C sample, the major observed phase is nepheline. This indicates that without selenium, sodalite is converted into nepheline (**Figure 4.1.7**). Additionally, selenium-doped samples reveal variations in the final crystalline phases depending on the selenium loading and/or doping method. Gel samples predominantly yield carnegieite crystalline phase, as illustrated in **Figure 4.1.7**.

Table 4.1.3 - Crystalline phases calculated by comparing the ICDD standards reference cards with the PXRD diffractograms.

Sample	Crystalline phase (%)		
	Sodalite	Nepheline	Carnegieite
Se_0 gel - 900 °C (blank)	3	97	0
$Se_{0.1}$ gel - 900 °C	2	5	94
Se_1 gel - 900 °C	1	4	95
$Se_{0.1}$ - 900 °C	12	55	36
Se_1 - 900 °C	66	22	12

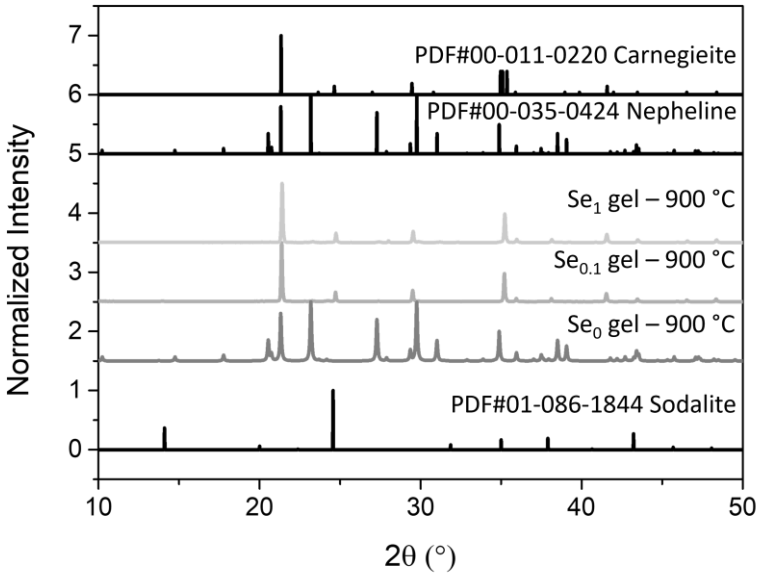


Figure 4.1.7 - PXRD diffractograms of samples Se_0 gel - 900 °C, $Se_{0.1}$ gel - 900 °C and Se_1 gel - 900 °C. Comparison with the ICDD standard reference card of 01-086-1844 sodalite ($Na_8Si_6Al_6O_{24}Cl_2$), 00-035-0424 nepheline ($Na_4Si_4Al_4O_{16}$) and 00-011-0220 carnegieite ($Na_4Si_4Al_4O_{16}$).

Alternatively, doping during the 900 °C synthesis results in a mixture of three different crystalline phases - sodalite, nepheline and carnegieite - (with a contribution >10%), as shown in **Figure 4.1.8**. The percentage composition of these phases depends on the selenium content. Nepheline prevails at lower concentrations ($Se_{0.1}$ - 900 °C), while sodalite becomes the majority at higher content (Se_1 - 900 °C).

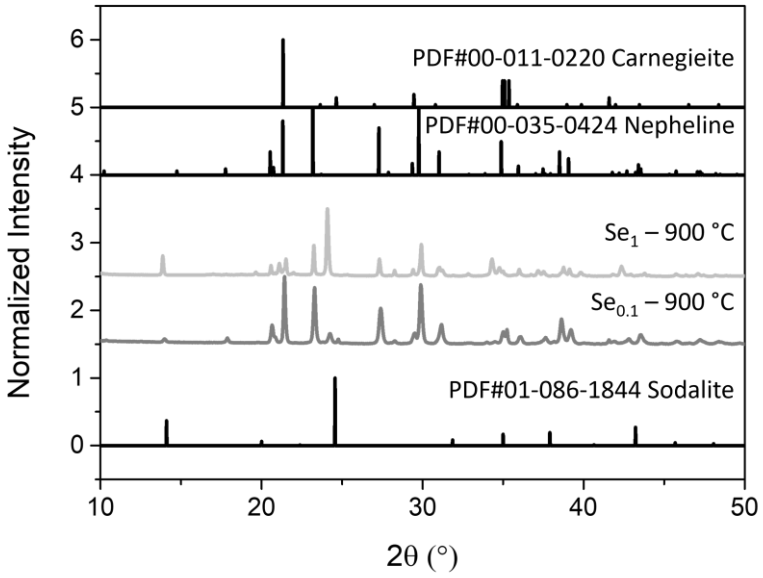


Figure 4.1.8 - PXRD diffractograms of samples $Se_{0.1}$ - 900 °C and Se_1 - 900 °C. Comparison with the ICDD standard reference card of 01-086-1844 sodalite ($Na_8Si_6Al_6O_{24}Cl_2$), 00-035-0424 nepheline ($Na_4Si_4Al_4O_{16}$) and 00-011-0220 carnegieite ($Na_4Si_4Al_4O_{16}$).

These results align with previous studies demonstrating that sodalite can thermally decompose into nepheline and carnegieite crystalline phases[73,74], transformations also observed in chapter **2**. As expected, the selenium content highly influences the produced phases. At low loadings, nepheline and/or carnegieite are observed, as demonstrated in **Table 4.1.3** for samples Se_0 gel - 900 °C, $Se_{0.1}$ gel - 900 °C, Se_1 gel - 900 °C and $Se_{0.1}$ - 900 °C. However, sodalite is stabilized at high loadings, as exemplified by sample Se_1 - 900 °C. This highlights, once more, the selenium effect in stabilizing sodalite zeolite.

The impact of these structural differences in the corresponding optical properties will be explored in the next section.

4.1.2 Optical and NIR photophysical characterization

In order to evaluate whether these produced samples exhibited the absorbing species responsible for the selenium NIR emission, they were first characterized by diffuse reflectance spectroscopy. After using the Kubelka-Munk theory[103], the obtained spectra are illustrated in **Figure 4.1.9**. (See section **7.2.2** for more details about this technique.) Upon comparing the two different doping methods, it is evident that selenium doping during high-temperature synthesis ($Se_{0.1}$ - 900 °C and Se_1 - 900 °C) is more efficient for forming chromophores than doping

before synthesis ($Se_{0.1}$ gel - 900 °C and Se_1 gel - 900 °C). This is supported by the difference in intensity found in the diffuse reflectance spectra.

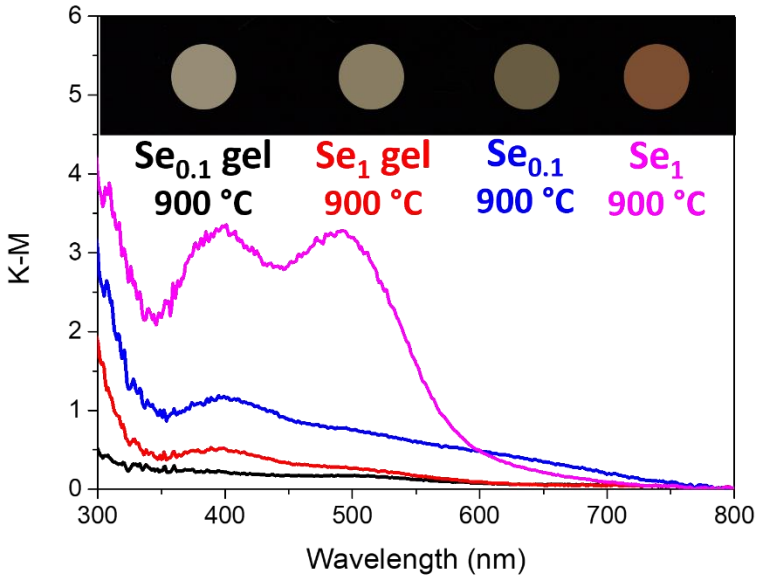


Figure 4.1.9 - Diffuse reflectance spectra of the synthesized samples. The insets show the photos of the samples under ambient light.

Among all the obtained diffuse reflectance spectra, only the spectrum from sample Se1 - 900 °C (pink line) exhibits distinguishable and discrete absorption bands. Therefore, to better understand the chromophores present, the analysis of these spectra begins with deconvoluting this particular spectrum (**Figure 4.1.10**), using information from the literature and insights gained from the study of selenium-doped zeolites in chapter **3**. Thus, the absorption spectrum of $[Se_2]^-$ clusters[87], with bands at 350 nm and 490 nm (blue line), and the absorption spectrum of NIR-emitting species peaking at 400 nm (red line) were used. These last-mentioned species were first discovered in KI crystals doped with selenium, and further photophysical characterization was conducted in this thesis. They are tentatively assigned to $[Se_3]^{2-}$ clusters and are associated with selenium NIR emission. An additional band with a maximum of 270 nm (green line) was necessary. This one can be assigned to the zeolite framework since it is reported to absorb above 333 nm[78]. Finally, a last band peaking at 600 nm was added. However, its nature is unknown to our current knowledge, as there is no information about these species in selenium-doped zeolites. Combining all these bands (black line) makes it possible to reproduce the experimental result accurately (pink line).

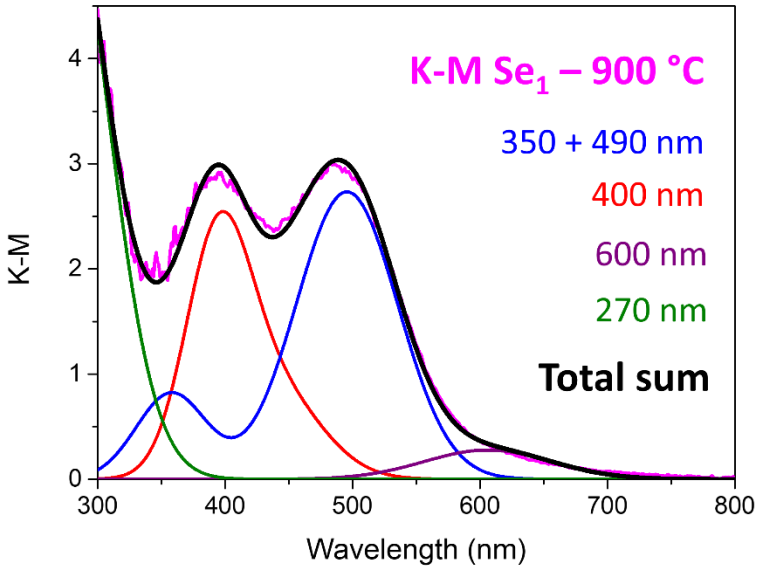


Figure 4.1.10 - Diffuse reflectance spectral deconvolution of sample Se_1 - 900 °C.

The remaining diffuse reflectance spectra of the other synthesized samples were also deconvoluted using the same absorption bands (**Figure C.1.1**). However, given that they do not present discrete bands, it was difficult to determine the presence of these chromophores.

Further characterization was then conducted using emission spectroscopy to better assess the presence of these species. In particular, their behavior when excited at 350, 400 and 480 nm, as both species are emissive. (Refer to section **7.2.3** for more details about this technique.) When exciting these materials at 400 nm, all produced samples exhibited the typical selenium NIR emission, peaking at around 815 nm, as depicted in **Figure 4.1.11.A-B**). These spectra are in good agreement with those previously observed in chapter **3** (**Figure 3.7.A**) for selenium-doped NIR-emitting zeolites.

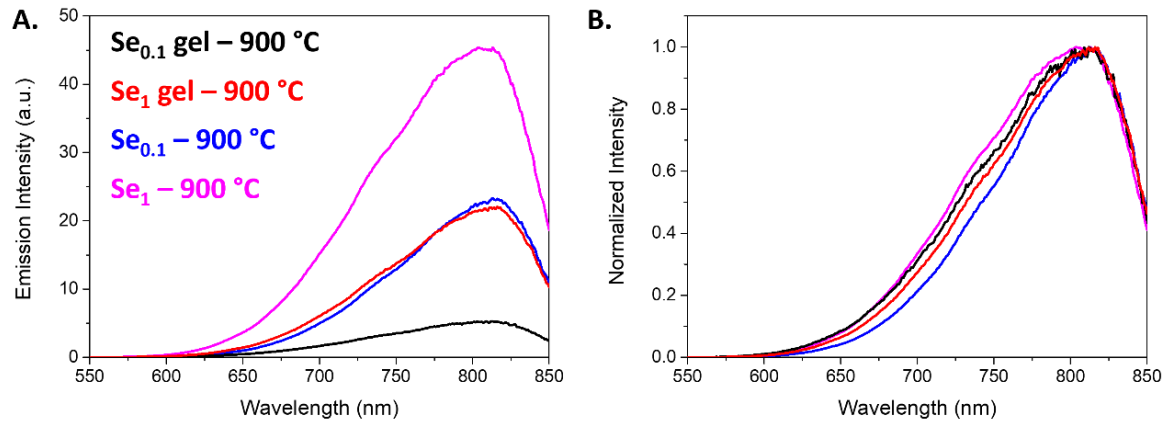


Figure 4.1.11 - (**A**) Emission, λ_{exc}=400 nm, and (**B**) corresponding normalized spectra of the synthesized samples after the high-temperature synthesis at 900 °C.

Additionally, bands centered at *ca.* 390 nm were identified in the excitation spectra corresponding to the emission at 800 nm (**Figure 4.1.12.A-B**). Analysis of the normalized spectra revealed similar profiles with slight variations in peak maxima, as shown in **Figure 4.1.12.B**. The peak shifted from 385 nm in sample $Se_{0.1}$ gel - 900 °C to 395 nm in samples $Se_{0.1}$ - 900 °C and Se_1 - 900 °C. Notably, these latter samples exhibited behavior closest to that observed in the previous study conducted in chapter 3 (**Figure 3.7.B**), where the peak occurred at 400 nm.

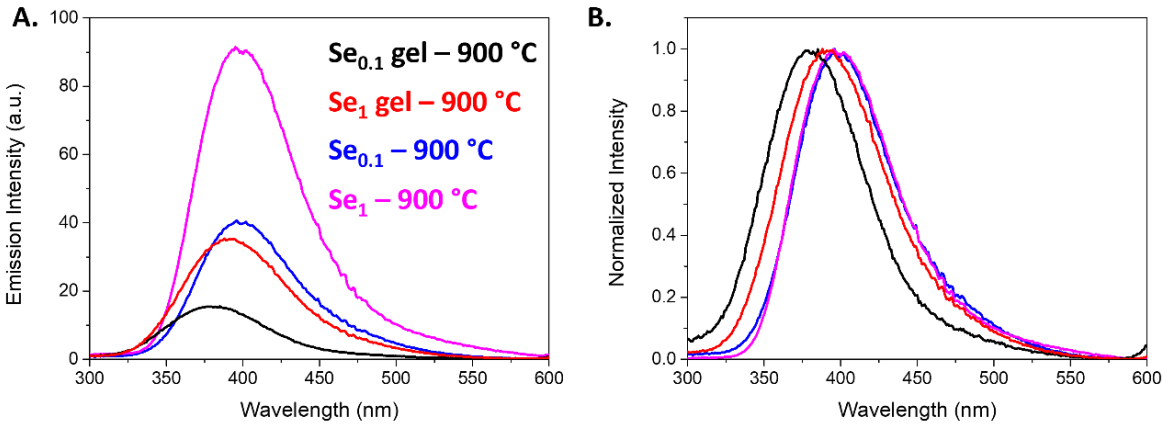


Figure 4.1.12 - (**A**) Excitation, λ_{em}=800 nm, and (**B**) corresponding normalized spectra of the synthesized samples after the high-temperature synthesist at 900 °C.

Overall, the observed intensities in emission (**Figure 4.1.11.A**) and excitation (**Figure 4.1.12.A**) spectra align with the elemental analysis of selenium element (**Table 4.1.2**), varying as follows: $Se_{0.1}$ gel - 900 °C < Se_1 gel - 900 °C ≈ $Se_{0.1}$ - 900 °C < Se_1 - 900 °C.

Furthermore, the emitting species appear consistent across all samples, as evidenced by identical emission and excitation profiles illustrated in **Figure 4.1.11.B** and **Figure 4.1.12.B**, respectively. However, the spectral shift observed in the excitation spectra suggests a ground-state effect of these emitting species, although a direct cause for this phenomenon remains inconclusive. However, a matrix effect was disregarded, as samples $Se_{0.1}$ gel - 900 °C and Se_1 gel - 900 °C exhibit minimal differences in phase composition (**Table 4.1.3**) yet display slight variations in their excitation spectra.

Additionally, when these samples were excited at 480 nm (main absorption band of $[Se_2]^-$ species), the characteristic red emission peaking at 740 nm was not observed[86]. Instead, these samples exhibit the same NIR emission discussed above (**Figure 4.1.13.A**). A comparison of the observed spectra with the obtained emission of $[Se_2]^-$ species obtained in chapter **3** is presented in **Figure 4.1.13.B**. Furthermore, these samples were also excited at 350 nm, at the second absorption band of $[Se_2]^-$, as illustrated **Figure C.1.2.A-B**, revealing once more the absence of $[Se_2]^-$ clusters.

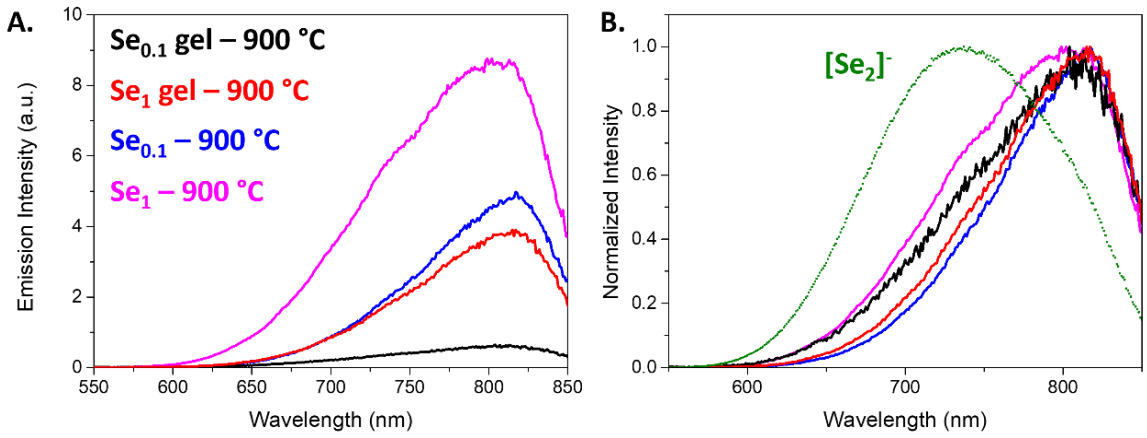


Figure 4.1.13 - (**A**) Emission, λ_{exc}=480 nm, and (**B**) corresponding normalized spectra of the synthesized samples after the high-temperature synthesist at 900 °C. The typical emission spectrum of $[Se_2]^-$ species found in the selenium-doped zeolites is represented in green, as discussed in **Figure 3.5.A-B**, chapter **3**.

The excitation spectra corresponding to the emission at 740 nm also confirm this behavior (**Figure 4.1.14.A-B**), lacking $[Se_2]^-$ detection and exhibiting the same spectral shifts as those already discussed in **Figure 4.1.12.B**.

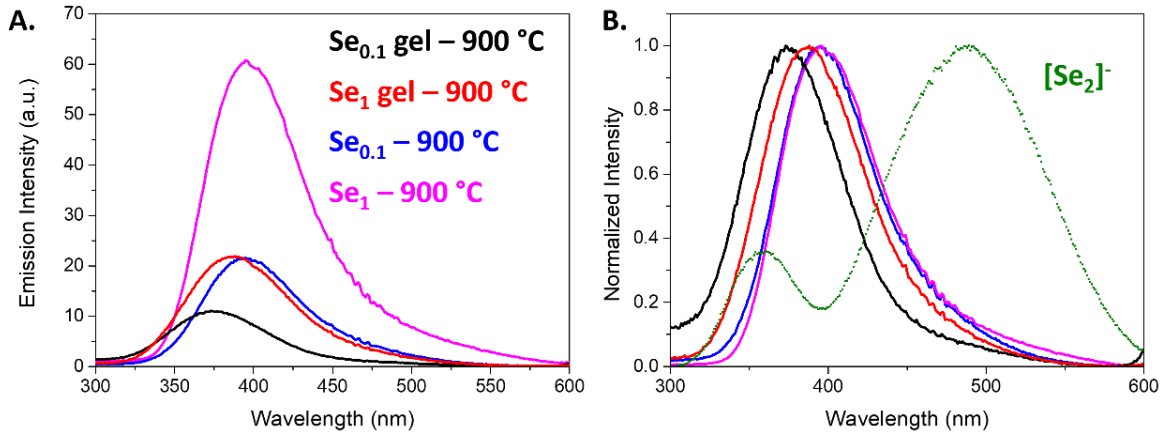


Figure 4.1.14 - (**A**) Excitation, λ em=740 nm, and (**B**) corresponding normalized spectra of the synthesized samples after the high-temperature synthesist at 900 °C. The typical excitation spectrum of $[Se_2]^-$ species found in the selenium-doped zeolites is represented in green, as discussed in **Figure 3.6**, chapter **3**.

Indeed, the absence of red emission detection attributed to the presence of $[Se_2]^-$ clusters contrasts with the diffuse reflectance spectra, where the absorption of these clusters was observed at 350 and 490 nm (at least undoubtedly in sample Se1 - 900 °C), as illustrated in **Figure 4.1.9**. However, a self-quenching effect produced by $[Se_2]^-$ species may explain these findings. As suggested in the preceding chapter, this phenomenon was attributed to a double electron transfer mechanism between $[Se_2]^-$ clusters (**Figure 3.11**) located within different sodalite cages (**Figure 3.10**). This effect is promoted by proximity between $[Se_2]^-$ clusters. Consequently, this quenching effect leads to a decrease in intensity in both emission and excitation spectra, faster decay times and a reduction in external quantum efficiencies. Nevertheless, the complete quenching of this red emission was only observed in the samples treated at high temperatures in the present study. Notably, this resulted in single NIR-emitting selenium-doped zeolites, which, to our knowledge, represent the first successful synthesis of such materials.

Similarly to the characterization conducted in the previous chapters, external quantum efficiencies (EQEs) and photoluminescence decay times of these materials were also measured, with the values summarized in **Table 4.1.4**. (See additional information about EQE in section **7.2.3** and photoluminescence decay times in section **7.2.4**.)

Starting with the EQEs, only the NIR emission was measured since the red emission was not detected. Therefore, values around 3% were calculated in all samples, as illustrated in **Figure 4.1.15**. These results are lower than those previously obtained for selenium-doped zeolites in chapter **3**, which yielded mean values of 6 ± 1%. However, considering the

approximations made in that study, since those samples presented two emissions (red and NIR), the differences in values are not significant. Indeed, the values obtained in the present study are more reliable since a single NIR emission was observed. Unfortunately, EQE measurement of sample $Se_{0.1}$ gel - 900 °C was not possible due to its low emission. The obtained EQE values do not exhibit significant variations with changes in selenium content.

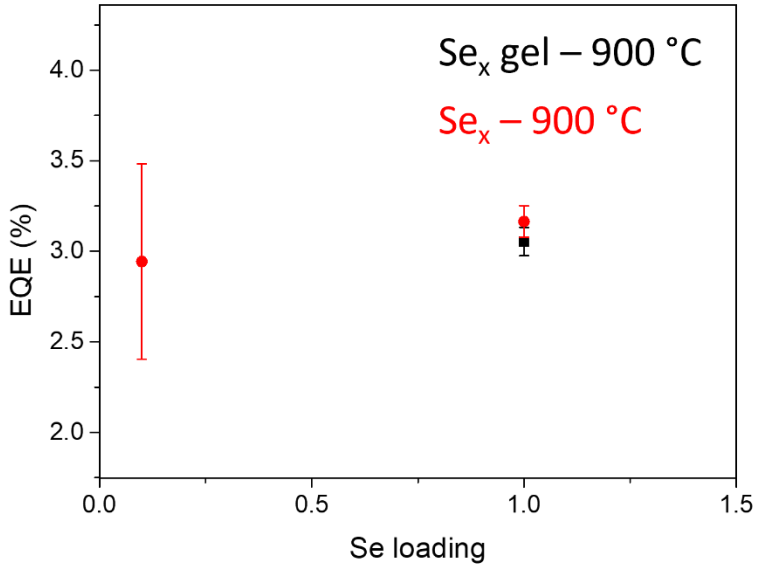


Figure 4.1.15 - External quantum efficiencies of the synthesized samples exciting at 400 nm.

Next, the photoluminescence decay times of these produced samples were investigated. From the study conducted on selenium-doped zeolites in chapter **3**, it was observed that both present emitting species decay on different timescales. $[Se_2]^-$ exhibits an average decay time of *ca.* 96 nanoseconds, while the average decay time of the NIR-emitting species is around 75 microseconds. Consequently, these timescales were thoroughly explored.

Decay times within the nanosecond range revealed a notable absence of emission in this timescale (**Figure 4.1.16**), reinforcing the earlier observations in steady-state measurements and supporting the assignment of red emission to the short-lived species.

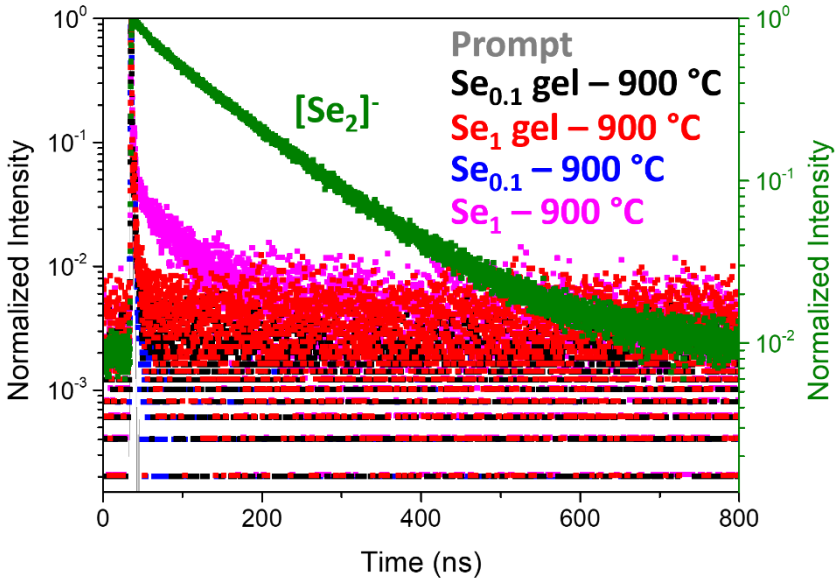


Figure 4.1.16 - Photoluminescence decay times of the synthesized samples at a nanosecond time scale, recorded with an λ_{exc}=445 nm and λ_{em}=750 nm. Comparing with the green line representing the photoluminescence decay times of $[Se_2]^-$ clusters excited at the same wavelength.

Moreover, decay times were detected at longer timescales, however, minor variations were observed based on the chosen doping method. In the case of samples doped before the 900 °C synthesis (**Figure 4.1.17.A**), three components were used in the fittings, with the slower one having less than 20% of the relative amplitude. Conversely, in samples doped during high-temperature synthesis (**Figure 4.1.17.B**), only two components were used, as summarized in **Table 4.1.4**. Except for the slower decay component (assigned to sulfur impurities detected by the WDXRF technique in these samples according to **Table 4.1.1**), all other components are consistent with those found in the previously synthesized selenium-doped zeolites described in **Table 3.3**, chapter **3**.

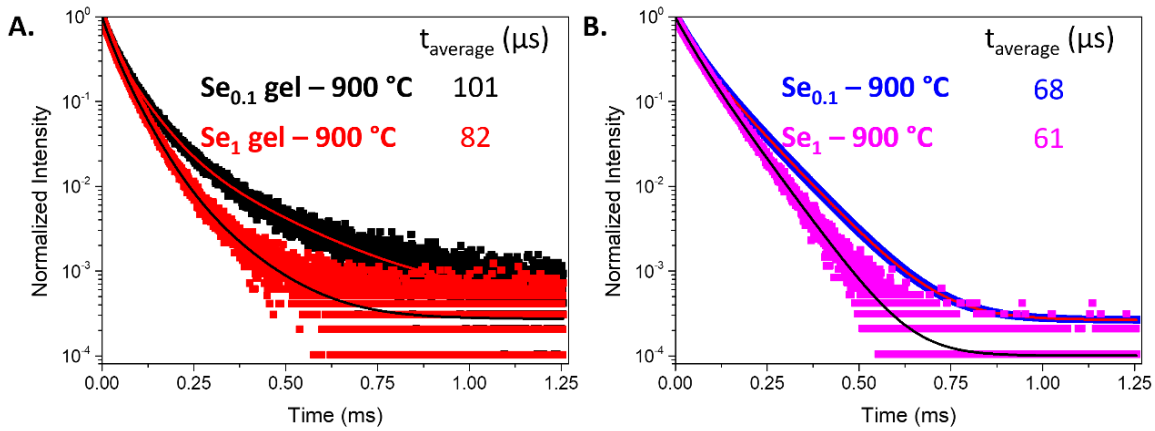


Figure 4.1.17 - Photoluminescence decay times (scatter) and corresponding fittings (line) of samples doped before (**A**) and during (**B**) high-temperature synthesis with respective average decay times, monitored at λ_{exc}=400 nm and λ_{em}=800 nm. The corresponding residuals of the fittings are present in **Figure C.1.3**.

The slower decay component (exclusively present in gel samples) presents values of 380 and 236 µs for $Se_{0.1}$ gel - 900 °C and Se_1 gel - 900 °C, respectively. $[S_3]^{2-}$ NIR-emitting species found in sulfur-doped zeolites, as discussed in subchapter **2.3**, also display similar slower decay components of approximately 270 and 670 µs. Indeed, this sulfur NIR emission was observed in the blank sample (Se_0 gel - 900 °C), as well as some contamination from $[S_2]^-$ clusters, which exhibit vibronic bands and peaks at 625 nm, as demonstrated in **Figure 4.1.18**.

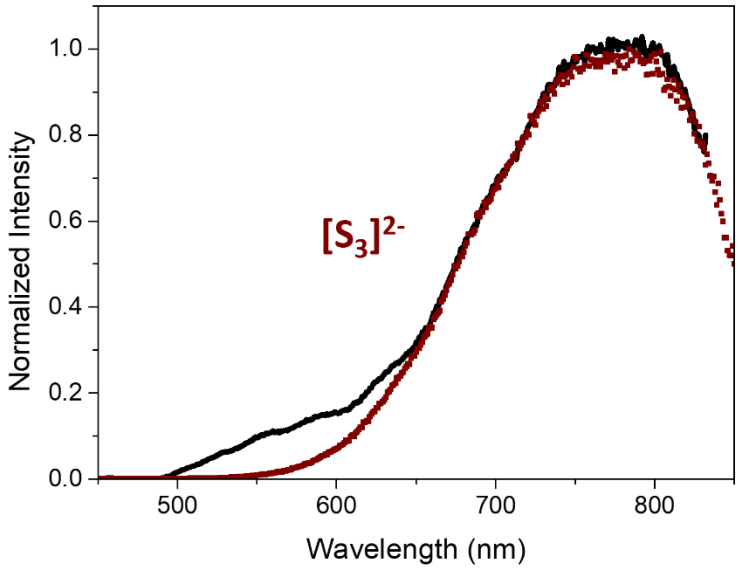


Figure 4.1.18 - Comparison of the emission spectra of sample Se_0 gel - 900 °C (black line) with the $[S_3]^{2-}$ species (dark-red line) obtained in sulfur-doped zeolites, as discussed in subchapter **2.3**, λ_{exc}=350 nm.

The presence of these components exclusively in gel samples could be attributed to their overall lower emission intensity. As evidenced in **Figure 4.1.11.A**, which compares the steady-state emission of the four synthesized samples in this study, sample $Se_{0.1}$ gel - 900 °C has the lowest intensity among them, followed by sample Se_1 gel - 900 °C. However, if this slower component is ignored, the average decay times for samples $Se_{0.1}$ gel - 900 °C and Se_1 gel - 900 °C would be approximately 87 and 76 µs, respectively.

Radiative (k_r) and non-radiative (k_{nr}) 'averaged' constants were calculated based on the EQEs and photoluminescence decay times measured, according to equations (**3.3**) and (**3.4**) of chapter **3**, as summarized in **Table 4.1.4**. Both constants demonstrated an increase with selenium loading as follows: Se_1 gel - 900 °C < $Se_{0.1}$ - 900 °C < Se_1 - 900 °C. This behavior and these values are similar to those discussed in selenium-doped zeolites in **Table 3.3**, chapter **3**.

Table 4.1.4 - External quantum efficiencies (EQEs), photoluminescence decay times with their respective components and relative amplitudes (A), alongside average decay times and corresponding radiative (k_r) and non-radiative (k_{nr}) 'averaged' constants of the NIR emission.

Sample	EQE (%)	τ_1 (µs)	A_1	τ_2 (µs)	A_2	τ_3 (µs)	A_3	$\tau_{average}$ (µs)*	k_r (s^{-1}) x10^2	k_{nr} (s^{-1}) x10^4
$Se_{0.1}$ gel - 900 °C	-	40	0.15	119	0.66	380	0.19	101	-	-
Se_1 gel - 900 °C	3	40	0.16	95	0.72	236	0.12	82	3.72	1.18
$Se_{0.1}$ - 900 °C	3	40	0.29	96	0.71	-	-	68	4.33	1.43
Se_1 - 900 °C	3	40	0.26	74	0.74	-	-	61	5.19	1.59

*Values calculated using the pre-exponential factors.

From the four synthesized samples, sample $Se_{0.1}$ - 900 °C demonstrated the optimal structural and optical properties, with a bi-exponential decay time and minimal (if some) contribution of $[Se_2]^-$ clusters. Therefore, this sample was further characterized through time-resolved emission spectroscopy (TRES). (Section **7.2.5** contains additional information about this technique.) When applying shorter delay times compatible with the average decay times of short-lived $[Se_2]^-$ species, i.e., on a nanosecond scale, the resulting emission spectra (**Figure 4.1.19**) revealed the absence of these mentioned species (see **Figure 3.14**, chapter **3** for additional information about the TRES spectra of these species). These resulting spectra are compatible with those found in the blank sample Se_0 gel - 900 °C (**Figure C.1.4.A**). Note that since the steady-state emission spectrum of this blank sample exhibits a sulfur NIR emission (**Figure 4.1.18**), TRES spectra were assigned to the emission of $[S_3]^{2-}$ impurities.

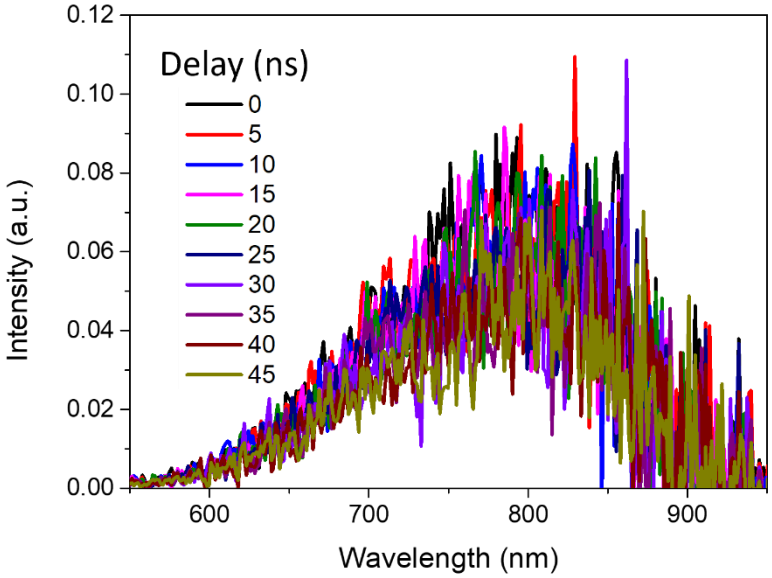


Figure 4.1.19 - Time-resolved emission spectroscopy of sample $Se_{0.1}$ - 900 °C applying shorter delay times and using an λ_{exc}=337 nm.

Furthermore, at longer delay times, selenium NIR emission peaking at around 825 nm was detected in sample $Se_{0.1}$ - 900 °C (**Figure 4.1.20**). This emission is consistent with the steady-state spectra illustrated in **Figure 4.1.11.A-B**.

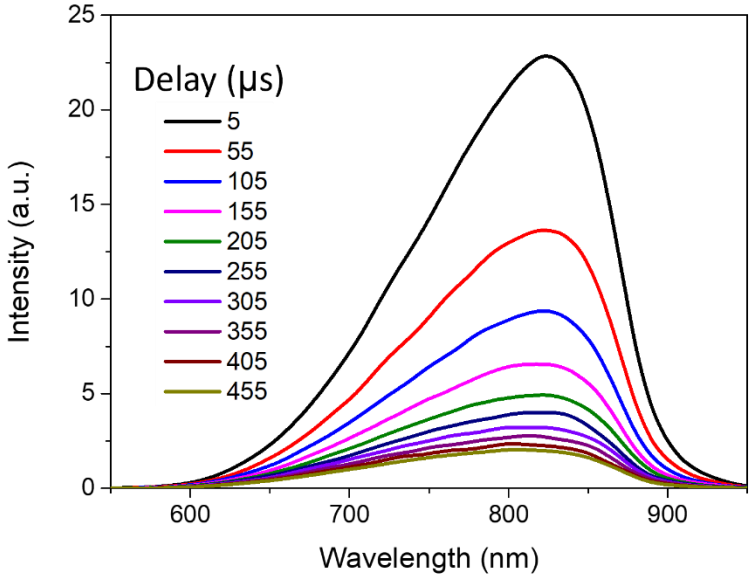


Figure 4.1.20 - Time-resolved emission spectroscopy of sample $Se_{0.1}$ - 900 °C by applying longer delay times, with λ_{exc}=337 nm.

Blank sample, Se_0 gel - 900 °C, at such or even longer delay times, exhibited the characteristic emission spectra of $[S_3]^{2-}$ clusters (**Figure C.1.4.B**), centered at around 790 nm.

4.1.2.1 Temperature Studies

The NIR emission of sample $Se_{0.1}$ - 900 °C was further investigated under 77 K. The steady-state emission and excitation spectra at this temperature and room temperature (RT) are illustrated in **Figure 4.1.21**. Once again, significant spectral broadening was observed, leading to a consequent shift in the emission spectra maxima with increasing temperature. The photoluminescence decay times were then investigated at 800 nm, around the emission maxima.

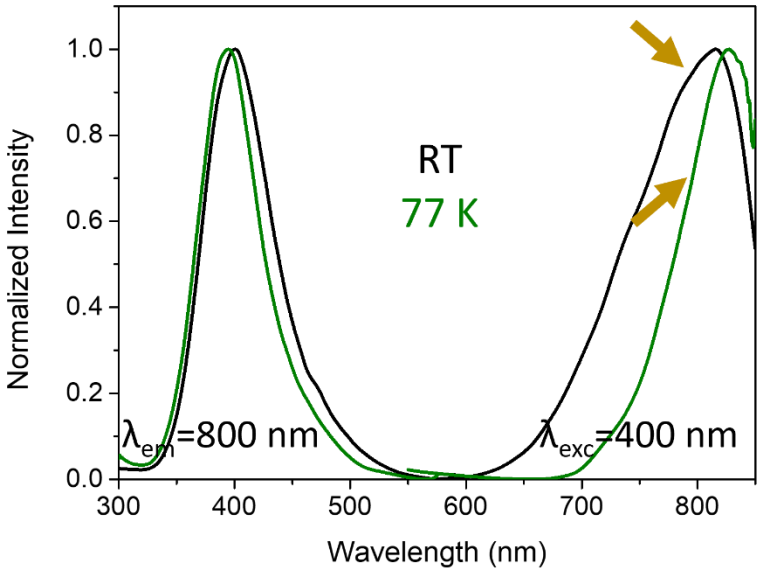


Figure 4.1.21 - Steady-state emission (λ_{exc}=400 nm) and excitation (λ_{em}=800 nm) spectra of sample $Se_{0.1}$ - 900 °C at room temperature (RT) represented in black and at 77 K represented in green.

Bi-exponential decay times were observed at both temperatures (**Figure 4.1.22**). This behavior was previously assigned to the presence of different local environments of the same emitting species, tentatively identified as $[Se_3]^{2-}$ clusters. Increasing the temperature resulted in faster decay components and consecutive average decay time. This phenomenon was expected since at least the vibrations and rotations of the clusters (non-radiative pathways) increase with temperature. Furthermore, these results closely match the ones from chapter **3** in selenium-doped zeolites with comparable selenium loadings (**Table 3.3**).

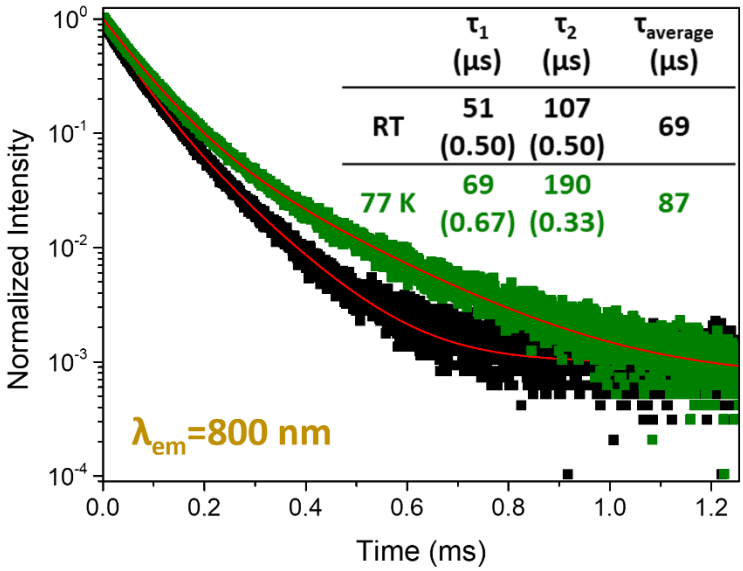


Figure 4.1.22 - Photoluminescence decay times of sample $Se_{0.1}$ - 900 °C at liquid nitrogen temperature (77 K) and at room temperature (RT) monitoring the emission at 800 nm. The insets show the components resulting from the decay fittings (see the resulting residuals in **Figure C.1.5**) and the average decay time. In brackets is the relative amplitude of each component. Note that the average decay times were calculated using the pre-exponential factors.

Additional experiments, detailed in sections **7.5** and **7.6**, reveal that the NIR emission remains unaffected by oxygen and humidity/water. This is consistent with the previous experiments performed on selenium NIR emission.

Remarkably, this study reveals a consistency in NIR emission across different starting zeolites, whether from commercial Na-LTA in chapter **3** or from nanosodalite. This outcome deviated from the initially expected behavior, given that nanozeolites typically exhibit enhanced surface areas than their bulk counterparts, such as commercial Na-LTA zeolite, which may affect their optical properties. The unexpected similarity among these samples may be attributed to the transformation of nano-sized zeolites following the high-temperature synthesis at 900 °C, as evidenced by SEM images in **Figure 4.1.1** and **Figure 4.1.3** for as-synthesized nanosodalite samples versus **Figure 4.1.4** and **Figure 4.1.5** for the same samples submitted to 900 °C. DLS analysis also confirms the agglomeration of these nanozeolites due to thermal treatment, as illustrated in **Figure 4.1.6**.

Overall, while these materials successfully produced a desirable single NIR emission, the high-temperature synthesis significantly impacted their integrity, causing agglomeration and destroying the once nano-sized zeolites. Consequently, they are deemed unsuitable for *in vivo* imaging.

4.1.3 Conclusions

This study provides important insights into the synthesis and optical properties of novel single NIR-emitting selenium zeolites starting from nanosodalite. When low amounts of selenium are used, nepheline and carnegieite structures formation is observed, whereas increasing selenium contents leads to sodalite zeolite predominance. This highlights the stabilizing effect that this element has on sodalite zeolite, hindering the formation of nepheline and carnegieite at higher concentrations. Similar to chloride, the relatively large size of selenium stabilizes the sodalite cages when confined in the center of these structures, preventing their conversion into other structures during high-temperature synthesis.

Furthermore, this investigation confirms previous observations from chapter **3**, indicating that two distinct selenium emissive species can be produced within these zeolites:

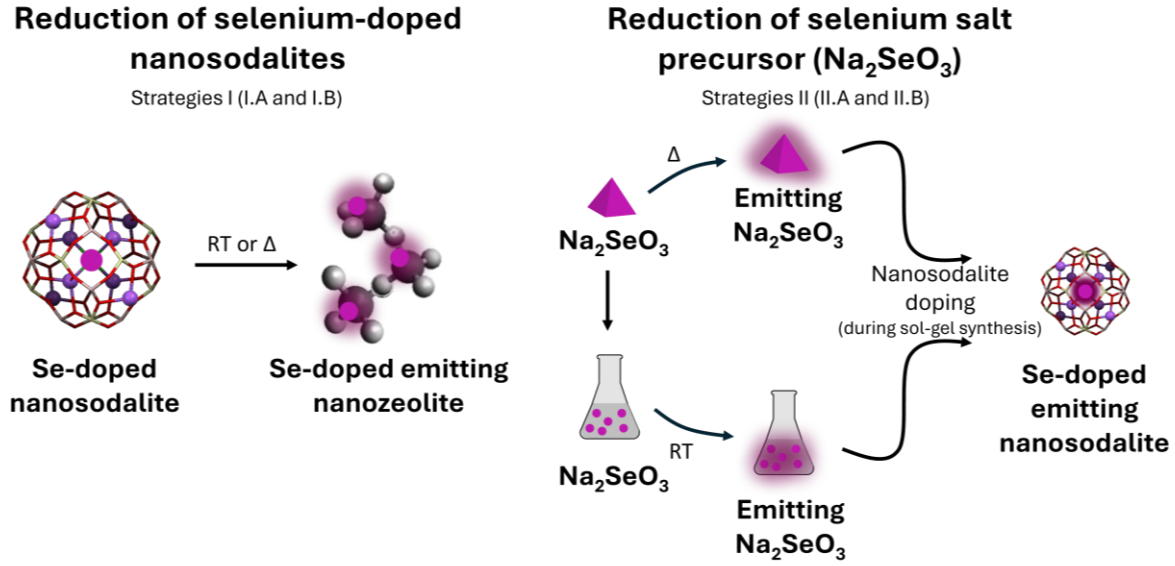
1) $[Se_2]^-$ clusters associated with sodalite zeolite become evident in diffuse reflectance spectra at higher selenium loadings. However, their characteristic red emission is completely quenched and thus not observed, presumably due to a double electron transfer mechanism between different $[Se_2]^-$ species.

2) NIR-emitting species, tentatively assigned to $[Se_3]^{2-}$ species, were previously related with nepheline and/or carnegieite structures. All samples produced in this study contain both types of aluminosilicates, and photophysical characterization only exhibits this NIR emission. However, some of these samples predominantly consist of carnegieite (up to 94%), suggesting a strong association of this structure with the selenium NIR-emitting species. Moreover, this emission displays external quantum efficiencies (EQEs) of 3% and average decay times of around 74 μs.

Unfortunately, the high-temperature synthesis at 900 °C used to produce these materials destroyed the as-synthesized nanozeolites, forming large, heterogeneous agglomerates unsuitable for *in vivo* imaging. However, as demonstrated in previous chapters, they are still suitable for security systems and veins imaging applications.

4.2 Exploring Several Synthetic Strategies to Obtain NIR-Emitting Nanozeolites

The previous subchapter demonstrated that subjecting nanosodalites to high-temperature synthesis at 900 °C resulted in zeolites with single NIR-emitting properties. However, these materials lost their nano-size dimensions in the process. For *in vivo* imaging applications, they must maintain sizes up to 100 nm and high dispersibility to facilitate cell uptake. Therefore, alternative synthetic strategies were explored in this subchapter to produce selenium-doped emitting nanozeolites successfully. **Scheme 4.2.1** illustrates the principal synthetic pathways pursued. These adopted strategies consisted of **1)** reducing selenium in nanosodalites already doped with sodium selenite, resulting in selenium-doped emiting nanozeolites and **2)** reducing the selenium precursor (Na_2SeO_3) and then using the resulting emitting product as a starting material in the sol-gel synthesis of nanosodalite zeolite. Both strategies were tested in solid-state and solution phases.



Scheme 4.2.1 - Synthetic pathways explored in this subchapter to achieve emissive selenium-doped nanosodalites. Strategies I.A and II.A involve high-temperature (Δ) synthesis in solid-state, while strategies I.B and II.B comprise room-temperature (RT) synthesis in solution.

4.2.1 Dispersibility studies of non-doped nanosodalite zeolites

This study was initiated by investigating the dispersibility of non-doped nanosodalites synthesized through a sol-gel synthesis. For further details on the experimental procedure, refer to

section **7.1.2**. This preliminary analysis aimed to evaluate the limitations in manipulating these materials before introducing selenium and subsequently focusing on their photophysical properties. The as-synthesized nanozeolites were primarily analyzed in their colloid form (a stable suspension of nanozeolite particles dispersed uniformly throughout MilliQ water), followed by examination after drying at 35 °C and subsequent manual milling, using dynamic light scattering (DLS) analysis. The aggregation of zeolites increases as follows: colloid < drying < milling, resulting in an average particle size distribution (z-average) of 87.5 nm < 2 µm < 9 µm, respectively, as illustrated in **Figure 4.2.1.A-C.**

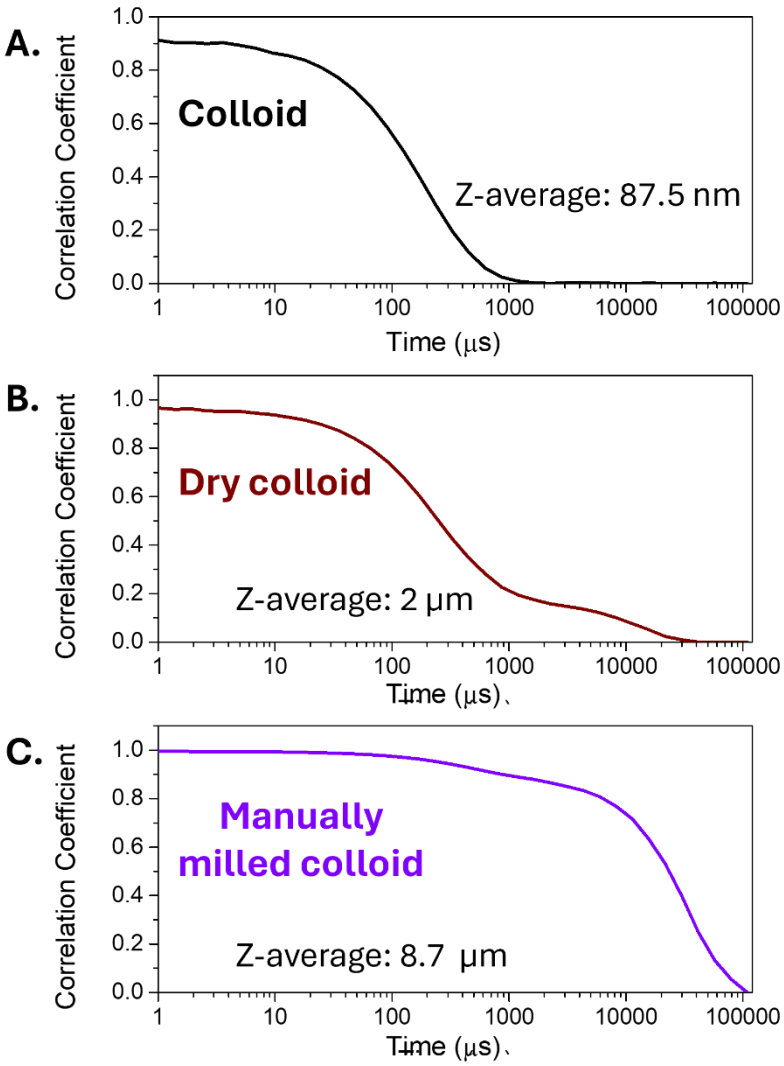


Figure 4.2.1 - Dynamic light scattering (DLS) autocorrelation functions of non-doped nanosodalite in colloid form (**A**) after colloid drying and (**B**) following manual milling of the colloid (**C**).

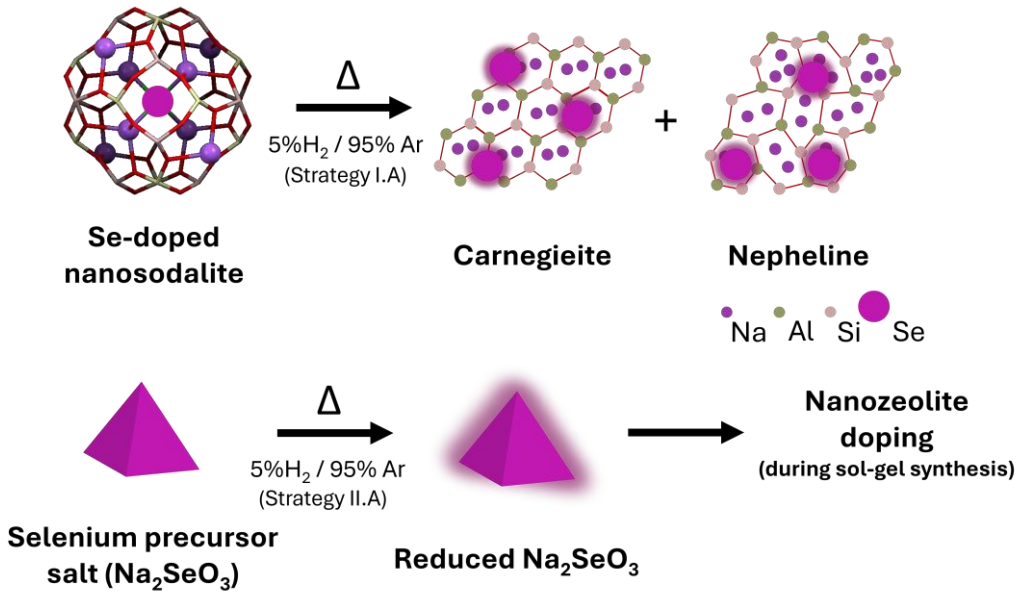
Aggregation may result from strong interactions or covalent bonding between the zeolite surfaces of different particles. Furthermore, this reduces the dispersibility of particles,

causing larger aggregates to be more challenging to keep suspended in solution, with some sedimentation observed. Various methods, including ball-milling, ultrasonic treatment and the use of surfactants, were attempted to disperse these aggregated particles. However, none of these methods yield satisfactory results. (Refer to section **7.2.9** for more information about the DLS technique, and see section **7.3** for the attempted dispersibility procedures.)

As a result, one of the previously used doping methods, which involved mixing non-doped zeolite with sodium selenite salt and homogenizing the mixture, was considered unsuitable. Instead, to address aggregation problems, preference was given to doped zeolite prepared through the sol-gel method (as used in gel samples in subchapter **4.1**).

4.2.2 Solid-state reduction

Based on the background of solid-state reduction conducted in this thesis, the solid-state reduction phase was examined first before performing selenium reduction in solution. Therefore, two different methods involving high-temperature synthesis (Δ) were tested: direct reduction of selenium-doped nanosodalites (strategy I.A) and reduction of selenium precursor salt - Na_2SeO_3 - (strategy II.A), as illustrated in **Scheme 4.2.2**.



Scheme 4.2.2 - Strategies adopted for selenium reduction in solid-state to produce emissive nanozeolites, encompassing strategies I.A and II.A, according to **Scheme 4.2.1**.

It is noteworthy that, based on previous work, there is strong evidence that nepheline and carnegieite structures (particularly the latter one, as evidenced in subchapter **4.1**) are related

with selenium NIR-emitting species. Furthermore, it has also been demonstrated that these aluminosilicates can be formed from sodalite zeolite during high-temperature synthesis.

4.2.2.1 Reduction in selenium-doped nanosodalite

Strategy I.A

Based on the initial dispersibility studies, a more concentrated selenium-doped nanosodalite was produced through a sol-gel synthesis, with the ideal final composition of $[Na_6(H_2O)_8][Si_6Al_6O_{24}]\underline{Se_7}$, further denominated as sample Se_7 gel. Refer to section **7.1.2** for more information about the experimental procedure. Dynamic light scattering (DLS) analysis of the as-synthesized colloid revealed the presence of highly dispersible nanoparticles with average sizes of around 136 nm, as illustrated in **Figure 4.2.2.A-B**.

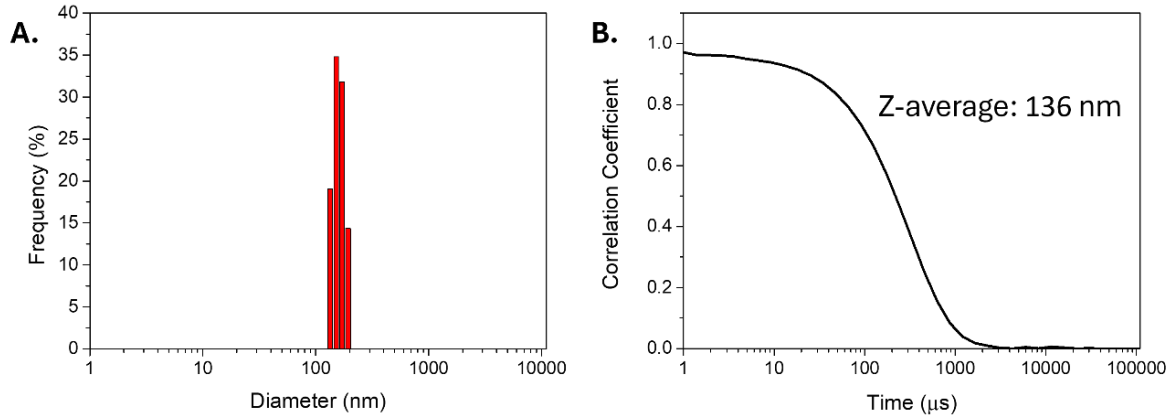


Figure 4.2.2 - Dynamic light scattering (DLS) analysis of selenium-doped nanosodalite (Se_7 gel) - (**A**) Size distribution and (**B**) autocorrelation function.

SEM images corroborate these results, showing nano-sized zeolite structures with sizes around 85 nm (**Figure 4.2.3.A-B**). For more information about this technique, see section **7.2.14**.

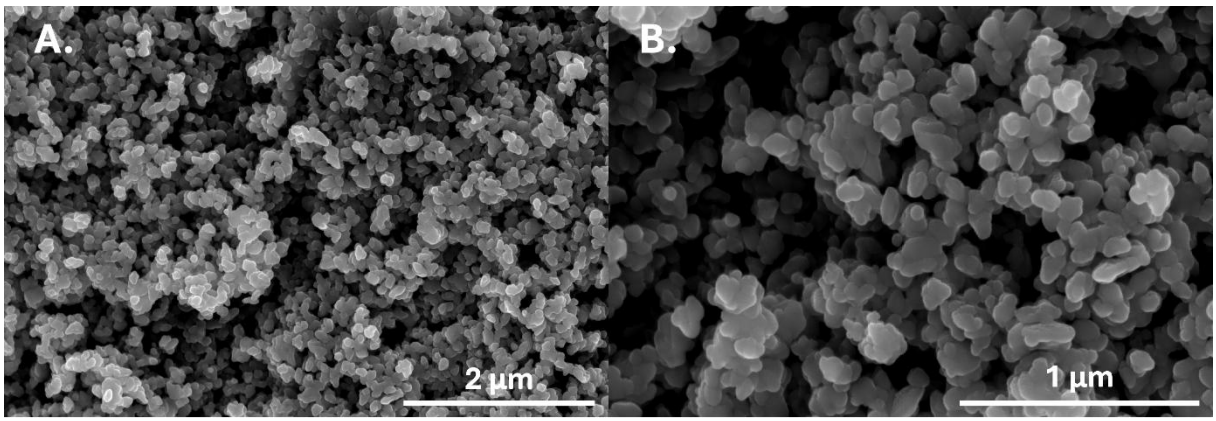


Figure 4.2.3 - (**A**, **B**) SEM images of the produced Se_7 gel nanozeolite sample using two different magnifications.

Elemental analysis performed using energy dispersive spectroscopy (EDS) alongside SEM analysis confirmed the incorporation of selenium into the produced zeolites (**Table 4.2.1**). Despite this success, the method was not the most efficient, as indicated by the discrepancies between the nominal Al/Se ratios and those obtained. However, higher selenium loadings were achieved compared to other selenium-doped samples discussed in subchapter **4.1**, with the exception of sample Se_1 - 900 °C (**Table 4.1.2**).

Table 4.2.1 - Elemental analysis of selenium-doped nanozeolite sample using EDS technique.

Sample	Nominal Al/Se	Molar percentage composition (%)						Obtained Al/Se
		Na	Si	Al	O	Se	Cu	
Se_7 gel	0.86	13.27	10.55	10.46	65.40	0.25	0.08	41.83

Powder X-ray diffraction (PXRD) analysis confirmed that the obtained material exhibits a pure sodalite crystalline phase (**Figure 4.2.4**), indicating a successful synthesis of selenium-doped nanosodalite. Refer to section **7.2.13** for more information about this technique.

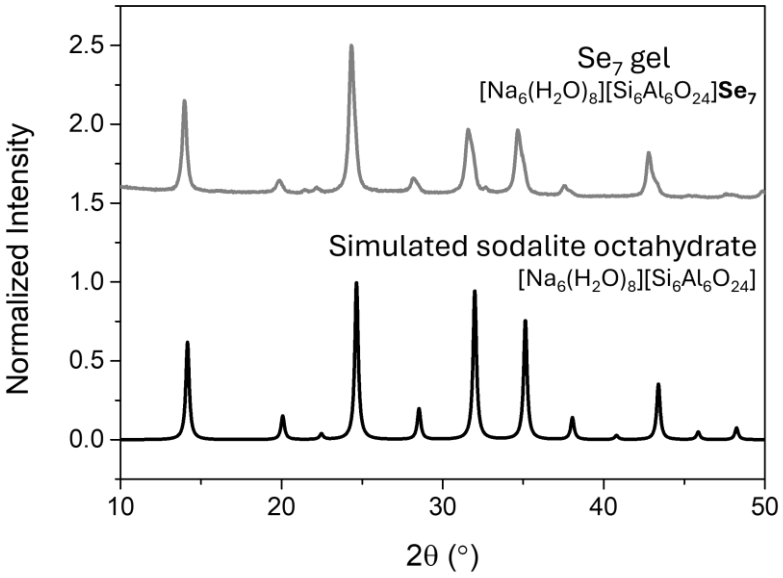


Figure 4.2.4 - PXRD diffractograms of the produced selenium-doped Se_7 gel nanosodalite sample compared with the simulated diffractogram of sodalite octahydrate, with the composition $[Na_6(H_2O)_8][Si_6Al_6O_{24}]$ in black, according to reference **145**.

Next, various strategies were attempted to induce the desirable emitting properties of these selenium-doped nanosodalites by directly reducing them. Two synthesis parameters were modified: the synthesis temperatures (700 °C, 800 °C, and 900 °C) and the milling of the material (considering the differences found in the dispersibility studies of non-doped nanosodalites discussed in section **4.2.1**). The high-temperature alumina crucible was then divided into two equal parts, one filled with manually milled zeolite and the other with non-milled zeolite. After 1 hour of synthesis under a reducing atmosphere, colored materials were observed only at 900 °C, as illustrated in **Figure 4.2.5**. Refer to section **7.1.3** for additional information about the sample experimental procedure.

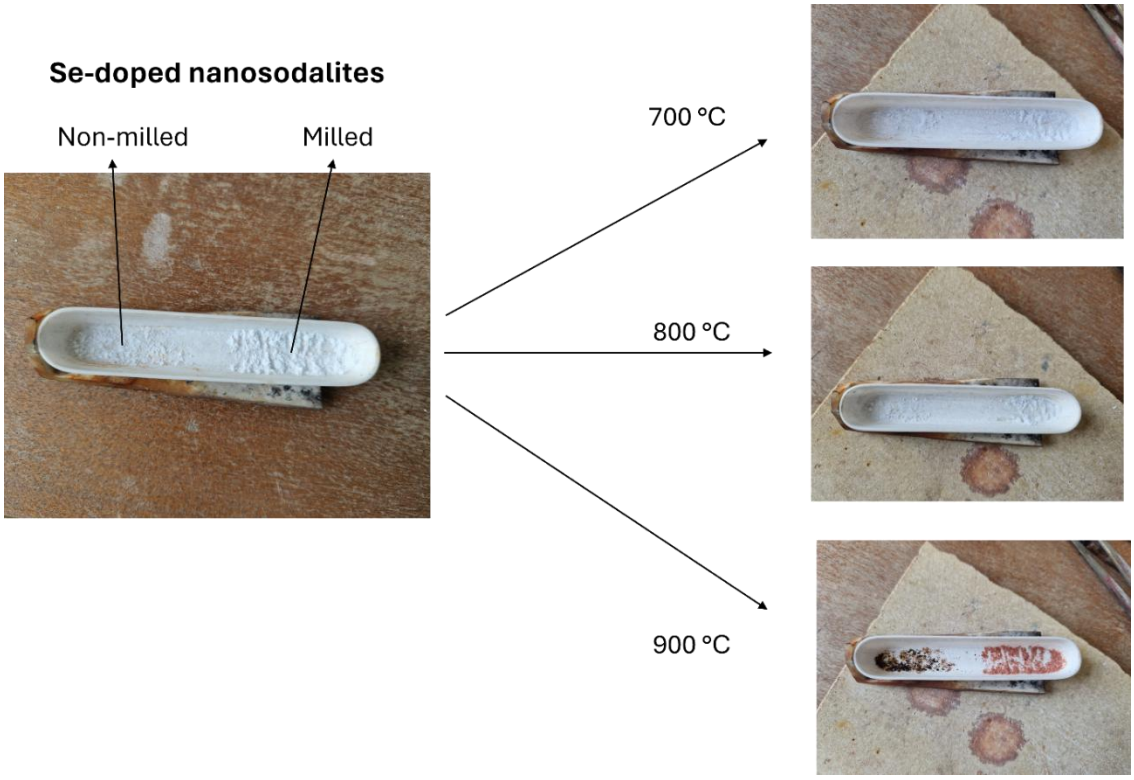


Figure 4.2.5 - Photographs of the synthesis alumina crucible filled with selenium-doped Se_7 gel nanosodalite before and after high-temperature synthesis at 700 °C, 800 °C and 900 °C.

To investigate whether this thermal treatment impacts the aggregation and dispersibility of these materials, they were analyzed once again using the DLS technique. The results revealed that the non-milling samples subjected to 700 °C and 800 °C were less aggregated and more dispersive than those milled (**Figure 4.2.6.A-B**). This finding is consistent with the initial studies on non-doped nanosodalites, which demonstrated a similar effect (**Figure 4.2.1.A-C**).

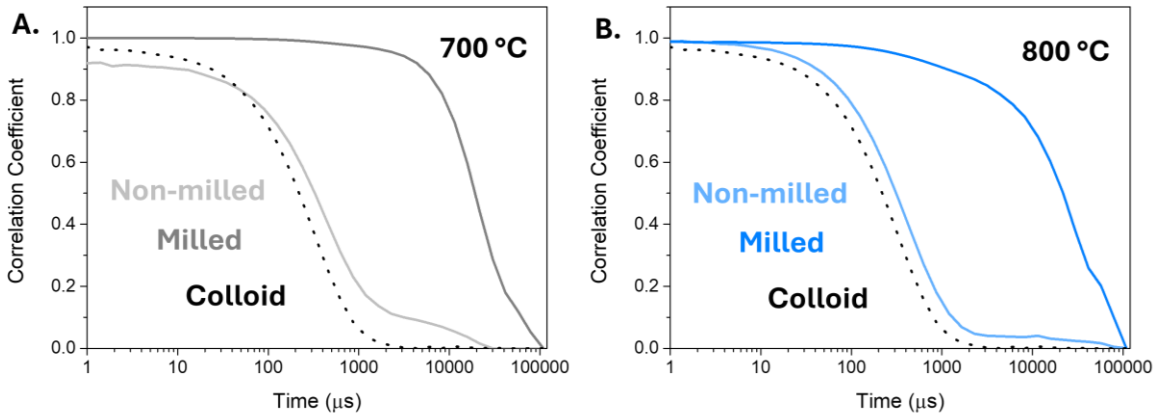


Figure 4.2.6 - Dynamic light scattering (DLS) autocorrelation function comparison of the colloid (**Figure 4.2.2.A-B**) with milled and non-milled selenium-doped Se_7 gel nanosodalite samples after high-temperature synthesis (**A**) at 700 °C and (**B**) 800 °C.

Alternatively, when submitted to 900 °C (the temperature that induced color changes in the samples), increased aggregation and lower dispersibility were detected in both milled and non-milled samples (**Figure 4.2.7**).

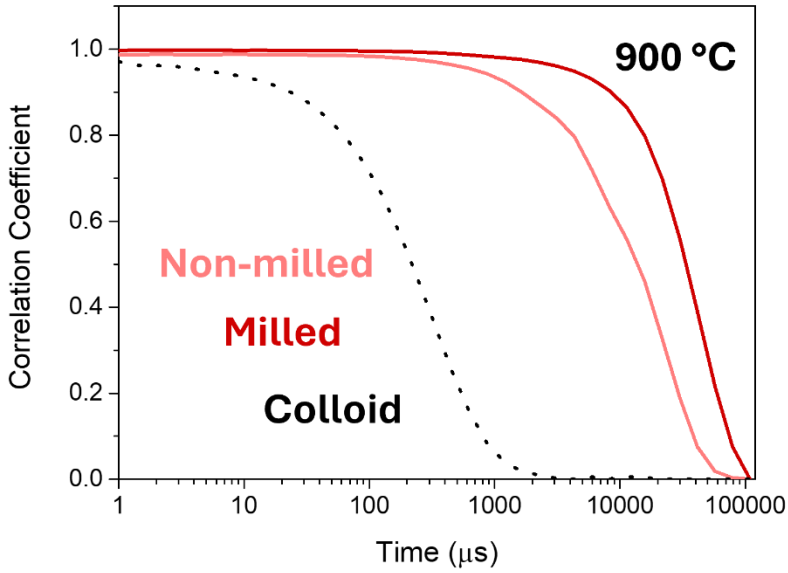


Figure 4.2.7 - Dynamic light scattering (DLS) autocorrelation function comparison of the colloid (**Figure 4.2.2.A-B**) with milled and non-milled selenium-doped Se_7 gel nanosodalite samples after high-temperature synthesis at 900 °C.

The mean z-average values of the analyzed samples are summarized in **Table 4.2.2**, showing a notable increase in non-milled samples from 700 °C and 800 °C to 900 °C. In milled samples, slight differences were observed, ranging from around 9 μm to 15 μm.

Table 4.2.2 - Mean z-average particle size values obtained from DLS measurements averaged over five scans. See **Figure 4.2.2**, **Figure 4.2.6.A-B** and **Figure 4.2.7**.

	Colloid	700 °C		800 °C		900 °C	
		Non-milled	Milled	Non-milled	Milled	Non-milled	Milled
Z-average	141 ± 14 nm	3.8 ± 1.7 μm	11.7 ± 2.3 μm	1.9 ± 0.5 μm	9.3 ± 2.0 μm	11.7 ± 2.9 μm	15.1 ± 2.2 μm

These values are consistent with those obtained on non-doped nanozeolites without thermal treatment, where z-average values of 2 μm and 8.7 μm were achieved after drying and manually milling these materials, respectively. This suggests that the values obtained at 700 °C and 800 °C may be attributed to strong surface interactions between different nanozeolite particles rather than structural alterations caused by temperature.

This observation aligns with the SEM images of nanosodalite samples subjected to 700 °C (**Figure 4.2.9.A-B**), demonstrating the preservation of zeolite integrity, size and shape at this temperature.

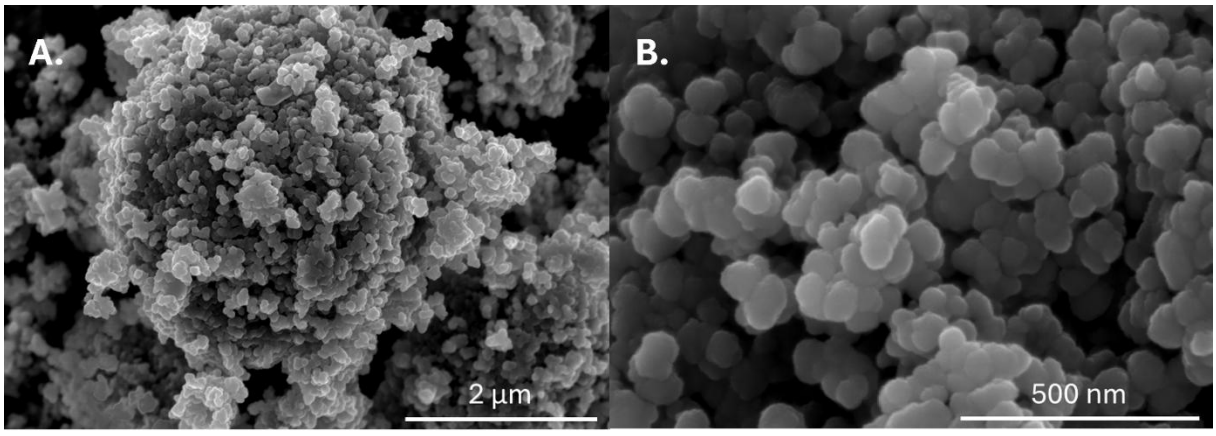


Figure 4.2.8 - (**A**, **B**) SEM images of the nanozeolite samples submitted to 700 °C using two magnifications. Note that this sample was milled before SEM analysis.

However, at 900 °C, a collapse of the zeolite structure was observed, wherein nano-sized particles fused together to form large agglomerates (**Figure 4.2.9.A-B**). This phenomenon indicates that the formation of large agglomerates, characterized by average sizes of around 13 μm and low dispersibility as detected by DLS analysis in both milled and non-milled samples, may be

due to a deep structural compromise rather than merely surface interaction, as observed at 700 °C and 800 °C.

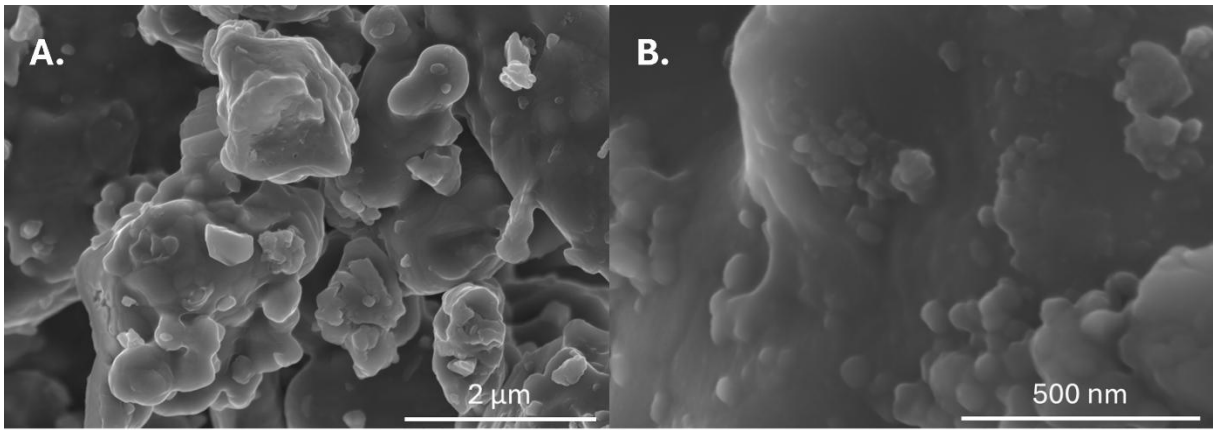


Figure 4.2.9 - (**A**, **B**) SEM images of the nanozeolite samples submitted to 900 °C using two magnifications. Note that this sample was milled before SEM analysis.

The PXRD diffractograms of these samples revealed that the thermal treatment at 700 °C and 800 °C did not affect the crystalline phases, demonstrating a pure sodalite crystalline phase (**Figure 4.2.10**). However, at 900 °C, a mixture of sodalite, nepheline and carnegieite was consistently present, with approximate contributions of 18%, 7% and 75%, respectively, regardless of the milling process.

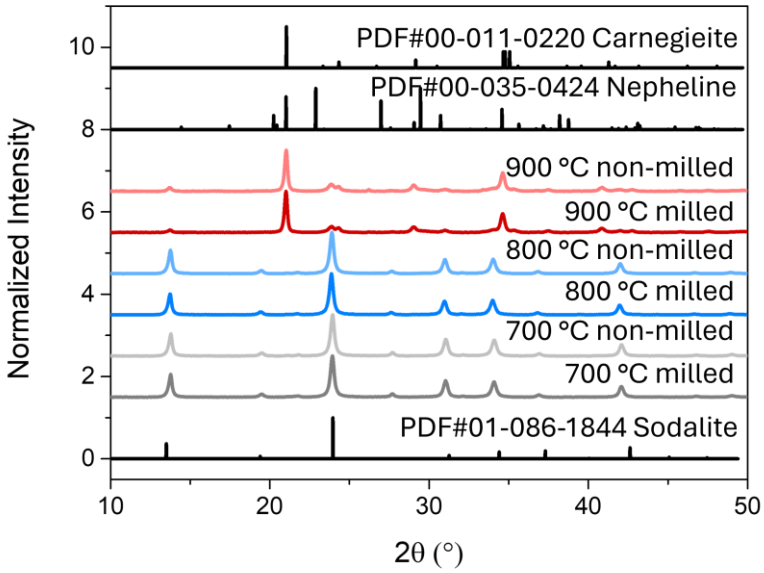


Figure 4.2.10 - PXRD diffractograms of the produced samples illustrating the impact of thermal treatment and milling. The samples were subjected to varying temperatures: 700 °C (gray), 800 °C (blue) and 900 °C (red). Non-milled samples exhibit lighter colors, while milled show darker colors. The ICDD standard reference card for comparison includes 01-086-1844 sodalite ($Na_8Si_6Al_6O_{24}Cl_2$), 00-035-0424 nepheline ($Na_4Si_4Al_4O_{16}$) and 00-011-0220 carnegieite ($Na_4Si_4Al_4O_{16}$).

These results indicate that the sodalite zeolite begins to undergo transformation at 900 °C, consistent with the observed changes in the SEM images, which demonstrate the impact of this temperature on the integrity of these materials. Furthermore, all these changes seem necessary to induce coloration in these samples (**Figure 4.2.5**).

Since differences were only detected in these mentioned samples i.e., the ones submitted at 900 °C, they were further investigated. Notably, the absorption properties at this temperature differ depending on the milling process, although the same crystalline structures were present. The diffuse reflectance spectra, after applying the Kubelka-Munk theory[103], are presented in **Figure 4.2.11** (see section **7.2.2** for more details about this technique and sample characterization). In the milled sample, a distinct $[Se_2]^-$ absorption band around 490 nm is evident, alongside an absorption band at 400 nm assigned to the absorption of the NIR-emitting species, tentatively assigned to $[Se_3]^{2-}$ clusters. The non-milled sample is brownish, with an absorption spectrum that extends across the visible region, making direct attributions challenging. However, similar spectra to those produced here were already observed in the synthesized samples in subchapter **4.1** (**Figure 4.1.9**).

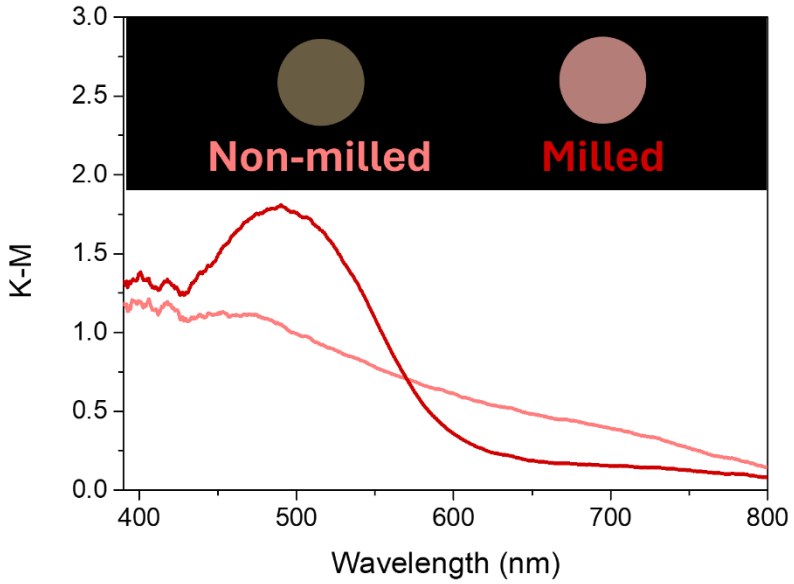


Figure 4.2.11 - Diffuse reflectance spectra of the milled and non-milled selenium-doped Se_7 gel nanosodalite samples after the high-temperature synthesis at 900 °C. The insets show the photos of the samples under ambient light.

Additionally, the photoluminescent properties of the NIR-emitting species in these samples were also studied (see section **7.2.3** for more details about this technique), with observed differences in emission and excitation spectra. NIR emission was detected in both samples, with the non-milled sample exhibiting a much higher intensity than the milled one (**Figure 4.2.12.A**). When comparing the normalized spectra, a slight contribution in the visible region is observed in the latter spectrum (**Figure 4.2.12.B**). This may be due to the presence of $[Se_2]^-$ clusters in this sample, as demonstrated in the diffuse reflectance spectra (**Figure 4.2.11**).

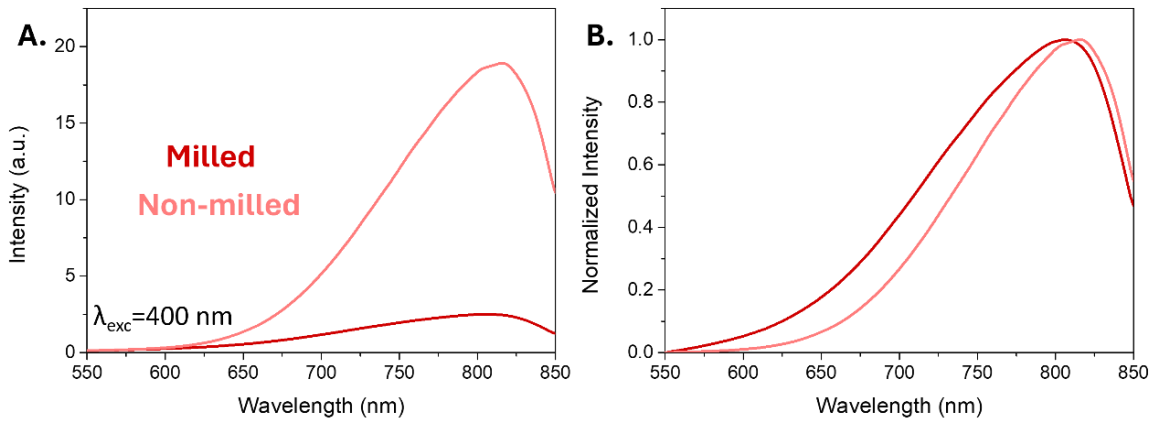


Figure 4.2.12 - (**A**) Emission, λ_{exc}=400 nm, and (**B**) corresponding normalized spectra of the milled and non-milled selenium-doped Se_7 gel nanosodalite samples after the high-temperature synthesis at 900 °C.

Indeed, the corresponding excitation spectra of the emission at 800 nm reflect these differences. In the non-milled sample, only the band at 400 nm associated with the NIR-emitting species is observed. In contrast, the milled sample exhibits additional characteristic bands of $[Se_2]^-$ clusters at 350 and 490 nm (**Figure 4.2.13.A-B**). This last finding may explain the differences in intensity found in emission and excitation spectra since, in the milled sample, a mixture of emitting species is formed.

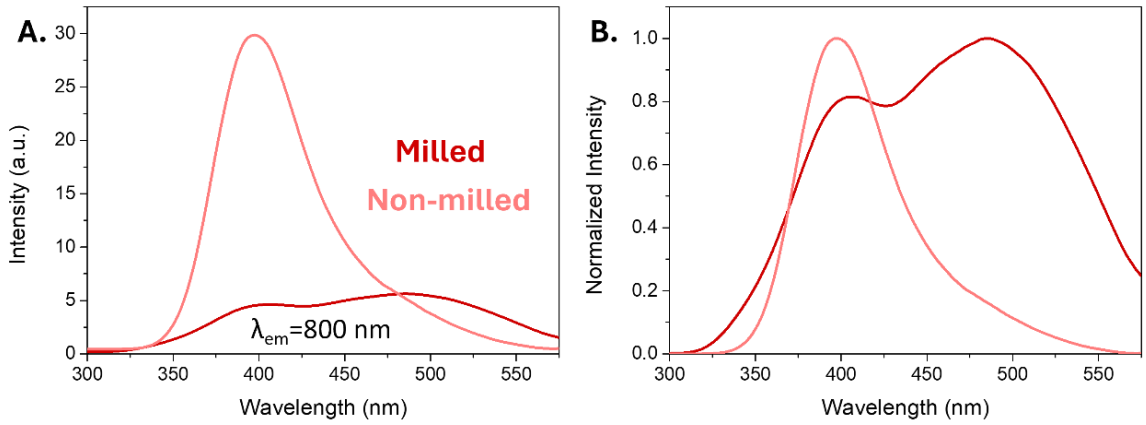


Figure 4.2.13 - (**A**) Excitation, λ_{em}=800 nm, and (**B**) corresponding normalized spectra of the milled and non-milled selenium-doped Se_7 gel nanosodalite samples after the high-temperature synthesis at 900 °C.

In summary, these studies suggest that the formation of desirable optical properties is intrinsically linked with the collapse of nano-sized zeolite structure and subsequent crystalline phase transformation, occurring at 900 °C. Furthermore, nanosodalite milling should be avoided, as it causes nanoparticle aggregation and lower dispersibility, probably due to strong surface interactions between different nanozeolite particles. **Table 4.2.3** summarizes all these findings, according to the achieved desirable optical properties and nanoparticle dispersibility, corresponding to the material milling and thermal treatment used.

Table 4.2.3 - Summary of results comparing the presence of the desirable optical properties and dispersibility of the samples after thermal treatment at 700 °C, 800 °C and 900 °C.

	700 °C		800 °C		900 °C	
	Non-milled	Milled	Non-milled	Milled	Non-milled	Milled
Optical properties	✘	✘	✘	✘	✓	✓
Dispersibility	✓	✘	✓	✘	✘	✘

4.2.2.2 Selenium salt reduction

Strategy II.A

Considering the limitations encountered while handling these nanozeolites, where mere drying impacts their tendency to aggregate and disperse, the ideal approach for manipulating these materials is to maintain them in solution as colloids. Therefore, the upcoming synthetic strategy will entail two steps: firstly, the reduction of the selenium precursor salt (Na_2SeO_3), followed by its use as raw material in nanozeolites sol-gel synthesis.

According to the safety data sheet for sodium selenite reagent, its melting point occurs at temperatures higher than 350 °C. Thus, this salt was subjected to a solid-state synthesis performed at a higher temperature of 500 °C for 1 hour under a reducing atmosphere of 5% H_2 / 95% Ar. Refer to section **7.1.4** for more information about the experimental procedure. This treatment yields a brownish powder, as shown in the corresponding diffuse reflectance spectrum depicted in **Figure 4.2.14.A**. The produced spectrum does not exhibit discrete absorption bands, absorbing along the visible region. This behavior was previously observed in samples with higher amounts of nepheline and carnegieite crystalline phases, as in those produced in subchapter **4.1** (**Figure 4.1.9**). The NIR-emitting species are associated with these aluminosilicates, absorbing at around 400 nm and emitting at *ca.* 815 nm. However, alternative to the previously discussed samples that display an absorption maxima at 400 nm, the spectrum of this reduced salt exhibits a maximum at around 350 nm (**Figure 4.2.14.A**). These differences may result from the formation of different chromophores due to the reduction of the selenium precursor in the absence of an aluminosilicate matrix. A direct comparison with existing literature was not feasible since no similar spectrum has been previously reported.

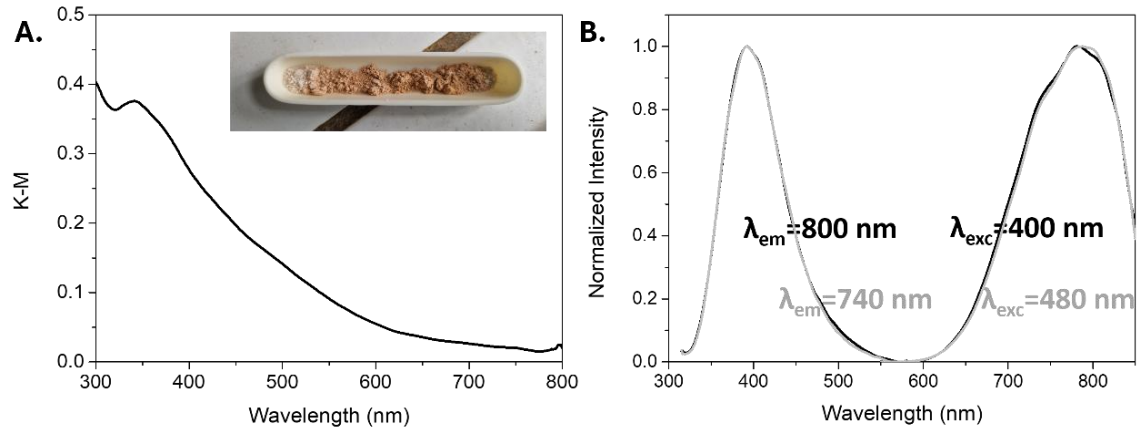


Figure 4.2.14 - Diffuse reflectance (**A**) and excitation (λ_{em}=740 and 800 nm) and emission (λ_{em}=400 and 480 nm) spectra (**B**) of the produced sample. The inset shows the photos of the sample under ambient light.

Further photophysical analysis of the steady-state emission of the produced sample revealed the absence of excitation and emission of $[Se_2]^-$ clusters, characterized by their red emission spectra. Instead, only the presence of the NIR emission was observed (**Figure 4.2.14.B**), which was tentatively assigned to the presence of $[Se_3]^{2-}$ species in previous studies.

Notably, the photoluminescence decay times monitoring this emission at 800 nm (λ_{em}=800 nm) showed a bi-exponential behavior with decay components of 34 µs and 54 µs at room temperature, resulting in an average decay time of 39 µs (**Figure 4.2.15**). This bi-exponential behavior may be due to the intrinsic different local environments of the emitters, as previously discussed. However, they are not related to the aluminosilicate matrix since only the reduced salt is present here. See additional information about photoluminescence decay times in section **7.2.4**.

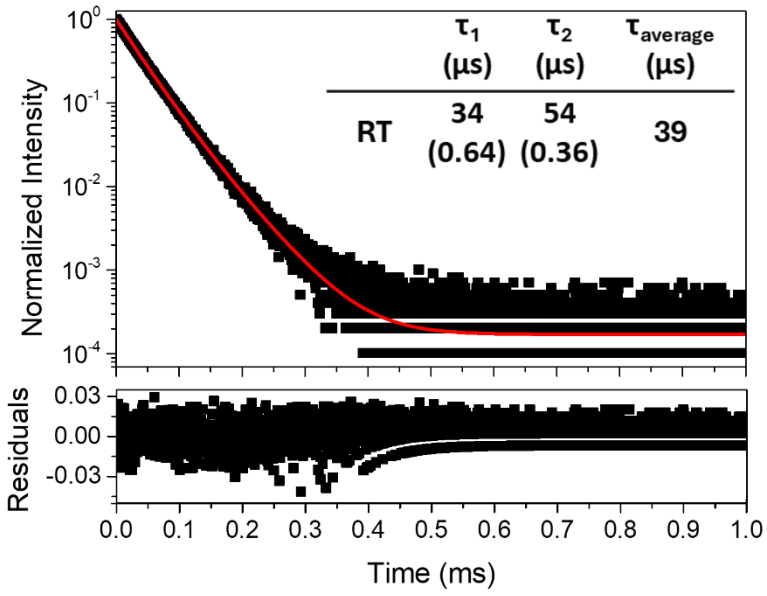


Figure 4.2.15 - (**Above)** Photoluminescence decay time of reduced sodium selenite acquired at room temperature (RT). The insets show the components resulting from the decay fitting and the average decay time. In brackets is the relative amplitude of each component. Note that the average decay times were calculated using the pre-exponential factors. (**Below**) corresponding residuals.

Both decay components were already observed in the produced samples that exhibited a single NIR emission starting from nanosodalite in subchapter **4.1** (samples $Se_{0.1}$ - 900 °C and Se_1 - 900 °C). **Table 4.2.4** summarizes the decay components of the photoluminescence decay times of these two samples, compared with the reduced salt (Na_2SeO_3). The average decay times of selenium NIR emission are slower in these two selected samples and in all synthesized

samples produced in this thesis, including the selenium-doped zeolites in chapter 3 (**Table 3.3**), compared to the reduced salt. This indicates that the aluminosilicate matrix may influence the photophysical properties of these emitters. For example, it could reduce non-radiative pathways by limiting vibrations through confinement or by increasing distances between clusters, thereby minimizing energy transfer mechanisms.

Table 4.2.4 - Resume of decay components, their relative amplitudes and average decay times monitored at 800 nm room temperature, compared with the reduced salt sample (Na_2SeO_3).

Samples	τ_1 (µs)	Relative amplitude (A_1)	τ_2 (µs)	Relative amplitude (A_2)	τ_3 (µs)	Relative amplitude (A_3)	$\tau_{Average}$ (µs)
$Se_{0.1}$ - 900 °C	-	-	51	0.50	107	0.50	69
Se_1 - 900 °C	34	0.18	72	0.82	-	-	60
Na_2SeO_3 - 500 °C	34	0.64	54	0.36	-	-	39

Although directly reducing sodium selenite successfully achieves the desired NIR emission, completing strategy II.A as proposed in **Scheme 4.2.1** requires the entrapment of these clusters within the aluminosilicates matrix. Nepheline and particularly carnegieite structures would be the optimal aluminosilicate matrices to confine these species. However, the high-temperature zeolite conversion route is the most commonly used synthetic methodology to synthesize these aluminosilicates. As demonstrated above, this approach was considered unsuitable since it increases particle aggregation and decreases dispersibility. Furthermore, to the best of our knowledge, there is no existing literature on solution-based synthesis protocols for producing nano-sized versions of these two materials. Thus, selenium-doped nanosodalites using once more an initial gel composition of $18Na_2O{:}5SiO_2{:}1Al_2O_3{:}240H_2O{:}\underline{0.34SeO_2}$, resulting in a final ideal composition of $[Na_6(H_2O)_8][Si_6Al_6O_{24}]\underline{Se_1}$ were produced. Note that selenium doping was achieved by using luminescent reduced sodium selenite as raw material during the sol-gel synthesis of nanosodalites. For additional details on the experimental procedure, refer to section **7.1.2**. The initial composition exhibited a light-brown coloration, consistent with the reduced sodium selenite. However, this coloration faded over the synthesis period, resulting in a final product lacking desirable optical properties (i.e., NIR-emitting zeolite). The degradation of these species may result from prolonged exposure to the harsh, high pH conditions present during the three-day synthesis, potentially leading to the formation of their oxide form[147]. Additionally, PXRD diffractograms reveal that pure nanosodalite zeolite was produced in this synthesis (**Figure 4.2.16**). This may also influence the previous outcome since the findings

obtained in subchapter **4.1** strongly relate the selenium NIR-emitting species with nepheline and particularly carnegieite structures.

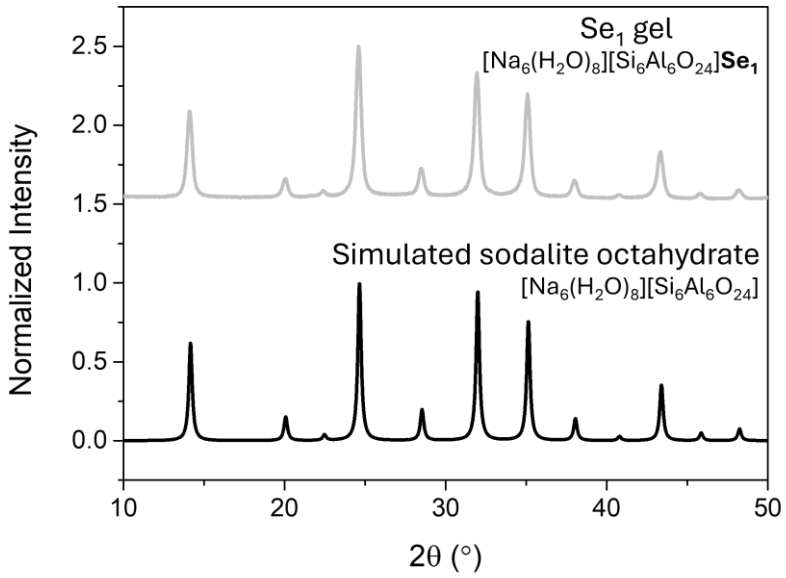


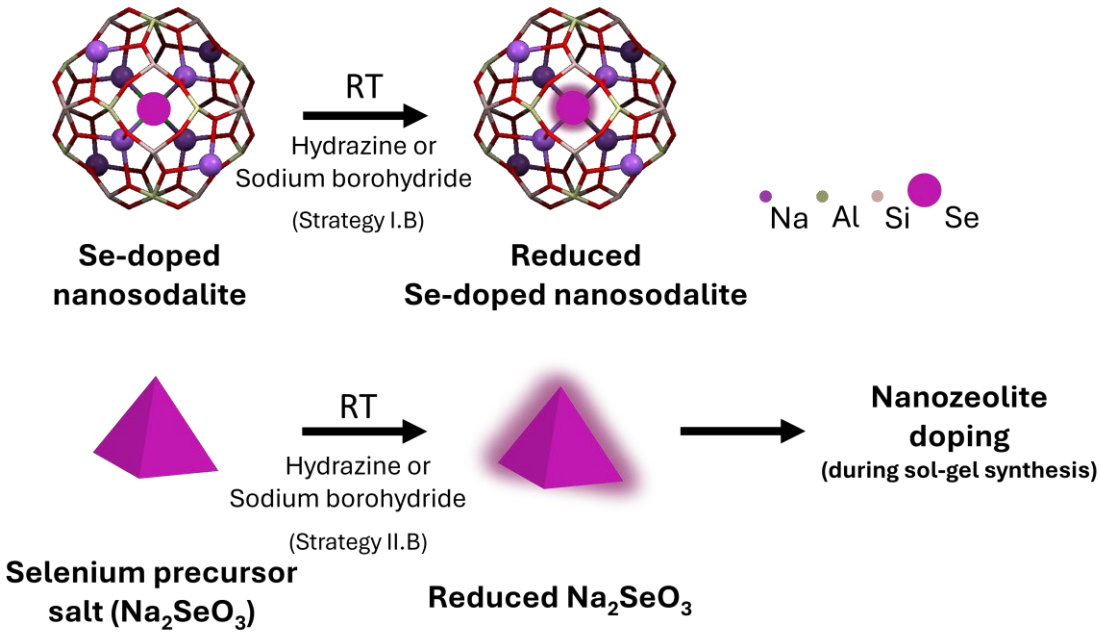
Figure 4.2.16 - PXRD diffractograms of the produced selenium-doped Se_1 gel nanosodalite sample compared with with the composition $[Na_6(H_2O)_8][Si_6Al_6O_{24}]$ in black, according to reference **145**.

In summary, the solid-state reduction methods tested did not produce the desired dispersible luminescent materials. Nevertheless, valuable information was obtained. It appears that there is a direct correlation between the disintegration of the nano-sized zeolite structure and the transformation of crystalline phases necessary to achieve the desirable optical properties in these selenium-doped nanosodalites. Additionally, the reduction of selenium precursor can lead to similar photophysical properties. However, its direct use as raw material during nanosodalite sol-gel synthesis was unsuitable, probably due to salt degradation caused by the high pH used and/or unsuitable aluminosilicate choice. Finally, working exclusively in solution with these materials was demonstrated to be the ideal method since drying processes increase nanoparticle agglomeration and decrease dispersibility.

4.2.3 Selenium reduction in solution

Since working in solution has proven to be the favored method for obtaining optimal dispersibility properties, similar reduction strategies to those used in the solid-state were tested. These processes involve the direct reduction of selenium-doped nanosodalites

(strategy I.B) and the reduction of selenium precursor salt - Na_2SeO_3 - (strategy II.B) at room temperature to obtain NIR-emitting materials, as illustrated in **Scheme 4.2.3**.



Scheme 4.2.3 - Strategies adopted for selenium reduction in solution to produce emissive nanozeolites, encompassing strategies I.B and II.B, according to **Scheme 4.2.1**.

Literature relative to selenium reduction in solution is quite limited. However, there are some reports starting from sodium selenite and even elemental selenium[148,149]. Krasowska et al.[149] provided a general overview of the reported reduction agents capable of reducing elemental selenium (Se) into disodium diselenide (Na_2Se_2). Examples of such agents include rongalite (sodium hydroxymethylsulfinate), sodium metal (Na), sodium borohydride ($NaBH_4$) and hydrazine (N_2H_4) (**Figure 4.2.17.A**). The necessity of synthesizing such $[Se_2]^{2-}$ species was driven by the need to link two organic molecules through a (Se-Se) bridge, thereby forming organic diselenide compounds for use in biological activities (**Figure 4.2.17.B**). Nevertheless, according to these mentioned studies, reduced selenium species were not isolated or analyzed. After their formation, they were directly added to the aromatic compound[150,151], with only the resulting compound being isolated and studied. A successful reduction of gray elemental selenium is characterized by a color change, described as a 'dark solution' or a 'brownish-red' coloration. Thus, to our knowledge, the existing literature does not provide insights into their behavior in solution.

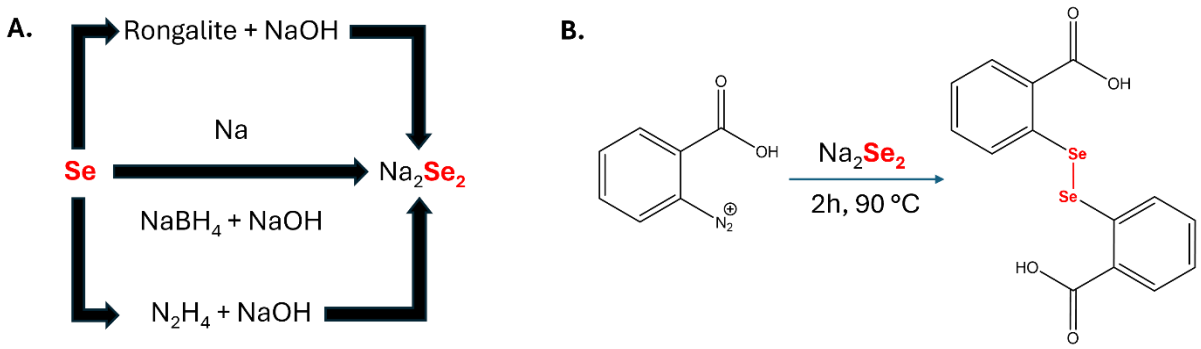


Figure 4.2.17 - (**A**) Strategies to obtain Na_2Se_2 starting from elemental selenium in solution. (**B**) Example of a reaction mechanism involving the use of Na_2Se_2. Adapted from reference **149**.

If $[Se_2]^{2-}$ species can indeed be produced, then it is expected that $[Se_2]^{-}$ clusters (one of the targeted selenium species which is associated with sodalite zeolite) will be formed immediately before their complete reduction. In zeolites, $[Se_2]^{-}$ and $[Se_2]^{2-}$ species are known and exhibit distinct properties. $[Se_2]^{2-}$ clusters produce photochromic properties, with a maximum induced-color occurring at around 500 nm[80]. In contrast, $[Se_2]^{-}$ species absorb around 350 nm and 490 nm and emit in the red region, as deeply investigated in chapter **3**. Consequently, their identification is expected to be easily confirmed if these reduced species are confined within zeolites (as proposed in **Scheme 4.2.3**).

Notably, for this work, which aims to produce highly dispersible selenium-doped NIR-emitting nanozeolites, it is more relevant to achieve these species in solution than to obtain the red-emitting $[Se_2]^{-}$ clusters. However, the nature of these responsible species remains unclear and has been tentatively assigned to $[Se_3]^{2-}$ clusters. Thus, designing a synthetic reduction pathway to successfully achieve these NIR-emitting species is challenging.

Nonetheless, the viability of using established protocols for reducing selenium in solution to obtain the desired emissive species was studied, employing the two different reduction approaches illustrated in **Scheme 4.2.3**, strategies I.B and II.B. As a starting point, the direct reduction of selenium-doped nanosodalites was initially explored.

4.2.3.1 Reduction in selenium-doped nanosodalite

Strategy I.B

Reduction in solution within zeolite cages has been previously demonstrated, such as the reduction of copper nanoparticles from Cu^{2+} to Cu^{0} in zeolite Linde Type L (LTL)[152]. Hydrazine and sodium borohydride were successfully used as reducing agents in that study. The relatively large pore opening of LTL zeolite, around 7.1 Å, allows for the diffusion of these agents into the pores of the material.

In the present study, the reduction of selenium-doped nanosodalite was investigated. For that, the Se_7 gel sample, whose characterization was previously demonstrated and discussed in section **4.2.2.1**, was subjected to reduction using hydrazine and sodium borohydride as the reducing agents. The protocols for these reductions are described in section **7.1.5**. However, no color change was observed following either reduction protocol. This may be explained by the small pore aperture of sodalite zeolite, around 2.4 Å[60], making it one of the smallest pore sizes within zeolites. When comparing the van der Waals size of the reducing agents, both are larger than the sodalite aperture[153]. Thus, available reducing agents capable of performing a reduction in solution involving the diffusion of the reducing agents inside the sodalite pores are quite limited. However, as pointed out in the previous section, hydrogen is a promising candidate.

4.2.3.2 Selenium salt reduction

Strategy II.B

Alongside the studies conducted above, the reduction of selenium precursor salt (Na_2SeO_3) was also tested, as illustrated in **Scheme 4.2.3**. Based on the background provided by Krasowska et al.[149] regarding the reduction of selenium in solution, sodium borohydride ($NaBH_4$) and hydrazine (N_2H_4) were chosen as reducing agents. Accordingly, these methods entitled different synthesis protocols: **1)** sonochemical synthesis in water using sodium borohydride[149] and **2)** synthesis in methanol using hydrazine[149,150]. In both cases, an inert atmosphere was employed to mitigate potential stability issues with the produced compounds. See section **7.1.6** for additional information on the experimental procedure.

A reddish coloration was observed after using both protocols. However, comparing the absorption spectra of the obtained materials with the limited existing literature did not clarify which species were formed, though elemental selenium (Se)[148] was excluded. (See section **7.2.1** for supplementary information about the absorption spectroscopy technique.) Furthermore, the expected red or NIR emissions were not detected when analyzing the emission properties of these produced compounds. Refer to Annex **I** in the supplementary information for the results and discussion regarding selenium reduction in solution.

However, since the behavior of these targeted emitting species, i.e., $[Se_2]^-$ and tentatively $[Se_3]^{2-}$, is better known when confined in zeolites, the colored reduced compounds were introduced as raw material during nanosodalite synthesis (as illustrated in **Scheme 4.2.3**, strategy II.B). For additional information on the experimental procedure, see section **7.1.2**. This resulted in pure colored nanosodalite zeolites, which do not exhibit either the red- or NIR-emitting

species. Additionally, the photochromic $[Se_2]^{2-}$ clusters were also not found. Refer to Annex I for more information about these results and discussion.

In summary, the final products from both methods do not exhibit the desirable luminescent properties. This suggests that the experimental conditions chosen may not be ideal. However, it remains unclear whether this is attributed to the unsuitable selection of reducing agents or if it is an inherent characteristic of the luminescent species, which might only form in solid-state (see section **4.2.2.2**). Factors such as solvent interactions and solvation could potentially influence this outcome. From a future perspective, it may be interesting to perform the reduction of this salt in solution using a reducing agent known to accurately reduce these species, thereby yielding the desirable luminescent selenium clusters, i.e., using hydrogen gas, in particular, the mixture 5% H_2 / 95% Ar.

4.2.4 Conclusions

The methodologies discussed in this subchapter reveal that combining solid-state and solution approaches yields the optimal results. Solid-state reduction leads to desirable NIR-emitting properties through a high-temperature synthesis of selenium-doped nanozeolites at 900 °C or by reducing the selenium precursor salt at 500 °C. The latter compound exhibits an average photoluminescence decay time of 39 μs at room temperature, showing a bi-exponential behavior with components of 34 μs and 54 μs. Alternatively, working in solution is the ideal method for manipulating these nanoparticles, as drying them causes aggregation and reduces their dispersibility. Thus, combining these methods could ideally produce the aimed highly dispersible NIR-emitting nanozeolites suitable for *in vivo* imaging.

Furthermore, according to the knowledge gathered around selenium NIR-emitters, they seem to be related with nepheline and especially with carnegieite structures. However, based on our understanding, the synthesis of these aluminosilicates typically involves high-temperature zeolite transformation at around 900 °C, consequently destroying nano-sized zeolites. Therefore, from a future perspective, it might be interesting to develop a synthesis protocol for nanonepheline and nanocarnegieite aluminosilicates using a sol-gel synthesis. Subsequently, reduced selenium precursor salt incorporation may be tested again in these materials.

5

NIR-EMITTING TELLURIUM-DOPED ZEOLITES

Tellurium is undoubtedly the least studied and explored of the three chalcogens proposed for investigation in this thesis. This may be driven by their emission falling completely within the NIR region when confined in zeolites. Nonetheless, there are a couple of works concerning tellurium-doped zeolites.

Lindner et al.[19] reported blue-green sodalite, characterized by three distinct absorption bands at 400 nm, 480 nm and 605 nm. The band at 605 nm was assigned to the transition $^2\Pi_g \rightarrow {}^2\Pi_u$ of $[Te_2]^-$ species. The corresponding emission spectrum of these clusters is centered at 870 nm, resulting from the transition $^2\Pi_u \rightarrow {}^2\Pi_g$, extending up to 1150 nm. Similar to observations in selenium-doped zeolites containing $[Se_2]^-$ clusters, the emission band does not present a vibronic structure. However, Raman spectroscopy reveals a fundamental vibrational energy of 230 cm^{-1}[78]. The Stokes shift of these species is approximately 265 nm (0.62 eV).

Given the limited available information on this system, the following study aims to comprehensively investigate the photophysical properties of tellurium NIR-emitting species, thereby addressing gaps in the existing literature.

5.1 Synthesis and structural characterization

NIR-emitting tellurium-doped zeolites were produced starting from Na-LTA zeolite, NaCl and Na_2TeO_3, followed by a high-temperature treatment at 900 °C, for one hour under a reducing atmosphere of 5% H_2 / 95% Ar, according to the stoichiometry $Na_8Si_6Al_6O_{24}Te_xCl_{2-2x}$. Samples with nominal molar ratios of Te/Cl=0, 0.06, 0.21, 0.75, and 4.5 were synthesized. Refer to section **7.1.1** for more information about the experimental procedure.

These materials were initially characterized by powder X-ray diffraction (**Figure 5.1.A**), revealing a mixture of three crystalline phases - sodalite ($Na_8Si_6Al_6O_{24}Cl_2$), nepheline ($Na_4Si_4Al_4O_{16}$) and carnegieite ($Na_4Si_4Al_4O_{16}$). As demonstrated in previous chapters and corroborated by the information in the literature, these phases can be converted from Na-LTA zeolite. PXRD diffractograms indicated a notable stabilization of the sodalite phase by tellurium, with values consistently exceeding 70%, while nepheline and carnegieite exhibited proportions around 20% and 10%, respectively (**Figure 5.1.B**). These results are consistent with the selenium-doped zeolites findings in chapter **3** (**Figure 3.1.A-B**), which showed sodalite phase percentages up to 60% at higher chalcogen loadings. This further demonstrates the crucial role of chalcogen size in influencing and effectively stabilizing the sodalite phase. For more details on the PXRD technique, see section **7.2.13**.

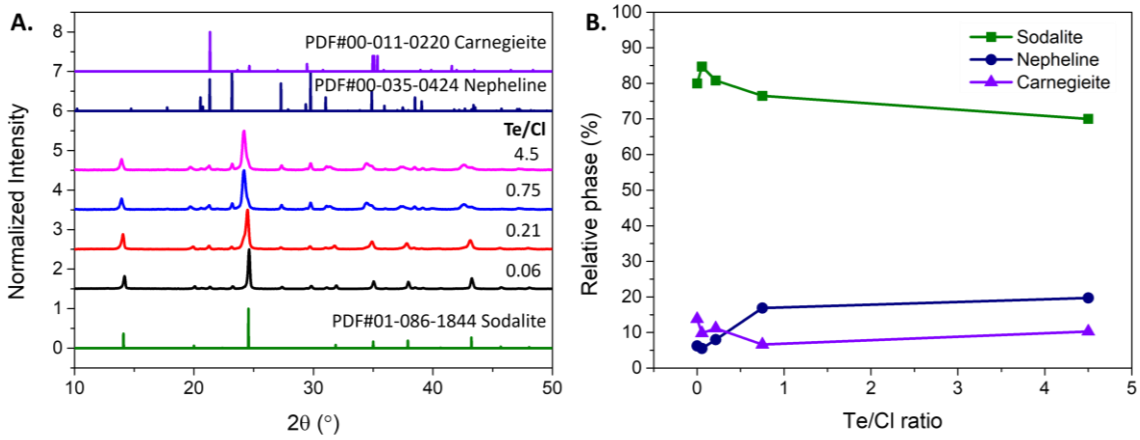


Figure 5.1 - (**A**) PXRD diffractograms of the synthesized samples according to the Te/Cl ratio and comparison with the ICDD standard reference card of 01-086-1844 sodalite ($Na_8Si_6Al_6O_{24}Cl_2$), 00-035-0424 nepheline ($Na_4Si_4Al_4O_{16}$) and 00-011-0220 carnegieite ($Na_4Si_4Al_4O_{16}$). (**B**) Corresponding crystalline phases calculated from the PXRD diffractograms.

The elemental analysis of the synthesized materials was determined using the particle-induced X-ray emission (PIXE) technique (**Table D.1**). **Table 5.1** summarizes the concentration of the most relevant elements found in molar percentage for the samples with Te/Cl=0.06, 0.21, and 4.5 and compares these with the theoretical values. These findings reflect the efficacy of the tellurium doping in the aluminosilicates, with the tellurium content increasing with the Te/Cl ratio and the chloride content decreasing accordingly. (Refer to section **7.2.10** for additional information about this technique.)

Table 5.1 - Molar percentage of each main element found in zeolite samples using the PIXE technique.

Nominal Te/Cl	Molar percentage composition (%)[a]						Obtained Te/Cl
	Na	Si	Al	O	Te	Cl	
0.06	17.23	12.82	12.71	53.80	0.11	3.01	0.04
0.21	17.13	12.66	12.63	54.17	0.54	2.56	0.21
4.5	16.72	12.60	12.59	55.88	1.58	0.32	5.01

[a]Calculated from the PIXE weight percentage (wt%) (**Table D.1**).

The nominal and obtained ratios are quite similar, contrary to initial expectations, since incorporating larger elements within small porous zeolites as sodalite can be more challenging. Comparing the elemental analysis conducted by PIXE on the sulfur-doped zeolites studied in subchapter **2.3** with similar nominal ratios (**Table 2.3.1**), the chloride amounts are identical, however, the detected sulfur is much lower than tellurium. These differences may arise from two different reasons. The first is related to higher PIXE sensitivity to heavier elements than lighter ones due to absorption in the detection window of the beryllium film of X-ray detector at such energies[154]. The second reason is related to reagent loss during high-temperature synthesis at 900 °C. The boiling points of sodium sulfite (Na_2SO_3) and sodium tellurite (Na_2TeO_3) are unknown, however, their melting points are around 500 °C and 700 °C, respectively. This indicates that sulfur is likely more susceptible to loss than tellurium during high-temperature synthesis at 900 °C.

5.2 Optical characterization

Tellurium doping influences the optical properties of the resulting zeolite samples, which exhibit a grayish-blue coloration (**Figure 5.2**). Therefore, the samples were initially examined using diffuse reflectance spectroscopy. Additional information about this technique can be found in section **7.2.2**. After applying the Kubelka-Munk theory[103], the resulting spectra are depicted in **Figure 5.2**. These spectra seem to consist of three distinct absorption bands at 395, 485 and 600 nm, with absorption increasing consistently with the Te/Cl ratios. The band at 600 nm was previously assigned to the transition $^2\Pi_g \rightarrow {}^2\Pi_u$ of $[Te_2]^-$ clusters[19] (see **Figure 1.4.8** of the introduction chapter).

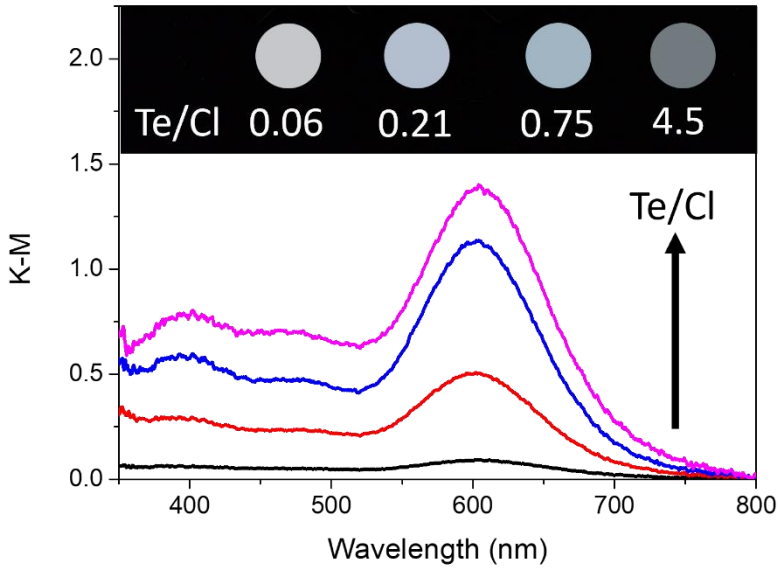


Figure 5.2 - Diffuse reflectance spectrum of samples with different Te/Cl ratios. Inset: photos of the samples under ambient light.

To better understand their behavior with tellurium doping, the obtained spectra were deconvoluted into three different absorption bands, which together simulate the experimental data. As shown in **Figure 5.3.A-C**, the original spectra consist of bands at 395, 485 and 600 nm.

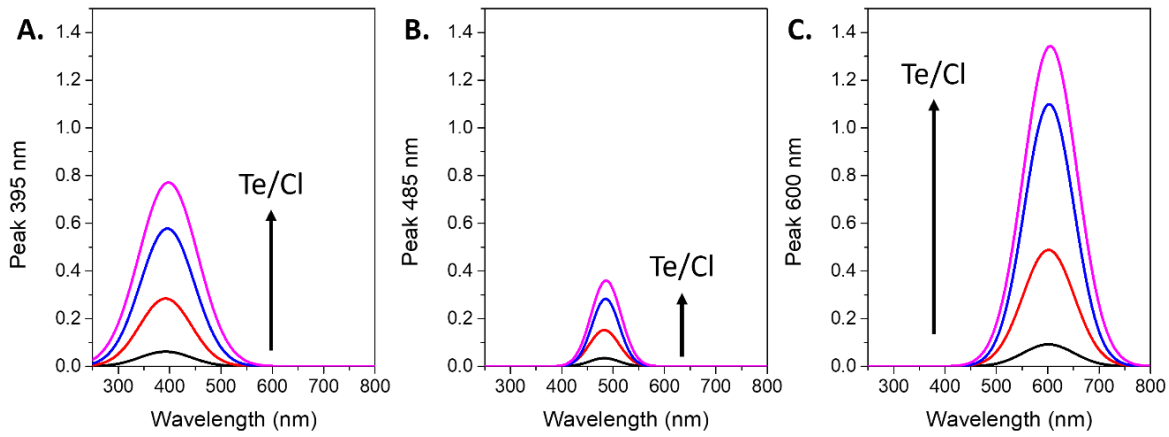


Figure 5.3 - Spectra deconvolution presented in **Figure 5.2**, using bands peaking at 395 nm (**A**), 485 nm (**B**) and 600 nm (**C**) and their behavior according to the Te/Cl ratio.

Figure 5.4 illustrates the deconvoluted spectrum of sample Te/Cl=4.5 using its three simulated bands present in **Figure 5.3.A-C**.

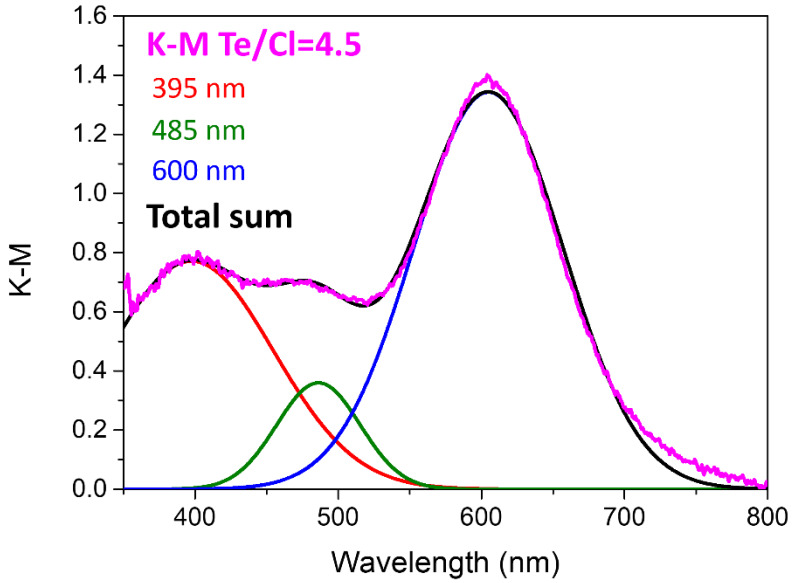


Figure 5.4 - Diffuse reflectance spectral deconvolution of the sample with Te/Cl=4.5.

Remarkably, no emission was visually detected when these samples were exposed to standard UV light at 365 nm. This could be attributed to either low emission intensity in the visible region or emission occurring in the NIR region. Emission spectra were then recorded by exciting the samples at the three different absorption wavelengths. (Refer to section **7.2.3** for more details about this technique.) When excited at 400 nm (**Figure 5.5**), the resulting spectra maxima of these samples appear at 800 nm. This is compatible with the described $^2\Pi_u \rightarrow {}^2\Pi_g$ transition of $[Te_2]^-$ clusters[19]. However, it is believed that a significant part of this emission is not detected using this detector's conditions, as it is supposed to peak around 870 nm and extend to approximately 1150 nm. The intensity of this emission decreases as the Te/Cl ratio increases. This phenomenon is consistent with the behavior observed in previously synthesized selenium-doped zeolites in chapter **3**, where a self-quenching effect was detected in $[Se_2]^-$ clusters, as explored below. Furthermore, the emission spectra of $[S_2]^-$ clusters, characterized by their vibronic structure and centered at around 650 nm, are also detected (**Figure 5.5**). This is especially evident in the sample with the lowest Te/Cl ratio and lower tellurium content. PIXE analysis confirms the presence of sulfur impurities in these samples (**Table D.1**), which appear to originate from commercial Na-LTA zeolite (**Table A.1.2**).

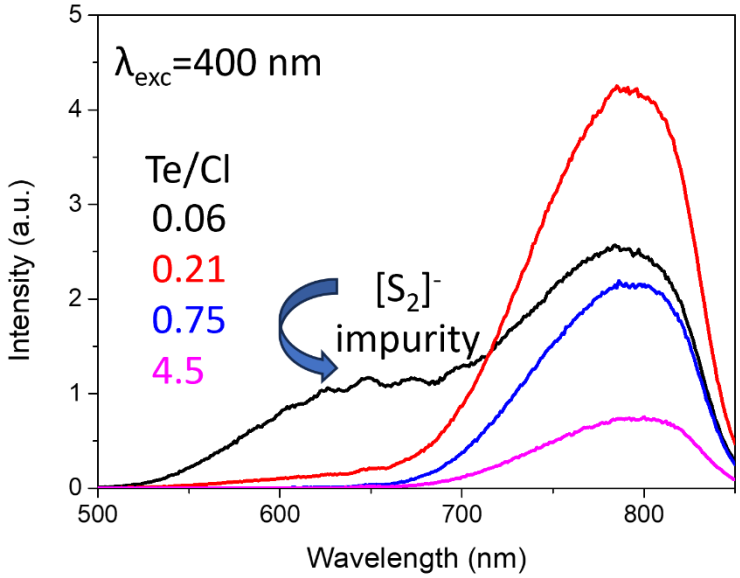


Figure 5.5 - Emission spectra of the synthesized tellurium-doped zeolite samples with different Te/Cl ratios, exciting at 400 nm.

Using these conditions, a similar intensity pattern was observed in the corresponding emission spectra when these samples were excited at 475 nm (**Figure 5.6.A**) and 600 nm (**Figure 5.6.B**). Additionally, when comparing the resulting emission spectra exciting the samples at 600 nm (where $[S_2]^-$ clusters no longer absorb energy), it is possible to conclude that the NIR emission intensity indeed increases from sample Te/Cl=0.06 to sample Te/Cl=0.21 and then constantly decreases until sample Te/Cl=4.5.

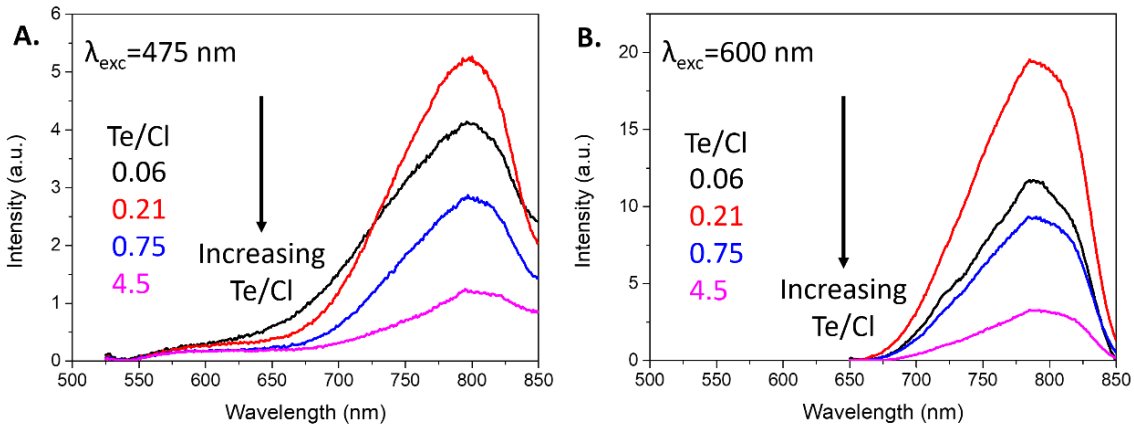


Figure 5.6 - Emission spectra of the synthesized samples with different Te/Cl ratios, exciting at (**A**) 475 nm and (**B**) 600 nm.

A comparable concentration-dependence was observed in selenium-doped zeolites, where the red emission of $[Se_2]^-$ clusters consistently decreased as selenium loading increased. This quenching effect was assigned to a double electron transfer mechanism occurring between the $[Se_2]^-$ species confined within sodalite cages of sodalite zeolite. This phenomenon is enhanced by the increasing proximity between these selenium radicals as selenium loading increases, see **Figure 3.10**, chapter **3**. Such an effect may also be observed in tellurium, as indicated by the findings from PIXE and PXRD analyses. Elemental analysis using PIXE revealed an effective increase in tellurium doping with the Te/Cl ratio (**Table 5.1**). Consequently, since $[Te_2]^-$ clusters are associated with sodalite zeolite[19], higher tellurium loadings are expected to increase the probability of these clusters being present in adjacent sodalite cages. The distances between these clusters range from 8.85 to 9.06 Å, depending on the Te/Cl ratio, according to the calculated unit cells of sodalite zeolite extracted from the PXRD diffractograms (**Figure 5.1.A**), as summarized in **Table D.2**. These distances are compatible with a DET mechanism, which typically occurs at distances up to 10 Å[127].

These findings suggest that once the same emission spectra were obtained when using these three different excitation wavelengths (400, 475 and 600 nm) as illustrated in **Figure 5.5** and **Figure 5.6.A-B**, $[Te_2]^-$ clusters may not exclusively absorb at 600 nm, as previously indicated in the literature. In fact, the excitation spectra corresponding to this NIR emission (λ_{em}=800 nm) revealed the same three distinct excitation bands, peaking at 395, 475, and 600 nm (**Figure 5.7.A**). The intensities of these bands exhibit a consistent behavior compared to those observed in the emission spectra presented in **Figure 5.6.B**. They increase from sample Te/Cl=0.06 to sample Te/Cl=0.21 and gradually decrease until sample Te/Cl=4.5. Additionally, the normalized excitation spectra (**Figure 5.7.B**) reveal similar relative band intensities across all samples, suggesting once again that these three bands are responsible for the tellurium NIR emission.

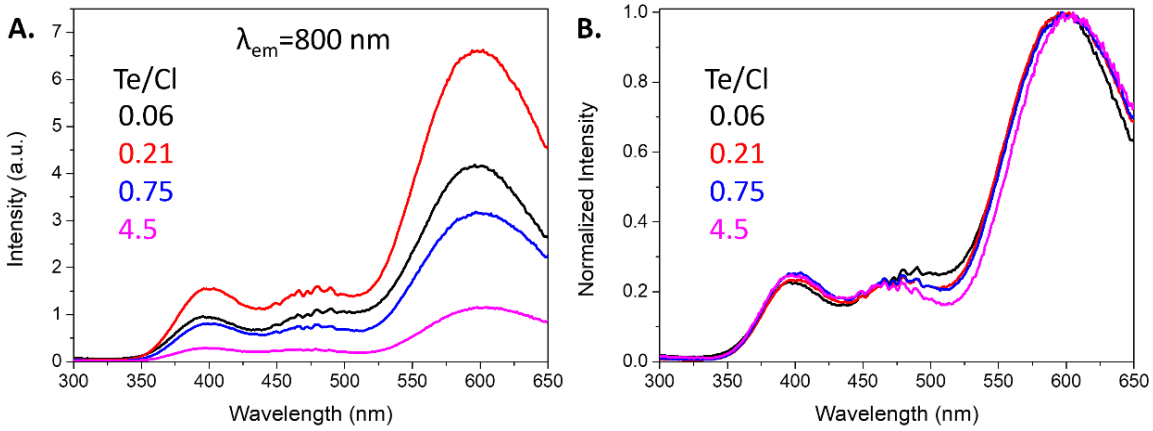


Figure 5.7 - Excitation spectra of the synthesized samples using different Te/Cl ratios at (**A**) λ_{em}=800 nm and (**B**) corresponding normalized spectra.

The results discussed above indicate that, unlike the sulfur and selenium systems, where an increase in doping led to the detection of additional absorption and corresponding emission bands, no such bands were observed with the increase in tellurium doping. Two possible explanations may account for this phenomenon. Firstly, it might be attributed to detection limitations, which make it impossible to detect signals above 800 and 850 nm for absorption and emission spectroscopies, respectively. Secondly, the size of tellurium may influence its doping in aluminosilicate matrices. Schlaich et al.[86] reported variances in sodalite occupancy influenced by the size of chalcogens. Drawing on insights from other chalcogen systems, it is proposed that these new species are larger than the diatomic chalcogen radicals $[X_2]^-$ (X=S, Se and Te), and are tentatively assigned to $[X_3]^{2-}$ (X=S, Se and Te) clusters. Moreover, these new species typically appear at higher chalcogen loadings and are associated with nepheline and carnegieite aluminosilicates. In this tellurium system, these two structures only represent about 30% of the relative crystalline phases in the sample with the highest tellurium content (**Figure 5.1A-B**), making them the minority. This suggests that in terms of tellurium distribution, smaller species such as $[Te_2]^-$ confined within sodalite zeolite may be favored, whereas the new tellurium species tentatively assigned to $[Te_3]^{2-}$ clusters, if present, are expected to be found in nepheline and/or carnegieite structures.

Additionally, chalcogen $[X_2]^-$ and $[X_3]^{2-}$ species exhibit different lifetimes, allowing for their differentiation using varying delay and integrating signal times through time-resolved emission spectroscopy (TRES) measurements. (Section **7.2.5** contains additional information about this technique.) Therefore, sample with higher Te/Cl ratio was further studied using this technique. At shorter delay times in the nanosecond timescale (**Figure 5.8.A**), the

corresponding emission spectra display maxima at around 825 nm, which is consistent with the steady-state measurements depicted in **Figure 5.6.B**. Additionally, it is possible to observe a decrease in the NIR emission intensity of these species when increasing the delay times applied. Plotting the intensity at the emission maximum against the delay time yields a decay time of 97 nanoseconds (**Figure 5.8.B**), providing an approximation of the lifetime of $[Te_2]^-$ species.

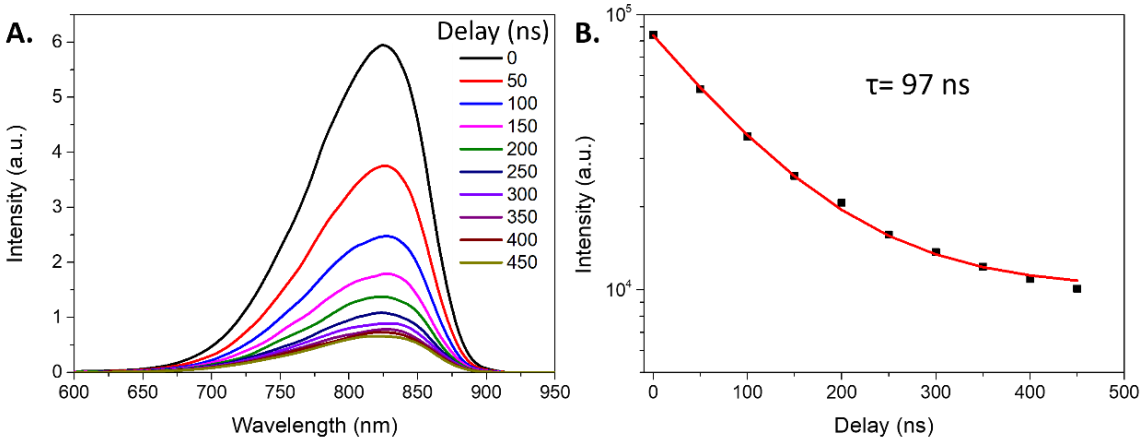


Figure 5.8 - (**A**) Time-resolved emission spectroscopy of sample with Te/Cl=4.5, excited at 337 nm, using short delay times on the nanosecond timescale. (**B**) An approximation of the decay time of this emission.

Moreover, when applying delay times in the microsecond range, a second emission was detected. The corresponding emission spectra closely resemble those of the previously mentioned species, with a similar profile and emission maxima observed at *ca.* 825 nm (**Figure 5.9.A**). However, upon analyzing the decay time using the same method, a bi-exponential decay was observed with components of 3 and 37 microseconds, resulting in an average decay time of 23 µs (**Figure 5.9.B**). Considering the similarities in photophysical behavior between this tellurium system and sulfur and selenium systems, particularly regarding differences between chalcogen $[X_2]^-$ and $[X_3]^{2-}$ species, it is reasonable to suggest that this long-lived emission arises from another tellurium species, tentatively $[Te_3]^{2-}$. The lack of differentiation between the corresponding obtained emission spectra using this TRES technique at shorter or longer delay times might be attributed to detection limitations at longer wavelengths.

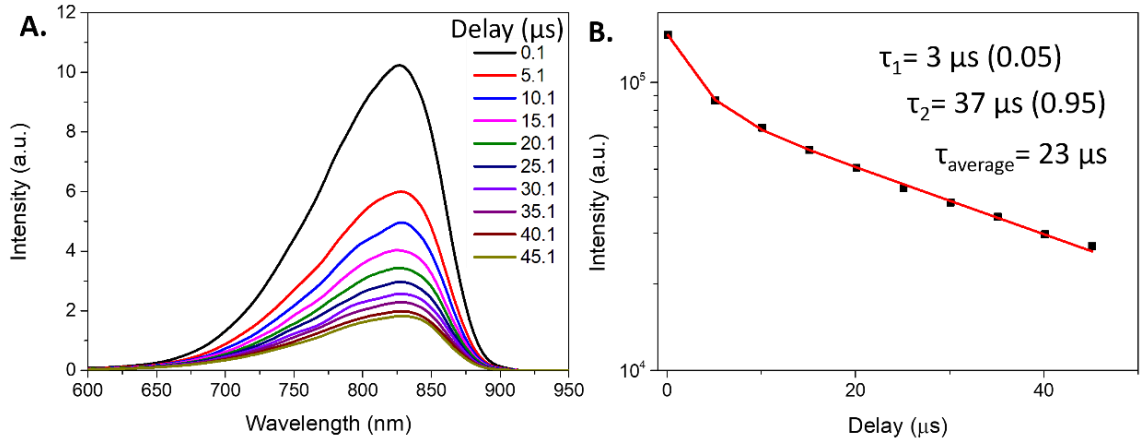


Figure 5.9 - (**A**) Time-resolved emission spectroscopy of sample with Te/Cl=4.5, excited at 337 nm, using long delay times on the microsecond timescale. (**B**) An approximation of the decay time of this emission. Note their respective components and amplitudes (in brackets) alongside the corresponding average decay times.

This long-lived emission was further investigated through the multichannel scaling (MCS) technique in all synthesized samples to produce more accurate results and verify if this NIR emission also becomes faster with the increasing Te/Cl ratio, as in the selenium system. (See additional information about the photoluminescence decay time technique in section **7.2.4**.). **Figure 5.10** resumes the measured decay times, revealing once again a bi-exponential behavior. The faster component (which exhibited lower variations) was fixed at 17 µs to better understand potential variations due to the doping effect. Consequently, the slower decay component demonstrated a variation from 106 to 56 µs with the Te/Cl ratio, resulting in average decay times ranging from 51 to 26 µs, as summarized in **Table 5.2**.

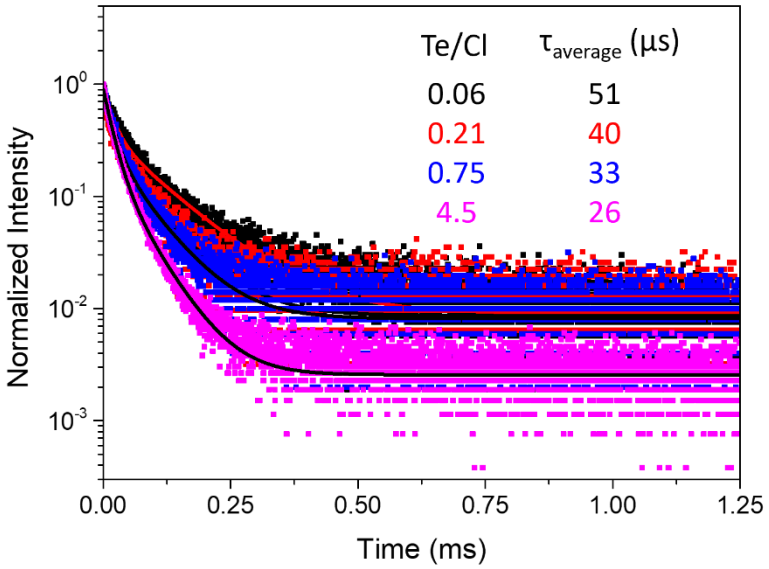


Figure 5.10 - Photoluminescence decay times in the microsecond timescale using the different Te/Cl ratios, with λ_{exc}=400 nm.

Unfortunately, the external quantum efficiencies (EQEs) were not calculated due to detector limitations, making it impossible to fully detect this NIR emission. As a result, the radiative and non-radiative 'averaged' constants could not be determined. However, based on the information produced on the NIR emission of selenium-doped zeolites, the decrease in decay times with increasing selenium loading was assigned to the increase of non-radiative pathways, potentially arising from energy transfer mechanisms between emitters.

Table 5.2 - Photoluminescence decay times of the NIR emission with the two components, their relative amplitudes and the average decay times.

Te/Cl ratio	τ_1 (μs)	Relative amplitude (A_1)	τ_2 (μs)	Relative amplitude (A_2)	$\tau_{average}$ (μs)*
0.06	17	0.21	106	0.79	51
0.21	17	0.27	76	0.73	40
0.75	17	0.37	70	0.63	33
4.5	17	0.52	56	0.48	26

*Values calculated using the pre-exponential factors.

Previous photophysical analysis suggests the presence of clusters such as $[Te_2]^-$ and $[Te_3]^{2-}$. Subsequently, electron paramagnetic resonance (EPR) spectroscopy was used to detect and quantify the existing EPR-active species, distinguishing between EPR-active $[Te_2]^-$ and diamagnetic $[Te_3]^{2-}$. (Refer to section **7.2.7** for additional information about this technique.) A temperature- and concentration-dependence was found in these synthesized tellurium-doped samples. Starting with sample Te/Cl=0.06 recorded at 150 K, a mixture of EPR signals was observed, as illustrated in **Figure 5.11**. When cooling this sample from 80 K to 30 K, notable changes were detected in the obtained spectra. This indicates the presence of new paramagnetic species with different temperature relaxations, which are only detected at lower temperatures. Consequently, the optimal detection temperature was determined to be 30 K.

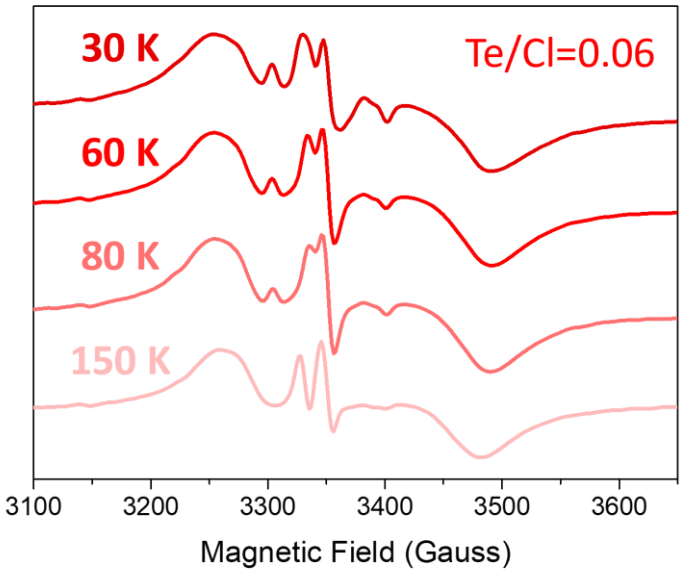


Figure 5.11 - Electronic paramagnetic resonance (EPR) spectra of sample Te/Cl=0.06 recorded at different temperatures from 150 K to 30 K.

This spectrum (acquired at 30 K) was then theoretically simulated using three species (A, B, and C), as shown in **Figure 5.12**. Species A was identified by its broad signals, making it distinct from the others. Species B was determined by subtracting the spectrum acquired at 30 K from the one recorded at 150 K. Species C was assigned to a mixture of paramagnetic sulfur species, $[SO_2]^-$ and $[S_2]^-$, as indicated in **Table 2.3.2**, subchapter **2.3.** These species were also identified in the blank sample (sample Te/Cl=0), represented by the black line in **Figure 5.16.A** below. Furthermore, the emission of $[S_2]^-$ species was detected in this sample when excited at 400 nm (**Figure 5.5**). PIXE analysis also revealed the presence of sulfur in all

synthesized samples with similar concentrations (**Table D.1**). The calculated relative contributions of each species (A, B and C) are summarized in **Table 5.3**, revealing the same amount of each species in this sample, i.e., ~33%.

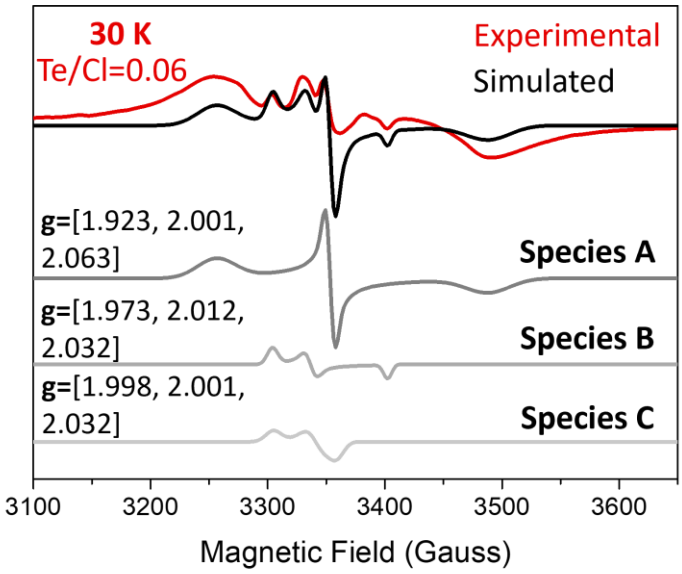


Figure 5.12 - EPR spectrum of sample Te/Cl=0.06 acquired at 30 K (red line) and corresponding simulations (gray lines) depicting species A, B and C. The black line shows the sum of these three species according to their calculated relative contributions, summarized in **Table 5.3**.

The EPR spectra of sample Te/Cl=0.21 (**Figure 5.13**) reveal additional changes compared to sample Te/Cl=0.06. The most evident one is the decrease in intensity of species A since the broad signal is less evident in this sample.

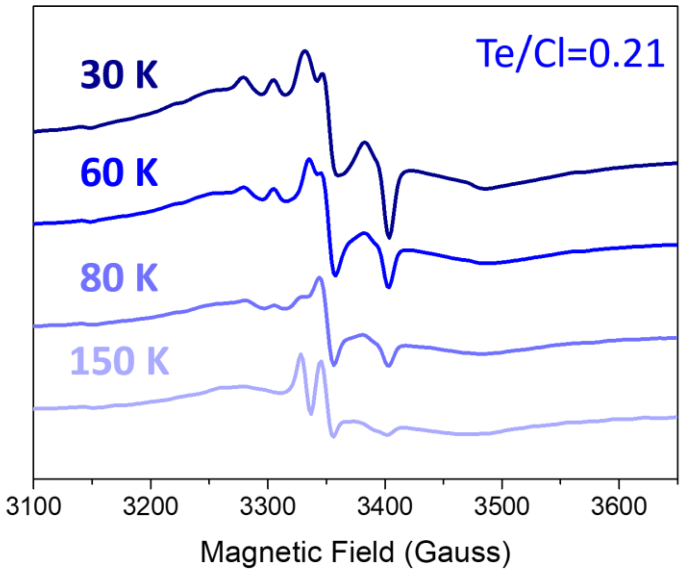


Figure 5.13 - Electronic paramagnetic resonance (EPR) spectra of sample Te/Cl=0.21 recorded at different temperatures from 150 K to 30 K.

To better understand these changes, the spectrum recorded at 30 K was theoretically simulated (**Figure 5.14**), confirming the decrease in the relative contribution of species A to approximately 19% (**Table 5.3**). Notably, adding a new tellurium species (species D), contributing around 37%, was necessary to simulate the experimental spectrum. It is not clear whether species D was already present in sample Te/Cl=0.06, as its detection (particularly the signal at g = 2.048), might have been masked by the signal from species A. However, the increase in the signal around g = 1.973 from sample Te/Cl=0.06 to sample Te/Cl=0.21 (**Figure 5.16.A**) suggests that this is a new species. Furthermore, species B maintains a similar relative contribution of around 37% as in sample Te/Cl=0.06, while sulfur impurities (species C) decrease to 7%.

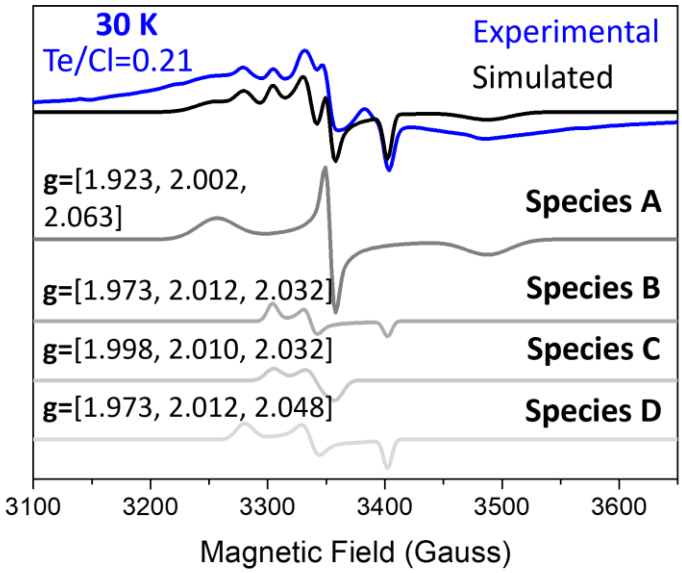


Figure 5.14 - EPR spectrum of sample Te/Cl=0.21 acquired at 30 K (blue line) and corresponding simulations (gray lines) depicting species A, B, C and D. The black line shows the sum of these three species according to their calculated relative contributions, summarized in **Table 5.3**.

Differences become even more evident in the EPR spectra of samples Te/Cl=0.75 and 4.5 (**Figure 5.15.A-B**). These signals significantly decrease their intensities compared to the previously discussed synthesized samples, as exemplified below in **Figure 5.16.A-B**. However, simulating these spectra proved challenging, given their broad nature. They might be composed of a combination of species A, B, C and D.

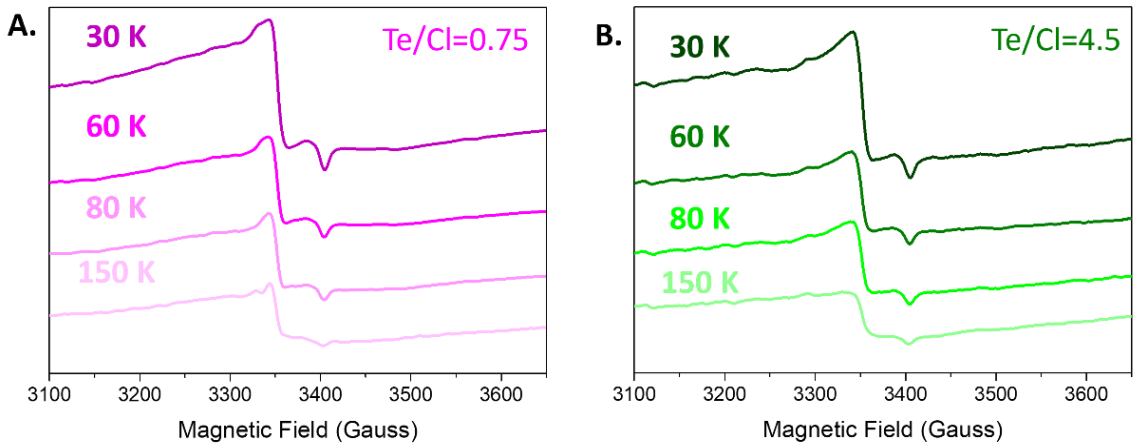


Figure 5.15 - Electronic paramagnetic resonance (EPR) spectra of samples Te/Cl=0.75 (**A**) and Te/Cl=4.5 (**B**) recorded at different temperatures from 150 K to 30 K.

At the optimal temperature of 30 K (**Figure 5.16.A**), a comparison of all recorded signals revealed variations in EPR signal intensity based on tellurium loading. The intensity increases from sample Te/Cl=0.06 to sample Te/Cl=0.21, then decreases in sample Te/Cl=0.75 (**Figure 5.16.B**), resulting in an overall decrease with increasing Te/Cl ratios. Note that in sample Te/Cl=4.5, the detected EPR intensity is minimal. These intensity variations are consistent with those found in steady-state emission spectroscopy (**Figure 5.6.B**). However, diffuse reflectance spectroscopy detected a constant increase in tellurium chromophore formation (**Figure 5.2**). These chromophores were assigned to $[Te_2]^-$ species, which are emissive and EPR-active. Therefore, diffuse reflectance spectroscopy findings contrast with those found in EPR and emission spectroscopy.

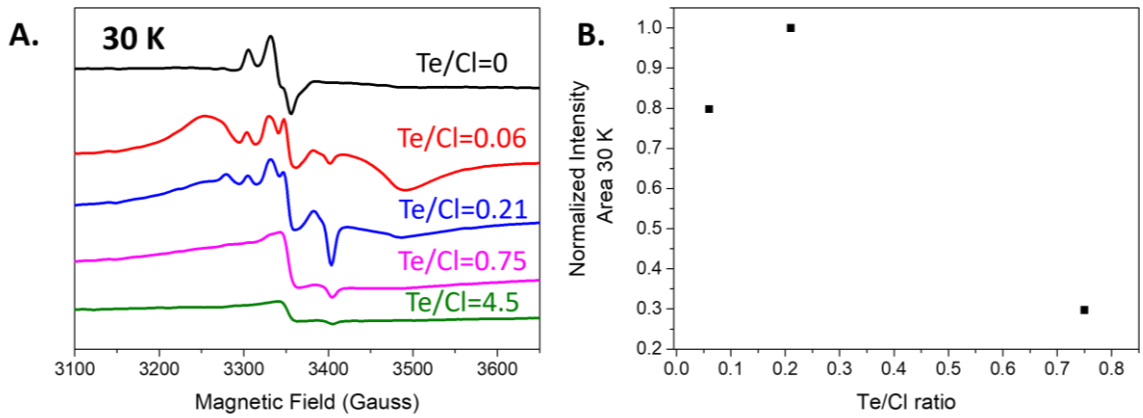


Figure 5.16 - (**A**) Comparison of all EPR signals recorded at 30 K (**B**) alongside their corresponding normalized signal areas. Note that the signal from sample Te/Cl=4.5 was not considered since its intensities is minimal.

A similar effect was observed in selenium-doped zeolites, where an emission quenching and a decrease in EPR area were also observed with increasing Se/Cl ratios (**Figure 3.5.A-B** and **Figure 3.31.A-B**, chapter **3**, respectively). These phenomena were attributed to interactions between different $[Se_2]^-$ clusters within sodalite zeolites. The emission quenching was assigned to a double electron transfer mechanism, while the EPR effect was attributed to an antiferromagnetic coupling. These effects are enhanced by the proximity of the selenium clusters, which increases with increasing selenium loading, i.e., at higher Se/Cl ratios.

In tellurium-doped zeolites, the existence of a DET mechanism was previously explored above to explain the decrease in $[Te_2]^-$ emission with increasing tellurium loading (**Figure 5.6.B**). Therefore, it is plausible that an antiferromagnetic coupling could occur between tellurium paramagnetic species, particularly between adjacent $[Te_2]^-$ clusters. This is especially likely

considering that tellurium is larger than selenium. Note that such close interactions are promoted at higher Te/Cl ratios.

In summary, these findings suggest the presence of at least three paramagnetic species of tellurium. Species A and B were observed in sample Te/Cl=0.06, while an additional one, species D, was detected in sample Te/Cl=0.21. If the g-iso values (average g-values) were consistent across species, it could imply the presence of the same species in different local environments. However, this scenario is unlikely as indicated by the varying g-iso values outlined in **Table 5.3**. Instead, it appears that there are three distinct tellurium species involved.

Table 5.3 - g-values and corresponding g-iso values (average g-values) of the species detected in samples Se/Cl=0.06 and 0.21. The relative contributions of each species were calculated in the spectra recorded at 30 K for these two synthesized samples.

Nominal Te/Cl ratio	Tellurium EPR active species	g_1	g_2	g_3	g_{iso}	Relative contribution at 30 K (%)
0.06	A	1.923	2.001	2.063	1.996	33
	B	1.973	2.012	2.032	2.006	33
	C (sulfur)	1.998	2.010	2.032	2.013	33
0.21	A	1.923	2.002	2.063	1.996	19
	B	1.973	2.012	2.032	2.006	37
	C (sulfur)	1.998	2.010	2.032	2.013	7
	D	1.973	2.012	2.048	2.011	37

The literature on paramagnetic species of tellurium is extremely limited, even more so than that of selenium, to the point of being practically non-existent. As a result, directly assigning species based on EPR spectra was not feasible. Other optical characterizations conducted in this chapter also failed to provide conclusive information for this analysis. Absorption and emission spectroscopies suggest the presence of $[Te_2]^-$, accounting for one of these EPR-active species. Additionally, time-resolved photoluminescence spectroscopy measurements indicate the presence of a second tellurium emissive species, although it remains uncertain whether it can be responsible for another of these signals, especially since it was tentatively assigned to diamagnetic $[Te_3]^{2-}$ species.

Besides the challenges with assigning these three tellurium species, it is noteworthy that these EPR spectra are being reported for the first time. Radical entrapment within zeolites

enables direct analysis of these species without the necessity of spin traps to stabilize the produced tellurium radicals[155], thus ensuring their long-term stability.

5.3 Conclusions

The study conducted in this chapter provides a better understanding of the behavior of the less-studied chalcogen in zeolites. The observation of three distinct bands in both absorption and excitation spectra - peaking at 400 nm, 485 nm and 600 nm, with consistent relative intensities with Te/Cl ratio - suggests that $[Te_2]^-$ species have indeed three different absorption bands. This finding contradicts previous literature, which exclusively assigned the absorption band at 600 nm (transition $^2\Pi_g \rightarrow {}^2\Pi_u$) to the absorption of $[Te_2]^-$ species. Additionally, when these samples were excited at these three mentioned wavelengths, the same NIR emission was observed (transition $^2\Pi_u \rightarrow {}^2\Pi_g$). However, it is believed that not all emissions were detected due to the intrinsic limitations of standard UV-VIS-NIR detectors.

The formation of a new tellurium species with the Te/Cl ratio was not detected in the absorption or steady-state emission spectra. Nevertheless, time-resolved photoluminescence spectroscopy measurements revealed two lifetimes on different timescales. Based on the knowledge of sulfur and selenium systems, two tellurium NIR-emitting species are believed to be present. Therefore, the species with a lifetime of around 100 nanoseconds was attributed to $[Te_2]^-$, while the species with an average decay time of *ca.* 40 µs was tentatively assigned to $[Te_3]^{2-}$.

Electron paramagnetic resonance (EPR) spectra identified three novel tellurium paramagnetic species. However, due to the lack of available information in the literature and limitations in the optical characterization provided in this chapter, assigning one of the EPR signals to the $[Te_2]^-$ species was not feasible. Furthermore, whether the species with a microsecond lifetime exhibited EPR activity remained inconclusive, especially since it was assumed that they may be due to $[Te_3]^{2-}$ clusters, which are diamagnetic, i.e., non-EPR active.

Tellurium doping also demonstrated a significant stabilization effect of sodalite zeolite, which is higher than the one observed in selenium and much higher than in sulfur. This suggests a direct relationship between chalcogen size and the stabilizing effect. However, this effect hindered the formation of nepheline and carnegieite aluminosilicates, which are associated with the confinement of the larger chalcogen species and are believed to contain the novel $[Te_3]^{2-}$ species. This may explain the low formation of these species and their lack of detection by steady-state spectroscopy. From a future perspective, it would be interesting to synthesize

tellurium-doped zeolites using low amounts of this chalcogen and avoiding chloride use. This approach is expected to result in higher amounts of nepheline and carnegieite formation, allowing for a better assessment of the new NIR-emitting species without the presence of $[Te_2]^-$ clusters.

Although the NIR applications were not explored for these tellurium NIR emitters, it is believed that their photophysical properties make them suitable for anticounterfeiting and security systems, as well as for use in NIR phosphor-converted LEDs.

Overall, this study significantly contributes to a better understanding of tellurium-doped zeolites despite the practical restrictions of working with an emitting system that falls entirely within the NIR region. It also represents the first report on photoluminescence decay times, excitation and EPR spectra.

6

General Conclusions And Future Perspectives

Nowadays, there is a growing need for alternatives to commonly used near-infrared (NIR) emitters due to their limited availability and stability. This thesis has explored various innovative solutions to address these challenges, demonstrating the potential of novel developed chalcogen NIR-emitting zeolites that exhibit improved stability and accessibility.

Novel NIR emitters were found to be confined within aluminosilicate matrices at higher sulfur and selenium concentrations. In contrast, NIR emission appeared at lower chalcogen doping levels for tellurium, demonstrating a dependence on both chalcogen concentration and size. Thus, two types of emitting chalcogen species were detected according to the chalcogen loading. At lower chalcogen loadings and associated with sodalite zeolite, diatomic radicals $[X_2]^-$ (X=S, Se and Te) were identified. **Figure 6.1** illustrates the chalcogen size-dependence, with the emitting properties of these materials shifting from the yellow-orange region with sulfur to the NIR region with tellurium.

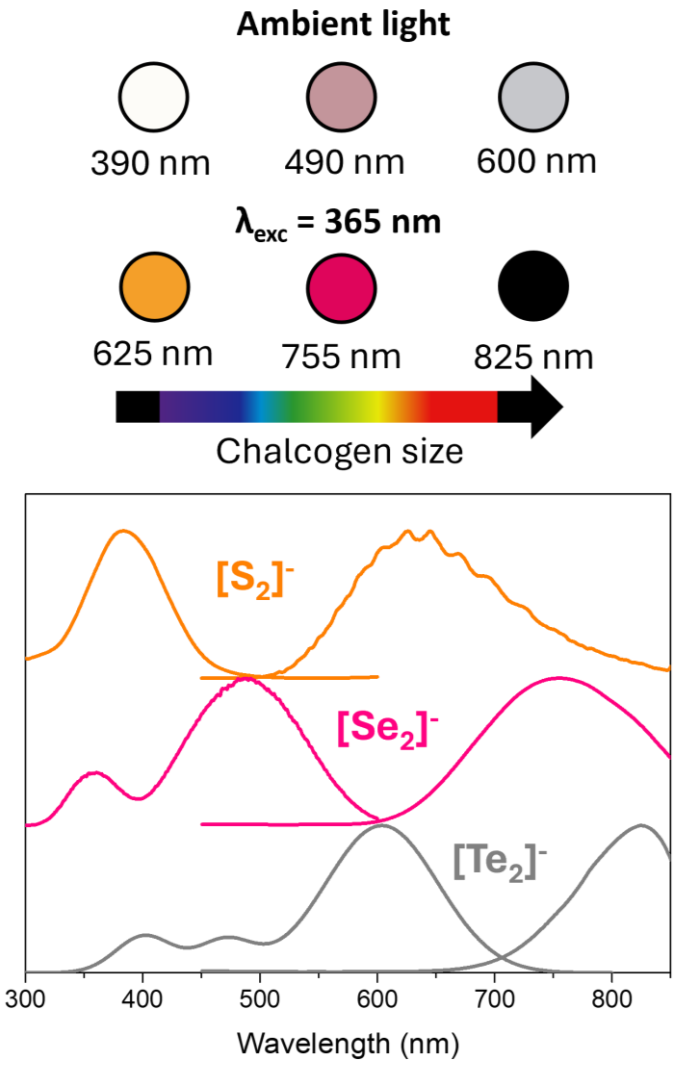


Figure 6.1 - (**Above**) Photos of the produced chalcogen-doped zeolite samples synthesized in chapters **2**, **3** and **5** under ambient light and standard UV ligth (λ_{exc}=365 nm). (**Below**) Resume of the emission and excitation spectra of the chalcogen $[X_2]^-$ radicals.

However, when increasing the chalcogen loading, new species were found and tentatively assigned to triatomic dianionic species $[X_3]^{2-}$ (X=S, Se and Te). As depicted in **Figure 6.2**, these species emit in the NIR region, exhibiting properties that significantly differ from those of diatomic radical species $[X_2]^{-}$. Furthermore, they seem to be related with different aluminosilicates than sodalite, specifically nepheline and carnegieite.

The presence of $[Te_3]^{2-}$ was not univocally confirmed, although the presence of a second emission lifetime in tellurium-doped zeolites indicates that besides $[Te_2]^{-}$ another emissive tellurium cluster may be present.

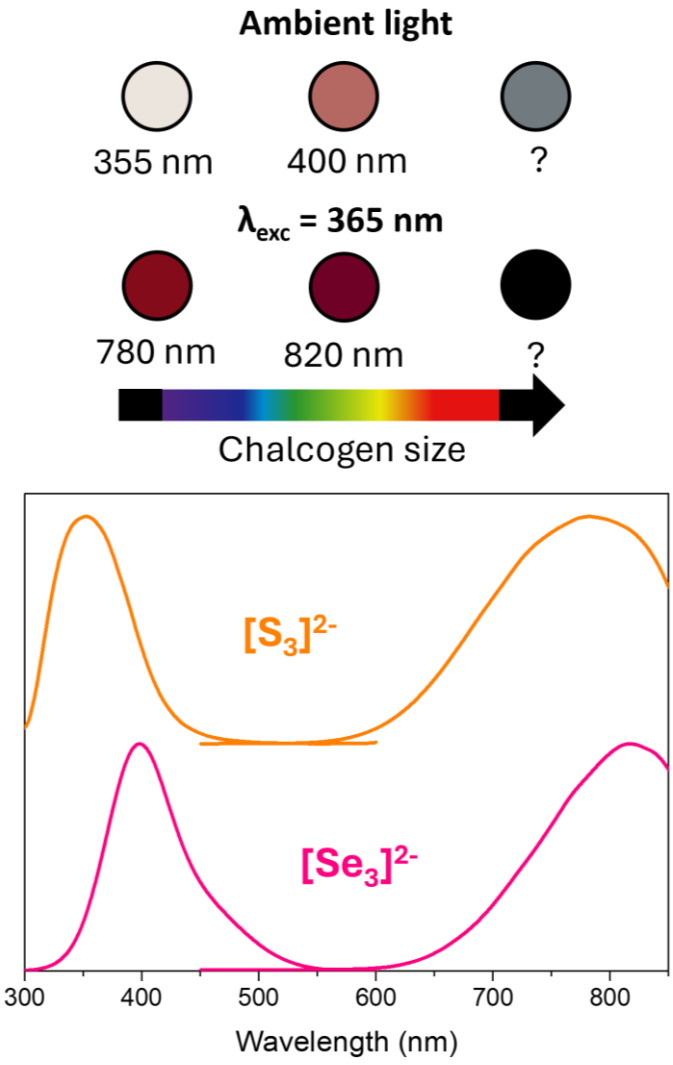
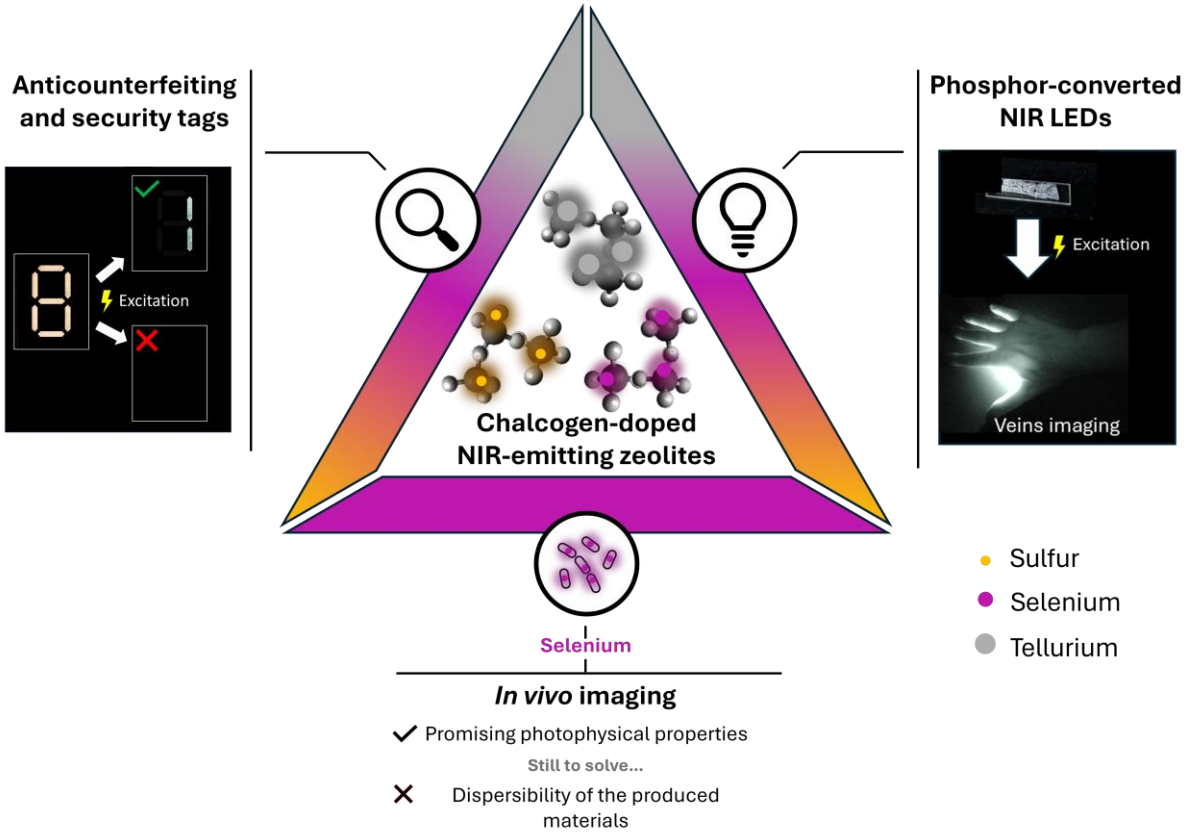


Figure 6.2 - (**Above**) Photos of the produced chalcogen-doped zeolite samples synthesized in chapters **2**, **3** and **5** under ambient light and standard UV ligth (λ_{exc}=365 nm). (**Below**) Resume of the emission and excitation spectra of the new chalcogen emitters, tentatively triatomic diradical $[X_3]^{2-}$ species.

These NIR-emitting zeolites represent novel materials whose optical properties have been thoroughly investigated for the first time, significantly advancing the current state-of-the-art regarding chalcogen-doped zeolites. In terms of applicability, they have demonstrated promising results in proof-of-concept NIR applications, such as security systems and phosphor-converted NIR LEDs for veins imaging (**Scheme 6.1**). Developing a more device-oriented concept based on such results may be interesting. This could involve exploring the immobilization of these zeolites in materials such as cellulose fibers, as demonstrated by Fang et al.[89] in photochromic sulfur-doped zeolites. Additionally, formulating an ink for inkjet printing and measuring the luminance of phosphor-converted LEDs are potential avenues for further investigation.



Scheme 6.1 - Resume of the NIR applications studied during this thesis that showed a good suitability for the produced chalcogen-doped NIR-emitting zeolites.

Moreover, selenium NIR-emitting zeolites exhibit promising photophysical properties for *in vivo* imaging, particularly due to their excitation wavelength falling within the visible region and the availability of this element (**Scheme 6.1**). The experiments focused on synthesizing highly dispersible selenium NIR-emitting nanozeolites offered valuable insights for future research. Working exclusively in solution proved to be the optimal approach for manipulating

these materials, preventing particle aggregation and assuring their dispersibility. Additionally, employing high-temperature solid-state reduction of selenium salt precursor (Na_2SeO_3) resulted in similar NIR emission properties. Hence, developing a synthesis protocol for nanonepheline and nanocarnegieite aluminosilicates would be worthwhile, as well as incorporating such NIR-emitting salts into the process. Furthermore, similar investigations could be conducted with tellurium to determine and characterize $[Te_3]^{2-}$ species without the presence of $[Te_2]^-$ clusters.

7

MATERIALS AND METHODS

7.1 Synthesis

7.1.1 High-temperature synthesis starting from commercial Na-LTA zeolite

Sulfur, selenium and tellurium (chapters **2**, **3** and **5**): Chalcogen-doped zeolites samples were prepared following equation (**7.1.1**), according to the stoichiometry $Na_8Si_6Al_6O_{24}X_xCl_{2-2x}$ (X=S, Se and Te), via solid-state synthesis.

$$3\,Na_2Si_2Al_2O_8 + x\,Na_2XO_3 + (2-2x)NaCl \rightarrow Na_8Si_6Al_6O_{24}X_xCl_{2-2x} + \frac{3}{2}xO_2 \quad (7.1.1)$$

Appropriate amounts of NaCl, Na_2XO_3 and commercial Na-LTA zeolite were mixed, considering the desired stoichiometry, with x=0, 0.1, 0.2, 0.3, 0.4, 0.5, 0.6, 0.7, 0.8, 0.9, when applied. Zeolite Na-LTA was first dried at 500 °C for 5 h. Afterward, these powder mixtures were ball-milled (Planetary Ball Mill Retsch PM 100) for 1 hour and homogenized in a shaker powder mixer (Turbula T2F) for 3 hours. The nominal molar ratios of X/Cl correspond to 0, 0.06, 0.13, 0.21, 0.33, 0.50, 0.75, 1.17, 2.0 and 4.5, respectively and when applied.

The synthesis was performed in an electric furnace (TH1300, Termolab) at 900 °C for 1 hour under a reducing atmosphere of 5% H_2 / 95% Ar (v/v) at 500 mL/min. These materials were washed with water and ethanol to remove any trace of reagents.

Sulfur (subchapter **2.1**): Samples with S/Cl ratios of 0.21 and 4.5 were also subjected to the same 900 °C treatment for 4 and 8 hours, alternatively to the 1 hour procedure mentioned previously.

Additionally, in samples containing a NaCl excess, the amount of this salt was adjusted in the produced samples labeled as (+NaCl) to investigate its impact on the final crystalline phases and consequent photophysical properties. Note that these samples present identical chemical compositions to those in subchapter **2.3**. PIXE results (**Table A.1.2**) revealed that the resulting unit cell differs from the ideal desired composition as specified in equation (**7.1.1**).

Therefore, the sulfur concentration remained unchanged in this study, with only the NaCl amounts adjusted to achieve this ideal composition. Calculations were performed to determine the necessary NaCl adjustments, considering the NaCl initially weighted in the original mixtures and the chloride measured by PIXE analysis after the 900 °C synthesis. These samples underwent the same synthesis procedure as the originals, involving a 1 hour synthesis at 900 °C under a reducing atmosphere of 5% H_2 / 95% Ar at 500 mL/min. These materials were washed with water and ethanol to remove any trace of reagents.

Sulfur (subchapter **2.2**): Samples were synthesized following two-step syntheses. The first one consists in transforming commercial Na-LTA into sodalite at 900 °C without a reducing atmosphere, (1) in equations (**7.1.2**) and (**7.1.3**). The second step consists of adding sodium sulfite or elemental sulfur to the produced sodalite, (2) in equations (**7.1.2**) and (**7.1.3**), respectively, at 900 °C for 1 hour under a reducing atmosphere. These materials were washed with water and ethanol to remove any trace of reagents.

$$3\ Na_2Al_2Si_2O_8 \xrightarrow[+2\ NaCl]{\mathbf{1}} Na_8Al_6Si_6O_{24}Cl_2 \xrightarrow[+x\ Na_2SO_3]{\mathbf{2}} Sulfur-doped\ zeolites \qquad (\mathbf{7.1.2})$$

$$3\ Na_2Al_2Si_2O_8 \xrightarrow[+2\ NaCl]{\mathbf{1}} Na_8Al_6Si_6O_{24}Cl_2 \xrightarrow[+x\ S]{\mathbf{2}} Sulfur-doped\ zeolites \qquad (\mathbf{7.1.3})$$

x=0.3 and 0.9

Sulfur (subchapter **2.3**): An additional sample of commercial Na-LTA zeolite without any pretreatment was submitted to the same synthesis procedure. This sample was then washed with water and ethanol to remove any trace of reagents.

7.1.2 Sol-gel synthesis of nanosodalite zeolite

Selenium (subchapter **4.1**): Nanosodalite was synthesized using Ludox colloidal silica HS-30, aluminum powder, MilliQ-water, sodium hydroxide, and, when applied, sodium selenite. Three gel compositions were prepared with ratios of $18Na_2O:5SiO_2:1Al_2O_3:240H_2O$, $18Na_2O:5SiO_2:1Al_2O_3:240H_2O:\underline{0.03SeO_2}$ and $18Na_2O:5SiO_2:1Al_2O_3:240H_2O:\underline{0.34SeO_2}$, corresponding to the final ideal compositions of $[Na_6(H_2O)_8][Si_6Al_6O_{24}]$, $[Na_6(H_2O)_8][Si_6Al_6O_{24}]\underline{Se_{0.1}}$ and $[Na_6(H_2O)_8][Si_6Al_6O_{24}]\underline{Se_1}$. These samples were denoted as Se_0 gel, $Se_{0.1}$ gel and Se_1 gel samples, respectively.

The synthesis protocol involved two separate mixtures: one containing silica, sodium hydroxide and water, and the other containing aluminum powder, water and sodium hydroxide. Sodium selenite was introduced into the latter mixture after the aluminum powder had completely dissolved. Subsequently, the aluminum and sodium selenite solution was added dropwise to the silica mixture, with the latter placed in an ice bath. The mixtures were stirred for 24 hours at room temperature and then heated at 60 °C under static conditions for 48 hours. The resulting zeolites were washed with MilliQ-water through successive cycles of centrifugation (48000 g, 15 minutes) and redispersion to reduce their pH (a minimum of 12 cycles were needed). This protocol was adapted from reference **144**.

Selenium (subchapter **4.2**): Non-doped nanosodalite was synthesized through a sol-gel synthesis using a gel composition with ratios of $18Na_2O:5SiO_2:1Al_2O_3:240H_2O$, with corresponding final ideal composition of $[Na_6(H_2O)_8][Si_6Al_6O_{24}]$. This sample is a new batch of Se_0 gel sample, as described in subchapter **4.1**.

An additional selenium-doped nanosodalite sample was synthesized using the same sol-gel protocol, using ratios of $18Na_2O:5SiO_2:1Al_2O_3:240H_2O:\underline{2.38SeO_2}$, corresponding to the final ideal composition of $[Na_6(H_2O)_8][Si_6Al_6O_{24}]\underline{Se_7}$. This sample is further described as Se_7 gel.

After obtaining colored compounds by following the reduction protocols starting from the selenium precursor - either through solid-state synthesis (see protocol in section **7.1.4**) or solution synthesis (see protocol in section **7.1.6**) - each compound was used as selenium raw material in the sol-gel synthesis of nanosodalite zeolites. Consequently, two gel samples with the compositions ratios of $18Na_2O:5SiO_2:1Al_2O_3:240H_2O:\underline{0.34SeO_2}$, resulting in the final ideal composition of $[Na_6(H_2O)_8][Si_6Al_6O_{24}]\underline{Se_1}$, were produced. These samples were denominated as Se_1 gel samples.

The same modified synthesis protocol from reference **144** was used to synthesize all nanosodalites samples described in this subchapter **4.2**.

7.1.3 High-temperature synthesis starting from nanosodalite zeolite

Selenium (subchapter **4.1**): As described in equation (**4.1.1**) in subchapter **4.1**, nanosodalite $Se_{0.1}$ gel and Se_1 gel samples (see synthesis protocol in section **7.1.2**) were dried, manually milled and subjected to 1 hour synthesis at 900 °C under reducing atmosphere of 5% H_2 / 95% Ar (v/v) at 500 mL/min., yielding samples $Se_{0.1}$ gel - 900 °C and Se_1 gel - 900 °C, respectively.

On the other hand, as described in equation (**4.1.2**) in subchapter **4.1**, the non-doped nanosodalite sample, Se_0 gel (see synthesis protocol in section **7.1.2**), was doped with sodium selenite using two different concentrations (x=0.1 and 1). These samples were then mixed using a ball mill and powder shaker before being placed in the furnace at 900 °C for 1 hour under reducing atmosphere of 5% H_2 / 95% Ar (v/v) at 500 mL/min., resulting in samples $Se_{0.1}$ - 900 °C and Se_1 - 900 °C, respectively.

After synthesis, all samples were washed with water and ethanol to remove any trace of reagents.

Selenium (subchapter **4.2**): Selenium-doped nanosodalite Se_7 gel sample (see synthesis protocol in section **7.1.2**) was dried overnight in a furnace at 35 °C in its pellet form, which was obtained after a centrifugation cycle (48000 g, 15 minutes). Subsequently, this sample was divided in half: one part remained non-milled (simply dried), while the other was manually milled. Each of these halves was then further divided into three portions.

For the high-temperature synthesis, a fraction of the non-milled sample and a fraction of the milled sample were loaded into the same synthesis alumina crucible and subjected to three different temperatures - 700 °C, 800 °C and 900 °C - for 1 hour under a reducing atmosphere of 5% H_2 / 95% Ar at 500 mL/min., see **Figure 4.2.5** for additional information. These materials were washed with water and ethanol to remove any trace of reagents.

7.1.4 Selenium precursor solid-state reduction

Selenium (subchapter **4.2**): Sodium selenite salt was placed directly into a furnace and heated at 500 °C for 1 hour under a reducing atmosphere of 5% H_2 / 95% Ar.

7.1.5 Reduction of selenium-doped nanosodalites in solution

Selenium (subchapter **4.2**): Method **1)** - 100 mg of Se_7 gel nanosodalite sample, along with 0.0275 mmol of sodium borohydride and 3.29 mmol of sodium hydroxide, were dissolved in 2 mL of Milli-Q water and charged into a Schlenk tube. Once the tube was purged one last time with argon, it was placed inside an ultrasound bath to initiate the synthesis process. This protocol was adapted from reference **149**.

Method **2)** - 685 mg of Se_7 gel nanosodalite sample, along with 0.4 mmol of hydrazine and 45 mmol of sodium hydroxide, were dissolved in 30 mL of methanol (HPLC grade) and charged into a two-neck round-bottom flask. The flask had a septum stopper and a take-off connected to an argon balloon. This protocol was adapted from reference **150**.

7.1.6 Selenium precursor reduction in solution

Selenium (subchapter **4.2**): Method **1)** - 2.19 mmol of either sodium sulfite or sodium selenite, 0.275 mmol of sodium borohydride and 3.29 mmol of sodium hydroxide were dissolved in 2 mL of Milli-Q water and charged into a Schlenk tube. Several consecutive vacuum and argon purging cycles were performed to eliminate the air inside the Schenk tube. The remaining experimental protocol for the free salt reduction was identical to that described above in section **7.1.5**.

Method **2)** - 15 mmol of either sodium sulfite or sodium selenite, along with 4 mmol of hydrazine and 45 mmol of sodium hydroxide, were dissolved in 30 mL of methanol (HPLC grade) and charged into a two-neck round-bottom flask. The remaining experimental protocol for the free salt reduction was identical to that described above in section **7.1.5**.

7.2 Experimental Techniques and Sample Characterization

7.2.1 Absorption Spectroscopy

Absorption spectroscopy is a powerful analytical technique used to measure the amount of light absorbed by a sample across different wavelengths. Two light sources are commonly used: a deuterium lamp and a tungsten-halogen lamp. These lamps cover different spectral ranges, with the deuterium lamp providing UV light and the tungsten-halogen lamp covering visible and near-infrared regions. The light from these lamps passes through a mirror assembly or lamp mirror, which directs it towards the monochromator (**Figure 7.2.1**).

Once the light reaches the monochromator, it is dispersed into its component wavelengths. In a double-beam spectrophotometer, this beam is then split into two: one for the sample and the other for the reference. Within the sample compartment, the incident light passes through the sample solution or material, interacting with the molecules present. The molecules absorb specific wavelengths of light depending on their chemical composition and concentration. Simultaneously, in the reference compartment, the incident light passes through a blank or reference solution that does not absorb light at the wavelengths of interest.

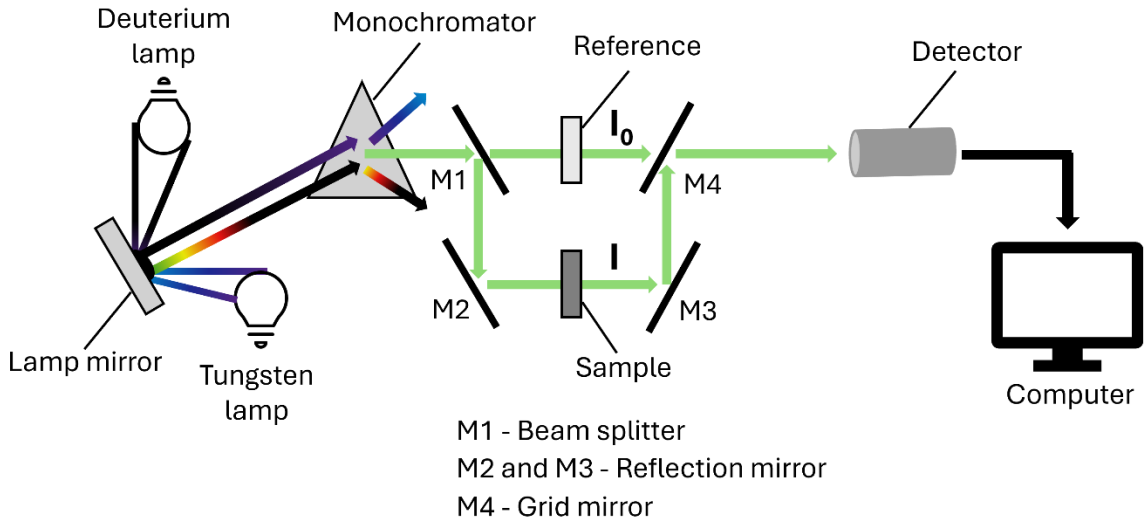


Figure 7.2.1 - Typical assembly of a double-beam spectrometer for absorption spectroscopy. Adapted from reference **156**.

Photodetectors then detect the light intensities from both compartments, converting them into electrical signals for analysis. The intensity ratio of the light from the sample (I) to the intensity from the reference (I_0) gives the transmittance (T) of the absorbing species. Transmittance can then be converted into absorbance (A), as described in equation (**7.2.1**).

$$A = -log_{10}\left(\frac{I}{I_0}\right) = -log_{10}(T) \qquad (7.2.1)$$

Furthermore, the empirical Beer-Lambert law relates the absorbance (A) to the molar concentration (C) of the absorbing species and optical pathlength (l), see equation (**7.2.2**).

$$A = \varepsilon . l . C \qquad (7.2.2)$$

where ε (epsilon) is the molar absorption coefficient. This value expresses the ability of a species to absorb light at a specific wavelength in a given solvent.

Selenium (subchapter **4.2**): The absorption studies were conducted in quartz cells using a Varian Cary 100 Bio UV-Visible Spectrophotometer. The collected data were acquired between 250 and 800 nm at room temperature, with a 1 nm interval, in double beam mode.

7.2.2 Diffuse Reflectance Spectroscopy

Diffuse reflectance spectroscopy refers to the scattering of light when it reaches a surface and is reflected in many different directions. This phenomenon occurs when light encounters a surface with irregularities or microscopic structures, causing the light to be scattered rather than reflected uniformly in a single direction.

In experimental measurements, a similar apparatus to absorption spectroscopy with a two-beam setup is often used. However, in diffuse reflectance spectroscopy, the integrating sphere is equipped with a standard reflectance sample (typically barium sulfate) and the sample of interest (**Figure 7.2.2**). This sphere collects and distributes the reflected light uniformly, allowing for accurate diffuse reflectance measurements across different wavelengths. The detector is placed in the middle of the sphere, allowing for the measurement of the reflected light from the reference (I_0) and the sample of interest (J). Note that when a 100% reflective reference as $BaSO_4$ is used, the reflected light (I_0) effectively represents the incident light emitted from the light source.

Furthermore, the Kubelka-Munk theory provides a mathematical approach for analyzing and interpreting the diffuse reflectance data obtained from such measurements. This is given by equation (**7.2.3**).

$$K - M = \frac{(1-R_\infty)^2}{2.R_\infty} \qquad (7.2.3)$$

where R_∞ represents the reflectance of the sample relative to the reflectance of a perfectly reflecting (or diffusing) material. It is calculated as the ratio of the reflected light intensity of the sample (J) to the reflected light intensity of the reference (I_0), see equation (**7.2.4**).

$$R_\infty = \frac{J}{I_0} \qquad (7.2.4)$$

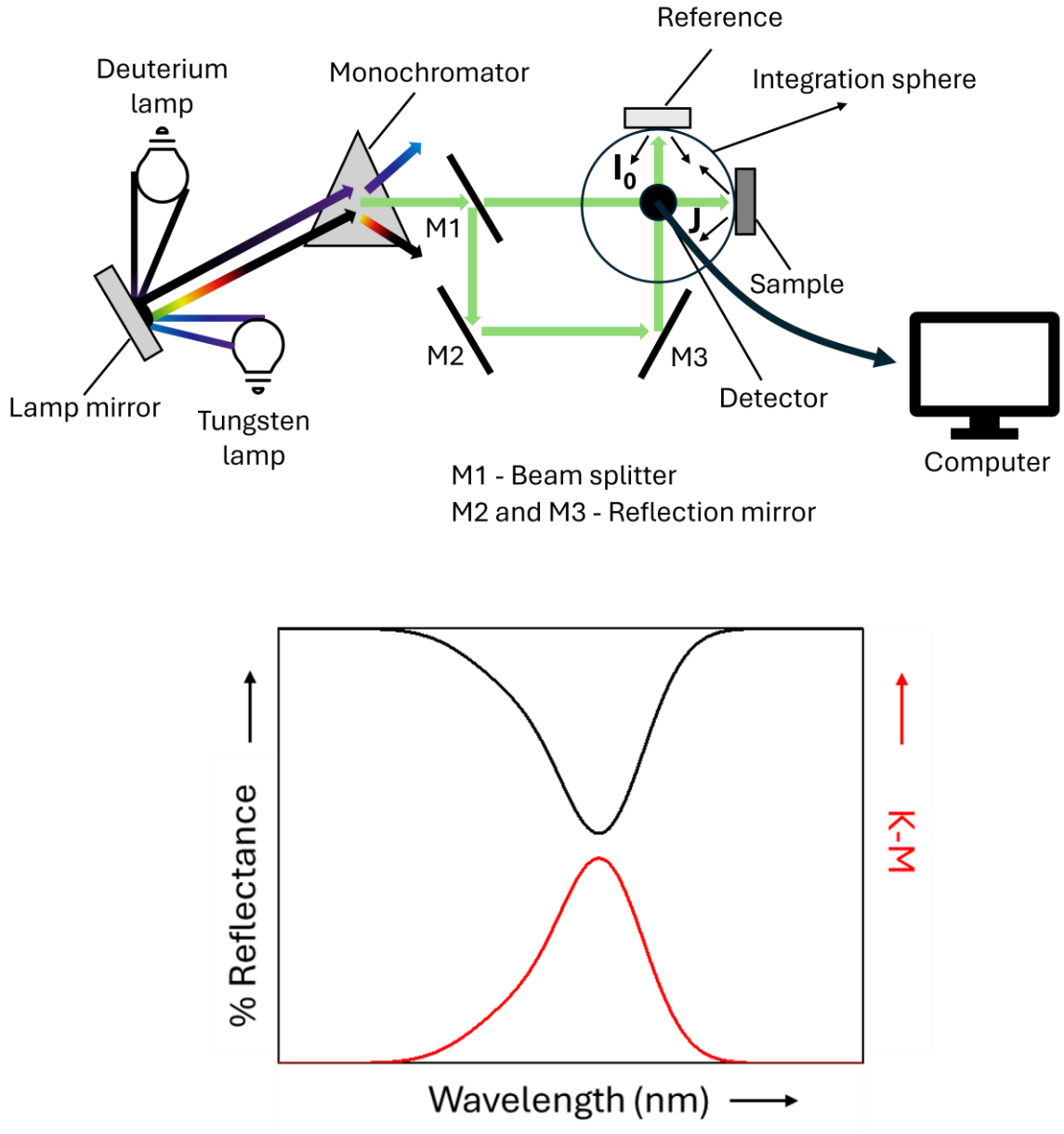


Figure 7.2.2 - (**Above**) Typical set-up of a diffuse reflectance spectroscopy experiment. (**Below**) Example of a reflectance spectrum (black) and corresponding one after applying Kubelka-Munk transformation (red). Adapted from reference **157**.

Sulfur, selenium and tellurium (chapters **2**, **3**, **4** and **5**): Diffuse reflectance measurements were performed inside an integrating sphere in a Shimadzu UV-2501PC using $BaSO_4$ as a reference sample.

The thermally treated samples in subchapter **4.2** (**Figure 4.2.11**) were characterized using a different apparatus. Here, the Avantes AvaSpec-2048 Fiber Optic Spectrometer, equipped with a 300 lines/mm grating and a Full Width at Half Maximum (FWHM) resolution of 2.4 nm,

was used to measure the produced reflectance spectra. The operational wavelength range extended from 380 to 800 nm, with a 2048-pixel linear array CCD detector. Furthermore, an AvaSphere-50 integrating sphere (250-2500 nm) with a 50 mm internal diameter and a 10 mm sample port diameter was used. The light source for this mode was a 10 Watt Tungsten Halogen Lamp. 600 μm fibers (FC-UV600-2) were utilized in this configuration.

Sulfur (subchapter **2.3**)**:** The ultramarine blue pigment (ultramarine blue DP-55 from Nubiola) was diluted with $BaSO_4$ until it matched the same absorbance at 600 nm found in the sample S/Cl=4.5. This diluted sample was used as a reference for $[S_3]^-$ species in Raman and EPR spectroscopies.

7.2.3 Steady-State Emission

Photoluminescence is a process where a molecule absorbs a photon, promoting one of its electrons to a higher electronic excited state. Subsequently, the molecule emits a photon as the electron returns to a lower energy state. This phenomenon follows the Franck-Condon principle, where electronic transitions occur between vibrational states of different energy levels. Fluorescence, phosphorescence, and delayed fluorescence are examples of emission processes.

In fluorescence, emission occurs with retention of spin multiplicity, typically from a singlet excited state to the ground state ($S_1 \rightarrow S_0$). Conversely, in phosphorescence, the spin multiplicity is altered: commonly, absorption occurs to a singlet state (S_1), which through intersystem crossing (ISC) transitions to the excited triplet state (T_1), and emission occurs from this state ($T_1 \rightarrow S_0$). This intersystem conversion causes longer-lived emissions, between 10^{-6} and 10 seconds, compared to fluorescence emission processes, which have lifetimes between 10^{-10} and 10^{-7} seconds. Delayed fluorescence results from two intersystem conversions, the first from $S_1 \rightarrow T_1$, followed by $T_1 \rightarrow S_1$, however, emission occurs from $S_1 \rightarrow S_0$, and this mechanism is thermally activated[116]. Jablonski diagram summarizes all the mentioned emission processes (**Figure 7.2.3**).

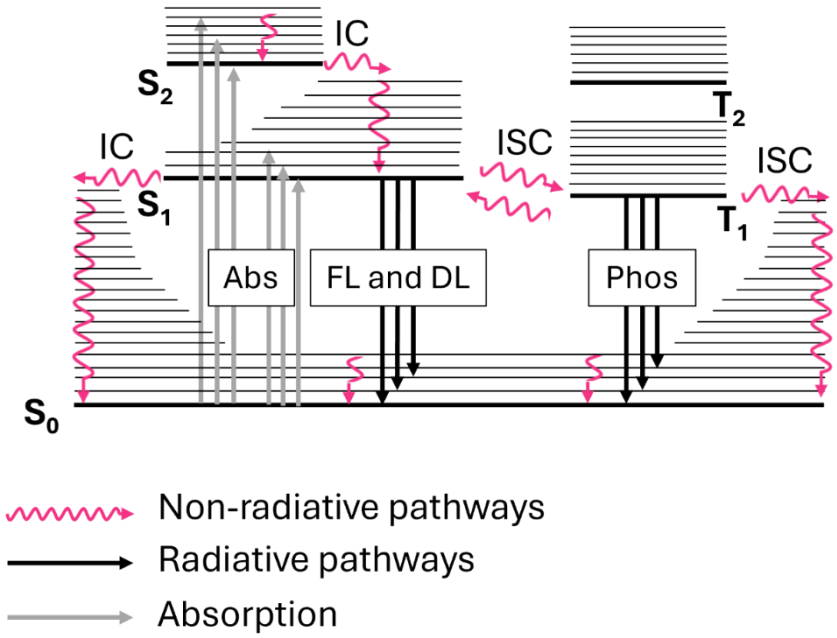


Figure 7.2.3 - Jablonski diagram demonstrating the mechanistic processes of fluorescence (FL), phosphorescence (Phos) and delayed fluorescence (DL) after absorption (Abs). Adapted from reference **116**.

Additionally, these transitions can be classified as radiative (emission of photons) or non-radiative (no photon emission). Internal conversion (IC), intersystem crossing (ISC), and vibrational relaxation (VR) are examples of non-radiative processes. The internal conversion (IC) process occurs between two energy levels with the same spin multiplicity, with an estimated time between 10^{-11} and 10^{-9} seconds. Intersystem crossing (ISC) and vibrational relaxation (VR) present mechanistic timescales of 10^{-10} to 10^{-8} seconds and 10^{-12} to 10^{-10} seconds, respectively. As mentioned earlier, these processes compete with the radiative ones, which include emission through fluorescence, phosphorescence, and delayed fluorescence processes[116].

A steady-state emission spectroscopy setup typically involves measuring emitted light from a sample at various wavelengths. A xenon lamp serves as the light source due to its ability to emit radiation across a wide range of wavelengths, from ultraviolet to near-infrared. The process begins with selecting an excitation wavelength, which is directed onto the sample through an excitation monochromator (**Figure 7.2.4**). This monochromator ensures that only the desired wavelength reaches the sample, effectively exciting it. Following excitation, the sample emits light across various wavelengths. A second monochromator, positioned at a 90° angle, accurately captures this emitted light. This emission monochromator scans the emitted light intensity across different wavelengths, providing detailed spectral information. The emitted light is then directed to a detector, which converts the optical signals into electrical

signals. These electrical signals are then processed to generate an emission spectrum, plotting the intensity of emitted light against the corresponding wavelengths.

Once the emission spectrum is known, the excitation spectrum can be recorded by measuring the intensity of the emitted light while exciting the sample with light of different wavelengths. This process helps identify the wavelengths of light that induce emission from the sample. Furthermore, comparing the excitation and absorption spectrum can provide important information about whether all the absorbing species are responsible for the emission.

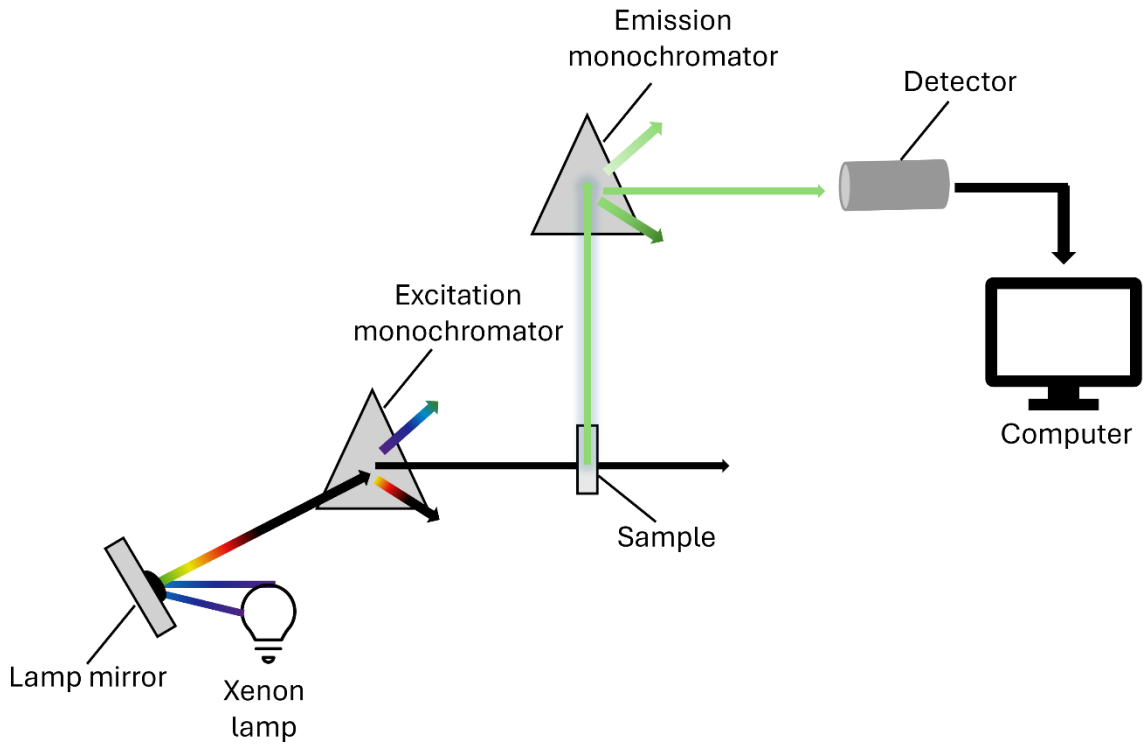


Figure 7.2.4 - Representation of a typical set-up for steady-state emission spectroscopy experiments. Adapted from reference **158**.

The effectiveness of radiative processes is often evaluated by measuring the quantum yield (QY). Quantum yield is defined as the ratio of the number of emitted photons to the number of absorbed photons. Ideally, when the QY (ϕ_F) is 1, it means that all absorbed photons are emitted. Quantum yield can also be expressed as the ratio of the radiative constant (k_r) to the sum of the radiative (k_r) and non-radiative (k_{nr}) constants, as indicated in equation (**7.2.5**).

$$\phi_F = \frac{Number\ of\ emitted\ photons}{Number\ of\ absorbed\ photons} = \frac{k_r}{k_r + k_{nr}} \qquad (7.2.5)$$

Quantum yields can be experimentally determined using either the absolute or relative methods. The absolute method involves placing the sample inside an integrating sphere, allowing for the precise measurement of the number of absorbed and emitted photons. Conversely, the relative method compares the sample to a standard with a known quantum yield. Ideally, this standard should absorb and emit within the same spectral region as the sample.

In material science, the term quantum yield is often replaced with external quantum efficiency (EQE). Therefore, the term EQE will be used throughout this thesis.

Sulfur, selenium and tellurium (chapters **2**, **3, 4** and **5**): The excitation and emission spectra were recorded using a Horiba Jobin Yvon fluorolog FL3-22 fluorimeter equipped with a xenon 450 W light source.

The temperature studies were conducted using a FL-1013 liquid nitrogen dewar assembly.

Sulfur (subchapter **2.3**)**:** The external quantum efficiencies of the powder samples were measured by the absolute method using an integrating sphere[70]. A NIST calibration lamp was used to compute the correction curve of the integrating sphere/detection system. The excitation source used was a 355 nm continuous laser (LaserTechnic, 10 mW). The signals were collected from the integrating sphere by a collimating beam probe coupled to an optical fiber (fused silica) in this way, assuring the connection to the monochromator entrance. A fixed monochromator (Andor, Shamrock 163) coupled to an ICCD detector (Andor, i-Star 720) with time gate capabilities was used in the accumulation mode[159].

Selenium (chapter **3** and subchapter **4.1**): The external quantum efficiencies of the powder samples were measured by the absolute method using an integrating sphere[70] in the mentioned Horiba Jobin Yvon fluorolog FL3-22 fluorimeter.

7.2.4 Photoluminescence Decay Times

As described above, emission processes may occur over various timescales, from picoseconds to nanoseconds for fluorescence and from microseconds to seconds for phosphorescence. This technique monitors the emission intensity over time after sample excitation, typically using a laser (**Figure 7.2.5**).

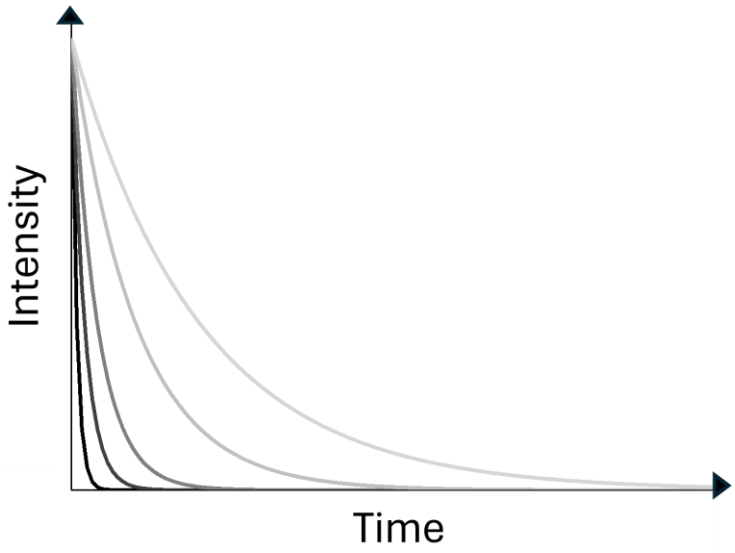


Figure 7.2.5 - Representation of five different photoluminescence decay times occurring at different timescales.

The luminescence lifetime represents the average time the emission intensity takes to decrease to 1/e (approximately 37%) of its initial value after excitation. This lifetime (τ) is dependent on the radiative (k_r) and non-radiative (k_{nr}) constants of the system[116]. An increase in either constant results in faster lifetimes, as described in equation (**7.2.6**).

$$\tau = \frac{1}{k_r + k_{nr}} \qquad (7.2.6)$$

7.2.4.1 Short timescale (nanoseconds)

Selenium and tellurium (chapters **3** and **5** and subchapter **4.1**): Fluorescence decays were obtained with a HORIBA Jobin Yvon IBH FluoroLog-3 spectrofluorometer adapted to time-correlated single photon counting (TCSPC), equipped with a Hamamatsu R928 photomultiplier tube. Samples were excited with nanosecond pulses of 445 nm generated by a NanoLED pulsed diode (Horiba). Emission decays were analyzed using the Fit convolution App of OriginPro 2023b software.

The temperature-dependent studies were conducted using an FL-1013 liquid nitrogen dewar assembly.

7.2.4.2 Long timescale (microseconds)

Sulfur, selenium and tellurium (chapters **3** and **5** and subchapters **2.3** and **4.1**): Phosphorescence decays were measured in multichannel scaling (MCS) mode using a Horiba DeltaFlex system with a BH 402.9 nm laser excitation, operating in burst mode for 50 MHz. Emission wavelengths were selected accordingly and detected with a PPD detection module.

The temperature-dependent studies were conducted using a Horiba FL-1013 liquid nitrogen dewar assembly.

7.2.5 Time-Resolved Emission Spectroscopy (TRES)

Time-resolved emission spectroscopy (TRES), as the name implies, measures the emission of light from a sample over time, meaning that photoluminescence decay times are measured using this technique. However, contrary to what was generally discussed in the previous section **7.2.4**, TRES introduces two key parameters: the gate width and the delay time (**Figure 7.2.6.A**). The gate width refers to the time during which the emitted signal is collected and integrated after the excitation pulse. On the other hand, delay time represents the time interval between the excitation pulse and the start of signal collection. These two parameters are commonly adjusted iteratively to optimize the measurement conditions for a specific sample and desired outcome (**Figure 7.2.6.B**). For example, shorter gate widths may be chosen to capture rapid emission processes, while longer delay times may be used to study longer-lived excited states.

Experimentally, the sample is excited by a short pulse of light, typically from a laser. The emitted light is then detected by monitoring a specific emission wavelength and analyzed over time using a high-temporal resolution detector. This detector is synchronized with the excitation source and the emitted light detection to accurately record the time-resolved emission data. Furthermore, the emitted light is often dispersed using a monochromator or a spectrometer (**Figure 7.2.6.C**). The intensity versus wavelength data obtained from the experiment can then be analyzed to extract various parameters, such as emission spectra.

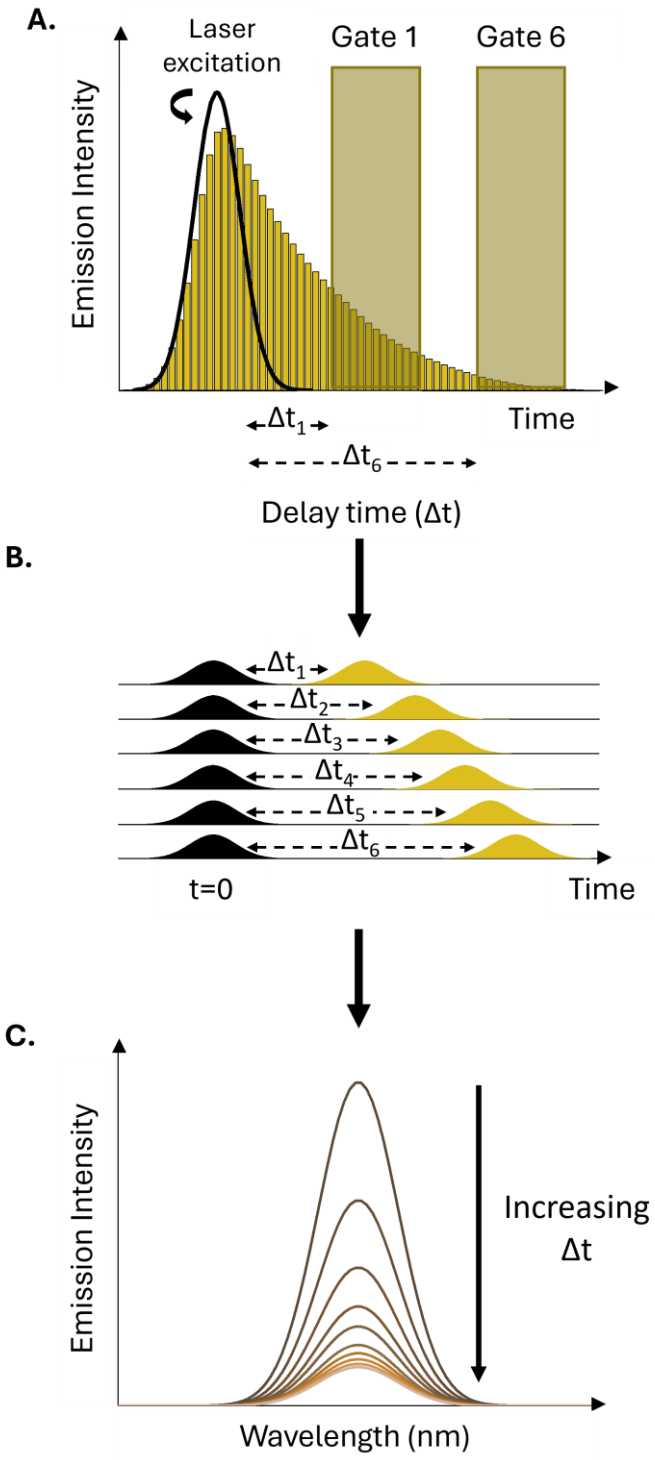


Figure 7.2.6 - **Basics of Time-Resolved Emission Spectroscopy (TRES) technique** - (**A**) Representation of a typical photoluminescence decay time exhibiting the entire temporal profile of the emitted photons, introducing important concepts like delay time and gate width (integration signal area) for TRES technique. (**B**) Representation of the signal acquisition of TRES technique based on the full photoluminescence decay time depicted in (A), applying different delay times while maintaining the gate widths constant. (**C**) Example of corresponding emission spectra acquired through TRES techniques, using the inputs in (B).

In the time-resolved emission spectroscopy study, two different detectors were used. One is more sensitive in the UV-Vis range, and the other is more accurate in the NIR region, according to reference **160**.

Sulfur (subchapter **2.3**): The phosphorescence emission spectra of all sulfur-doped zeolites samples were carried out in a UV-Vis detector. A Jobin Yvon FluoroLog fluorescence spectrometer with a pulsed xenon lamp with full width at a half-maximum of 3 μs was used. A delay time of 0.1 ms was applied. In addition, room-temperature lifetime measurements of all synthesized powders were carried out in the same UV-Vis detector.

In the temperature ramp conducted in this subchapter (**Figure 2.3.19** and **Figure 2.3.20**), a model liquid nitrogen cryostat (Janis Research) was used. The sample was then heated from 77 K to 348 K, with a stabilization period of 20 minutes at each temperature, ensuring temperature uniformity throughout the system.

Sulfur, selenium and tellurium (chapters **3** and **5** and subchapters **2.3** and **4.1**): For more accurate results in the NIR region, a NIR sensitive detector ICCD (with a minimum temporal gate of 2.2 ns) was used. A N_2 laser at 337 nm (OBB, model 4500 with ~1mJ per pulse) was used. A fixed monochromator (Andor, Shemrock 163) coupled to an ICCD detector (Andor, i-Star 720) with time gate capabilities and in the kinetics mode was used here to detect the fluorescence or phosphorescence signals. The signals were collected by a collimating beam probe coupled to an optical fiber (fused silica) in this way, assuring the connection to the monochromator entrance.

In the temperature-dependent studies conducted in chapter **3** and subchapter **4.1**, the analyzing quartz cuvette was submerged in liquid nitrogen for approximately five minutes before each analysis. It was then immediately placed in the sample holder, followed by acquisition.

7.2.6 Transient Absorption (TA) spectroscopy

Transient absorption (TA) spectroscopy investigates changes in light absorption of a sample over time after excitation with a short light pulse. This technique monitors variations in absorption spectra, providing insights into the dynamics of photoexcited states and transient intermediates.

Following initial excitation with a short pulse (pump), typically emitted from a laser and lasting from femtoseconds to nanoseconds, a second light pulse, known as the probe pulse, is

used to monitor changes in the absorption spectrum of the sample over time. Absorption of the probe light by the sample is quantified using a spectrometer or other detection systems (**Figure 7.2.7**).

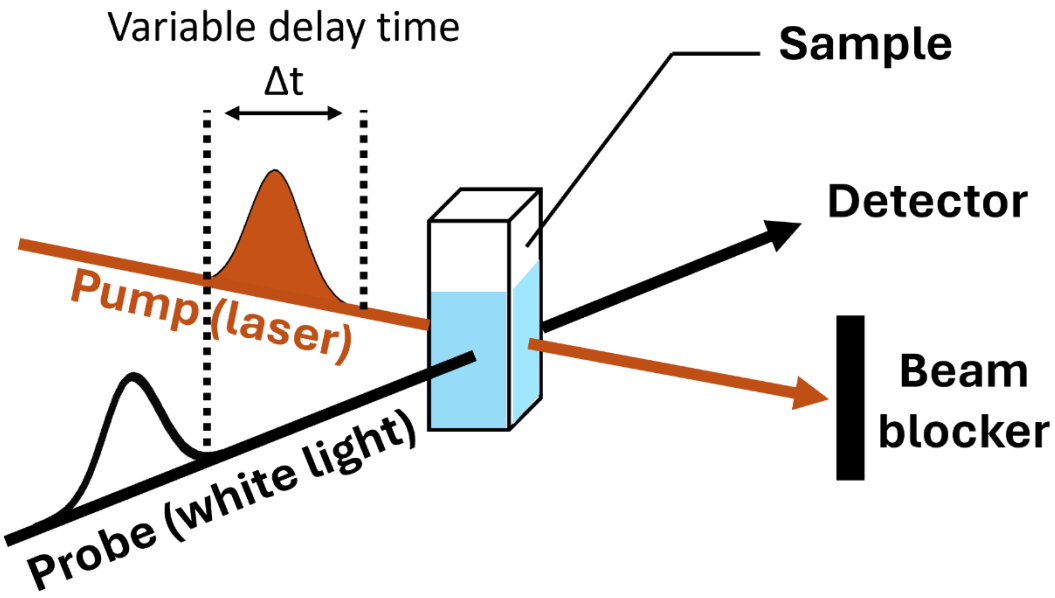


Figure 7.2.7 - Typical transient absorption (TA) set-up with the pump pulse photoexciting the sample, while the probe pulse is used to observe the absorption response of the sample at different times after photoexcitation. Adapted from reference **161**.

The Jablonski diagram (**Figure 7.2.8.A**) illustrates the possible electronic states and radiative and non-radiative pathways following pump and probe pulses. The transient spectra obtained from TA experiments (**Figure 7.2.8.B**) illustrate changes in sample absorption as a function of wavelength and delay time, providing valuable information into the excited states and transient species present.

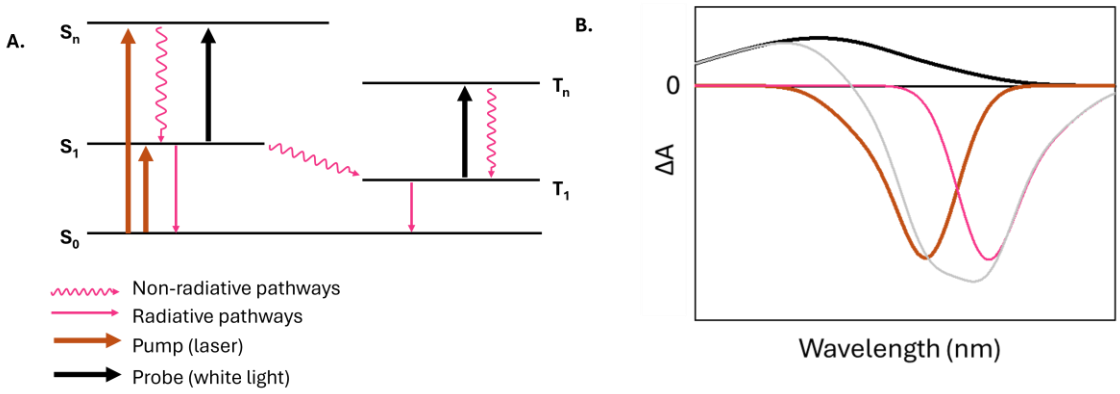


Figure 7.2.8 - (**A**) Jablonski diagram with possible states and pathways occurring after pump and probe pulses. (**B**) Example of a typical TA spectrum (gray) deconvoluted with positive and negative ΔA contributions. Ground-state bleach (brown) and stimulated emission (pink) have negative contributions and excited-state absorption (black) exhibits a positive contribution to ΔA. Adapted from reference **161**.

Sulfur (subchapter **2.3**): Laser flash photolysis experiments were carried out with the fourth harmonic of a Nd:YAG laser (266 nm, ca. 6 ns FWHM, 35 mJ/pulse) in the diffuse reflectance mode. The light arising from the irradiation of solid samples by the laser pulse and monitoring lamp (Xe 450 W) was collected by a collimating beam probe coupled to an optical fiber (fused silica) and was detected by a gated intensified charge-coupled device Oriel model Instaspec V, (Andor ICCD, based on the Hamamatsu S57 69-0907). The ICCD was coupled to a fixed imaging compact spectrograph (Oriel, model FICS 77441). The system can be used either by capturing all light emitted by the sample or in a time-resolved mode by using a delay box (Stanford Research Systems, model D6535). The ICCD has high-speed gating electronics (2.2 ns) and an intensifier that covers the 200-950 nm wavelength range. Time-resolved absorption spectra of the powdered sample have been acquired in short- or long-time domains using a fixed gate width of 2 μs and suitable start delays. For a small percentage of conversion (high concentration of ground-state absorbers and low laser fluencies), the concentration of transients decreases exponentially and transient absorption data were reported as a percentage of absorption (% Abs.), as defined in equation (**7.2.7**).

$$\%\, Abs = 100\, \frac{\Delta J_t}{J_0} = \left(1 - \frac{J_t}{J_0}\right) 100 \qquad (7.2.7)$$

where J_o and J_t are diffuse reflected light from the sample before exposure to the exciting laser pulse and at time t after excitation, respectively[162].

7.2.7 Electron Paramagnetic Resonance (EPR) spectroscopy

Electron paramagnetic resonance (EPR) exploits the electronic and magnetic properties of unpaired electrons. When exposed to an external magnetic field, these electrons generate a magnetic moment and can absorb electromagnetic radiation at a specific magnetic field ("field of resonance"). This magnetic field depends on the surrounding environment of the electron.

During an EPR experiment, a sample containing paramagnetic substances is exposed to a strong magnetic field created by a magnet. Simultaneously, microwave radiation is directed at the sample while scanning the magnetic field strength (**Figure 7.2.9.A**). When the resonance condition is satisfied, see equation (**7.2.8**), energy absorption occurs, leading to a decrease in detected microwave power. This absorption phenomenon constitutes the basis of the EPR signal, reflecting the microwave energy absorbed by the sample at a certain magnetic field (**Figure 7.2.9.B**).

$$\Delta E = g\beta B_0 = h\nu \qquad (7.2.8)$$

where ΔE represents the energy difference between two electron spin states, g is the spectroscopic g-factor of the free electron, β is the Bohr magneton, representing the magnetic moment of the electron, B_0 stands for the magnetic field strength, h is Plank's constant and ν represents the frequency of the electromagnetic radiation.

Through the computation of the first derivative of the absorption spectrum concerning the magnetic field strength, the rate of change of absorbed microwave power with respect to the magnetic field is determined. This mathematical operation accentuates abrupt changes or peaks in the absorption spectrum, thereby generating a derivative-like signal (**Figure 7.2.9.C**). This signal tends to produce sharper and clearer peaks compared to the absorption spectrum, with each peak corresponding to a resonance frequency where unpaired electrons in the sample absorb microwave energy. These distinct peaks facilitate easier interpretation and analysis, offering valuable insights into the paramagnetic species present in the sample, including their g-values, which elucidate their electronic structure and coordination environment.

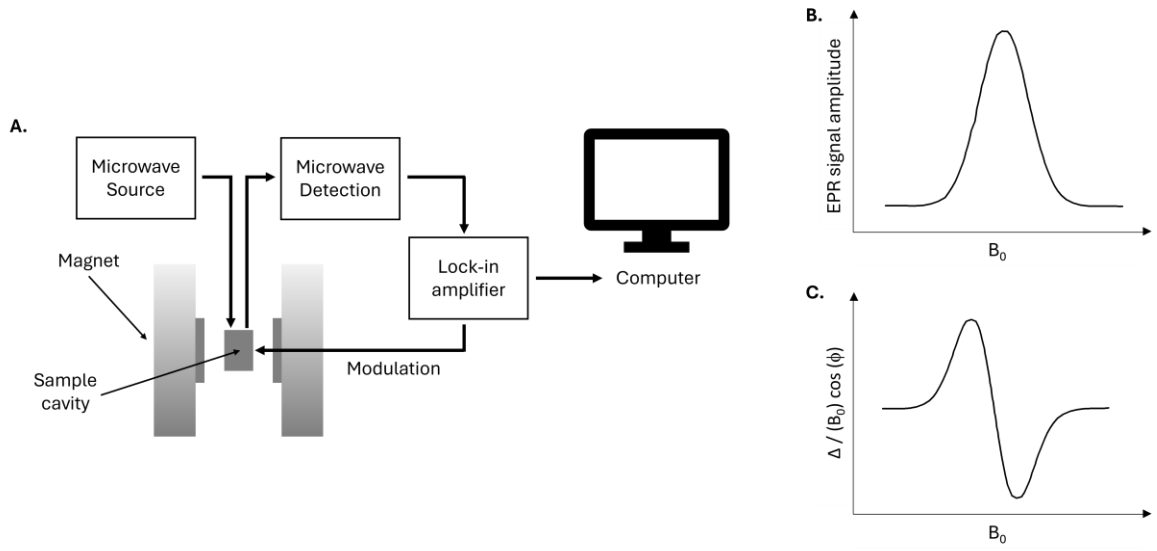


Figure 7.2.9 - (**A**) Schematic representation of a simple continuous wave (CW)-EPR spectrometer, illustrating the key components involved in the experiment. (**B**) Typical EPR absorption line, depicted as a Gaussian absorption band. (**C**) Corresponding derivative-like signal. Adapted from reference **163**.

Sulfur (subchapter **2.3**): X-band EPR spectra were obtained at 120 K using a Bruker EMX spectrometer equipped with a liquid nitrogen continuous flow cryostat and a high sensitivity perpendicular mode rectangular cavity. Powder samples were packed into quartz EPR tubes (3mm I.D.). All spectra were recorded using a microwave frequency of 9.45 GHz, a modulation amplitude of 0.1 mT, and a microwave power of 2 mW. Spectra were analyzed and simulated using SpinCount[164].

Selenium and tellurium (chapters **3** and **5**)**:** X-band EPR spectra were obtained at various temperatures from 4 to 180 K using a Bruker EMX spectrometer equipped with an Oxford Instruments ESR-900 continuous-flow helium cryostat and a high sensitivity perpendicular mode rectangular cavity. Powder samples were packed into quartz EPR tubes (3mm I.D.). All spectra were recorded using a microwave frequency of 9.40 GHz, a modulation amplitude of 1 mT, and a microwave power of 2 mW. Spectra were analyzed and simulated using SpinCount[164].

7.2.8 Micro-Raman Microscopy

Raman spectroscopy is based on inelastic scattering by molecular vibrations. When monochromatic light, often from a laser, interacts with a sample, two types of scattering occur: elastic (Rayleigh scattering) and inelastic (Raman scattering), see **Figure 7.2.10**. While most photons

undergo elastic scattering, a small fraction undergoes Raman scattering, where the energy of scattered photons changes due to interaction with molecular vibrations. This energy difference is known as the Raman shift, indicative of molecular vibrations within the sample. The Raman spectrum, plotting intensity against Raman shift (usually in wavenumbers, cm^{-1}), reveals signals corresponding to different molecular vibrational modes (**Figure 7.2.10**). Their analysis allows for identifying chemical composition, molecular structure, and symmetry.

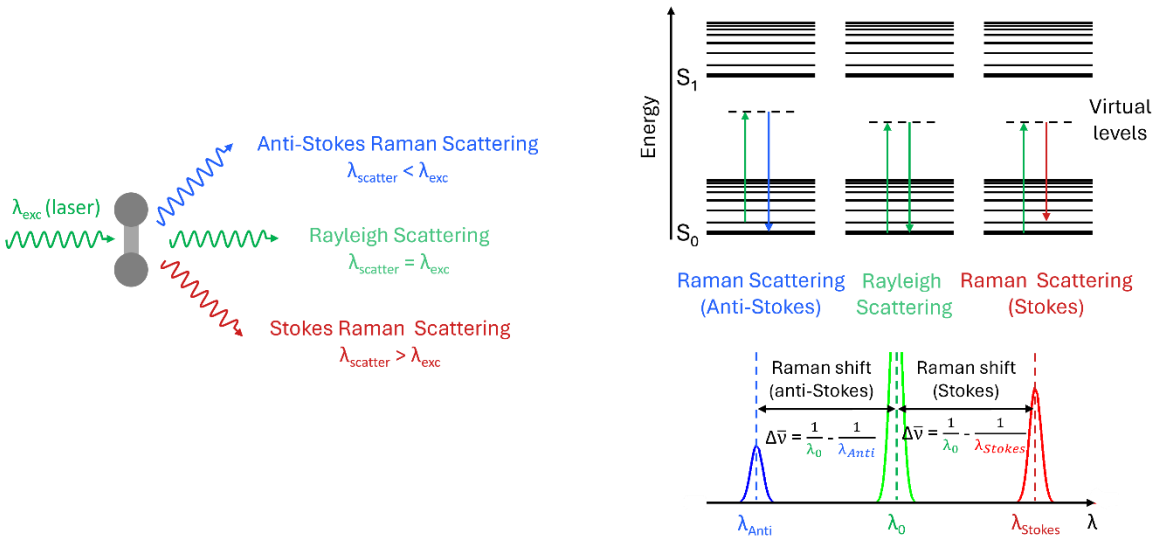


Figure 7.2.10 - (**Left**) Basic representation of Raman spectroscopy technique and (**Right**) Jablonski diagram showing Raman shifts. Adapted from reference **165**.

Micro-Raman microscopy integrates this technique with optical microscopy. By focusing the laser beam to a micron-scale spot size, micro-Raman microscopy enables spatially resolved analysis, allowing researchers to investigate specific regions of interest, map chemical distributions, and study heterogeneous materials at high resolution.

Sulfur (subchapter **2.3**): Raman microspectroscopy was carried out using a Labram 300 Jobin Yvon spectrometer equipped with a HeNe laser. Each spectrum was collected using 632.8 nm excitation and a 50x objective.

7.2.9 Dynamic Light Scattering (DLS)

Dynamic light scattering (DLS) relies on Brownian motion, wherein particles suspended in a fluid undergo random movements due to collisions with solvent molecules. These movements cause fluctuations in scattered light intensity, enabling particle size determination.

Experimentally, a laser beam passes through a sample containing suspended particles, scattering light in all directions (**Figure 7.2.11.A**). A detector measures scattered light intensity over time (**Figure 7.2.11.B**). The correlation function quantifies how scattered light intensity changes over time, revealing particle dynamics influenced by Brownian motion. Larger particles exhibit slower movement, leading to slower fluctuations in scattered light intensity, whereas smaller particles demonstrate faster movement and fluctuations (**Figure 7.2.11.C**). Additionally, the Stokes-Einstein relationship plays a crucial role in DLS analysis. This relationship establishes a connection between particles diffusion coefficient (D) and their size (d). According to the Stokes-Einstein, described in equation (**7.2.9**).

$$D = \frac{k_B.T}{6.\pi.\eta.d} \qquad (7.2.9)$$

where k_B stands for Boltzmann's constant, T for the absolute temperature and η for the solvent viscosity.

This equation reveals that the diffusion coefficient (D) is inversely proportional to the particle size (d). Therefore, the size of the particles in the sample can be determined by measuring the diffusion coefficient from the autocorrelation function and applying the Stokes-Einstein equation (**Figure 7.2.11.D**).

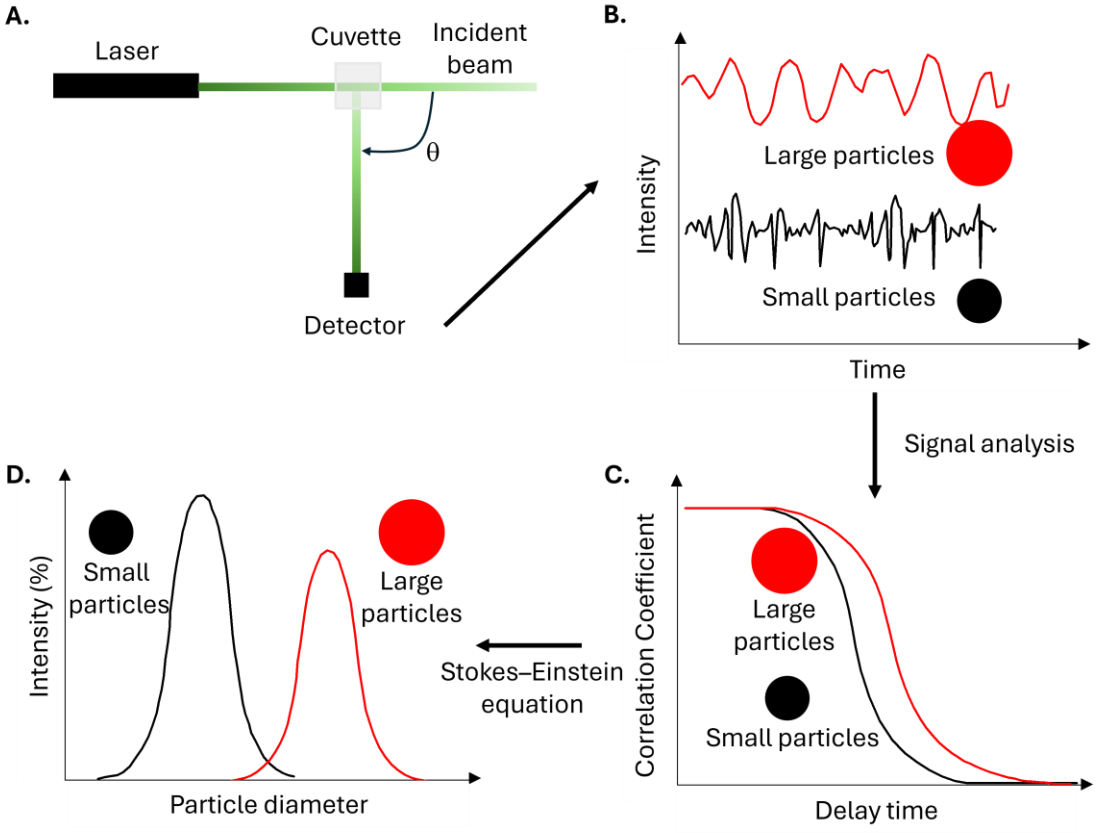


Figure 7.2.11 - (**A**) DLS principle representation, with an incident laser beam into a cuvette containing particles and with the light scattered by these particles detected under a defined angle, θ. (**B**) Variations of scattered light over time according to the particle size. (**C**) Respective correlation functions after signal processing. (**D**) Particle size distribution according to the Stokes-Einstein relationship. Adapted from reference **166**.

Selenium (chapter **4**): Nanozeolite dispersibility was evaluated using the Horiba nanoPartica nanoparticle analyzer SZ-100, equipped with a 532 nm laser. All samples were analyzed using a quartz cuvette and double-filtered MilliQ-water as the solvent.

7.2.10 Particle-Induced X-ray Emission (PIXE)

In particle-induced X-ray emission (PIXE), high-energy charged particles, such as protons or alpha particles, interact with the atoms of a sample, resulting in the ejection of inner-shell electrons and the creation of vacancies in atomic electron shells. When an inner-shell electron is ejected, an outer-shell electron may transition into the vacant shell, emitting characteristic X-rays specific to the elements involved (**Figure 7.2.12.A**).

The emitted X-rays correspond to transitions between electron energy levels, notably in the K and L shells. K transitions involve electrons moving to the innermost K shell from higher

energy levels (e.g., L or M shells). In comparison, L transitions involve electrons transitioning to the L shell from higher energy levels (e.g., M or N shells), see **Figure 7.2.12.B**. Each transition results in the release of X-rays with energies corresponding to the energy differences between the initial and final electronic states, as depicted for selenium in **Figure 7.2.12.C**. These characteristic energies are detected using an X-ray detector, allowing for the identification of the elements present and the quantification of their concentrations.

Additionally, samples should be thin and homogeneous for an effective analysis to ensure uniform penetration of incident particles. Thus, samples are commonly prepared as thin films on suitable substrates or as pressed pellets.

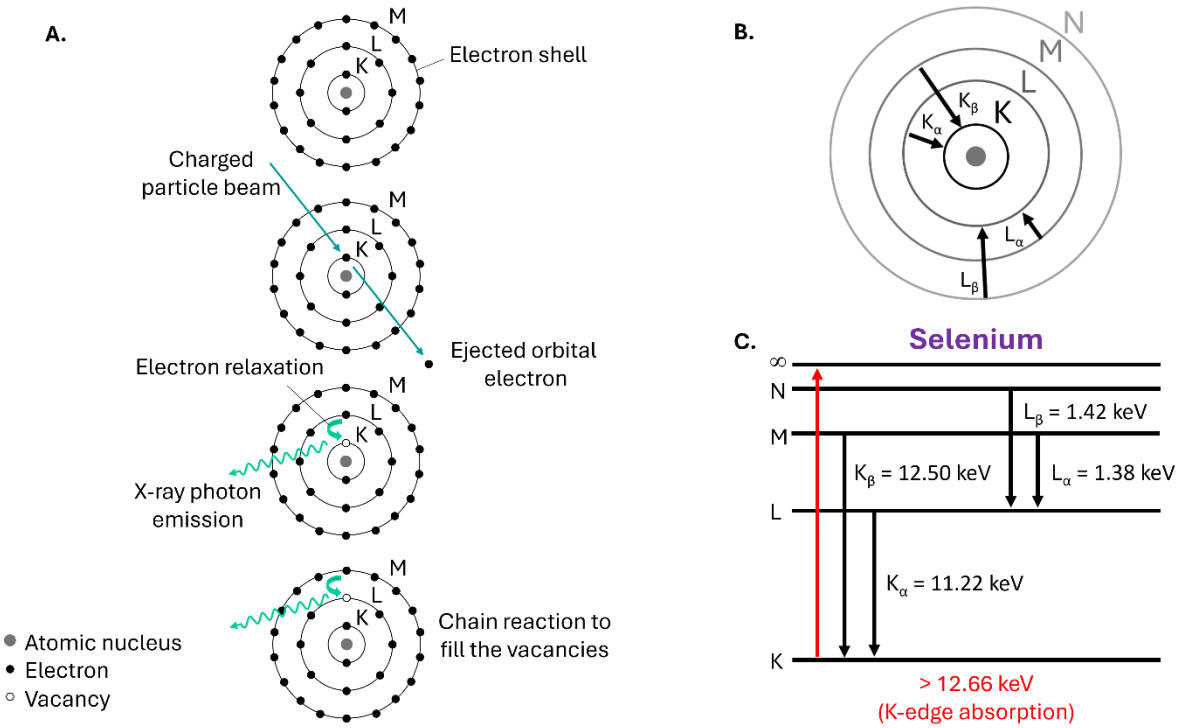


Figure 7.2.12 - Schematic representation illustrating the generation of X-rays in PIXE technique (**A**), along with typical X-ray transitions (**B**). Example of X-ray transitions of selenium element (**C**). Adapted from reference **167**.

Sulfur and tellurium (subchapter **2.3** and chapter **5**): The powdered samples were compressed into pellets and analyzed with a 700 keV proton beam generated by the 2.5 MV Van de Graaff accelerator installed at CTN/IST through the PIXE technique. An 8 μm Be windowed SDD detector was used to acquire the produced X-rays, while GupixWin software accounted for the spectra deconvolution and quantitative analysis. The major sample constituent elements (for Na and heavier elements) were taken in their oxide form and composition normalized to 100%.

The average and standard deviation were obtained by analyzing three different pellets for each sample type. The validation of experimental conditions and procedures was determined by analyzing Corning B glass reference material.

7.2.11 Wavelength Dispersive X-ray Fluorescence (WDXRF)

Wavelength Dispersive X-ray Fluorescence (WDXRF) spectroscopy operates on the same principle as in the PIXE technique (see **Figure 7.2.12** of section **7.2.10**), however, the main difference lies in the method of X-ray generation. In PIXE, X-rays are produced through the interaction of high-energy charged particles with the sample. In contrast, in WDXRF, X-rays are generated by bombarding the sample with accelerated electrons. These emitted X-rays are then detected and analyzed to determine the elemental composition of the sample.

The incident X-rays must have energy higher than the binding energy of the inner-shell electrons of the sample atoms to induce X-ray fluorescence. Characteristic X-rays emitted by the sample are dispersed by a crystal monochromator based on their wavelengths. This dispersion separates the X-rays according to their energies, enabling the detection of individual X-ray lines corresponding to specific elements. The intensity of the detected X-ray lines is proportional to the concentration of corresponding elements in the sample. By measuring these intensities and comparing them to calibration standards, the elemental composition of the sample can be quantitatively determined.

Selenium (chapter **3** and subchapter **4.1**): The chemical composition was determined using a PANalytical–Axios 4.0 wavelength dispersive X-ray fluorescence (WDXRF) spectrometer with a rhodium X-ray tube (20.21 keV) in conditions optimized for element quantification. The analyzing crystals of LiF220, LiF200, Ge, PE, and PX1 were used for the separation of fluorescent X-ray peaks covering all measurable ranges. The analyses were performed under a helium (He) flow and spectra deconvolution was achieved using the iterative least-squares method and semiquantitative analysis based on the fundamental parameter approach with the SuperQ IQ+ software package (PANalytical B.V., Almelo, The Netherlands).

7.2.12 Differential Scanning Calorimetry (DSC)

Differential scanning calorimetry (DSC) measures the heat flow differences between a sample and a reference material as they undergo the same temperature program. Materials absorb or release energy during thermal processes like melting, crystallization, phase transitions, or

chemical reactions. These transformations alter the internal energy of the material, resulting in observable changes in temperature or heat flow within the DSC instrument (**Figure 7.2.13**).

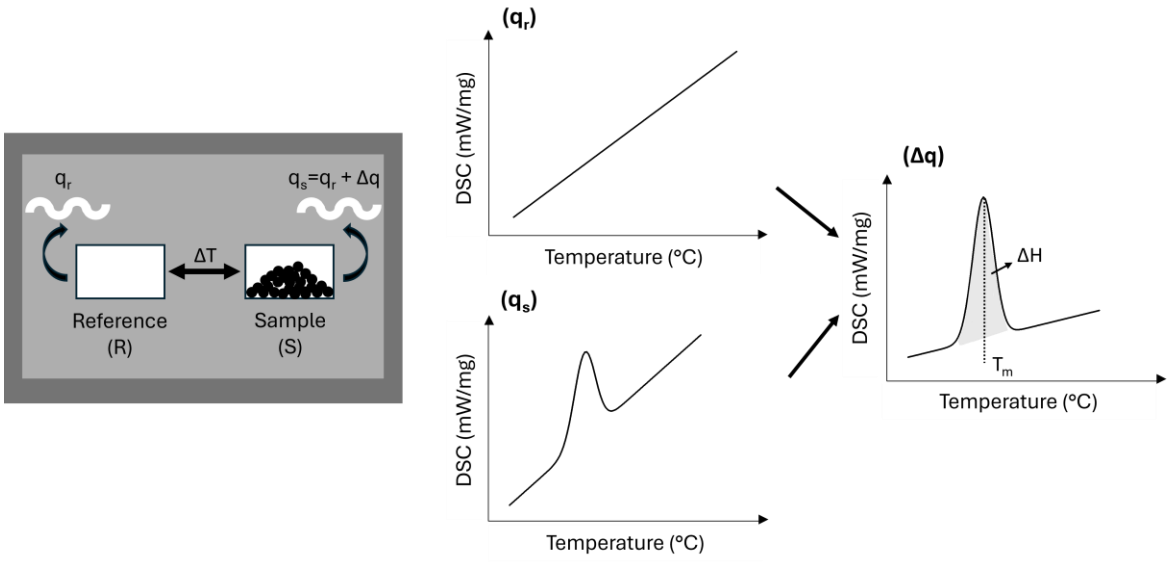


Figure 7.2.13 - Experimental setup for a DSC experiment. The amount of heat required to increase the temperature by the same increment (ΔT) of a sample cell (q_s) is higher than that required for the reference cell (q_r) by the excess heat absorbed by the sample (Δq). The resulting DSC scans with the reference subtracted from the sample show how this excess heat changes as a function of temperature. ΔH stands for change in enthalpy and T_m for transition and melting point. Adapted from reference **168**.

The thermal analyses of samples S/Cl=0 and Se_0 gel (**Figure 7.5.1**) were performed using a Netzsch Pegasus® DSC 404 F3 (Netzsch, Selb, Germany), which is equipped with a kiln that can reach temperatures up to 1550 °C. The experiments were conducted using a platinum crucible at a heating rate of 10 K/min. in a nitrogen atmosphere and using alumina as a reference.

7.2.13 Powder X-Ray Diffraction (PXRD)

Powder X-ray diffraction (PXRD) relies on Bragg's law, which describes the relationship between the angles of X-ray diffraction, θ, and the spacing between crystalline planes, d, within a crystalline lattice, see equation (**7.2.10**).

$$2dsin(\theta) = n\lambda \qquad (7.2.10)$$

where λ stands for the wavelength of the incident radiation and n is an integer representing the order of the X-ray diffraction peak.

When Braggs's law is fulfilled, constructive interference occurs between the incident X-ray beam and specific crystalline planes, producing diffracted X-ray beams (**Figure 7.2.14.A**).

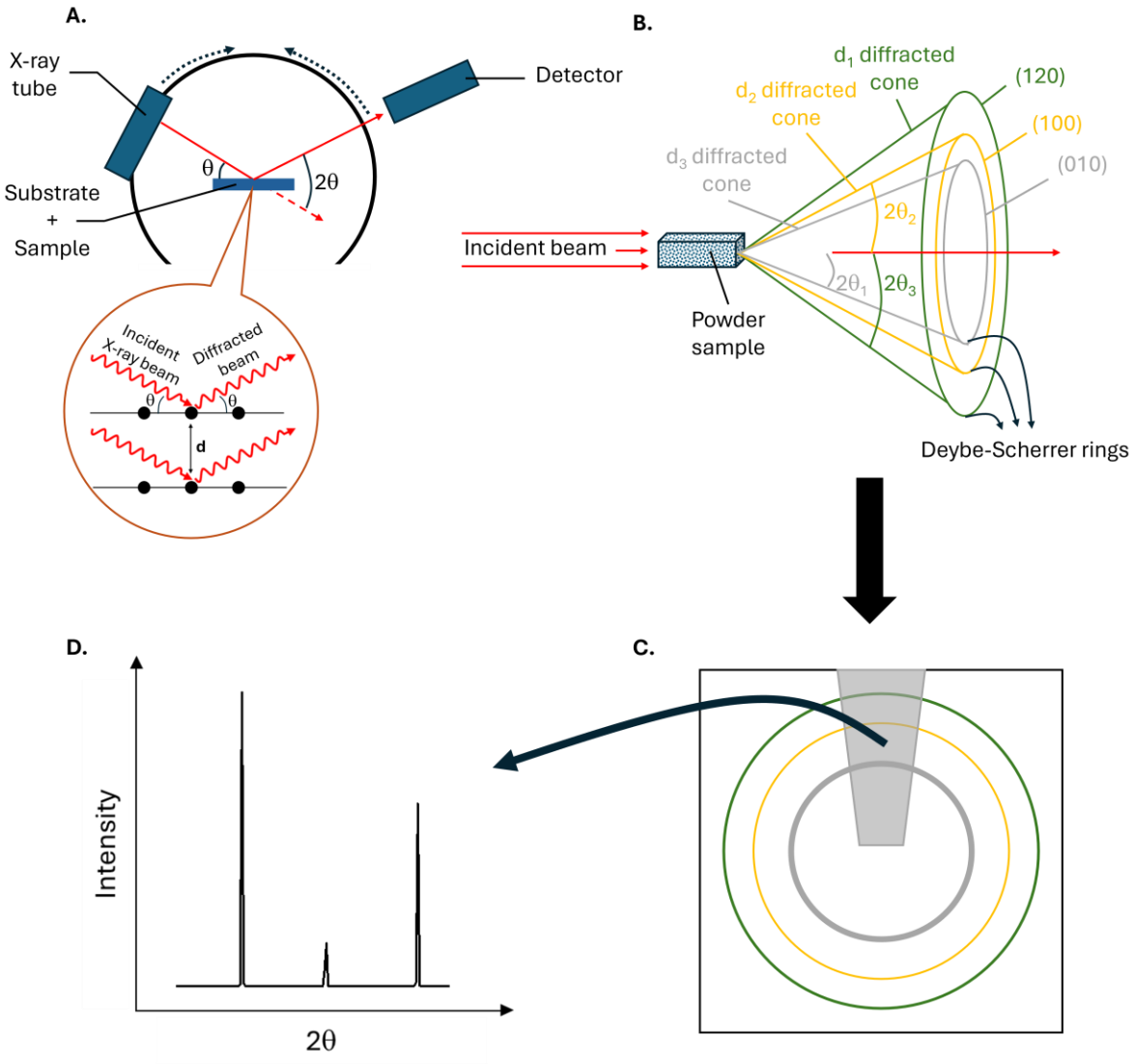


Figure 7.2.14 - (**A**) Illustration of a typical powder X-ray crystallography apparatus, with a close-up of the sample and the crystal, showing Bragg's law. (**B**) Debye-Scherrer rings representation of several crystalline planes according to the angles. (**C**) Corresponding detected powder diffraction pattern (**D**) and powder diffractogram. Adapted from reference **169**.

Each detected signal in a PXRD experiment is characterized by forming a series of Debye-Scherrer rings (**Figure 7.2.14.B**). These rings are concentric circles that form on the detector when the X-rays are diffracted by the randomly orientated crystallites in the powdered sample. Each ring corresponds to a specific set of lattice planes (defined by their Miller indices (hkl) that satisfy Braggs's law at a particular angle.

Therefore, by scanning the sample through different angles, the diffraction pattern of the sample is obtained (**Figure 7.2.14.C**). This pattern can subsequently be transformed into a typical powder diffractogram, which plots the intensity of diffracted X-rays as a function of the scattering angle 2θ (**Figure 7.2.14.D**). The crystalline structure, lattice parameters, and crystalline orientation of a sample can be extracted from the produced diffractogram.

Sulfur, selenium, and tellurium (chapters **3** and **5** and subchapter **2.3**): An X-ray diffractometer Rigaku, model MiniFlex II, with a Cu X-ray tube (30 KV/15 mA) was used over a 2θ range of 10° to 50° with a scan speed of 1°/min.

Sulfur and selenium (chapter **4** and subchapters **2.1** and **2.2**): A PANalytical X'Pert Pro diffractometer was used, equipped with a Cu X-ray tube (K_α, λ=1.541 Å). The X-ray generator was operated at a voltage of 45 kV and a tube current of 40 mA. PXRD data were collected over the 2θ range of 10–50° with a step size of 0.02°.

7.2.14 Scanning Electron Microscopy (SEM)

Scanning Electron Microscopy (SEM) is an imaging technique that operates by scanning a focused electron beam across the surface of a sample. Electrons emitted from a heated filament or field-emission source are accelerated towards the sample using an electric field, then focused and scanned across the surface using electromagnetic lenses and deflection coils. Samples must be conductive or coated with a thin conductive layer to prevent charging effects. Common conductive coating materials include gold/palladium, carbon, platinum, silver, or conductive carbon tape for mounting irregularly shaped or delicate samples.

Interactions between the electron beam and the sample surface generate various signals, including secondary electrons, backscattered electrons, and characteristic X-rays (**Figure 7.2.15**). Secondary electrons, ejected from the surface, provide high-resolution, three-dimensional images, while backscattered electrons, reflected from the sample, reveal variations in atomic number or density. Additionally, characteristic X-rays emitted by the sample can be detected by energy-dispersive X-ray spectrometry (EDS) to analyze the elemental composition of the sample, enabling qualitative and quantitative analysis of its chemical composition.

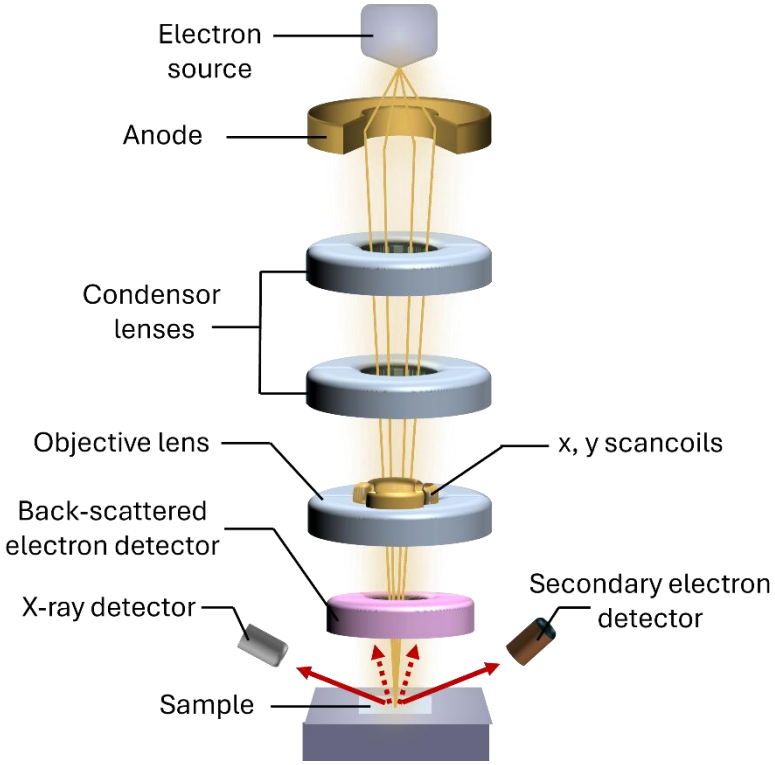


Figure 7.2.15 - Schematic diagram of the core components of a SEM microscope. Adapted from reference **170**.

Selenium (Chapter **4**): SEM images were acquired using a Hitachi Regulus 8220 Scanning Electron Microscope (Mito, Japan) equipped with an Oxford EDS detector.
The chemical analysis acquired through EDS represents an average of measurements taken from three distinct areas of each sample.

Sulfur and selenium (subchapters **2.3** and **4.1**): Samples were scanned using scanning electron microscopy (SEM) under 20 kV using a Tescan Mira I LMH.

7.2.15 Transmission Electron Microscopy (TEM)

Transmission Electron Microscopy (TEM) operates similarly to light microscopy, but instead of using visible light, it employs a beam of electrons for imaging, offering significantly higher resolution due to the shorter wavelengths of electrons. Here, electrons emitted from a heated filament are accelerated towards the sample by electromagnetic lenses, allowing precise electron beam focusing for high-resolution imaging.

When the electron beam interacts with the sample, it undergoes various interactions with the atoms, including elastic scattering, inelastic scattering, and diffraction. Detectors collect

electrons that pass through the sample, generating an image based on their intensity (**Figure 7.2.16**).

Moreover, TEM can be coupled with techniques such as energy-dispersive X-ray spectroscopy (EDS) and X-ray diffraction (XRD) to provide complementary structural and compositional information. EDS enables the analysis of the elemental composition of the sample by detecting characteristic X-rays emitted when the electron beam interacts with the sample. On the other hand, XRD analysis provides information about the crystalline structure and orientation of materials by analyzing the diffraction patterns generated when X-rays interact with the sample.

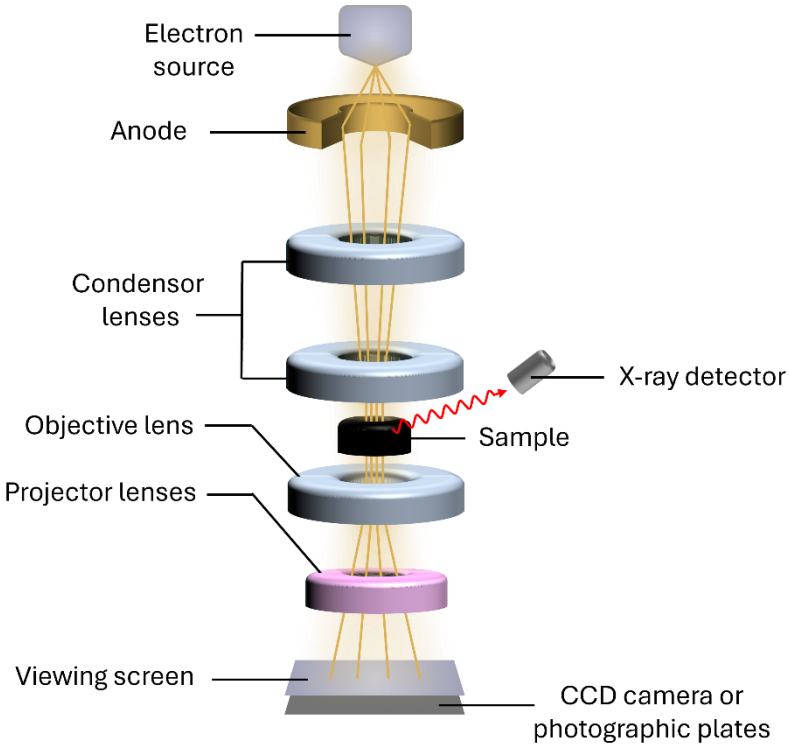


Figure 7.2.16 - Schematic diagram of the core components of a TEM microscope. Adapted from reference **170**.

Sulfur (subchapter **2.3**): Electron microscopy imaging was performed using a JEOL F200 transmission electron microscope (TEM) operated at 300 kV equipped with a Gatan RIO16 camera.

7.2.16 Computational Studies

Computational chemistry focuses on solving the Schrödinger equation for a given molecule or material using methods such as ab initio, semi-empirical, and density functional theory (DFT)[171].

Ab initio methods directly solve the Schrödinger equation without relying on empirical parameters or experimental data. They aim for high accuracy by adhering strictly to the fundamental principles of quantum mechanics. Typically, these methods employ wave function-based approaches such as Hartree-Fock (HF) theory or post-HF methods such as Møller–Plesset perturbation theory (MPn), generalized valence bond (GVB) method, multi-configurations self-consistent field (MCSCF), configuration interaction (CI), and coupled cluster theory (CC). While *ab initio* methods offer high accuracy, they come with significant computational costs, especially for larger systems, due to the need to solve the many-body Schrödinger equation with high precision.

On the other hand, semi-empirical methods are set up in the Hartree–Fock formalism but offer a compromise between computational efficiency and accuracy in quantum mechanical calculations. These methods incorporate empirical parameters or experimental data to approximate the behavior of electrons. Instead of fully solving the Schrödinger equation, semi-empirical methods often use simplified mathematical models and empirical parameters derived from experimental data or higher-level *ab initio* calculations. Examples include the Hückel method or semi-empirical molecular orbital (SEMO) theory. These semi-empirical methods are particularly useful for studying inorganic species or large molecular systems where full *ab initio* methods are computationally unaffordable.

An increasingly popular alternative to *ab initio* method is density functional theory (DFT), which simplifies the calculations by representing total energy in relation to the electron density (ρ) rather than the wavefunction (ψ) directly. The Schrödinger equation, when reformulated in terms of ρ, transforms into a series of equations known as the Kohn–Sham equations. These equations are solved iteratively, beginning with an initial estimate and progressing until they reach self-consistency. The appeal of the DFT arises from its reduced computational demands, lower time requirements, and, in certain scenarios such as d-metal complexes, its tendency to align more closely with experimental data than alternative methods.

Computational modeling is a valuable tool for predicting the behavior of individual molecules and materials. This includes analyzing electronic states and molecular orbitals involved in processes such as absorption and emission.

Sulfur and selenium (chapter **3** and subchapter **2.3**): DFT calculations have been carried out with the program Gaussian 16 using the B3LYP functional and Def2TZVP triple zeta basis set for sulfur and selenium. Geometry optimization and time-dependent density-functional theory

(TD-DFT) calculations were performed in the gas phase. Avogadro 1.2.0 was employed for molecular orbital visualization.

7.3 Dispersibility studies of non-doped nanosodalites

Selenium (subchapter **4.2**): Three different methods were tested to disperse non-doped and selenium-doped samples: ball-milling, sonication and surfactant doping. Several programs were evaluated for ball-milling by varying the milling time and rotation velocity, using a planetary ball mill Retsch PM 100. The milling times ranged from 10 minutes to 1 hour, and the rotation speeds from 500 rpm to 650 rpm.

Sonication was conducted using an ultrasonic homogenizer (HD 3200, Bandelin Sonopuls) equipped with a titanium probe (TT 13, Bandelin Sonopuls). The ultrasound was transmitted to the medium through this probe, and amplitude mode was chosen for regulation, operating In percentage (%). A 10% setting corresponds to a probe amplitude of 16.5 μm_{ss}. Various times and amplitudes were tested, including (10%, 1 min.), (10%, 10 min.), (50%, 1 min.), (50%, 10 min.), (100%, 1 min.) and (100%, 10 min.).

Additionally, several surfactants were tested, including Triton-X and cetyltrimethylammonium bromide (CTAB).

These methods were also combined to attempt to obtain ideal dispersive conditions.

7.4 External quantum efficiencies calculations of phosphorescent species in a mixture with two emitting species

Selenium (chapter **3**): External quantum efficiencies (EQE) were measured by the absolute method using an integrating sphere in a Horiba Jobin Yvon fluorolog FL3-22 fluorimeter equipped with a xenon 450 W light source. These values were calculated for the red region (λ_{exc}=480 nm) and NIR region (λ_{exc}=400 nm) using the same experimental parameters, including excitation and emission slits and sample position. This allowed for the comparison of absorption and emission at both wavelengths. These calculations aimed to isolate the NIR emission contribution in samples excited at 400 nm, which exhibit a mixture of red and NIR emissions, with the red emission being more pronounced in samples with lower Se/Cl ratios.

Note that EQE is defined by the ratio of the number of emitted photons to the number of absorbed photons, as described in equation (**7.2.5**). Therefore, in samples exhibiting both emissions, the EQE of the NIR species was determined by the following equation (**7.4.1**).

$$EQE = \frac{NIR\ emission\ contribution\ in\ the\ mixture}{Total\ absorption\ in\ the\ mixture - Absorption\ of\ the\ red\ emission\ in\ the\ mixture} \quad (7.4.1)$$

where the 'NIR emission contribution in the mixture' was determined by decomposing the experimental emission spectrum using pure red emission and pure NIR emission spectra (**Figure 7.4.1**).

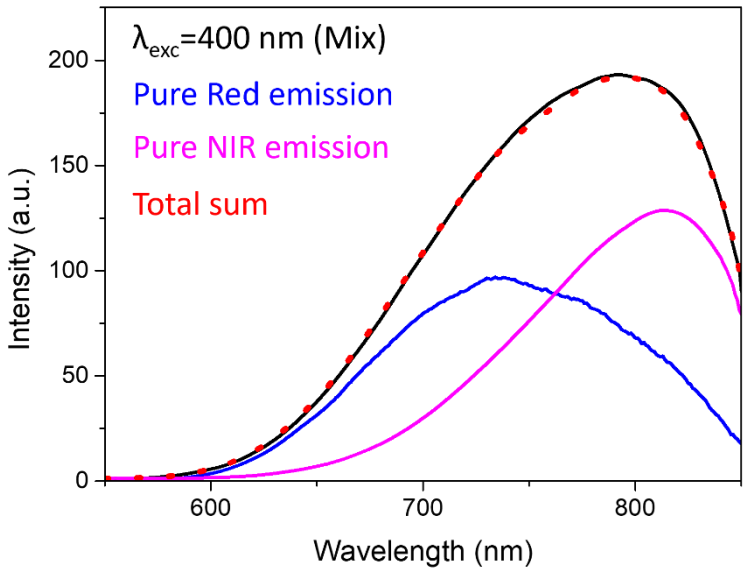


Figure 7.4.1 - Decomposition of the experimental emission spectra of sample Se/Cl=0.21 with the two pure red emission and NIR emissions

The pure red emission spectrum was derived from sample Se/Cl=0.06, using λ_{exc}=480 nm, while the pure NIR emission spectrum was obtained from sample Se_1 - 900 °C, using λ_{exc}=400 nm. The resulting simulation matched well with the pure spectra of both emissions (**Figure 7.4.2.A-B**). Therefore, the term 'NIR emission contribution in the mixture' was calculated by integrating the resulting spectrum of the difference between the experimental spectrum and the simulated NIR emission spectrum, as exemplified in **Figure 7.4.2.B**.

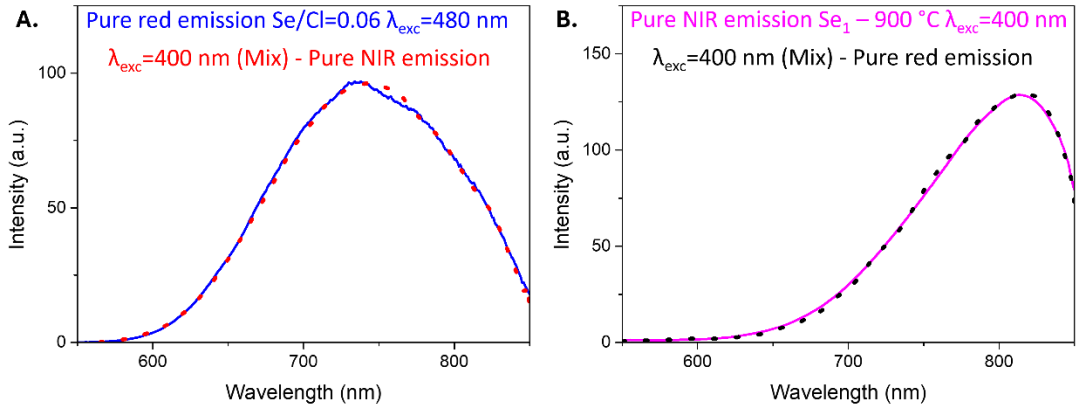


Figure 7.4.2 - Comparison of the pure red (**A**) and the NIR (**B**) emission spectra with the corresponding decomposed fractions calculated from the experimental emission spectrum, where a mixture of these mentioned emissions was found.

Additionally, the term 'Total absorption in the mixture' in equation (**7.4.1**) represents the difference between the integrals of photon flux not absorbed by the sample at the excitation wavelength (λ_{exc}=400 nm) due to indirect (Lb) and direct absorption (Lc). Lb and Lc spectra are obtained when measuring the absolute EQE, according to reference **70**.

To calculate the term 'Absorption of the red emission in the mixture' in equation (**7.4.1**), the absorption and emission of pure red emission need to be estimated at 400 nm. This involved using EQE measurement data of the pure red emission (λ_{exc}=480 nm) along with the diffuse reflectance of the sample. First, the diffuse reflectance spectrum was decomposed with the absorption spectra of the species responsible for the red and NIR emissions (**Figure 7.4.3**). Then, the values at 400 nm ($A_{400\ nm}$) and 480 nm ($A_{480\ nm}$)of the species responsible for the red emission (shown in blue) were extracted.

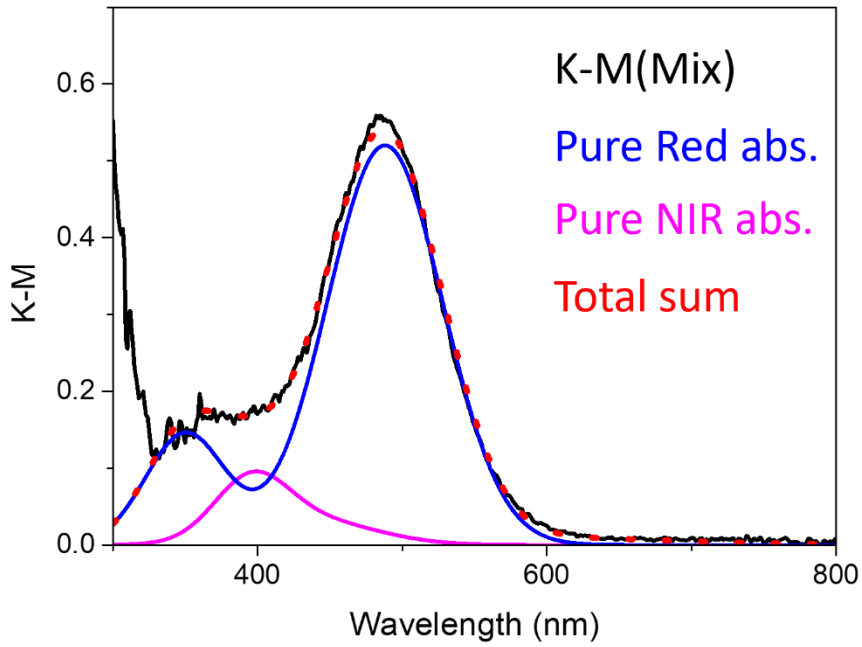


Figure 7.4.3 - Decomposition of the experimental diffuse reflectance spectra of sample Se/Cl=0.21 with the species responsible for the red and NIR emissions.

Next, the absorption and emission of pure red emission calculated in the EQE at λ_{exc}=480 nm were multiplied by the ratio of the values extracted from the diffuse reflectance spectroscopy at 400 nm ($A_{400\ nm}$) to those at 480 nm ($A_{480\ nm}$). These calculations provided estimates of the absorption and emission at 400 nm for the pure red emission, as described in equation (**7.4.2**) and equation (**7.4.3**), respectively.

$$\begin{matrix} Estimated\ absorption\ of \\ red\ emission\ at\ 400\ nm \end{matrix} = (Lb - Lc)_{\substack{EQE\ at \\ 480\ nm}} \times \frac{A_{400\ nm}}{A_{480\ nm}} \qquad (7.4.2)$$

$$\begin{matrix} Estimated\ emission\ of \\ red\ emission\ at\ 400\ nm \end{matrix} = (Emission\ integral)_{\substack{EQE\ at \\ 480\ nm}} \times \frac{A_{400\ nm}}{A_{480\ nm}} \qquad (7.4.3)$$

Finally, the 'Absorption of the red emission in the mixture' in equation (**7.4.1**) was calculated by multiplying the integral of the pure red emission in the mixture (**Figure 7.4.2.A**) by the ratio of estimated absorption to emission for this red emission at 400 nm, as described in equation (**7.4.4**).

$$\text{Absorption of the red emission in the mixture} = \text{Red emission contribution in the mixture} \times \frac{Estimated\ absorption\ of\ red\ emission\ at\ 400\ nm}{Estimated\ emission\ of\ red\ emission\ at\ 400\ nm} \quad (7.4.4)$$

7.5 Humidity/water-sensitive emission studies

Sulfur and **selenium** (chapter **3** and subchapters **2.3** and **4.1**): Films containing 10% polyvinyl alcohol (PVA) in water were prepared for samples with S/Cl and Se/Cl ratios of 0.21 and 4.5, as well as for Se1 - 900 °C. Two quartz cells were assembled, each containing a saturated salt solution with different relative humidity. One cell contained lithium bromide (LiBr), resulting in a relative humidity of 6% at 25 °C, while the other contained potassium sulfate (K_2SO_4), resulting in a relative humidity of 97% at 25 °C[172]. The films were placed inside quartz cells, then sealed with septum stoppers and allowed to stabilize. Emission spectra were recorded every 5 minutes and compared across different acquisition times and relative humidities.

External quantum efficiencies (EQEs) were also measured after the powders were dried. These samples were loaded into quartz ampoules and dried at 250 °C overnight under vacuum. Afterward, the ampoules were sealed, and the EQEs were measured. It is worth noting that differential scanning calorimetry (DSC) analysis showed that these samples lose water up to around 200 °C (**Figure 7.5.1**). (Refer to section **7.2.12** for supplementary information about the DSC technique.)

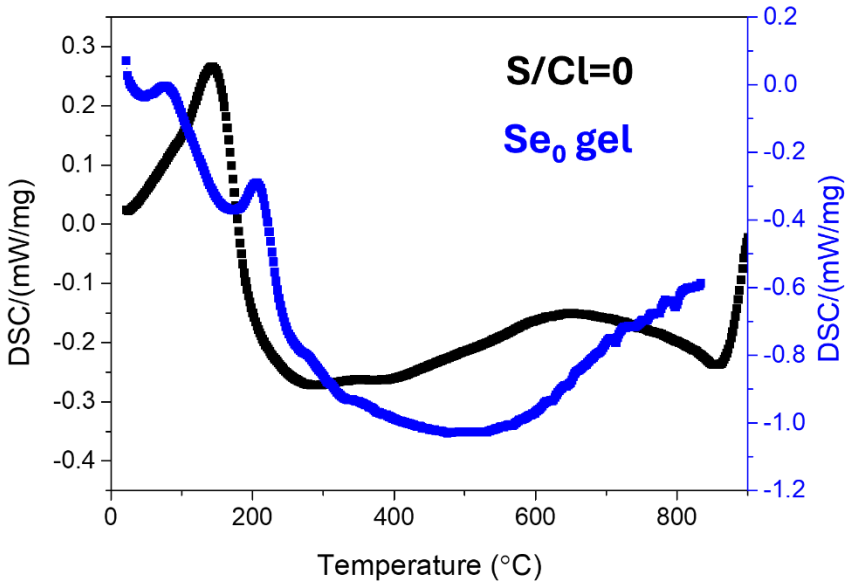


Figure 7.5.1 - Differential scanning calorimetry analysis of sample S/Cl=0 (black) and Se_0 gel (blue).

7.6 Oxygen-sensitive emission studies

Sulfur and **selenium** (chapter **3** and subchapters **2.3** and **4.1**): Films containing 10% zeonex in toluene were prepared for samples with S/Cl and Se/Cl ratios of 0.21 and 4.5, as well as for Se1 - 900 °C. These films were assembled into a quartz cell, then sealed with a septum stopper. Subsequently, oxygen from an Alphagaz O_2 gas bottle was purged directly into the cell. The emission spectra were recorded every 5 minutes and the emission was compared between different times and before any purging occurred.

8

WORK DISSEMINATION

8.1 Papers Contributing to the Dissertation

Viola, C. *et al*. Long-lived NIR emission in sulfur-doped zeolites due to the presence of $[S_3]^{2-}$ clusters. *Mater. Today Chem.* **30**, (2023).

8.2 Other Research Papers

Baekelant, W. *et al.* Tunable white emission of silver-sulfur-zeolites as single-phase LED phosphors. *Methods Appl. Fluoresc.* **8**, (2020).

Cerdeira, A. C. *et al.* Multifunctionality of the [C2mim][Ln(fod)4] series (Ln = Nd-Tm except Pm): magnetic, luminescence and thermochemical studies. *New J. Chem.* **46**, 9858–9870 (2022).

Submitted

Pereira, Cláudia; Monteiro Bernardo; Fernandes, Susete, Paulo, Pedro; Viola, Catarina; " Irradiation for Improving Violet-Blue Light Contribution of Tri- and Polychromatic Polysulfone Host-Guest Systems" *Dyes and Pigments*

8.3 Communications in Conferences

Speaker

Viola, Catarina; C. Lima, João; Ruivo, Andreia; Avó, João; Teixeira, Miguel; Outis, Mani. (2022) " Long-lived NIR emitting $[S_3]^{2-}$ clusters in sulfur-doped sodalite". 28th PhotoIUPAC. European Photochemistry Association. Amsterdam, 17-22 July 2022.

Viola, Catarina; Ruivo, Andreia; A. T. Laia, César; Avó, João; Outis, Mani; C. Lima, João; F. V. Ferreira, Luís; C. Alves, Luís; Teixeira, Miguel. (2021). "Entrapped [S3]2- clusters with long-lived NIR emission in artificial hackmanite". Iberian Symposium of Young Photochemists 2021. Photochemistry division of the Royal Spanish Chemical Society. Online event, 18-22 October 2021.

Posters

Viola, Catarina; Ruivo, Andreia; A. T. Laia, César; Avó, João; C. Lima, João; Outis, Mani. (2021). "Emissive sulfur species present in artificial hackmanite". 7th Portuguese Young Chemists Meeting. Online event, 19-21 May 2021.

Viola, Catarina; Ruivo, Andreia; A. T. Laia, César; Avó, João; Alves, Luís; F. V. Ferreira, Luís; Teixeira, Miguel; Folgosa, Filipe; C. Lima, João; Outis, Mani. " Luminescent sulfur-doped sodalite starting from Na-LTA zeolite". 20th International Zeolite Conference. Grupo Español de Zeolitas. Valencia, 2-9 July 2022.

BIBLIOGRAPHY

1 A. Zampetti, A. Minotto and F. Cacialli, *Adv. Funct. Mater.*, 2019, **29**, 1–22.

2 B. Pashaei, S. Karimi, H. Shahroosvand and M. Pilkington, *Adv. Funct. Mater.*, 2020, **30**, 1–31.

3 M. Y. Berezin, W. J. Akers, K. Guo, G. M. Fischer, E. Daltrozzo, A. Zumbusch and S. Achilefu, *Biophys. J.*, 2009, **97**, L22–L24.

4 W. J. Akers, M. Y. Berezin, H. Lee and S. Achilefu, *J. Biomed. Opt.*, 2008, **13**, 1–9.

5 J. I. Deneff, K. S. Butler, L. E. S. Rohwer, C. J. Pearce, N. R. Valdez, M. A. Rodriguez, T. S. Luk and D. F. Sava Gallis, *Angew. Chemie - Int. Ed.*, 2021, **60**, 1203–1211.

6 Z. Zhang, H. Chang, B. Xue, S. Zhang, X. Li, W. K. Wong, K. Li and X. Zhu, *Cellulose*, 2018, **25**, 377–389.

7 G. Pramanik, J. Humpolickova, J. Valenta, P. Kundu, S. Bals, P. Bour, M. Dracinsky and P. Cigler, *Nanoscale*, 2018, **10**, 3792–3798.

8 Q. Zhao, C. Huang and F. Li, *Chem. Soc. Rev.*, 2011, **40**, 2508–2524.

9 E. Alonso, A. M. Sherman, T. J. Wallington, M. P. Everson, F. R. Field, R. Roth and R. E. Kirchain, *Environ. Sci. Technol.*, 2012, **46**, 3406–3414.

10 K. H. Kim, S. Singha, Y. W. Jun, Y. J. Reo, H. R. Kim, H. G. Ryu, S. Bhunia and K. H. Ahn, *Chem. Sci.*, 2019, **10**, 9028–9037.

11 J. Weitkamp, 2000, **131**, 175–188.

12 M. Khodadadi Yazdi, P. Zarrintaj, H. Hosseiniamoli, A. H. Mashhadzadeh, M. R. Saeb, J. D. Ramsey, M. R. Ganjali and M. Mozafari, *J. Mater. Chem. B*, 2020, **8**, 5992–6012.

13 A. Khaleque, M. M. Alam, M. Hoque, S. Mondal, J. Bin Haider, B. Xu, M. A. H. Johir, A. K. Karmakar, J. L. Zhou, M. B. Ahmed and M. A. Moni, *Environ. Adv.*, 2020, **2**, 100019.

14 Y. Wada, T. Okubo, M. Ryo, T. Nakazawa, Y. Hasegawa and S. Yanagida, *J. Am. Chem. Soc.*, 2000, **122**, 8583–8584.

15 L. Gigli, R. Arletti, J. G. Vitillo, G. Alberto, G. Martra, A. Devaux and G. Vezzalini, *J. Phys. Chem. C*, 2015, **119**, 16156–16165.

16 A. R. Bertão, O. Güney, M. Costa, P. Fontão, O. Martinho, S. P. G. Costa, A. M. Fonseca, O.

S. G. P. Soares, M. Bañobre-López, F. Baltazar and I. C. Neves, *Chem. Eng. J.*, 2023, **473**, 145109.

17 M. Lezhnina, F. Laeri, L. Benmouhadi and U. Kynast, *Adv. Mater.*, 2006, **18**, 280–283.

18 H.-T. Sun, M. Fujii, Y. Sakka, Z. Bai, N. Shirahata, L. Zhang, Y. Miwa and H. Gao, *Opt. Lett.*, 2010, **35**, 1743.

19 G.-G. Lindner, K. Witke, H. Schlaich and D. Reinen, *Inorganica Chim.*, 1996, **252**, 39–45.

20 A. Ruivo, E. Coutiño-Gonzalez, M. Santos, W. Baekelant, E. Fron, M. Roeffaers, F. Pina, J. Hofkens and C. Laia, *J. Phys. Chem. C*, 2018, **122**, 14761–14770.

21 *European Commission, Study on the EU's list of Critical Raw Materials (2020): Final Report*, Brussels, 2020.

22 I. Norrbo, A. Curutchet, A. Kuusisto, J. Mäkelä, P. Laukkanen, P. Paturi, T. Laihinen, J. Sinkkonen, E. Wetterskog, F. Mamedov, T. Le Bahers and M. Lastusaari, *Mater. Horizons*, 2018, **5**, 569–576.

23 H. G. Infante, J. Warren, J. Chalmers, G. Dent, J. L. Todoli, J. Collingwood, N. Telling, M. Resano, A. Limbeck, T. Schoenberger, D. B. Hibbert, A. Legresley, K. Adams and D. Craston, *Pure Appl. Chem.*, 2021, **93**, 647–776.

24 P. Jiang, Z. Tian, C. Zhu, Z. Zhang and D. Pang, *Chem. Mater.*, 2012, **24**, 3–5.

25 A. Barbieri, E. Bandini, F. Monti, V. K. Praveen and N. Armaroli, *Top. Curr. Chem.*, 2016, **374**, 269–307.

26 J. Gayton, S. A. Autry, W. Meador, S. R. Parkin, G. A. Hill, N. I. Hammer and J. H. Delcamp, *J. Org. Chem.*, 2019, **84**, 687–697.

27 M. H. Liu, T. C. Chen, J. R. Vicente, C. N. Yao, Y. C. Yang, C. P. Chen, P. W. Lin, Y. C. Ho, J. Chen, S. Y. Lin, Y. H. Chan, Y. H. Chan and Y. H. Chan, *ACS Appl. Bio Mater.*, 2020, **3**, 3846–3858.

28 Y. Zhong and H. Dai, *Nano Res.*, 2020, **13**, 1281–1294.

29 S. Comby and J. C. G. Bünzli, in *Handbook on the Physics and Chemistry of Rare Earths*, Elsevier, 2007, vol. 37, pp. 217–470.

30 Z. Gan, Y. Liu, L. Wang, S. Jiang, N. Xia, Z. Yan, X. Wu, J. Zhang, W. Gu, L. He, J. Dong, X. Ma, J. Kim, Z. Wu, Y. Xu, Y. Li and Z. Wu, *Nat. Commun.*, 2020, **11**, 1–10.

31 F. Liu, J. Jiang, Y. Zhang, C. Ding, T. Toyoda, S. Hayase, R. Wang, S. Tao and S. Qing, *Angew. Chemie*, 2020, **132**, 8499–8502.

32 D. Huang, H. Zhou, Y. Wu, T. Wang, L. Sun, P. Gao, Y. Sun, H. Huang, G. Zhou and J. Hu, *Carbon N. Y.*, 2019, **142**, 673–684.

33 T. Wang, Y. Chen, B. Wang, X. Gao and M. Wu, *Biomolecules*, , DOI:10.3390/biom12081044.

34 H. Zhu, J. Fan, J. Du and X. Peng, *Acc. Chem. Res.*, 2016, **49**, 2115–2126.

35 Y. Sun, C. Qu, H. Chen, M. He, C. Tang, K. Shou, S. Hong, M. Yang, Y. Jiang, B. Ding, Y. Xiao, L. Xing, X. Hong and Z. Cheng, *Chem. Sci.*, 2016, **7**, 6203–6207.

36 W. Kun, Y. Du, Z. Zhang, K. He, Z. Cheng, L. Yin, D. Dong, C. Li, W. Li, Z. Hu, C. Zhang, H. Hui, C. Chi and J. Tian, *Nat. Rev. Bioeng.*, 2023, **1**, 161–179.

37 T. Nagaya, Y. A. Nakamura, P. L. Choyke and H. Kobayashi, *Front. Oncol.*, , DOI:10.3389/fonc.2017.00314.

38 Z. Wu, X. Han, Y. Zhou, K. Xing, S. Cao, L. Chen, R. Zeng, J. Zhao and B. Zou, *Chem. Eng. J.*, 2022, **427**, 131740.

39 J. Qiao, G. Zhou, Y. Zhou, Q. Zhang and Z. Xia, *Nat. Commun.*, 2019, **10**, 1–7.

40 H. Peng, X. Wang, W. Huang, S. Yu, L. Kong, Q. Wei, J. Zhao and B. Zou, *Chinese Chem. Lett.*, 2024, 109462.

41 J. Cao, L. Wondraczek, Y. Wang, L. Wang, J. Li, S. Xu and M. Peng, *ACS Photonics*, 2018, **5**, 4393–4401.

42 W. L. F. Armarego, in *Purification of Laboratory Chemicals (Ninth Edition)*, ed. W. L. F. Armarego, Butterworth-Heinemann, Ninth Edit., 2022, pp. 1–81.

43 I. Calinescu, E. Sarbu and A. Trifan, *Rev. Chim.*, 2013, **64**, 1146–1150.

44 P. Misaelides, *Microporous Mesoporous Mater.*, 2011, **144**, 15–18.

45 S. Wang and Y. Peng, *Chem. Eng. J.*, 2010, **156**, 11–24.

46 R. O. A. Rahman, A. M. El-Kamash and Y. T. Hung, *Water*, , DOI:10.3390/w14020137.

47 A. M. Najafi, S. Soltanali and H. Ghassabzadeh, *Chem. Eng. J.*, 2023, **468**, 143719.

48 M. Sun, C. Ku, Z. Tao, T. Wang, C. Wen, A. Hanif, C. Wang, Q. Gu, P. Sit and J. Shang, *Results Eng.*, 2023, **18**, 101134.

49 D. G. Boer, J. Langerak and P. P. Pescarmona, *ACS Appl. Energy Mater.*, 2023, **6**, 2634–2656.

50 L. Alalga, A. Benamar and M. Trari, *Int. J. Hydrogen Energy*, 2021, **46**, 28501–28512.

51 Y. Liu, E. H. Osta, A. S. Poryvaev, M. V. Fedin, A. Longo, A. Nefedov and N. Kosinov, *Carbon N. Y.*, 2023, **201**, 535–541.

52 M. Servatan, P. Zarrintaj, G. Mahmodi, S. Kim, M. R. Ganjali, M. R. Saeb and M. Mozafari, *Drug Discov. Today*, 2020, **25**, 642–656.

53 Y. Wan, W. Xu, X. Ren, Y. Wang, B. Dong and L. Wang, *Front. Bioeng. Biotechnol.*, 2020, **8**, 1–20.

54 R. Amorim, N. Vilaça, O. Martinho, R. M. Reis, M. Sardo, J. Rocha, A. M. Fonseca, F. Baltazar and I. C. Neves, *J. Phys. Chem. C*, 2012, **116**, 25642−25650.

55 E. A. Prasetyanto, Y. Atoini, L. Donato, C. W. Hsu and L. De Cola, *Front. Chem.*, 2022, **10**, 1–7.

56 J. W. Ye, H. L. Zhou, S. Y. Liu, X. N. Cheng, R. B. Lin, X. L. Qi, J. P. Zhang and X. M. Chen, *Chem. Mater.*, 2015, **27**, 8255–8260.

57 E. Coutino-Gonzalez, W. Baekelant, D. Grandjean, M. B. J. Roeffaers, E. Fron, M. S. Aghakhani, N. Bovet, M. Van Der Auweraer, P. Lievens, T. Vosch, B. Sels and J. Hofkens,

J. Mater. Chem. C, 2015, **3**, 11857–11867.

58 M. Gaft, G. Panczer, L. Nagli and H. Yeates, *Phys. Chem. Miner.*, 2009, **36**, 127–141.

59 H. Tounsi, S. Mseddi and S. Djemel, *Phys. Procedia*, 2009, **2**, 1065–1074.

60 L. Ding, H. Yang, P. Rahimi, O. Omotoso, W. Friesen, C. Fairbridge, Y. Shi and S. Ng, *Microporous Mesoporous Mater.*, 2010, **130**, 303–308.

61 T. Warner and H. Andersen, *Phys. Chem. Miner.*, 2012, **39**, 163–168.

62 M. S. Nabavi, T. Mohammadi and M. Kazemimoghadam, *Ceram. Int.*, 2014, **40**, 5889–5896.

63 S. Khajavi, F. Kapteijn and J. C. Jansen, *J. Memb. Sci.*, 2007, **299**, 63–72.

64 Z. Ghasemi, H. Younesi and H. Kazemian, *Can. J. Chem. Eng.*, 2011, **89**, 601–608.

65 V. Grover, B. P. Mandal and A. K. Tyagi, in *Handbook on Synthesis Strategies for Advanced Materials : Volume-I: Techniques and Fundamentals*, eds. A. K. Tyagi and R. S. Ningthoujam, Springer Singapore, Singapore, 2021, pp. 1–49.

66 H. Byron, I. Norrbo and M. Lastusaari, *J. Alloys Compd.*, 2021, **872**, 159671.

67 S. Kowalak, M. Pawłowska, M. Miluśka, M. Strózyk, J. Kania and W. Przystajko, *Colloids Surfaces A Physicochem. Eng. Asp.*, 1995, **101**, 179–185.

68 S. Calero, D. Dubbeldam, R. Krishna, B. Smit, T. J. H. Vlugt, J. F. M. Denayer, J. A. Martens and T. L. M. Maesen, *J. AM. CHEM. SOC.*, 2004, **126**, 11377–11386.

69 M. D. Foster, I. Rivin, M. M. J. Treacy and O. D. Friedrichs, *Microporous Mesoporous Mater.*, 2006, **90**, 32–38.

70 E. Coutino-Gonzalez, M. Roeffaers, B. Dieu, G. De Cremer, S. Leyre, P. Hanselaer, W. Fyen, B. Sels and J. Hofkens, *J. Phys. Chem. C*, 2013, **117**, 6998–7004.

71 R. Dimitrijevic, V. Dondur, P. Vulic, S. Markovic and S. Macura, *J. Phys. Chem. Solids*, 2004, **65**, 1623–1633.

72 A. Radulović, V. Dondur, P. Vulić, Z. Miladinović, G. Ćirić-Marjanović and R. Dimitrijević, *J. Phys. Chem. Solids*, 2013, **74**, 1212–1220.

73 I. Padilla, A. López-delgado and M. Romero, *J Am Ceram Soc.*, 2022, **105**, 4336–4347.

74 D. J. SCHIPPER, T. W. LATHOUWERS and C. Z. van DOORN, *J. Am. Ceram. Soc.*, 1973, **56**, 523–525.

75 I. Norrbo, P. Gluchowski, P. Paturi, J. Sinkkonen and M. Lastusaari, *Inorg. Chem.*, 2015, **54**, 7717–7724.

76 T. Zahoransky, H. Friis and M. Marks, *Phys. Chem. Miner.*, 2016, **43**, 459–480.

77 C. Agamah, S. Vuori, P. Colinet, I. Norrbo, J. M. de Carvalho, L. K. Okada Nakamura, J. Lindblom, L. van Goethem, A. Emmermann, T. Saarinen, T. Laihinen, E. Laakkonen, J. Linden, J. Konu, H. Vrielinck, D. van der Heggen, P. F. Smet, T. Le Bahers and M. Lastusaari, *Chem. Mater.*, 2020, **32**, 8895–8905.

78 D. Reinen and G.-G. Lindner, *Chem. Soc. Rev.*, 1999, **28**, 75–84.

79 A. Curutchet and T. Le Bahers, *Inorg. Chem.*, 2017, **56**, 414–423.

80 H. C. Byron, C. Swain, P. Paturi, P. Colinet, R. Rullan, V. Halava, T. Le Bahers and M. Lastusaari, *Adv. Funct. Mater.*, , DOI:10.1002/adfm.202303398.

81 I. Norrbo, P. Gluchowski, I. Hyppänen, T. Laihinen, P. Laukkanen, J. Mäkelä, F. Mamedov, H. Santos, J. Sinkkonen, M. Tuomisto, A. Viinikanoja and M. Lastusaari, *ACS Appl. Mater. Interfaces*, 2016, **8**, 11592–11602.

82 S. Vuori, P. Colinet, I. Norrbo, R. Steininger, T. Saarinen, H. Palonen, P. Paturi, L. C. V Rodrigues, J. Göttlicher, T. Le Bahers and M. Lastusaari, *Adv. Opt. Mater.*, , DOI:10.1002/adom.202100762.

83 D. Ballentyne and K. Bye, *J. Phys. D. Appl. Phys.*, 1970, **3**, 1438–1443.

84 R. D. Kirk, *J. Electrochem. Soc.*, 1954, 461–465.

85 A. Sidike, A. Sawuti, X. Wang, H. Zhu, S. Kobayashi, I. Kusachi and N. Yamashita, *Phys. Chem. Miner.*, 2007, **34**, 477–484.

86 H. Schlaich, G.-G. Lindner, J. Feldmann, E. Göbel and D. Reinen, *Inorg. Chem.*, 2000, **39**, 2740–2746.

87 M. Hiroshi, K. Toru and K. Riso, *J. Phys. Soc. Japan*, 1990, 59, 506–515.

88 I. Norrbo, J. Carvalho, P. Laukkanen, J. Mäkelä, F. Mamedov, M. Peurla, H. Helminen, S. Pihlasalo, H. Härmä, J. Sinkkonen and M. Lastusaari, *Adv. Funct. Mater.*, 2017, **27**, 1606547.

89 W. Fang, E. Sairanen, S. Vuori, M. Rissanen, I. Norrbo, M. Lastusaari and H. Sixta, *ACS Sustain. Chem. Eng.*, 2021, **9**, 16338−16346.

90 T. Laine, I. Norrbo, J. Holvitie and M. Lastusaari, *Priv Softw.*, 2020, 2020.

91 W. Baekelant, G. Romolini, L. Sun, M. De Ras, E. Fron, T. Moreira, C. Viola, A. Ruivo, C. A. T. Laia, J. Martens, C. Martin, C. W. Kim, M. van der Auweraer, M. B. J. Roeffaers, J. Hofkens and E. Coutino-Gonzalez, *Methods Appl. Fluoresc.*, , DOI:10.1088/2050-6120/ab7169.

92 *Phosphorescent Pigments and Products – Part 1: Measurement and Marking at the Producer*, DIN 67510-1:2009-11, DIN, Berlin, Germany 2009.

93 R. Masuma, S. Kashima, M. Kurasaki and T. Okuno, *J. Photochem. Photobiol. B Biol.*, 2013, **125**, 202–208.

94 A. Gambardella, C. Patterson, S. Webb and M. Walton, *Microchem. J.*, 2016, **125**, 299–307.

95 J. Goslar, S. Lijewski, S. K. Hoffmann, A. Jankowska and S. Kowalak, *J. Chem. Phys.*, 2009, **130**, 204504.

96 H. Berke, *Chem. Soc. Rev.*, 2007, **36**, 15–30.

97 The Metropolitan Museum of Art, https://www.metmuseum.org/, (accessed 25 March 2024).

98 I. F. Chang, *J. Electrochem. Soc.*, 1974, **121**, 815–820.

99 R. Y. Vanagida, A. A. Amaro and K. Seff, *J. Phys. Chemstiy*, 1973, **77**, 805–809.

100 I. S. Hassan, S. Y. M. Antao and J. O. H. N. B. Parise, *Am. Mineral.*, 2004, **89**, 359–364.

101 B. Hippler and H. Bohm, *Zeitschrift für Krist.*, 1989, **187**, 39–53.

102 F. W. Barth and E. Posnjak, *Zeitschrift für Krist. - Cryst. Mater.*, 1932, **81**, 135–141.

103 H. G. Hecht, *J. Res. Natl. Bur. Stand. (1934).*, 1976, **80**, 567–583.

104 E. Climent-Pascual, J. Romero De Paz, J. Rodríguez-Carvajal, E. Suard and R. Sáez-Puche, *Inorg. Chem.*, 2009, **48**, 6526–6533.

105 R. Kirk, *Glass*, 1955, 22–31.

106 K. Raulin, N. Gobeltz, V. Hervé, N. Touati, B. Ledé and A. Moissette, *Phys. Chem. Chem. Phys.*, 2011, **13**, 9253–9259.

107 D. Arieli, D. E. W. Vaughan and D. Goldfarb, *J. Am. Chem. Soc.*, 2004, **126**, 5776–5788.

108 N. V. Chukanov, A. N. Sapozhnikov, R. Y. Shendrik, M. F. Vigasina and R. Steudel, *Minerals*, 2020, **10**, 1042.

109 B. Ledé, A. Demortier, N. Gobeltz-Hautecœur, J.-P. Lelieur, E. Picquenard and C. Duhayon, *J. Raman Spectrosc.*, 2007, **38**, 1461–1468.

110 J. A. Creighton, H. W. Deckman and J. M. Newsam, *J. Phys. Chem.*, 1994, **98**, 448–459.

111 C. L. Angell, *J. Phys. Chem.*, 1973, **77**, 222–227.

112 D. W. Matson, S. K. Sharma and J. A. Philpotts, *Am. Mineral.*, 1986, **71**, 694–704.

113 S. Kowalak, A. Jankowska, S. Zeidler and A. B. Więckowski, *J. Solid State Chem.*, 2007, **180**, 1119–1124.

114 J. Schneider, B. Dischler and A. Räuber, *Phys. Status Solidi*, 1966, **13**, 141–157.

115 A. L. Antaris, H. Chen, S. Diao, Z. Ma, Z. Zhang, S. Zhu, J. Wang, A. X. Lozano, Q. Fan, L. Chew, M. Zhu, K. Cheng, X. Hong, H. Dai and Z. Cheng, *Nat. Commun.*, 2017, **8**, 1–11.

116 B. Valeur and M. Berberan-Santos, *Molecular Fluorescence: Principles and Applications*, John Wiley & Sons, 2nd edn., 2012.

117 F. Blumentritt, C. Latouche, Y. Morizet, Y. Morizet, M. T. Caldes, S. Jobic and E. Fritsch, *J. Phys. Chem. Lett.*, 2020, **11**, 4591–4596.

118 W. Giggenbach, *Inorg. Chem.*, 1972, **11**, 1201–1207.

119 C. Barchasz, Fl. Molton, C. Duboc, J.-C. Leprêtre, S. Patoux and F. Alloin, *Anal. Chem.*, 2012, **84**, 3973−3980.

120 C. M. Marian, *Wiley Interdiscip. Rev. Comput. Mol. Sci.*, 2012, **2**, 187–203.

121 K. K. Rohatgi-Mukherjee, *Fundamentals of Photochemistry*, 1978.

122 L. Wei, D. Pang, L. He and C. Deng, *Ceram. Int.*, 2017, **43**, 16141–16148.

123 M. Kaiheriman, A. Maimaitinaisier, A. Rehiman and Aierken Sidike, *Phys. Chem. Miner.*, 2014, **41**, 227–235.

124 R. B. Singh, S. Mahanta, A. Bagchi and N. Guchhait, *Photochem. Photobiol. Sci.*, 2009, **8**, 101–110.

125 I. Norrbo, I. Hyppänen and M. Lastusaari, *J. Lumin.*, 2017, **191**, 28–34.

126 D. L. Dexter, *J. Chem. Phys.*, 1953, **21**, 836–850.

127 H. Xu, R. Chen, Q. Sun, W. Lai, Q. Su, W. Huang and X. Liu, *Chem. Soc. Rev.*, 2014, **43**, 3259–3302.

128 L. E. Vannotti and J. R. Morton, *J. Chem. Phys.*, 1967, **47**, 4210–4214.

129 T. Nakano, S. Araki, N. H. Nam, T. Umemoto, K. Tsuchihashi, Y. Kubo, A. Owaki and Y. Nozue, 2020, 1–18.

130 R. Windiks and J. Sauer, *Phys. Chem. Chem. Phys.*, 1999, **1**, 4505–4513.

131 I. Gessner and I. Neundorf, *Int. J. Mol. Sci.*, 2020, **21**, 1–21.

132 T. Hyeon and V. Rotello, *Chem. Soc. Rev.*, 2012, **41**, 2718–2739.

133 J. Yang, J. Tu, G. E. M. Lamers, R. C. L. Olsthoorn and A. Kros, *Adv. Healthc. Mater.*, 2017, **6**, 1–7.

134 S. Salatin, S. Maleki Dizaj and A. Yari Khosroushahi, *Cell Biol. Int.*, 2015, **39**, 881–890.

135 T. Kihara, Y. Zhang, Y. Hu, Q. Mao, Y. Tang and J. Miyake, *J. Biosci. Bioeng.*, 2011, **111**, 725–730.

136 S. Y. Ong, C. Zhang, X. Dong and S. Q. Yao, *Angew. Chemie - Int. Ed.*, 2021, **60**, 17797–17809.

137 Z. Qu, J. Shen, Q. Li, F. Xu, F. Wang, X. Zhang and C. Fan, *Theranostics*, 2020, **10**, 2631–2644.

138 J. Estelrich and M. Antònia Busquets, *Molecules*, , DOI:10.3390/molecules23071567.

139 L. Colombeau, S. Acherar, F. Baros, P. Arnoux, A. M. Gazzali, K. Zaghdoudi, M. Toussaint, R. Vanderesse and C. Frochot, *Light-Responsive Nanostructured Systems for Applications in Nanomedicine*, Springer International Publishing, 2016, vol. 370.

140 A. V. Naumov, *Metallurgist*, 2010, **54**, 197–200.

141 A. G. Christy, *Mineral. Mag.*, 2015, **79**, 33–49.

142 S. Mintova, N. H. Olson, V. Valtchev and T. Bein1, *Scopus*, 1999, **283**, 958–960.

143 F. Collins, A. Rozhkovskaya, J. G. Outram and G. J. Millar, *Microporous Mesoporous Mater.*, 2020, **291**, 109667.

144 G. Yang, H. Guo, Z. Kang, L. Zhao, S. Feng, F. Jiao and S. Mintova, *ChemSusChem*, 2019, 4529.

145 M. M. J. Treacy and J. B. Higgins, *Collection of Simulated XRD Powder Patterns for Zeolites*, Elsevier Science B.V., 4th edn., 2001.

146 A. O. Bokuniaeva and A. S. Vorokh, *J. Phys. Conf. Ser.*, 2019, **1410**, 012057.

147 B. Morgan and O. Lahav, *Chemosphere*, 2007, **68**, 2080–2084.

148 K. C. Biswas, L. L. Barton, W. L. Tsui, K. Shuman, J. Gillespie and C. S. Eze, *J. Microbiol. Methods*, 2011, **86**, 140–144.

149 D. Krasowska, F. Begini, C. Santi, F. Mangiavacchi, J. Drabowicz and L. Sancineto, *Arkivoc*, 2019, **2019**, 24–37.

150 J. Küppers, A. C. Schulz-Fincke, J. Palus, M. Giurg, J. Skarżewski and M. Gütschow, *Pharmaceuticals*, , DOI:10.3390/ph9030043.

151 V. Nascimento, N. L. Ferreira, R. F. S. Canto, K. L. Schott, E. P. Waczuk, L. Sancineto, C. Santi, J. B. T. Rocha and A. L. Braga, *Eur. J. Med. Chem.*, 2014, **87**, 131–139.

152 A. Kharchenko, O. I. Lebedev, V. Zholobenko, V. De Waele and S. Mintova, *J. Phys. Chem. C*, 2016, **120**, 26300–26308.

153 S. Khajavi, J. C. Jansen and F. Kapteijn, *J. Memb. Sci.*, 2010, **356**, 52–57.

154 K. Ishii, *Quantum Beam Sci.*, 2019, **3**, 1–14.

155 A. F. Keppler, G. Cerchiaro, O. Augusto, S. Miyamoto, F. Prado, P. Di Mascio and J. V. Comasseto, *Organometallics*, 2006, **25**, 5059–5066.

156 S. Jena, R. B. Tokas, S. Thakur and N. K. Sahoo, *SMC Bull.*

157 S. U. N. Jiulong, National University Of Singapore, 2014.

158 A. J. Gomes, C. N. Lunardi, F. S. Rocha and G. S. Patience, *Can. J. Chem. Eng.*, 2019, **97**, 2168–2175.

159 D. P. Ferreira, D. S. Conceição, F. Fernandes, T. Sousa, R. C. Calhelha, I. C. F. R. Ferreira, P. F. Santos and L. F. Vieira Ferreira, *J. Phys. Chem. B*, 2016, **120**, 1212–1220.

160 L. Vieira Ferreira and I. Ferreira Machado, *Curr. Drug Discov. Technol.*, 2007, **4**, 229–245.

161 J. Lauth, S. Kinge and L. D. A. Siebbeles, *Zeitschrift für Phys. Chemie*, 2017, **231**, 107–119.

162 D. S. Conceição and L. F. Vieira Ferreira, *ChemistrySelect*, 2018, **3**, 773–778.

163 D. Goldfarb and S. Stoll, *EPR Spectroscopy: Fundamentals and Methods*, Wiley, 2018.

164 D. T. Petasis and M. P. Hendrich, *Quantitative interpretation of multifrequency multimode EPR spectra of metal containing proteins, enzymes, and biomimetic complexes*, Elsevier Inc., 1st edn., 2015, vol. 563.

165 T. Dey, *Nanotechnol. Environ. Eng.*, 2023, **8**, 41–48.

166 F. Babick, in *Characterization of Nanoparticles*, Elsevier Inc., 2020, pp. 137–172.

167 Y. Leng, *Materials characterization: Introduction to microscopic and spectroscopic methods*, WILEY-VCH, 2nd edn., 2013.

168 P. Gill, T. T. Moghadam and B. Ranjbar, *J. Biomol. Tech.*, 2010, **21**, 167–193.

169 K. Fucke and J. W. Steed, *Water (Switzerland)*, 2010, **2**, 333–350.

170 B. J. Inkson, *Scanning Electron Microscopy (SEM) and Transmission Electron Microscopy (TEM) for Materials Characterization*, Elsevier Ltd, 2016.

171 P. Atkins, T. Overton, J. Rourke, M. Weller and F. Armstrong, *Shriver and Atkins' Inorganic*

Chemistry, Oxford, 5th edn., 2010.

172 A. H. Johnstone, *J. Chem. Technol. Biotechnol.*, 1991, **50**, 2400.

173 W. Clegg, *Crystal Structure Determination*, Oxford University Press, 1998.

174 Y. Waseda, E. Matsubara and K. Shinoda, *X-Ray Diffraction Crystallography: Introduction, Examples and Solved Problems*, Springer, 2011.

175 C. Heinemann, W. Koch, G.-G. Lindner and D. Reinen, *Phys. Rev. A*, 1995, **52**, 1024–1038.

A

APPENDIX: CHAPTER 2

A.1 Exploring NIR Emission and Applications of Sulfur-Doped Zeolites

Table A.1.1 - Fractions of sodalite, nepheline and carnegieite phases found in all synthesized samples extracted from PXRD data.

Nominal S/Cl	Sodalite	Nepheline	Carnegieite	Nepheline/Carnegieite ratio
0	0.77	0.02	0.21	0.10
0.06	0.86	0.05	0.09	0.57
0.13	0.84	0.08	0.08	1.05
0.21	0.77	0.10	0.13	0.81
0.33	0.70	0.12	0.18	0.63
0.50	0.61	0.15	0.25	0.60
0.75	0.48	0.18	0.35	0.51
1.17	0.48	0.22	0.30	0.75
2.0	0.43	0.22	0.34	0.65
4.5	0.33	0.27	0.40	0.68

Table A.1.2 - Oxide weight percentage (wt%) of the elements found in the produced zeolite samples using the PIXE technique.

Nominal S/Cl	Oxides (wt%)											
	Na_2O	Al_2O_3	SiO_2	SO_3	Cl	K_2O	CaO	TiO_2	Fe_2O_3	CuO	MgO	P_2O_5
0	23.3	31.8	38.5	-	5.5	0.48	0.31	0.014	0.026	0.011	-	-
0.21	23.5	32.0	38.8	0.5	4.5	0.47	0.30	0.015	0.020	0.042	-	-
4.5	23.6	32.9	40.3	2.0	0.5	0.53	0.25	0.014	0.024	0.004	-	-
Na-LTA	19.9	34.7	43.2	0.09	0.03	0.52	0.41	0.04	0.05	-	0.54	0.09

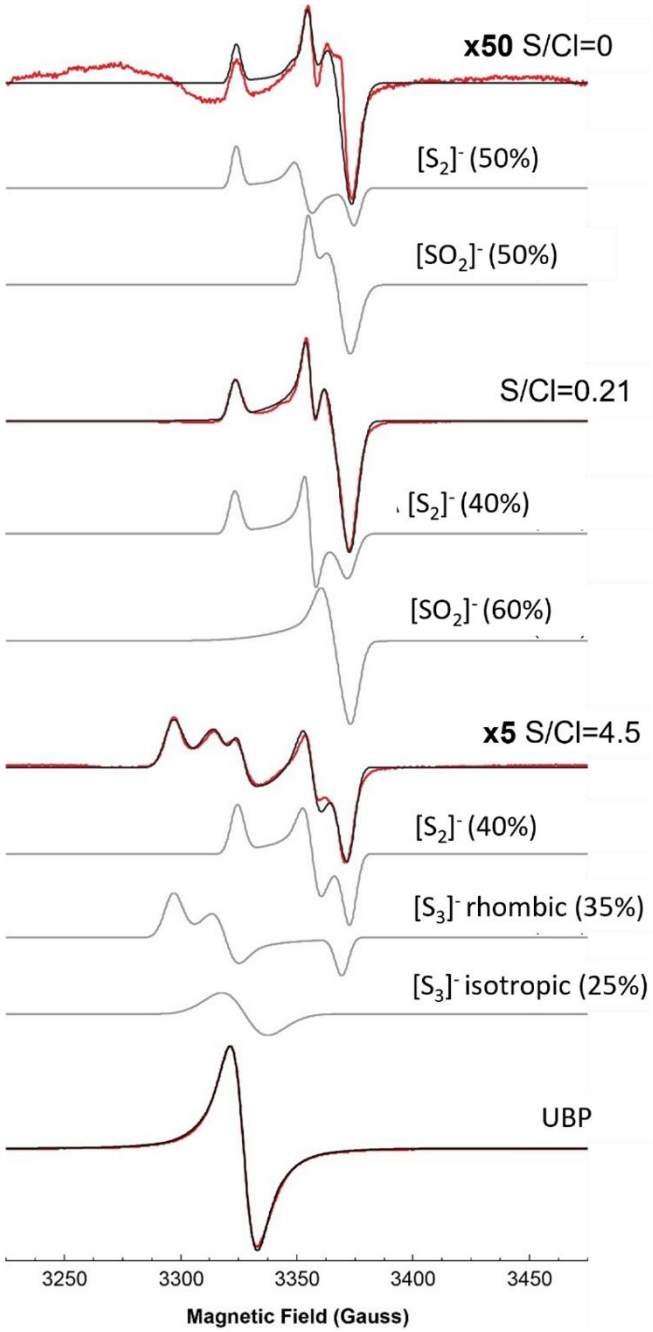


Figure A.1.1 - EPR spectra (red lines) and respective simulations (grey lines) of the samples S/Cl=0, 0.21 and 4.5 and commercial ultramarine blue pigment (UBP), recorded at 120 K, 2 mW and 9.45 GHz; in some cases, a multiplication factor was applied; the individual components simulations are presented below each spectrum, and were added with the indicated percentages to obtain the full spectrum overlaid with the experimental one.

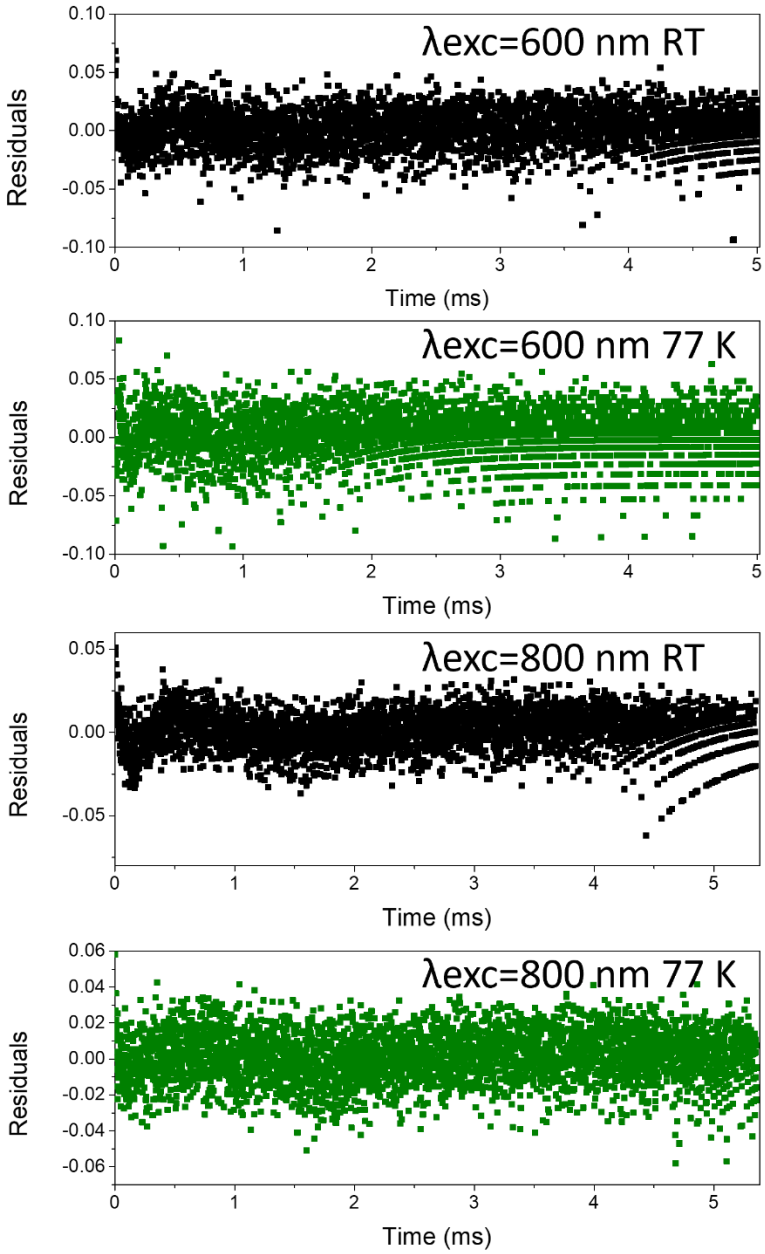
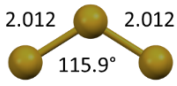
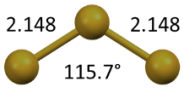
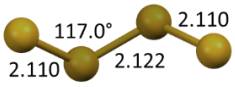
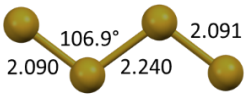
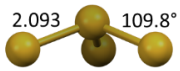


Figure A.1.2 - Corresponding residuals of the fittings presented in **Figure 2.3.17** and **Figure 2.3.18**.

Table A.1.3 - Vertical electronic excitation energies (above 300 nm), oscillator strengths and optimized structures of several sulfur species.

Species	Structures	Predicted absorption bands		Oscillator strengths
		E (eV)	λ(nm)	
$[S_3]^-$ (C_{2v})		2.13	582	0.0509
$[S_3]^{2-}$ (C_{2v})		2.09	592	0.0018
		3.54	351	0.0062
		3.61	343	0.0410
$[S_4]^{2-}$ (C_2)		2.41	514	0.0022
		2.54	488	0.0066
		3.21	386	0.0354
		3.63	341	0.0595
$[S_4]^{2-}$ (C_{2h})		2.74	453	0.0016
		3.72	334	0.1753
		4.01	309	0.0563
$[S_4]^{2-}$ (C_{3v})		2.80	442	0.0018
		3.52	352	0.0109
		3.99	311	0.0012
		4.12	301	0.0075

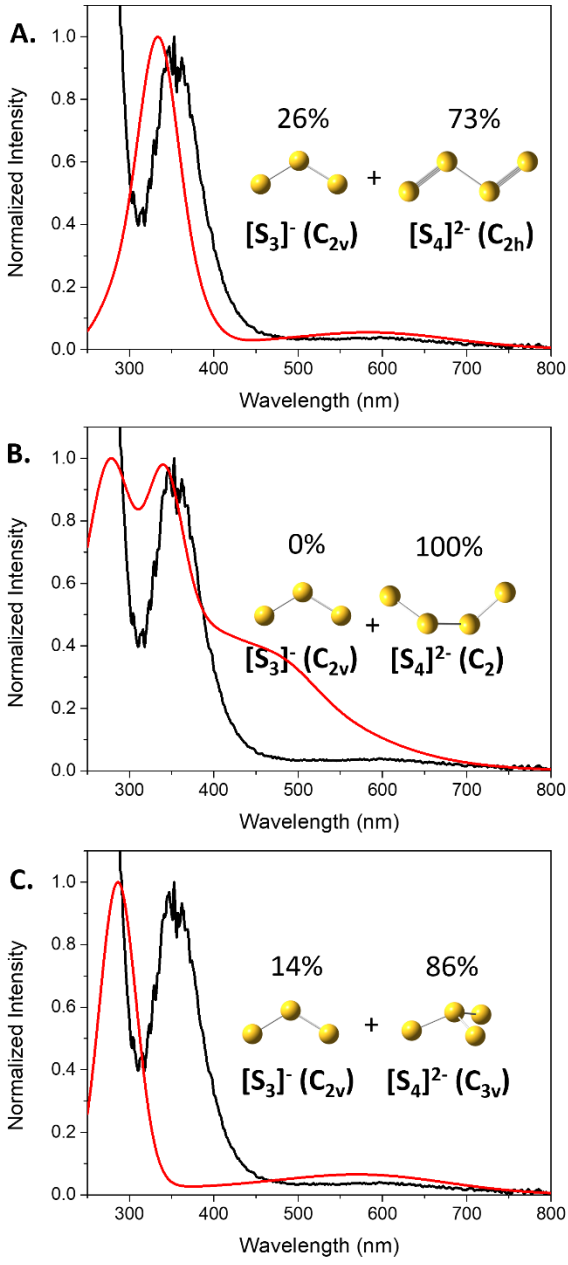


Figure A.1.3 - (**A-C**) Overlap of the diffuse reflectance spectrum of sample S/Cl=4.5 (black) with the combined calculated spectra of calculated sulfur species with $[S_3]^-$ clusters (red).

Table A.1.4 - Electronic configuration of the most important singlet and triplet states. The main molecular orbitals (MO), oscillator strength (f) and excitation energy (E) of every state are also shown.

State	E (eV)	f	λ(nm)	MO(%)	Symmetry
T1	1.53	0.0000*	809	HOMO→LUMO (99%)	$^3B_1$
S1	2.09	0.0018	592	HOMO→LUMO (100%)	$^1B_1$
T5	3.31	0.0000*	374	HOMO-3→LUMO (77%)	$^3A_2$
S3	3.54	0.0062	351	HOMO-2→LUMO (99%)	$^1A_1$
S5	3.62	0.0410	343	HOMO-1→LUMO (95%)	$^1B_2$
S6	4.63	0.0042	268	HOMO-1→LUMO+1 (98%)	$^1A_1$
T8	4.36	0.0000*	284	HOMO-3→LUMO+1 (83%)	$^3B_1$

*Calculations were done without SOC inclusion

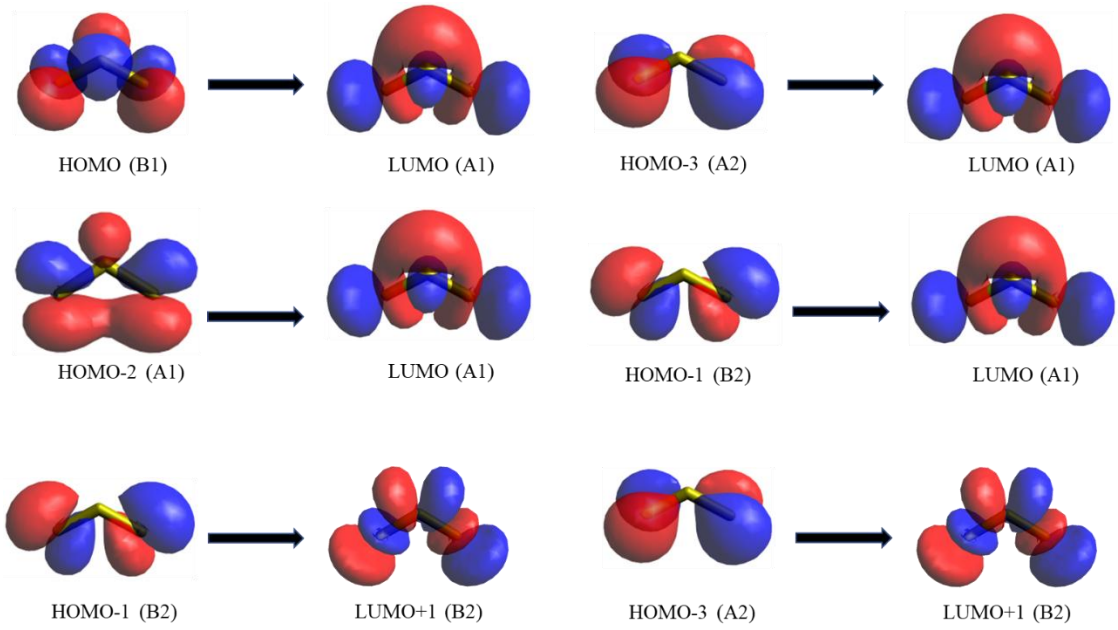


Figure A.1.4 - Kohn-Sham molecular orbitals and their symmetries.

B

APPENDIX: CHAPTER 3

Table B.1 - Elemental composition in weight percentage (wt%) of the produced zeolite samples using the WDXRF technique.

Nominal Se/Cl ratio	Oxides (wt%)						
	Na_2O	SiO_2	Al_2O_3	SeO_2	Cl	K_2O	CaO
0.06	20.5	40.5	31.2	0.77	6	0.71	0.24
0.21	21.5	39	31.1	1.88	5.53	0.62	0.39
0.75	21.3	38.7	31.8	4.29	2.85	0.69	0.44
4.5	20.8	39	31.6	6.80	0.76	0.66	0.36

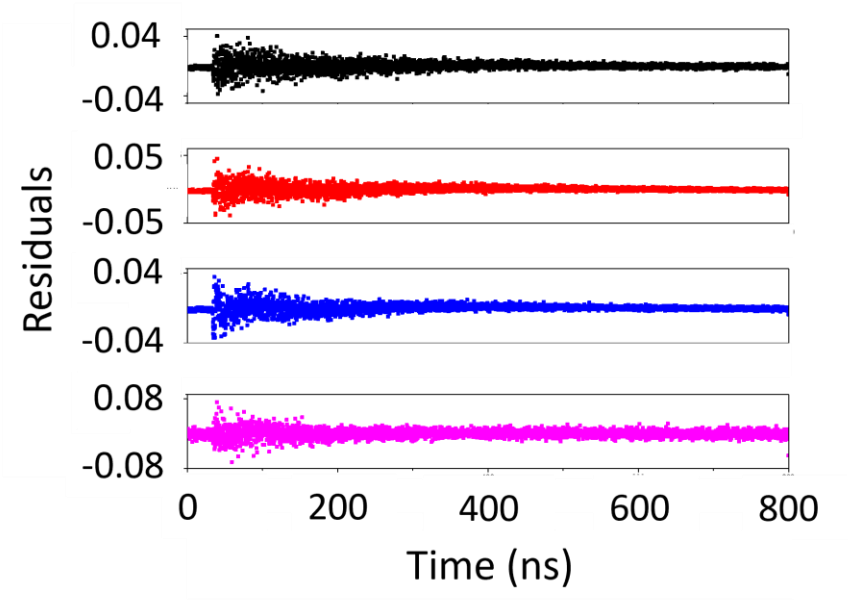


Figure B.1 - Residuals of the fittings performed in **Figure 3.9**.

Table B.2 - Sodalite unit cell parameters of the synthesized samples with different Se/Cl ratios calculated from PXRD data illustrated in **Figure 3.1.A**, considering the diffraction plan [211].

Nominal Se/Cl ratio	d-spacing (Å)	Unit cell parameters a=b=c (Å)*
0.06	3.62	8.88
0.21	3.63	8.89
0.75	3.66	8.97
4.5	3.69	9.03

*Considering the cubic system of sodalite, where the cell parameters are equal (a=b=c) and the angles are all 90° (α=β=γ=90°)[173], the following equation was used for the calculations[174]: $\frac{1}{d^2} = \frac{h^2+k^2+l^2}{a^2}$, where d is the spacing between crystalline planes within a crystalline lattice, a is the unit cell parameter, and h, k, l are the Miller indices of the diffracted plane (in this particular case, the values are [211]).

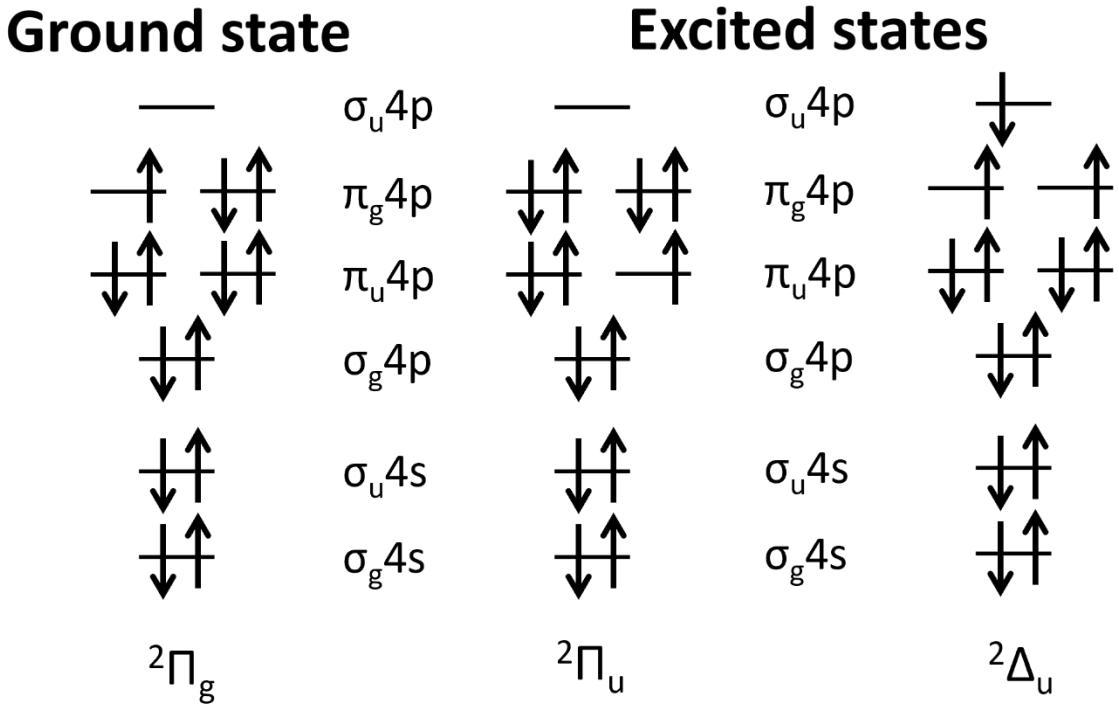


Figure B.2 - Molecular orbitals of ground and excited states of luminescent $[Se_2]^-$ species[175].

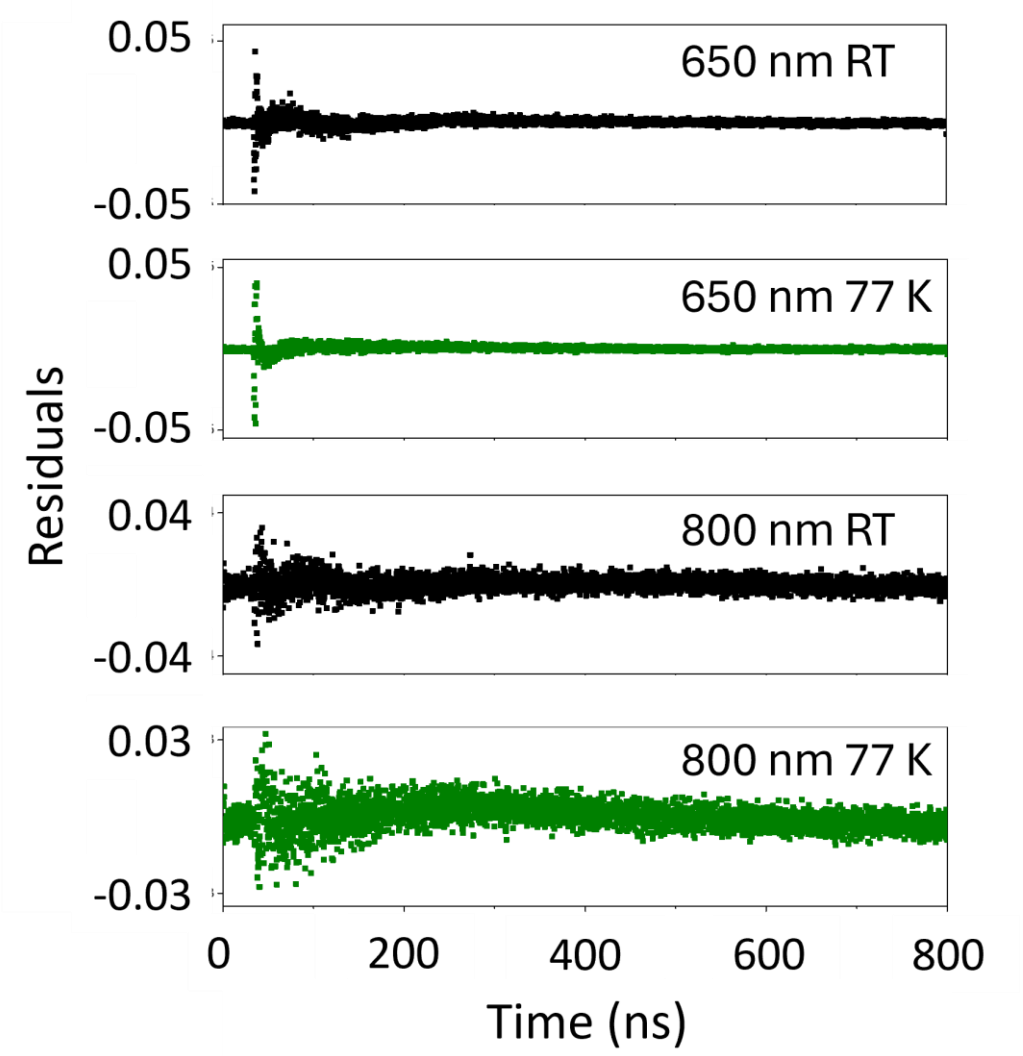


Figure B.3 - Residuals of the fittings performed in **Figure 3.16** and **Figure 3.17**.

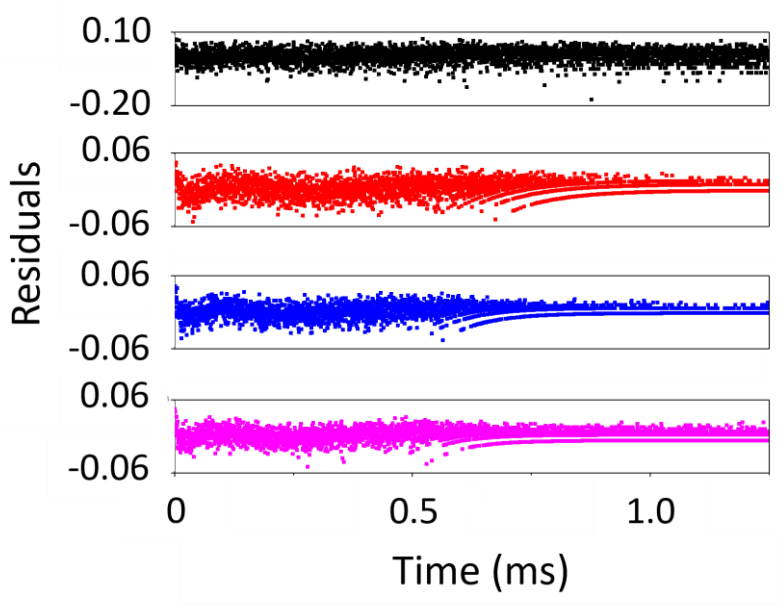


Figure B.4 - Residuals of the fittings performed in **Figure 3.19**.

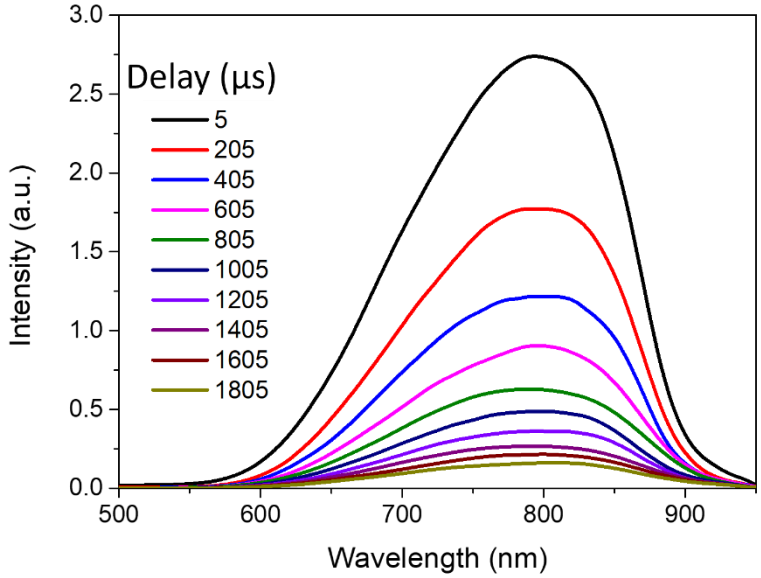


Figure B.5 - Time-resolved emission of the sample with Se/Cl=0, using a λ_{exc}=337 nm.

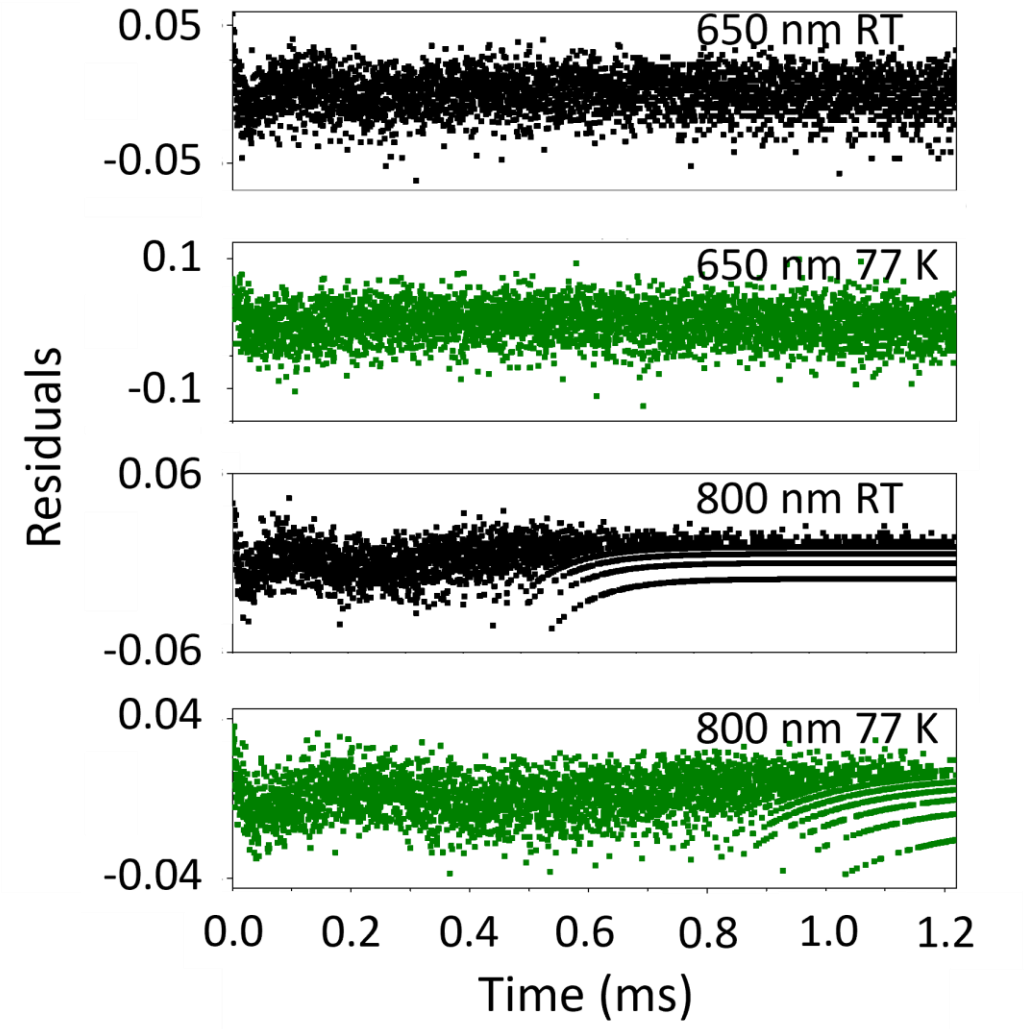


Figure B.6 - Residuals of the fittings performed in **Figure 3.25** and **Figure 3.26**.

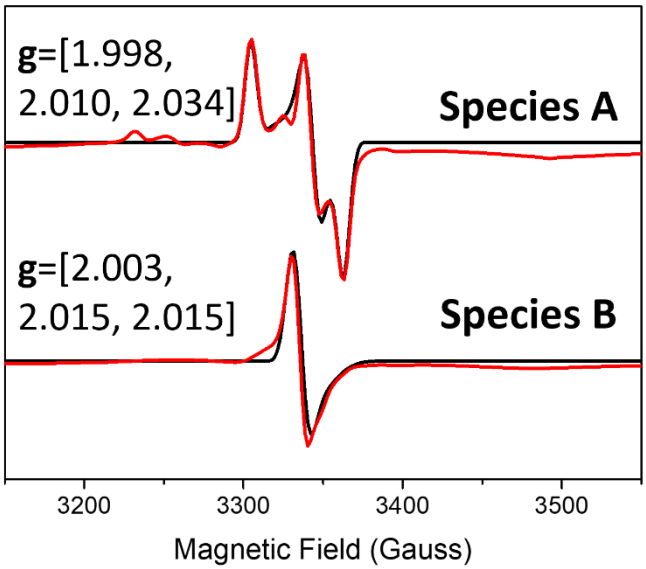


Figure B.7 - EPR spectra (red lines) and corresponding simulations (black lines) depicting species A (detected at lower temperatures) and B (detected at 150 K) in sample Se/Cl=0.06.

C

APPENDIX: CHAPTER 4

C.1 Single NIR-Emitting Selenium-Doped Zeolites Staring From Nanozeolites

Table C.1.1 - Elemental analysis in weight percentage (wt%) of the synthesized nanozeolites using the WDXRF technique.

Sample	Oxides (wt%)					
	Na_2O	SiO_2	Al_2O_3	SeO_2	SO_3	Cl
$Se_{0.1}$ gel	16.6	48.2	35	0.03	0.12	0.05
Se_1 gel	15.5	49	35	0.26	0.16	0.08

Table C.1.2 - Elemental analysis of the impurities detected using the EDS technique in nanozeolite samples submitted to high-temperature synthesis at 900 °C.

Sample	Molar percentage composition (%)[a]						
	Cl	K	Ca	Mn	Fe	Cu	W
$Se_{0.1}$ gel - 900 °C	-	0.05	0.02	-	-	0.05	-
Se_1 gel - 900 °C	-	-	-	-	0.08	0.21	0.28
$Se_{0.1}$ - 900 °C	-	0.11	-	0.24	0.30	0.31	0.31
Se_1 - 900 °C	0.07	0.04	-	-	0.03	0.09	-

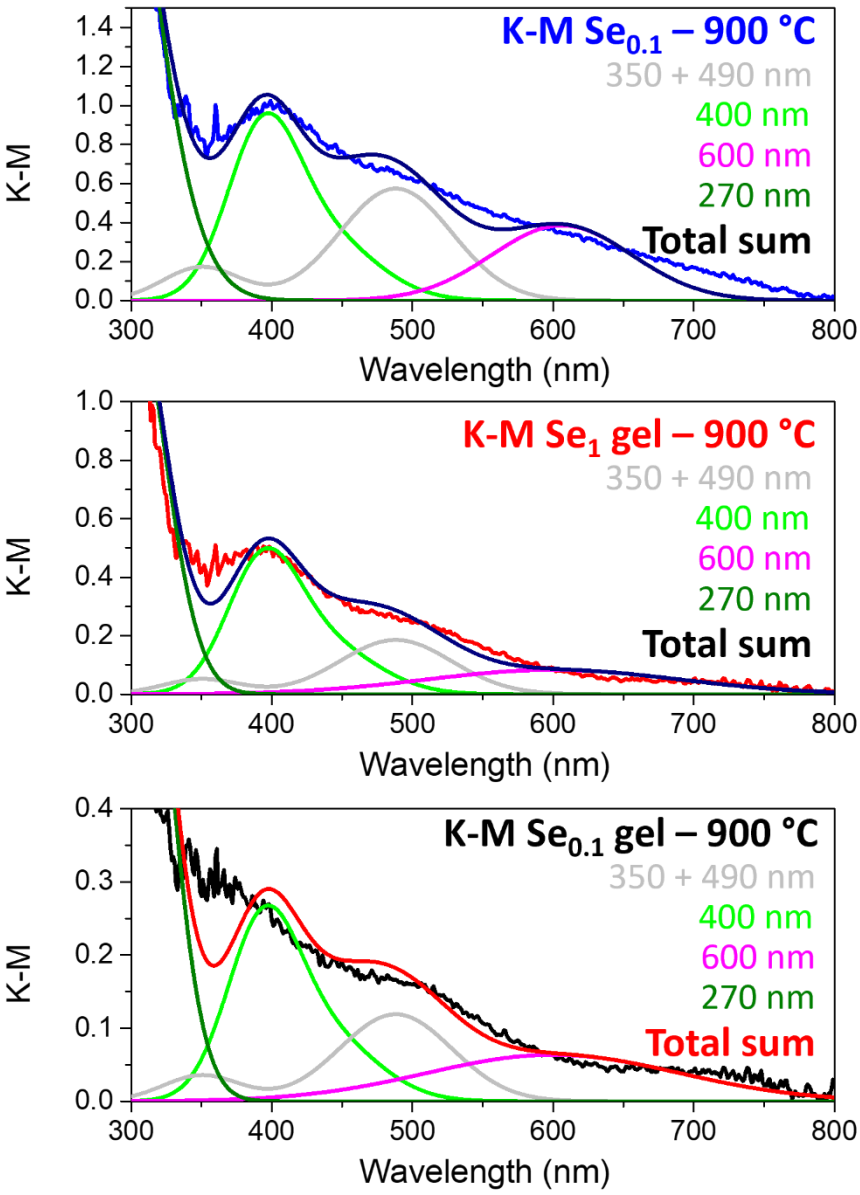


Figure C.1.1 - Diffuse reflectance spectral deconvolution of samples $Se_{0.1}$ gel - 900 °C (black), Se_1 gel - 900 °C (red) and $Se_{0.1}$ - 900 °C (blue).

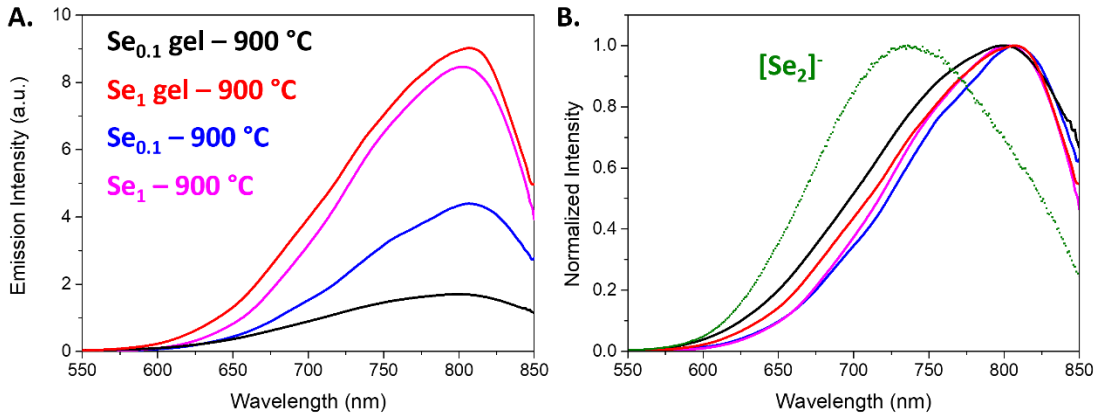


Figure C.1.2 - (**A**) Emission spectra of the synthesized samples with λ_{exc}=350 nm and (**B**) corresponding normalized spectra, with the green line representing the emission spectra of $[Se_2]^-$ clusters excited at the same wavelength.

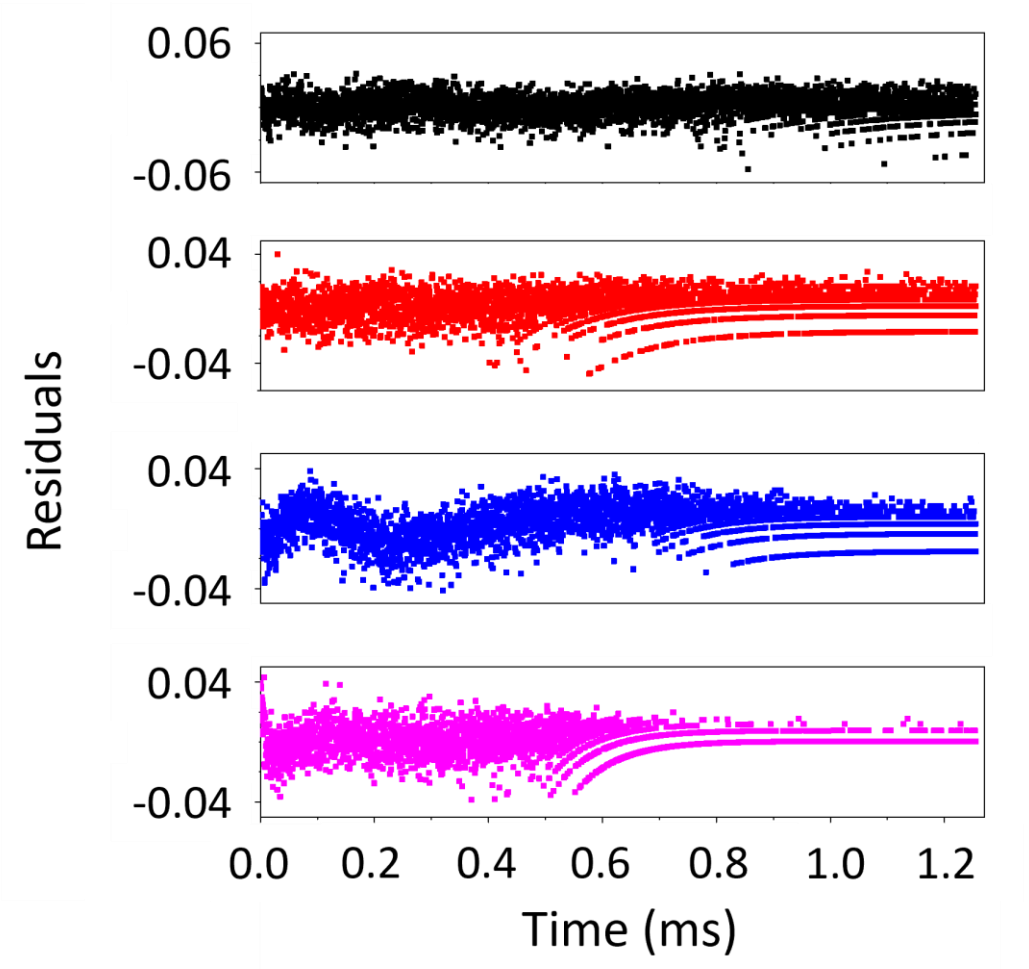


Figure C.1.3 - Corresponding residuals of the fittings of the photoluminescence decay times present in **Figure 4.1.17**.

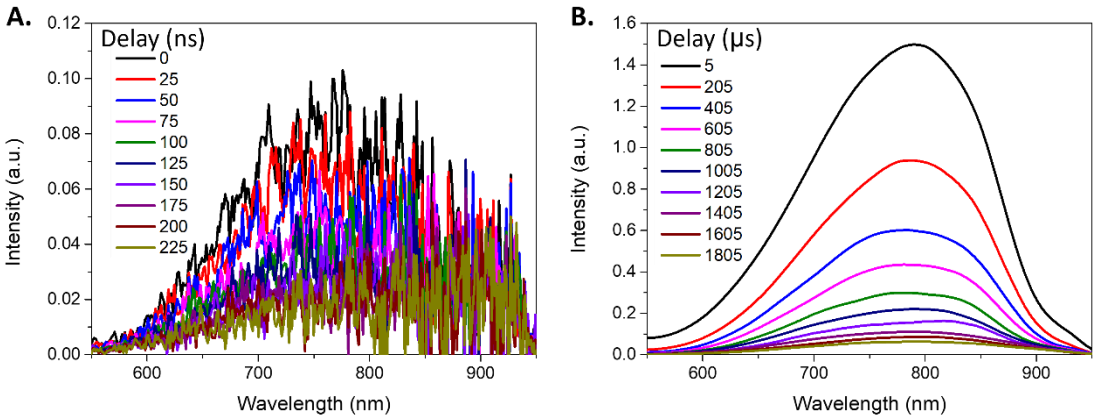


Figure C.1.4 - Time-resolved emission spectroscopy of sample Se_0 gel - 900 °C applying shorter (**A**) and longer (**B**) delay times, λ_{exc}=337 nm.

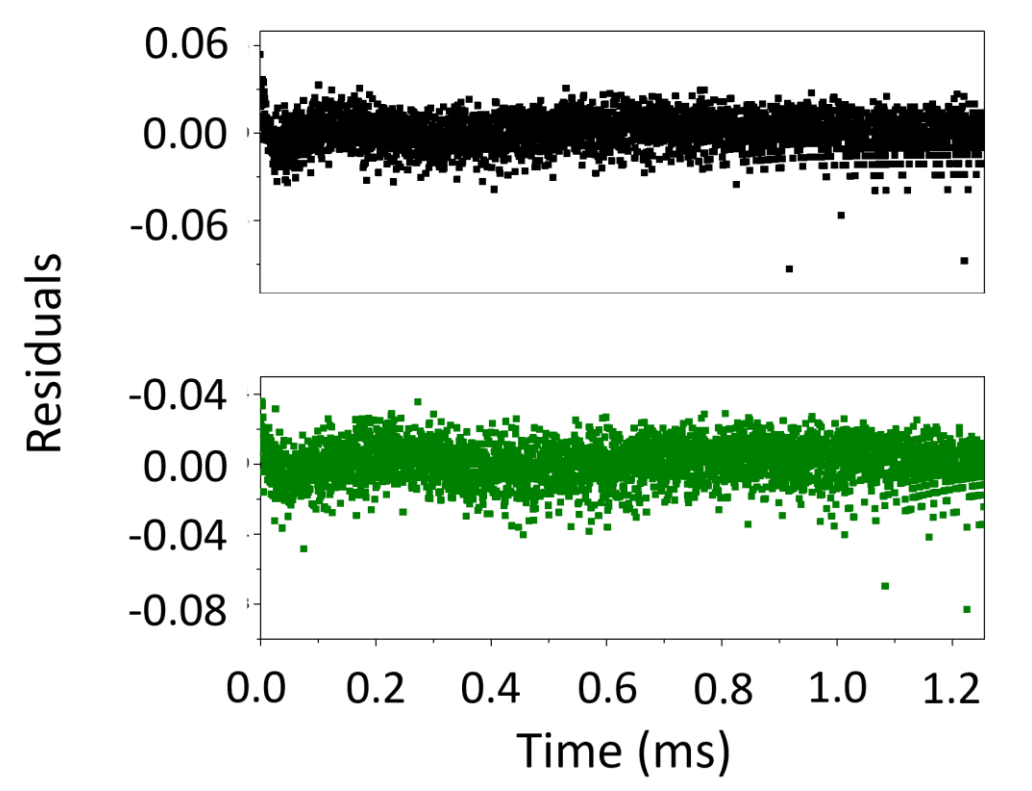


Figure C.1.5 - Residuals of the fittings present in **Figure 4.1.22**.

D

APPENDIX: CHAPTER 5

Table D.1 - Oxide weight percentage (wt%) of the elements found in the produced zeolite samples using the PIXE technique.

Nominal Te/Cl	Oxides (wt%)								
	Na_2O	Al_2O_3	SiO_2	SO_3	Cl	K_2O	CaO	Fe_2O_3	TeO_2
0.06	25.38	30.81	36.62	0.08	5.08	0.40	0.29	-	0.81
0.21	24.83	30.13	35.58	0.05	4.24	0.39	0.31	0.03	4.05
4.5	23.49	29.09	34.32	0.06	0.51	0.37	0.29	0.05	11.44

Table D.2 - Sodalite unit cell parameters of the synthesized samples with different Te/Cl ratios calculated from PXRD data illustrated in **Figure 5.1.A**, considering the diffraction plan [211].

Nominal Te/Cl ratio	d-spacing (Å)	Unit cell parameters a=b=c (Å)*
0.06	3.61	8.85
0.21	3.63	8.90
0.75	3.67	9.00
4.5	3.70	9.06

*Considering the cubic system of sodalite, where the cell parameters are equal (a=b=c) and the angles are all 90° (α=β=γ=90°)[173], the following equation was used for the calculations[174]: $\frac{1}{d^2} = \frac{h^2+k^2+l^2}{a^2}$, where d is the spacing between crystalline planes within a crystalline lattice, a is the unit cell parameter, and h, k, l are the Miller indices of the diffracted plane (in this particular case, the values are [211]).

I

ANNEX: CHAPTER 4

I.I Exploring Several Synthetic Strategies to Obtain NIR-emitting Nanozeolites

Selenium reduction in solution

As described in equation (**I.I**), the reduction of sodium selenite (Na_2SeO_3) to sodium diselenide should occur via two consecutive reduction steps[148,149].

$$[SeO_3]^{2-} \xrightarrow[NH_2OH]{\mathbf{1}} [Se]^0 \xrightarrow[N_2H_4\ or\ NaBH_4]{\mathbf{2}} [Se_2]^{2-} \qquad \text{(I.I)}$$

The effectiveness of employing established protocols to reduce selenium salt in solution and achieve the desired emissive species was investigated.

Selenium salt reduction

Sodium borohydride ($NaBH_4$) and hydrazine (N_2H_4) were chosen as reducing agents to fulfill the equation (**I.I**). Accordingly, two different synthetic conditions were employed. The first **1)** involved sonochemical synthesis in water using sodium borohydride[149], while the second **2)** involved a synthesis in methanol with hydrazine[149,150]. In both cases, an inert atmosphere was employed to mitigate potential stability issues with the produced compounds. Additional information on the experimental procedure can be found in section **7.1.6**.

Method **1)** resulted in a selenium product that exhibited a noticeable color change, producing a deep red solution (**Figure I.I.A**). Comparison of the absorption spectra of non-

reduced sodium selenite (black line) with the produced absorption spectra (red line) revealed three new absorption bands at around 360, 465 and 545 nm, as depicted in **Figure I.I.B**. (See section **7.2.1** for supplementary information about the absorption spectroscopy technique).

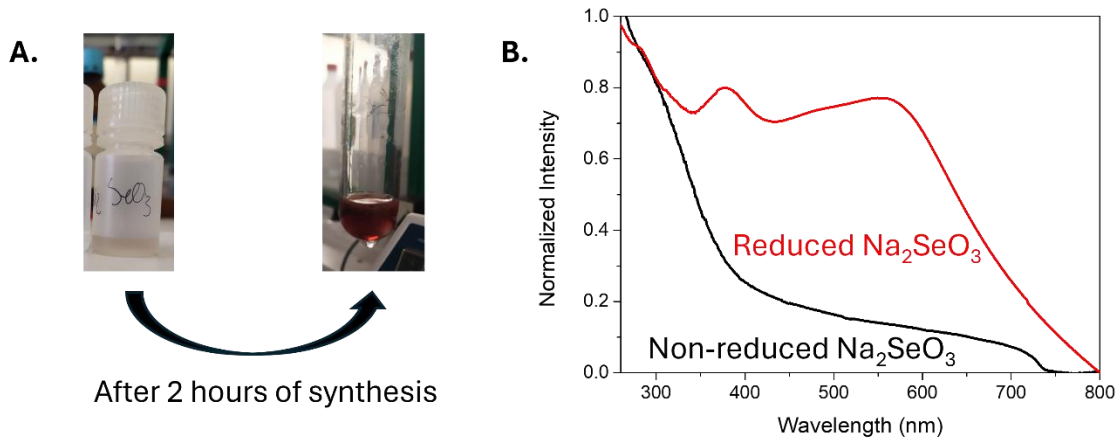


Figure I.I - Comparison between the initial and final selenium compounds after sonochemical synthesis. (**A**) Photos taken under ambient light and (**B**) corresponding absorption spectra.

The possibility that this red solution might be due to the presence of elemental selenium was further investigated. Elemental selenium typically manifests in either gray or red forms, both insoluble in water. The presence of gray elemental selenium was confirmed by observing a gray precipitate at the bottom of the synthesis Schlenk tube. The presence of red elemental selenium was ruled out after comparing the obtained spectrum in **Figure I.I.B** with the reported absorption spectrum of these species, which shows absorption bands around 345 and 520 nm[148]. Additionally, no emitting properties were detected when the red solution was observed under standard UV light (λ_{exc}=365 nm). For all these reasons, a direct assignment of the species present in the solution was not possible.

In zeolites, $[Se_2]^{2-}$ clusters exhibit photochromic properties, with non-induced color appearing at around 475 nm and, after UV excitation, around 500 nm[80]. Since the produced red species have an absorption band around 475 nm, these species were introduced into nanozeolites during the sol-gel synthesis of nanosodalite (**Figure I.II**). The gel ratio composition used consisted of $18Na_2O{:}5SiO_2{:}1Al_2O_3{:}240H_2O{:}\underline{0.34SeO_2}$, resulting in a final ideal composition of $[Na_6(H_2O)_8][Si_6Al_6O_{24}]\underline{Se_1}$. For additional information on the experimental procedure, see section **7.1.2**.

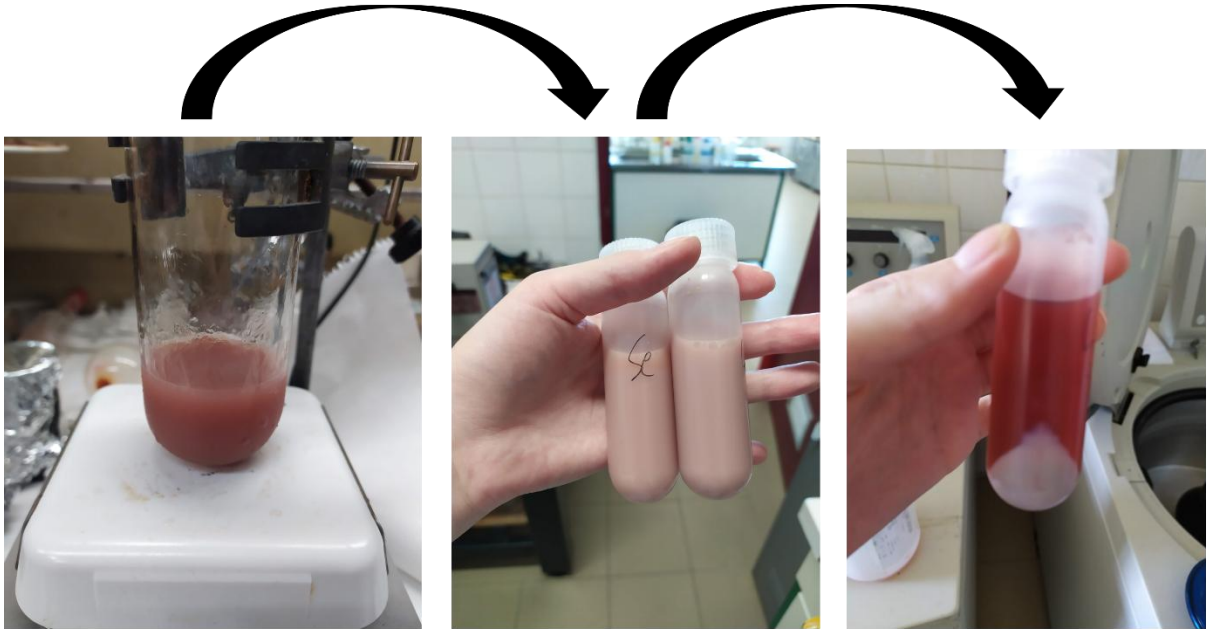


Figure I.II - Photos of the mixture during and after synthesizing the selenium-doped Se_1 gel nanosodalite sample.

The resulting product exhibits a pinkish color, with a broad absorption band peaking at around 575 nm (**Figure I.III.A**). This is not consistent with the formation of the targeted selenium luminescent species $[Se_2]^-$ and $[Se_3]^{2-}$ or with the photochromic $[Se_2]^{2-}$ clusters. Furthermore, the lack of emissive properties was confirmed by exciting these materials at the wavelengths of the emissive species of interest.

Furthermore, incorporating these species during the synthesis of nanosodalite did not affect the resulting product, as evidenced by the identical PXRD diffractogram observed for both doped and non-doped nanosodalite samples, see **Figure I.III.B**.

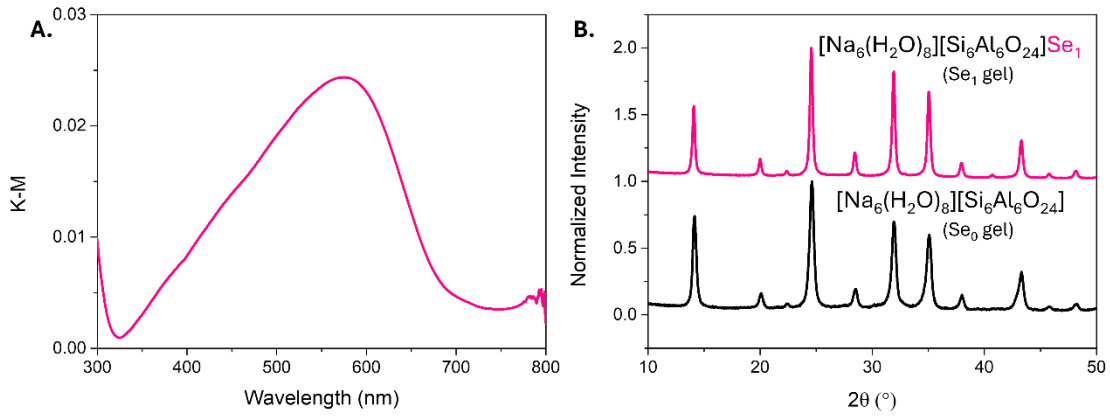


Figure I.III - (**A**) Diffuse reflectance spectra and (**B**) PXRD diffractogram of the produced selenium-doped Se_1 gel nanosodalite sample compared with the non-doped nanosodalite Se_0 gel sample.

Method **2)** revealed an orange product with two absorption bands at 340 nm and a lower one at 560 nm (**Figure I.IV.A**). This spectrum differs significantly from that obtained using method **1)**.

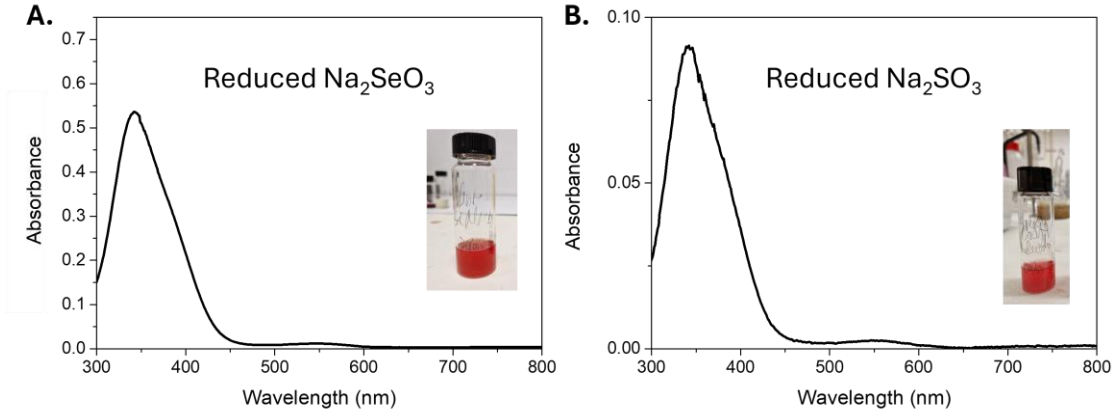


Figure I.IV - Absorption spectra of an aliquot of the products resulting from the reduction of sodium selenite (**A**) and sodium sulfite (**B**) salt in methanol, along with corresponding photos of the products in the insets.

However, once more, a direct assignment of these species was difficult, particularly since the reduction of sodium sulfite (Na_2SO_3) led to the formation of the same species (**Figure I.IV.B**). Thus, the solutions produced by method (**2**) do not seem to be due to reduced chalcogen salts.

2024

CATARINA SOFIA MIRANDA VIOLA

CHALCOGEN-DOPED LUMINESCENT ZEOLITES FOR NEAR-INFRARED APPLICATIONS